SEDIMENTING LIGHT CHAINS:

a biophysical analysis of pathological immunoglobulin free light chains from patients with multiple myeloma

Inaugural dissertation

For the attainment of the title of doctor
in the Faculty of Mathematics and Natural Sciences
at the Heinrich Heine University Düsseldorf

presented by
Florian T. Tucholski
from Duisburg, Germany

Düsseldorf, April 2026

From the Institut für Physikalische Biologie
at Heinrich Heine University Düsseldorf

Published with the permission of the
Faculty of Mathematics and Natural Sciences
at Heinrich Heine University Düsseldorf

Supervision

1. Prof. Dr. Dieter Willbold
2. Prof. Dr. Rainer Haas
3. Dr. Luitgard Nagel

Date of oral examination: 28.08.2026

Acknowledgement

I gratefully acknowledge the doctoral fellowship awarded by the Jürgen Manchot Foundation. I also thank the Beatrix Erbslöh Foundation for additional financial support.

I would like to express my sincere gratitude to Prof. Dr. Dieter Willbold for giving me the opportunity to conduct my doctoral studies in his laboratory and for his continuous support throughout this time. I am equally grateful to Prof. Dr. Rainer Haas for his valuable input, thoughtful guidance, and continued encouragement throughout this work.

I am very grateful to Dr. Luitgard Nagel for her continuous experimental supervision, insightful discussions, and constant support throughout this project.

I would also like to thank Prof. Dr. Alexander K. Buell for his support and for enabling my research stay at the Technical University of Denmark (DTU), which greatly enriched this work.

My sincere thanks go to Dr. Hamed Shaykhalishahi and Dr. Shuangyan Wang for their invaluable assistance with recombinant expression experiments. I also thank Dr. Rebecca Sternke-Hoffmann for her support during the early stages of this work, and Dr. Thomas Pauly for his assistance during the course of the project.

I thank Dr. Lothar Gremer for many insightful discussions and valuable scientific input. I also thank Dr. Katharina Vormann for her support, as well as Nazanin Fazelnia for valuable scientific exchange within the research group of Dr. Luitgard Nagel.

I would like to thank all past and present members of the IPB for the pleasant and supportive working environment, and in particular the technical staff for maintaining the laboratory infrastructure. I am especially grateful to Dr. Tina Jacob and Luis Gardon for their constant support, companionship, and the many moments we shared throughout this time.

I would like to thank Constanze Rana Parwez for her tireless support throughout my doctoral studies. Whenever it was difficult to maintain momentum, her strength and courage carried me forward.

I am deeply grateful to my family for their unwavering support.

Finally, I would like to thank all patients who participated in this study. Their contribution made this work possible.

Table of contents

List of abbreviations

6xHis	polyhistidine tag
AEC	anion-exchange chromatography
AKI	acute kidney injury
AL amyloidosis	light chain amyloidosis
ALS	amyotrophic lateral sclerosis
AmpR	ampicillin resistance gene
AOX1	alcohol oxidase 1
AUC	analytical ultracentrifugation
B cell	B lymphocyte
BJP	Bence Jones protein
BMGY	buffered glycerol-complex medium
BMMY	buffered methanol-complex medium
BSA	bovine serum albumin
CD	circular dichroism
CDR	complementarity-determining region
CJD	Creutzfeldt-Jakob disease
CKD	chronic kidney disease
C_L	light chain constant region
CRAB	hypercalcemia, renal dysfunction, anemia, and bone lesions
$c(s)$	continuous sedimentation coefficient distributions
CtsD/L/E	cathepsin D/L/E
dFLC	difference between involved and non-involved free light chains
Dsb	disulfide bond protein
DSC	differential scanning calorimetry
DSF	differential scanning fluorimetry
DTT	dithiothreitol
E. coli	*Escherichia coli*
EDTA	ethylenediaminetetraacetic acid
eGFR	estimated glomerular filtration rate
ER	endoplasmic reticulum
Ero1	ER oxidoreductin 1
F-ratio	confidence level
Fab domain	fragment antigen-binding domain
Fc domain	fragment crystallizable domain
FkpA	FK506-binding protein A
FLC	free light chain
FR	framework region

GdnHCl	guanidine hydrochloride
GFR	glomerular filtration rate
Grx	glutaredoxin
GSH	reduced glutathione
GSSG	oxidized glutathione
H_2O_2	hydrogen peroxide
HC	heavy chain
HEK293	human embryonic kidney cells
HRP	horseradish peroxidase
HAS	human serum albumin
HT	high tension
IB	inclusion body
IDP	intrinsically disordered protein
IgG	immunoglobulin G
IGKV1-33	immunoglobulin kappa variable 1-33
IMAC	immobilized metal affinity chromatography
IL-1β	interleukin-1 beta
IL-6	interleukin-6
IPTG	isopropyl β-D-1-thiogalactopyranoside
J_L	light chain joining segment
KDIGO	Kidney Disease: Improving Global Outcomes
LC	light chain
LCCN	light chain cast nephropathy
LCMM	light chain multiple myeloma
MGRS	monoclonal gammopathy of renal significance
MGUS	monoclonal gammopathy of undetermined significance
MM	multiple myeloma
MQ	menaquinone
MWCO	molecular weight cut-off
NaCl	sodium chloride
NMWL	nominal molecular weight limit
OD	optical density
OMP	outer membrane protein
PCD	plasma cell disorder
pCHAP	pET-derived, chaperone-assisted periplasmic expression
PCR	polymerase chain reaction
PDI	protein disulfide isomerase
PMSF	phenylmethylsulfonyl fluoride
P. pastoris	*Pichia pastoris*
PrP	prion protein
PTM	post-translational modification

PVDF	polyvinylidene fluoride
RI	radial-invariant
rLC	recombinant light chain
RMSD	root mean square deviation
RNaseA	ribonuclease A
ROS	reactive oxygen species
s-value	sedimentation coefficient
scFv	single-chain antibody fragments
SDS-PAGE	sodium dodecyl sulphate-polyacrylamide gel electrophoresis
SE	sedimentation equilibrium
SEC	size-exclusion chromatography
SH	thiol group
Skp	seventeen-kilodalton protein
SMM	smoldering multiple myeloma
SOC	super optimal broth with catabolic repression
SOD1	superoxide dismutase 1
sPCL	secondary plasma cell leukemia
SurA	survival protein A
SV	sedimentation velocity
TAE	Tris-Acetate-EDTA
TBS	Tris-buffered saline
TBST	Tris-buffered saline with Tween 20
TCEP	tris(2-carboxyethyl)phosphine
TE	test expression
TGF-β	transforming growth factor-beta
THP	Tamm-Horsfall protein
TI	time-invariant
Trx	thioredoxin
TrxA	thioredoxin 1
UMOD	uromodulin
UQ	ubiquinone
UV	ultraviolet
V_L	light chain variable region
YNB	yeast nitrogen base
YPD	yeast extract peptone dextrose
YPDS	yeast extract peptone dextrose sorbitol
α-MF	prepro-alpha mating factor

Summary

Plasma cell disorders such as multiple myeloma and light chain amyloidosis are characterized by the production of monoclonal immunoglobulin free light chains (FLCs), which can contribute to organ injury, most commonly affecting the kidneys. Although the risk of organ involvement increases with rising serum FLC concentrations, patients with comparable FLC levels can present with markedly different patterns and severity of organ damage. This indicates that pathogenicity is determined not only by clonal burden but also by intrinsic, sequence-dependent physicochemical properties of the FLCs and by local tissue microenvironments that influence destabilization and self-association. Pathological FLCs display pronounced molecular heterogeneity and exist as mixtures of monomers, covalent and non-covalent dimers, higher-order oligomers, and fragments, with relative abundances that depend on environmental conditions. Resolving these dynamic distributions under defined conditions is therefore essential for linking molecular behavior to disease-relevant mechanisms.

In this thesis, sedimentation velocity analytical ultracentrifugation (SV-AUC) was employed to quantify FLC species distributions and to monitor their redistribution under controlled destabilizing conditions. Urinary FLCs from nine multiple myeloma patients exhibited substantial molecular heterogeneity and sample-specific responses to disulfide bond destabilization. Reduction induced redistribution of molecular species with variable extent and kinetics. Dimeric species typically declined at early time points without generating stable monomers, resulting instead in transient, aggregation-prone intermediates. In several samples, persisting dimers were observed, suggesting sequence-dependent disulfide protection or additional non-covalent stabilization. Aggregation behavior varied widely among samples and showed no association with clinical parameters, underscoring the multifactorial nature of organ involvement. To relate these findings to structural stability, SV-AUC was complemented by differential scanning fluorimetry and circular dichroism spectroscopy. Disulfide reduction decreased thermal stability as a function of oligomerization and ionic strength. Prolonged reducing conditions were accompanied by gradual changes in secondary-structure and reproducible fragmentation in FLCs of shared genetic origin, which could not be attributed to a single underlying mechanism.

To enable mechanistic investigations under defined redox and folding conditions, recombinant expression systems were established. Full-length patient-derived FLCs were produced in *Escherichia coli* using cytoplasmic inclusion body expression followed by *in vitro* refolding, as well as periplasmic secretion to promote oxidative folding *in vivo*. Minor alterations in redox balance markedly affected species distributions, yielding soluble but non-native conformations with altered molecular profiles. To approximate the eukaryotic folding environment more closely, FLCs were additionally expressed in *Pichia pastoris*. Recombinant FLCs obtained from this system displayed native-like secondary structure and hydrodynamic properties comparable to the patient-derived counterpart, including sedimentation coefficients for monomeric species, with minor differences in dimeric and higher-order oligomeric species.

Overall, pathological FLCs behave as redox- and environment-dependent conformational ensembles. Disulfide chemistry and folding context shape species distributions and modulate, under destabilized conditions, both redistribution toward higher-order assemblies and fragmentation of FLCs. By integrating analyses of patient-derived samples with recombinant material, this work

provides a biophysical basis for investigating redox-response signatures and species distributions of FLCs in the context of multiple myeloma and other light chain disorders.

Zusammenfassung

Plasmazellerkrankungen wie das multiple Myelom und die Leichtketten-Amyloidose sind durch die Produktion monoklonaler freier Immunglobulin-Leichtketten (FLCs) gekennzeichnet, die zu Organschädigungen führen können, wobei die Nieren am häufigsten betroffen sind. Während höhere Serum-FLC-Konzentrationen das Risiko einer Organbeteiligung steigern, können Patienten mit vergleichbaren Konzentrationen deutlich unterschiedliche Muster und Schweregrade von Organschädigungen zeigen. Dies verdeutlicht, dass die Pathogenität nicht allein durch die klonale Belastung bestimmt wird, sondern zusätzlich durch intrinsische, sequenzabhängige physikochemische Eigenschaften der FLCs sowie durch lokale Gewebemilieus, die Destabilisierung und Selbstassoziation beeinflussen. Pathologische FLCs weisen eine ausgeprägte molekulare Heterogenität auf und liegen als Gemische aus Monomeren, kovalenten und nicht-kovalenten Dimeren, höhergeordneten Oligomeren sowie Fragmenten vor, deren relative Anteile von den jeweiligen Umgebungsbedingungen abhängen. Die Charakterisierung dieser dynamischen Verteilung unter definierten Bedingungen ist daher entscheidend, um molekulares Verhalten mit krankheitsrelevanten Mechanismen zu verknüpfen.

In dieser Arbeit wurde die analytischer Ultrazentrifugation in Sedimentationsgeschwindigkeitsexperimenten (SV-AUC) eingesetzt, um die Speziesverteilungen der FLCs zu quantifizieren und deren Umverteilung unter kontrollierten destabilisierenden Bedingungen zu untersuchen. Die aus dem Urin isolierten FLCs von neun Patienten mit multiplem Myelom zeigten jeweils eine ausgeprägte molekulare Heterogenität sowie probenspezifische Reaktionen auf die Destabilisierung von Disulfidbrücken. Die Reduktion führte zu einer Umverteilung der molekularen Spezies mit variabler Ausprägung und Kinetik. Dimere nahmen typischerweise bereits zu frühen Zeitpunkten ab, ohne stabile Monomere freizusetzen, sondern bildeten stattdessen transiente, aggregationsanfällige Intermediate. In mehreren Proben blieben dimere Spezies erhalten, was auf eine sequenzabhängige Stabilisierung der Disulfidbrücken oder zusätzliche nicht-kovalente Wechselwirkungen hinweist. Das Aggregationsverhalten variierte deutlich zwischen den Proben und zeigte keine Korrelation mit klinischen Parametern, was die multifaktorielle Natur der Organbeteiligung weiter verdeutlicht. Zur Einordnung dieser Beobachtungen im Hinblick auf die strukturelle Stabilität wurden ergänzende Analysen mittels *Differential Scanning Fluorimetry* und *Circulardichroism Spectroscopy* durchgeführt. Die Reduktion von Disulfidbrücken führte zu einer Abnahme der thermischen Stabilität in Abhängigkeit vom Oligomerisierungsgrad und der Ionenstärke. Unter verlängerten reduzierenden Bedingungen traten graduelle Veränderungen der Sekundärstruktur sowie reproduzierbare Fragmentierung bei FLCs gemeinsamen genetischen Ursprungs auf, ohne dass ein einzelner zugrunde liegender Mechanismus identifiziert werden konnte.

Für mechanistischer Untersuchungen unter definierten Redox- und Faltungsbedingungen wurden rekombinante Expressionssysteme etabliert. Basierend auf sequenzierten Patientenproben wurden FLCs voller Länge in *Escherichia coli* sowohl durch zytoplasmatische Expression in Einschlusskörperchen mit anschließender Rückfaltung *in vitro* als auch durch periplasmatische Sekretion zur Förderung oxidativer Faltung *in vivo* hergestellt. Bereits geringe Veränderungen im Redoxgleichgewicht führten zu deutlichen Verschiebungen der Speziesverteilungen und resultierten in löslichen, jedoch nicht-nativen Konformationen mit veränderten molekularen Profilen. Zur

Annäherung an die eukaryotische Faltungsumgebung wurden FLCs zusätzlich in *Pichia pastoris* exprimiert. Die dort gewonnenen rekombinanten FLCs zeigten eine nativ-ähnliche Sekundärstruktur und hydrodynamische Eigenschaften, die mit der entsprechenden Patientenprobe vergleichbar waren, einschließlich übereinstimmender Sedimentationskoeffizienten für monomere Spezies, jedoch mit geringfügigen Unterschieden bei dimeren und höhergeordneten Oligomeren.

Insgesamt verhalten sich pathologische FLCs als redox- und umgebungsabhängige konformationelle Ensembles. Disulfidchemie und Faltungskontext prägen die Speziesverteilungen und modulieren unter destabilisierenden Bedingungen sowohl die Umverteilung hin zu höhergeordneten Spezies als auch die Fragmentierung der FLCs. Durch die Kombination von Patientenproben und rekombinantem Material liefert diese Arbeit eine biophysikalische Grundlage zur Untersuchung von Redoxreaktionsmustern und Speziesverteilungen von FLCs im Kontext von multiplem Myelom und anderen Leichtkettenerkrankungen.

1

General introduction

1.1 Clinical background and motivation

1.1.1 Multiple myeloma within the spectrum of plasma cell disorders

Multiple myeloma (MM) is a malignant plasma cell disorder (PCD) characterized by clonal expansion of terminally differentiated plasma cells within the bone marrow and secretion of a monoclonal immunoglobulin, commonly referred to as M-protein or paraprotein (Kumar et al. 2017; Van De Donk et al. 2021; Cowan et al. 2022; Neumeister et al. 2022; Malard et al. 2024; Tasbihi and Bruns 2025). As a post-germinal center B-lineage malignancy, MM develops within a spectrum of PCDs (Fig. 1.1) in which monoclonal gammopathy of undetermined significance (MGUS) and smoldering multiple myeloma (SMM) represent asymptomatic precursor states (Furukawa and Kikuchi 2015; Kumar et al. 2017; Van De Donk et al. 2021; Neumeister et al. 2022; Petrilla et al. 2023; Plano et al. 2023; Malard et al. 2024). MGUS is characterized by a low plasma cell burden and M-protein production without end-organ damage, whereas SMM reflects increased clonal expansion in the absence of myeloma-defining events (Kumar et al. 2017; Gámez and Edwards 2018; Petrilla et al. 2023; Plano et al. 2023). MM is a chronically progressive and ultimately incurable hematologic malignancy (Neumeister et al. 2022; Tasbihi and Bruns 2025) that predominantly affects older adults (median age ~65 years), although diagnoses in younger patients are increasingly observed (Pinto et al. 2020; Muylaert et al. 2022). The etiology remains unclear, but age, sex, ethnicity, genetic predisposition, lifestyle, and environmental factors are recognized contributors to disease risk (Kumar et al. 2017; Plano et al. 2023). Epidemiological observations further implicate environmental exposures, exemplified by increased MGUS prevalence and earlier MM onset in firefighter and 9/11 first responder cohorts, particularly for light chain-associated gammopathies (LeMasters et al. 2006; Landgren et al. 2018; Van De Donk et al. 2021; Cowan et al. 2022).

At a mechanistic level, environmental stressors and reactive oxygen species (ROS) can contribute to genomic instability, while malignant plasma cells exhibit elevated mutational burdens driven by replication stress, oncogene activation, and altered DNA damage responses (Petrilla et al. 2023). Symptomatic MM is defined by significant clonal plasma cell infiltration together with myeloma-defining events, which are summarized by the CRAB criteria (hyper<u>c</u>alcemia, <u>r</u>enal dysfunction, <u>a</u>nemia, and <u>b</u>one lesions) or by biomarkers of imminent organ damage (Rajkumar et al. 2014; Cowan et al. 2022). Clinical presentation is heterogeneous and ranges from asymptomatic disease to hematopoietic insufficiency and organ damage, including anemia-associated fatigue, renal injury,

osteolytic bone destruction with fractures, hypercalcemia, and increased susceptibility to infection (Petrilla et al. 2023; Plano et al. 2023; Tasbihi and Bruns 2025). While many patients secrete intact immunoglobulins, a substantial subgroup produces only monoclonal free light chains (FLCs), which is also referred to as light chain multiple myeloma (LCMM; Malard et al. 2024).

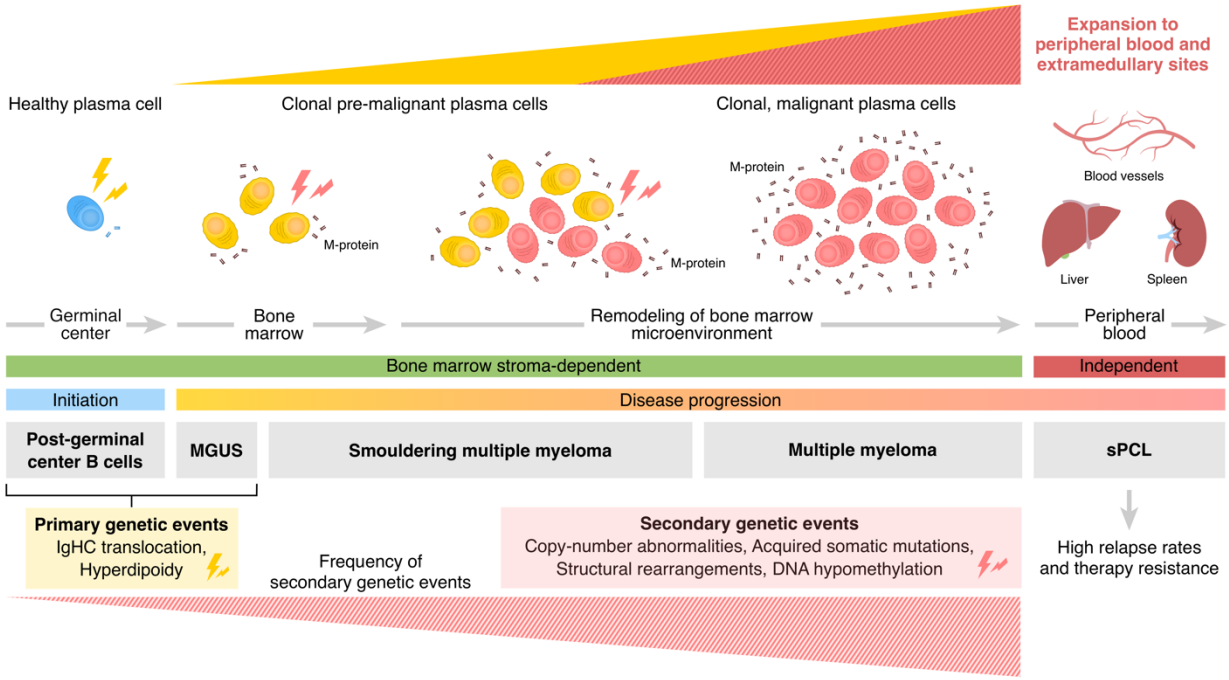

Figure 1.1: Multistep development of PCDs. Schematic overview of MM evolution from a post-germinal center B lymphocyte (B cell; blue) through the precursor states MGUS and SMM to overt MM with end-organ damage. The figure illustrates the progressive increase in clonal pre-malignant (yellow) and malignant (red) plasma cell burden and circulating M-protein levels, the emergence of early primary genetic lesions with subsequent accumulation of secondary genetic and epigenetic alterations, and progressive remodeling of the bone marrow microenvironment. Early disease stages remain dependent on stromal interactions within the bone marrow niche, whereas advanced disease acquires relative stromal independence, facilitating extramedullary dissemination and, in late stages, peripheral blood involvement which leads to secondary plasma cell leukemia (sPCL). Figure adapted from Furukawa and Kikuchi 2015; Kumar et al. 2017; Gámez and Edwards 2018; Neumeister et al. 2022; Petrilla et al. 2023; Plano et al. 2023; Tasbihi and Bruns 2025.

Across the spectrum of PCDs, the physicochemical properties of the monoclonal protein, particularly FLCs, critically influence organ involvement, as exemplified by monoclonal gammopathy of renal significance (MGRS) and light chain (AL) amyloidosis (Bridoux et al. 2025). MM is biologically and genetically heterogeneous and develops through multiple stages. Primary genomic events, including hyperdiploidy and immunoglobulin heavy-chain translocations, can be detected at early disease stages, whereas secondary genetic and epigenetic alterations, such as copy-number abnormalities and somatic mutations, accumulate during progression from MGUS to SMM and MM and drive subclonal expansion and therapeutic resistance (Bergsagel et al. 2005; Kumar et al. 2017; Ramakrishnan and Kumar 2018; Petrilla et al. 2023; Plano et al. 2023; Tasbihi and Bruns 2025). A defining hallmark of MM is the dysregulation of DNA damage responses and DNA repair pathways, which facilitates tumor evolution and resistance to therapy (Petrilla et al. 2023). In parallel, reciprocal

interactions between malignant plasma cells and the bone marrow microenvironment play a central role in disease initiation, progression, and relapse (Neumeister et al. 2022; Plano et al. 2023; Tasbihi and Bruns 2025). Early disease stages are characterized by strong dependence on stromal support and soluble factors, including interleukin-6 (IL-6), whereas advanced MM can acquire relative stromal independence, enabling extramedullary dissemination and aggressive clinical behavior (Furukawa and Kikuchi 2015). Expansion of clonal plasma cells into peripheral blood following previously diagnosed MM defines sPCL, representing a late and particularly aggressive disease manifestation (Furukawa and Kikuchi 2015; Kumar et al. 2017; Tasbihi and Bruns 2025). Despite substantial improvements in outcome achieved through advances in disease understanding, risk stratification, autologous stem cell transplantation, and novel therapeutic agents, MM remains incurable, with frequent relapse and development of multidrug-refractory disease (Pinto et al. 2020; Van De Donk et al. 2021; Cowan et al. 2022; Petrilla et al. 2023; Malard et al. 2024; Tasbihi and Bruns 2025).

1.1.2 Renal involvement in PCD

Renal impairment is one of the most frequent and clinically consequential complications of MM, contributing markedly to morbidity and early mortality (Van De Donk et al. 2021; Cowan et al. 2022; Malard et al. 2024). At diagnosis, 16-31% of patients present with acute kidney injury (AKI), and 36-45% show reduced renal function (estimated glomerular filtration rate (eGFR) <60 mL/min/1.73 m^2), with 12-17% presenting with severe impairment (eGFR <30 ml/min/1.73 m^2), and 6-13% ultimately requiring dialysis (Leung and Rajkumar 2023; Bridoux et al. 2025). Light chain cast nephropathy (LCCN) is classified as myeloma-defining event and the predominant cause of MM-associated AKI. Excessively filtered monoclonal FLCs can interact with uromodulin (UMOD) also known as Tamm-Horsfall protein (THP) in the distal nephron, forming obstructive casts that induce tubular rupture, inflammation, oxidative stress, and tubulointerstitial fibrosis (Leung and Rajkumar 2023; Malard et al. 2024). AKI risk correlates with serum FLC concentration and is rare below ~50 mg/L but increases sharply above 80-200 mg/L, particularly with high urinary FLC excretion. Rapid FLC reduction is the key determinant of renal recovery and a ≥50-60% decline within 1-2 weeks significantly improves outcomes (Yadav et al. 2020). Early therapeutic intervention, together with supportive measures and, in selected cases, extracorporeal FLC removal, is therefore essential (Bridoux et al. 2025). Diagnostic classification of renal injury remains crucial. While biopsy is the diagnostic standard, it may be omitted when clinical features suggest LCCN, such as predominant light chain proteinuria combined with markedly elevated serum FLC levels above 150 mg/L (Leung and Rajkumar 2023).

Beyond their pathogenic role, FLCs serve as indispensable biomarkers. Serum FLC analysis show near-complete sensitivity for diagnosing LCMM and detect AL amyloidosis and LCDD with sensitivities above 80-90% (Siegel et al. 2009). Baseline FLC levels provide prognostic information across PCDs, while abnormalities in FLC ratio identify MGUS patients at increased risk of progression and serial FLC monitoring is essential for evaluating treatment response (Siegel et al. 2009). FLCs thus serve as both biomarkers of clonal activity and direct mediators of tissue injury. Their physicochemical and structural properties govern organ involvement, renal toxicity, and clinical

outcome. Defining the molecular determinants that control FLC stability, misfolding, and aggregation is thus essential for understanding organ damage in MM and related PCDs.

1.2 Structural and molecular basis of FLC pathology

1.2.1 Molecular architecture of immunoglobulin light chains

Immunoglobulins are central effectors of the humoral adaptive immune response and are secreted by terminally differentiated plasma cells. Structurally, antibodies adopt a conserved H_2L_2 quaternary architecture composed of two identical heavy chains (HCs) and two identical light chains (LCs) covalently linked by disulfide bonds, resulting in a Y-shaped molecule, as schematically illustrated for immunoglobulin G (IgG) in Figure 1.2 (Edelman et al. 1968; Janeway 2001; Nakano et al. 2011; Gudowska-Sawczuk and Mroczko 2023). LCs are ~22 kDa polypeptides consisting of an N-terminal variable (V_L) domain and a C-terminal constant (C_L) domain, connected by a short joining segment (J_L). Both domains adopt the immunoglobulin β-sandwich fold stabilized by a conserved intradomain disulfide bond (Schroeder and Cavacini 2010; Feige et al. 2010; Nakano et al. 2011; Andrich et al. 2017; Ezawa et al. 2025). One LC associates with the N-terminal portion of an HC to form the fragment antigen-binding (Fab) domain, which contains the paratope responsible for antigen recognition and determines antigen specificity and affinity. The remaining C-terminal regions of the two HCs constitute the fragment crystallizable (Fc) domain, which mediates effector functions through interactions with Fc receptors, complement proteins, as well as immune effector cells (Janeway 2001; Feige et al. 2010).

Two LC isotypes exist: Kappa (κ) and Lambda (λ), which are encoded on distinct chromosomal loci. Each mature B cell expresses only one LC isotype, a phenomenon termed isotype exclusion, although the regulatory mechanisms remain incompletely understood (Neuberger et al. 1989; Schroeder and Cavacini 2010; Nakano et al. 2011; Gudowska-Sawczuk and Mroczko 2023). The V_L domain displays extensive sequence heterogeneity generated by V-J recombination and somatic hypermutations, particularly within the complementarity-determining regions (CDRs), which form solvent-exposed loops defining antigen recognition and specificity. In contrast, the C_L domain is highly conserved within and across individuals (Feige et al. 2010; Roth 2014). During immunoglobulin biosynthesis, HCs and LCs are synthesized asynchronously on separate ribosomes and are co-translationally translocated into the endoplasmic reticulum (ER), where folding, disulfide bond formation, and assembly occur (Feige et al. 2010). LCs are physiologically produced in excess, typically by 10-40% relative to HCs, ensuring efficient H_2L_2 assembly and preventing intracellular aggregation of unpaired HCs (Bradwell et al. 2002; Nakano et al. 2011). Excess LCs are secretion-competent and are released into the circulation as FLCs (Solomon et al. 1964). In healthy individuals, polyclonal FLC serum concentrations are approximately 1000-fold lower than intact immunoglobulins due to rapid renal clearance, with a physiological κ/λ ratio close to 2:1 (Bradwell et al. 2002; Bradwell 2005; Nakano et al. 2011; Gudowska-Sawczuk and Mroczko 2023).

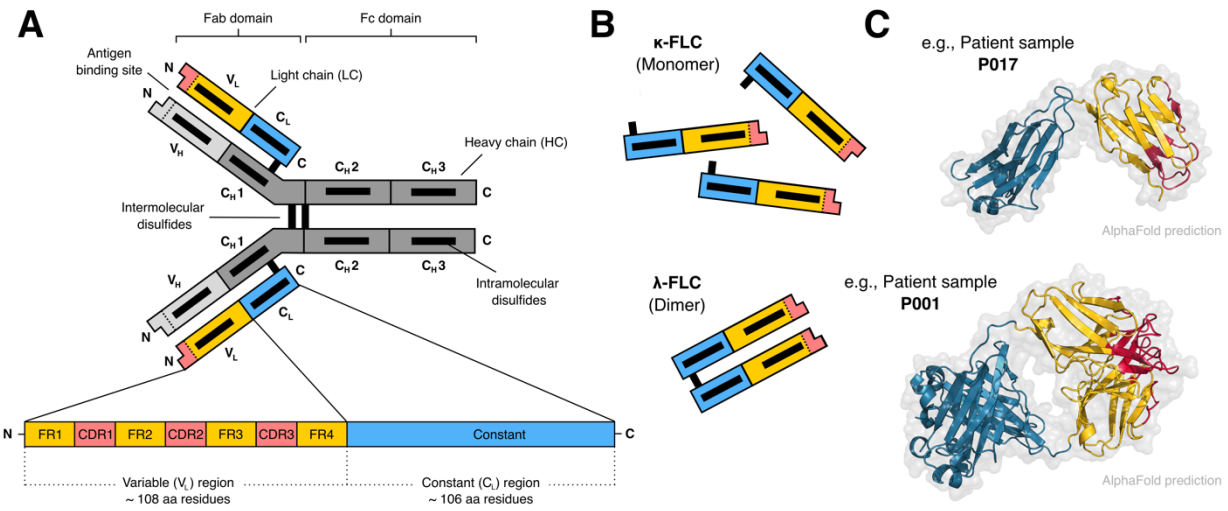

Figure 1.2: FLC structure and assembly states. (**A**) Schematic representation of an IgG antibody, showing its Y-shaped H_2L_2 architecture. HCs are shown in grey, and LCs are highlighted in color, with the C_L domain in blue and framework regions (FRs) of the V_L domain in yellow, as well as CDRs in red. Inter- and intrachain disulfide bonds (black bars) and the N- and C-termini are indicated. (**B**) Association states of FLCs in solution. κ-FLCs predominantly occur as monomers, whereas λ-FLCs preferentially form covalently linked dimers via intermolecular disulfide bonds. (**C**) Predicted structures of the patient-derived κ-FLC P017 and λ-FLC P001, generated with AlphaFold 3 (Jumper et al. 2021). Highlighted are C_L regions (blue) and V_L regions with FRs (yellow) and CDRs (red). Structural visualization was performed using PyMOL version 2.5.8 (Schrödinger, LLC 2015). Figure adapted from Dispenzieri et al. 2009; Mirsky et al. 2015; Gudowska-Sawczuk and Mroczko 2023.

1.2.2 Conformational heterogeneity and quaternary assembly of FLCs

FLCs exist as monomers, dimers, and higher-order assemblies. While κ-FLCs predominantly occur as monomers or non-covalently associated dimers, λ-FLCs preferentially form covalent homodimers via an intermolecular disulfide bond involving the conserved C-terminal cysteine within the C_L domain (Klein et al. 1977; Roussel et al. 1999; Andrich et al. 2017; Džupponová and Žoldák 2023). These structural differences influence hydrodynamic behavior, renal handling, and clearance kinetics. At elevated concentrations, as encountered in PCDs, mass action favors the formation of higher-order assemblies (Džupponová and Žoldák 2023). Early studies also described non-covalently associated tetramers composed of two dimers in patients with MM, and subsequent work identified a broad spectrum of circulating disulfide-linked FLC species in AL amyloidosis, including assemblies between full-length molecules and proteolytic fragments (Grey and Kohler 1968; Kaplan et al. 2009). Such structural heterogeneity may interfere with physiological clearance mechanisms and further promote tissue deposition beyond the effect of elevated FLC concentrations alone. At molecular level, this complexity is reflected in the relationship between dimerization and aggregation propensity. Covalent dimerization can increase kinetic stability and suppress unfolding, yet it may also favor the formation of aggregation-prone intermediates under pathological conditions or upon destabilization (Kaplan et al. 2011; Morgan and Kelly 2016; Andrich et al. 2017). Disruption of stabilizing disulfide bonds in FLCs has been shown to alter folding pathways, promote misfolded off-pathway species, and drive the formation of large, branched aggregates via monomer-addition mechanisms, suggesting quaternary

structure and disulfide chemistry as key determinants of FLC behavior *in vivo* (Andrich et al. 2017; Džupponová and Žoldák 2023; Ezawa et al. 2025).

1.2.3 Sequence variability, redox regulation, and aggregation pathways

The extraordinary diversity of FLC sequences is a defining feature of their biology and a major determinant of pathological behavior. Patient-specific mutations within the V_L domain can modulate thermodynamic stability, conformational dynamics, dimer interfaces, susceptibility to proteolysis, and reduction-oxidation (redox) sensitivity, which influences the aggregation propensity of FLCs (Andrich et al. 2017; Ezawa et al. 2025). In AL amyloidosis, monoclonal FLCs assemble into highly ordered amyloid fibrils characterized by cross-β-sheet architecture. High-resolution structural studies have revealed that fibril cores are frequently deriving from the V_L domain, which retain their conserved intradomain disulfide bond, yet adopt conformations fundamentally distinct from their native fold, indicating extensive unfolding and structural rearrangements during fibrillogenesis (Andrich et al. 2017; Ezawa et al. 2025). In contrast, amyloid fibril formation is rarely observed in MM, despite similarly high circulating FLC levels, further highlighting that pathology is not solely concentration-driven but is modulated by intrinsic sequence features, post-translational modifications (PTMs), fragmentation, and redox state (Andrich et al. 2017). Disulfide bonds are a key structural determinant in this context. Intradomain disulfides stabilize the native fold and suppress alternative conformations, whereas perturbation or reduction of these bonds destabilizes the protein and promotes aggregation. Reduced and oxidized FLCs can adopt immunoglobulin-like folds under native conditions, however, reduced forms preferentially form misfolded off-pathway intermediates, emphasizing the importance of the redox environment in controlling FLC folding and aggregation (Andrich et al. 2017; Džupponová and Žoldák 2023; Ezawa et al. 2025).

1.2.4 Renal clearance and structural consequences

The kidney is the principal site of FLC catabolism. Under physiological conditions, FLCs are freely filtered through the glomerular barrier and are efficiently reabsorbed by proximal tubular epithelial cells, where they bind low-affinity, high-capacity receptors at the brush border, undergo endocytosis, and are degraded within lysosomes. The renal system can process up to 10-30 g of FLCs per day, explaining the low concentrations observed in healthy serum und urine. Glomerular filtration is size-dependent, with progressive restriction above ~30 kDa and near-complete exclusion above ~60 kDa. As a result, monomeric FLCs are cleared more rapidly than dimeric FLC species, contributing to isotype-specific differences in serum persistence and κ/λ ratios (Waldmann et al. 1972; Bradwell et al. 2002; Bradwell 2005; Nakano et al. 2011). As FLC production increases, serum concentrations rise while urinary excretion remains limited until proximal tubular reabsorptive capacity is exceeded. Beyond this threshold, urinary overflow occurs and FLCs enter the distal nephron, where interaction with UMOD promotes cast formation and tubular injury (Huang and Sanders 1997). Progressive nephron loss further amplifies serum FLC accumulation, creating a nonlinear feedback loop between

FLC concentration, oligomeric state, renal clearance, and tissue toxicity (Bradwell et al. 2002; Bradwell 2005; Džupponová and Žoldák 2023; Ezawa et al. 2025).

1.2.5 FLCs as biomarkers and pathogenic mediators

FLCs were historically regarded as inert by-products of antibody synthesis, however, their presence in urine, historically termed Bence Jones protein (BJP), has served as a diagnostic hallmark of MM and represents the earliest cancer biomarker in clinical medicine (Bradwell et al. 2002; Bradwell 2005). Analogous to the transition from urine to blood glucose testing in diabetes mellitus, serum FLC measurements provide a more direct and reliable readout of production dynamics than urine analyses, which are influenced by renal handling (Bradwell et al. 2002; Bradwell 2005). Serum FLC concentrations reflect the balance between synthesis by B-linage cells and renal clearance. In polyclonal immune activation or renal impairment, both κ- and λ-FLCs may increase in parallel, preserving the κ/λ ratio. In contrast, PCDs produce a monoclonal excess of a single LC with suppression of the alternative isotype, resulting in highly abnormal κ/λ ratios that serve as robust indicators of clonality (Katzmann et al. 2002).

Beyond PCDs, elevated FLC levels and altered κ/λ ratios have been documented in a wide range of inflammatory and immune-mediated conditions, including autoimmune diseases, infections, multiple sclerosis, diabetes, cardiovascular disorders, and other malignancies (Nakano et al. 2011). In these contexts, FLC concentrations correlate with disease activity, prognosis, and risk of progression, reflecting heightened B cell activation rather than clonal malignancy (Konen et al. 2021). FLCs have also been shown to interact directly with immune cells, modulating mast cell activation and neutrophil apoptosis, supporting a role as active mediators of inflammation (Nakano et al. 2011; Gudowska-Sawczuk and Mroczko 2023).

Collectively, literature established FLCs as structurally diverse and redox-sensitive proteins whose folding state, oligomerization behavior, and renal handling are closely linked to both their pathogenic potential and their utility as clinical biomarkers. Patient-specific sequence variation, disulfide chemistry, quaternary assembly, and clearance mechanisms together influence whether FLCs remain soluble, form non-native aggregates, or deposit as amyloid.

1.3 Sedimenting light chains

1.3.1 Resolving FLC heterogeneity in solution

The molecular features underlying FLC pathogenicity also contribute to pronounced molecular heterogeneity in solution. Patient-derived FLC preparations rarely exist as a single, well-defined species but rather as a mixture of monomers, covalent and non-covalent dimers, higher-order oligomers, and proteolytic fragments (Absmeier et al. 2023; Klimtchuk et al. 2024). The relative abundance of these components can change dynamically depending on concentration, redox potential, and solvent conditions. This reflects intrinsic aspects of FLC biology: oligomeric state, conformational

flexibility, and assembly behavior are directly linked to renal handling, aggregation propensity, and tissue deposition. Consequently, pathological FLCs require analysis as heterogeneous ensembles rather than as discrete molecular species. Methods that can resolve coexisting molecular species directly in solution while preserving disease-relevant distributions and interconversion behavior are therefore required for the characterization of pathological FLCs. Quantifying species distributions, monitoring condition-dependent changes, and detecting weak, transient, or partially irreversible assemblies are central to linking molecular properties to pathological outcomes. Solution-based hydrodynamic approaches are particularly well suited for this investigation, as they analyze macromolecules under defined physicochemical conditions, without separation or surface immobilization that could further alter disease-related distributions (Scott et al. 2007; Schuck and Zhao 2017).

1.3.2 Sedimentation velocity analytical ultracentrifugation

Analytical ultracentrifugation (AUC) remains a fundamental method for quantifying the size, shape, and self-association of macromolecules in solution or dispersion, providing a rigorous technique for analyzing heterogeneous and interacting systems (Ralston 1993; Scott et al. 2007; Cölfen 2010; Schuck et al. 2016; Schuck and Zhao 2017). Developed by Theodor Svedberg (Svedberg and Nichols 1923; Svedberg and Rinde 1924; Svedberg and Fåhraeus 1926) and refined through advances in rotor design, optical detection, and numerical analysis, AUC monitors the redistribution of solutes in a defined centrifugal field as a function of time and radial position. This provides direct insights into macromolecular transport without labeling, immobilization, or external calibration standards (Ralston 1993; Scott et al. 2007; Schuck et al. 2016).

Sedimentation velocity (SV) experiments follow the time-dependent migration of sedimentation boundaries under high centrifugal fields, whereas sedimentation equilibrium (SE) experiments exploit concentration gradients at lower rotor speeds to determine buoyant molar masses and association equilibria (Ralston 1993; Scott et al. 2007; Schuck et al. 2016). Because SV directly reports on transport behavior and particle distributions in heterogeneous systems, the present work focuses exclusively on SV-AUC (Ralston 1993; Scott et al. 2007; Schuck et al. 2016; Schuck and Zhao 2017). In SV-AUC, macromolecules migrate through the solvent under the influence of a centrifugal field whose magnitude increases with radial distance from the axis of rotation (Fig. 1.3).

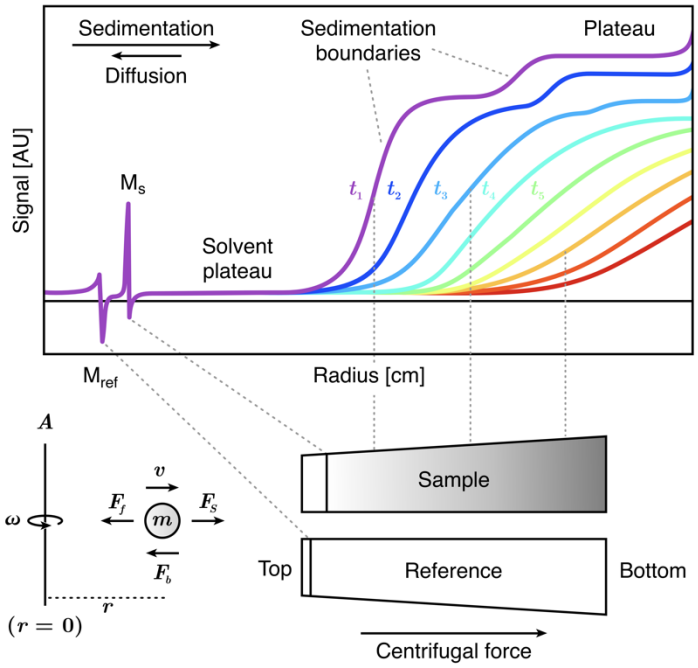

Figure 1.3: Principle of SV-AUC. Schematic representation of an SV experiment in a sector-shaped cell. Under a centrifugal field, a particle at radial position r is subjected to sedimentation (F_s), buoyancy (F_b), and frictional (F_f) forces and the resulting migration velocity v is set by their balance. Field strength increases with angular rotor speed ω and radial distance from the axis of rotation. The sector geometry favors radial transport and suppresses convection. Grey shading indicates changes in sample concentration over the course of the experiment. Time-resolved radial concentration profiles show sedimentation boundaries whose migration reports on macromolecular transport, while boundary broadening reflects diffusion and radial dilution. $c(s)$ distributions are obtained by fitting the full time- and radius-dependent profiles using numerical solutions of the Lamm sedimentation-diffusion equation (Ralston 1993; Van Holde et al. 2006).

Sedimentation is driven by the balance of three forces acting on each particle. The centrifugal driving force F_s is given by

$$F_s = m\omega^2 r \tag{1.1}$$

where m is the particle mass, ω the angular velocity of the rotor, and r the radial distance from the axis of rotation. Opposing sedimentation acts the buoyant force F_b, which arises from displacement of solvent according to Archimedes' principle,

$$F_b = -m\bar{v}\rho\omega^2 r \tag{1.2}$$

where $\bar{v}$ is the partial-specific volume of the solute and ρ the solvent density. Migration through the solvent is further opposed by the frictional force F_f,

$$F_f = -fv \tag{1.3}$$

with f denoting the translational friction coefficient and v the migration velocity (Ralston 1993; Scott et al. 2007; Schuck et al. 2016).

Under experimental conditions, these forces rapidly reach steady-state balance, resulting in a constant migration velocity. This balance defines the sedimentation coefficient s (s-value) as the velocity per unit of centrifugal acceleration,

$$s = \frac{v}{\omega^2 r} \tag{1.4}$$

which constitutes an intrinsic descriptor of macromolecular transport behavior (Ralston 1993; Scott et al. 2007; Schuck et al. 2016). In molecular terms, the s-value reflects the combined contributions of buoyant molar mass and hydrodynamic friction,

$$s = \frac{M(1 - \bar{v}\rho)}{N_A f} \tag{1.5}$$

where M is the molar mass and N_A Avogadro's number (Ralston 1993; Scott et al. 2007; Schuck et al. 2016). Sedimentation and diffusion are intrinsically coupled transport processes that share the same translational friction coefficient. Their relationship is expressed by the Svedberg equation,

$$\frac{s}{D} = \frac{M(1 - \bar{v}\rho)}{RT} \tag{1.6}$$

where D is the diffusion coefficient, R the gas constant, and T the absolute temperature (Scott et al. 2007; Schuck et al. 2016).

Together, these relationships establish a direct physical link between experimentally accessible transport properties and molecular parameters by relating sedimentation and diffusion behavior to molar mass, hydrodynamic friction, and consequently to molecular size, shape, and hydration (Scott et al. 2007; Schuck et al. 2016). The s-values are reported in Svedberg units (1 S = 10^{-13} s) and are conventionally corrected to standard conditions of water at 20°C and infinite dilution, resulting in $s_{20,w}$ values, which are suitable for comparison across experiments (Scott et al. 2007; Schuck et al. 2016). The translational friction coefficient can be related to solvent viscosity η and the Stokes radius R_S through Stokes' law,

$$f = 6\pi\eta R_S \tag{1.7}$$

Comparison with the frictional coefficient f_0 of an equivalent smooth, compact sphere of identical mass and density defines the frictional ratio f/f_0, or f_r, which is commonly used as a low-resolution parameter of molecular shape and hydration. However, in heterogeneous or dynamically associating systems, fitted frictional ratios represent population-averaged quantities rather than unique molecular species. Consequently, their quantitative interpretability is limited for samples such as FLCs, and f/f_0 values are therefore not used for quantitative analysis in this thesis (Schuck et al. 2016; Schuck and Zhao 2017).

A rigorous descriptor of SV experiments is provided by the Lamm equation, which captures the time evolution of concentration profiles in the sector-shaped solution column under the combined influence of sedimentation and diffusion,

$$\frac{\delta c(r,t)}{\delta t} = \frac{1}{r}\left\{\frac{\delta}{\delta r}\left[Dr\frac{\delta c(r,t)}{\delta r} - s\omega^2 r^2 c(r,t)\right]\right\} \tag{1.8}$$

where *c(r,t)* denotes the solute concentration as a function of radial position *r* and time *t* (Scott et al. 2007; Schuck et al. 2016). Modern numerical solutions of the Lamm equation enable extraction of continuous *s*-value distributions, *c*(*s*), without prior assumptions about the number or discreteness of species. The experimentally observed signal is modeled as a superposition of Lamm equation solutions over a defined range of *s*-values, with diffusion included in each solution rather than represented by an empirical boundary-broadening term. The resulting diffusion-deconvoluted, population-based *c*(*s*) distributions are scaled such that the integral over a given *s*-interval reports the signal-proportional concentration of material sedimenting in that range. This ensemble-based analysis is particularly powerful for heterogeneous and interacting systems, in which stable species coexist with assemblies that may interconvert on the experimental timescale, without requiring global thermodynamic equilibrium (Scott et al. 2007; Schuck and Zhao 2017). Consequently, *c*(*s*) distributions are used as primary observables for quantifying macromolecular heterogeneity and assembly behavior of pathological FLCs under different solvent conditions.

2

Preliminary studies

2.1 Project background

The work presented in this thesis builds on preliminary studies initiated during my Master's thesis, *"Characterization of the aggregation potential of disease-associated human free light chains"*, supervised by Dr. Luitgard Nagel-Steger and Prof. Dr. Alexander K. Buell at the Institut für Physikalische Biologie of Heinrich Heine University Düsseldorf. A subset of SV-AUC data of the patient-derived FLC samples presented in Chapter 3 was acquired during this period and reported in part previously (Sternke-Hoffmann et al. 2023). Further analyses of this subset and additional experimental work were performed during the doctoral studies and contributed to the results presented in Chapter 3 and in Tucholski et al. (2025).

This thesis further builds on a collaborative research project on pathological FLCs in MM and AL amyloidosis, established by Dr. Rebecca Sternke-Hoffmann, Prof. Dr. Alexander K. Buell, and Prof. Dr. Rainer Haas, together with Prof. Dr. Roland Fenk, and Dr. Amelie Boquoi, as a joint effort between the Institut für Physikalische Biologie and the Department of Hematology, Oncology, and Clinical Immunology at University Hospital Düsseldorf. Within this collaboration, a MM patient cohort was assembled and corresponding FLC samples were collected, purification workflows were established, and initial biophysical characterization was performed. Further, all FLC samples were sequenced by mass spectrometry as reported previously (Dupré et al. 2021). Expanded clinical metadata (Tab. 8.1), FLC sequences (Tab. 8.2) and intrinsic physicochemical FLC parameters (Tab. 8.3) are provided in the Supplementary information.

Together, these prior studies provided the experimental and conceptual context for the SV-AUC analyses presented in Chapter 3 and the subsequent investigations described in this thesis, with citations provided throughout.

3

Tracking reduction-induced molecular changes in pathological free light chains by SV-AUC

This chapter contains a peer-reviewed research article. The original structure of the article has been preserved to maintain the integrity of the manuscript and to ensure readability. Any overlap with other chapters is limited to essential background information.

3.1 Article information

Title: Tracking reduction-induced molecular changes in pathological free light chains by SV-AUC

Journal: European Biophysics Journal

Status: Received: 20.12.24 / Revised: 21.07.25 / Accepted: 27.07.25 / Published: 05.08.25

Authors: Florian T. Tucholski[1], Rebecca Sternke-Hoffmann[2], Thomas Pauly[1,3], Rasmus K. Norrild[4], Amelie Boquoi[5,6], Roland Fenk[5], Luitgard Nagel[1,3], Alexander K. Buell[4], Rainer Haas[5], Dieter Willbold[1,3]

Affiliation: [1]Institut für Physikalische Biologie, Heinrich Heine University Düsseldorf, Germany
[2]PSI Center for Life Sciences, 5232 Villigen PSI, Switzerland
[3]Institute of Biological Information Processing (IBI-7: Structural Biochemistry), Research Center Jülich, Jülich, Germany
[4]Protein Biophysics Group, Department of Biotechnology and Biomedicine, Technical University of Denmark, Søltofts Plads, Building 227, Kgs. Lyngby, Denmark
[5]Department of Hematology, Oncology and Clinical Oncology, Heinrich Heine University Düsseldorf, Germany
[6]Department of Hematology and Stem Cell Transplantation, West German Cancer Center and German Cancer Consortium, University Hospital Essen, University of Duisburg-Essen, Essen, Germany

3.2 Declaration of contributions

D.W., R.H., A.K.B., L.N., R.F., A.B.: Conceptualization; F.T.T., R.S.-H., T.P., R.K.N.: Methodology, Investigation, Formal analysis; F.T.T., R.S.-H., T.P. R.K.N.: Validation; F.T.T., T.P.: Visualization; D.W., R.H., A.K.B., L.N.: Supervision, Resources, Project administration; F.T.T., R.S.-H., A.K.B., L.N.: Writing original draft; All authors: Writing, review, and editing; All authors read and approved the final manuscript.

3.3 Abstract

Multiple myeloma is a blood cancer characterized by plasma cell proliferation and excessive production of monoclonal proteins, often leading to renal complications and other forms of organ damage. A set of nine immunoglobulin free light chains (FLC) samples purified from urine of multiple myeloma patients was subjected to sedimentation velocity analysis. Aim of the study was to track changes of the oligomerization state of each FLC while triggering reduction-induced aggregation into larger structures. Sedimentation velocity experiments, combined with further techniques sensitive to structural changes, were performed to determine the degree of FLC oligomerization in each patient sample under different experimental conditions. Structurally, the FLC monomers are stabilized by two intramolecular disulfide bonds, while covalent dimerization occurs through an unpaired C-terminal cysteine residue. Incubation with the reducing agent TCEP cleaves intra- and intermolecular disulfide bonds, destabilizing both monomers and dimers. Remarkably, different incubation times revealed that destabilized dimers do not dissociate into stable monomers but instead accumulate directly into oligomers and higher-order aggregates. In addition to larger aggregates, fragments with sizes around 1 S were detected with increasing TCEP incubation time. This fragmentation behavior was consistent among FLCs originating from the immunoglobulin kappa variable 1-33 gene (IGKV1-33). Sedimentation velocity-based characterization of FLCs can provide insights into the relationship between their stability and aggregation capacity. An understanding of this relationship is crucial for the development of therapeutic strategies to prevent renal complications associated with monoclonal gammopathies such as multiple myeloma.

Keywords: Analytical ultracentrifugation, Patient-derived immunoglobulin free light chains, Multiple myeloma, Monomer-dimer distribution, Aggregation

3.4 Introduction

Immunoglobulins form the humoral component of the adaptive immune system and are secreted by plasma cells in the bone marrow after their terminal differentiation from B lymphocytes. They consist of paired heavy and light polypeptide chains that are covalently linked via disulfide bonds, resulting in a Y-shaped structure (Fleischman et al. 1963; Edelman et al. 1968; Amzel and Poljak 1979). When LCs are released into the serum unbound to their HC counterpart, they are referred to as FLCs. Excessive production of monoclonal protein is a key pathological feature of a heterogeneous group of diseases known as monoclonal gammopathies (Ríos-Tamayo et al. 2023). As a result of malignant transformation, clonal expansion of a single neoplastic plasma cell can lead to the continuous overproduction of monoclonal FLCs. Under these pathological conditions, elevated FLC levels can be detected in the serum, cerebrospinal and synovial fluid and urine, where they are also referred to as BJP (Jones 1848; Kyle 2000). In AL amyloidosis, these elevated levels of circulating FLCs lead to the formation and deposition of highly ordered amyloid fibrils, which progressively disrupt the function of multiple organ systems (Kaplan et al. 2014; Merlini et al. 2018). In MM, the clinical focus often centers on renal damage caused by the accumulation of insoluble FLC deposits in the renal tubules (Sathick et al. 2019). These deposits also manifest as geometrically shaped crystalline casts or amorphous and granular aggregates often lacking a defined high-order structure (Zanetti and Capra 1999; Bliznyukov et al. 2005; Sun et al. 2021; Sternke-Hoffmann et al. 2023). Each form is distinguishable by its morphology and clinical relevance and the microenvironment has been shown to play a critical role in determining whether and how those different types of aggregates form (Bliznyukov et al. 2005).

Due to the structural diversity of FLCs and the variety of clinical manifestations, the underlying aggregation mechanism remains largely unclear. It is assumed that the severity of this damage is often linked to the structural properties of FLCs and their ability to interact with different tissue types (Del Pozo-Yauner et al. 2022; Gudowska-Sawczuk and Mroczko 2023). Structurally, LCs are divided into the isotypes κ and λ, each consisting of a C_L and a V_L domain, adopting a β-sandwich structure. A set of different gene segments encodes the C_L and V_L domains of both κ- and λ-LCs. The immunoglobulin kappa variable 1-33 (IGKV1-33) gene segment is the most frequently expressed κ-V_L domain gene in AL amyloidosis and is associated with both higher dFLC levels (defined as the difference between involved and uninvolved FLC concentrations) and an increased incidence of hepatic involvement (Kourelis et al. 2017). Three of the nine FLC samples analysed in this study (P006, P016, and P017) originated from IGKV1-33 (Sternke-Hoffmann et al. 2023). LCs encoded by this gene exhibit a greater number of somatic mutations (Morgan et al. 2024), a feature that may underlie the distinct fragmentation behavior reported here. Both isotypes contain around 214 amino acids each with a molecular weight of approximately 25 kDa. They typically include five cysteine residues forming disulfide bonds; two intramolecular bonds stabilizing the monomeric conformation, while a third C-terminal cysteine is associated with covalent dimerization (Janeway 2001; Thio et al. 2008; Liu and May 2012). While κ-FLCs are mostly present as monomers, λ-FLCs form dimers, with dimerization generally occurring through both covalent and non-covalent interactions (Klein et al. 1977; Roussel et al. 1999). Although dimers are typically kinetically stable and resistant to endoproteolysis, unstable forms have been identified that unfold more rapidly, increasing their susceptibility to proteolytic

digestion and resulting in fragmentation (Morgan and Kelly 2016; Morgan et al. 2019). In particular, fragments of the N-terminal V_L domain have demonstrated a high aggregation potential and have been identified as the primary component of amyloid fibrils (Glenner et al. 1970). The mechanisms regulating the formation of disulfide-bonded dimers remain largely unknown, but it is believed that they are catalyzed by oxidoreductases, whose activity depends on the redox potential of the cell compartment (Migrino et al. 2010). This redox potential can be altered by pathological conditions that include oxidative stress, thereby affecting the dithiol-disulfide state of FLCs. In various diseases, an abnormal increase in FLC dimerization has been observed, suggesting its pathological relevance (Kaplan et al. 2011). It is known that the disruption of disulfide bonds can trigger the aggregation of FLCs (Andrich et al. 2017). A variety of reducing agents can be utilized for this purpose *in vitro*, and studies have demonstrated that the choice of reducing agent significantly impacts both the kinetics of aggregation and the morphology of the resulting aggregates (Džupponová and Žoldák 2023).

This study investigates the impact of reducing conditions on the molecular species of FLCs during the aggregation process, aiming to explore a potential correlation between their propensity to aggregate and the extend of tissue damage. Therefore, nine pathological FLC samples purified from the urine of patients with MM were characterized using AUC (Krayukhina and Uchiyama 2016). Size and shape distributions of the FLC samples were determined under different conditions by SV analysis. Measurements were repeated after different incubation periods in the presence of the reducing agent tris(2-carboxyethyl)phosphine (TCEP) to investigate the role of intra- and intermolecular disulfide bonds in stabilizing FLCs and mitigating their aggregation. As an absolute technique based on fundamental physical principles, SV centrifugation provides a direct measurement without the need for reference standards or calibration (Schuck et al. 2016). A defined sample volume is subjected to high-speed centrifugation, which facilitates the separation of species based on their hydrodynamic properties and the determination of their respective *s*-values. This method allows the quantification of monomeric and dimeric FLC fractions, while also allowing the identification of higher order oligomeric species over a range of experimental conditions. In this study, we distinguish between physiologically occurring oligomeric forms – including both reversible (non-covalent) and irreversible (covalent) interactions – and pathologically relevant aggregates. In this context, 'aggregation' refers to the formation of irreversible, misfolded assemblies that arise from structural destabilization and are implicated in the pathogenicity of FLCs in MM and AL amyloidosis.

In search for prognostic markers capable of providing insights into the expected course of disease, this study builds upon prior research conducted using the same set of patient samples (Sternke-Hoffmann et al. 2020, 2023; Dupré et al. 2021). Understanding the molecular changes in sample composition during aggregation and amyloid fibril formation may lead to valuable insights into the nephrotoxicity of FLCs.

3.5 Methods

3.5.1 Sample collection and purification

All samples analyzed in this work were obtained from a 24-hour urine collection of both inpatients and outpatients at the University Hospital Düsseldorf. Prior to sample collection, all patients provided written informed consent, and the study was approved by the ethics committee of the University Hospital Düsseldorf (study number 5926R and registration ID 201706). Patient samples were prepared as described previously (Sternke-Hoffmann et al. 2020). Briefly, FLCs were isolated from collected urine of patients with multiple myeloma through ammonium sulphate precipitation. The precipitation reaction involved the saturation of collected urine with 70% (w/v) ammonium sulphate following incubation at 4°C for 2 h with stirring on the day of collection. The solution containing precipitated protein fractions was then centrifuged at 6000 x *g* and 4°C for 25 min. To remove residual ammonium sulphate and other impurities, precipitate resuspended in 30 mM Tris-HCl buffer at pH 7.4 was dialysed against the same buffer for 72 h at 4°C with gentle stirring. To maintain the concentration gradient, a buffer change was carried out every 24 h. The samples were fractionated using size-exclusion chromatography (SEC) with an ÄKTA pure chromatography system from GE Healthcare (Illinois, USA) and a Superdex 75 10/300 GL Tricorn column with a separation range of 3 to 70 kDa. Elution was performed using 30 mM Tris-HCl buffer at pH 7.4. Prior to SEC, samples were concentrated using Sartorius Vivaspin 2 centrifugal concentrators with polyethersulfone membrane and 10 kDa molecular weight cut-off (MWCO). Individual SEC fractions were measured in a V-650 spectrophotometer from Jasco (Pfungstadt, Germany). Based on the individual amino acid compositions of the FLC samples (Dupré et al. 2021), the respective extinction coefficient was calculated by the Edelhoch method (Edelhoch 1967) implemented in ProtParam (Expasy). Individual SEC fractions were combined according to their concentration, snap-frozen with liquid nitrogen and stored at −80°C until further use.

3.5.2 Quantification of species distribution with SV-AUC

SV experiments were performed in ProteomeLab XL-A and Optima XL-A ultracentrifuges from Beckman Coulter (California, USA) equipped with UV/Vis absorption optics. Standard double-sector measuring cells with quartz glass windows and aluminum centerpieces with 12 mm optical path length were used, along with an An-60Ti 4-hole rotor (Beckman Coulter). A reference volume of 400 µL and a sample volume of 390 µL were used for all measurements. Unless stated otherwise, all AUC experiments were performed with sample concentrations of 35 µM in 30 mM Tris-HCl buffer at pH 7.4. To promote disulfide bond reduction, the samples were incubated with 7 mM TCEP adjusted to pH 7.4 for 1.25 h, 5 h or 15 h at 37°C with shaking at 600 rpm, prior to loading samples into the AUC cells. Alternatively, 0.1 M and 1 M NaCl were added to the samples following 24 h incubation at room temperature to evaluate how changes in ionic strength affect the species distribution of FLCs. As different samples were measured together per run, the wavelength for sample detection was individually set for optimal resolution (between 260 and 270 nm) based on wavelength scans taken at

3000 rpm before each measurement. The SV experiments were carried out at a rotor speed of 60,000 rpm and a temperature of 20°C. After loading, samples were equilibrated in the rotor at 20°C for approximately 60 minutes prior to the start of sedimentation. This equilibration period included vacuum establishment, temperature stabilization, and low-speed wavelength scans at 3000 rpm, ensuring thermal and hydrodynamic equilibrium before high-speed centrifugation. SV experiments were carried out at the maximum rotor speed of 60,000 rpm, which was sufficient to achieve complete sedimentation of monomeric, dimeric, higher-order oligomeric species, and aggregates within approximately 5 hours. Theoretical estimates indicate that monomers sediment in about 4.5 hours and dimers in approximately 3.5 hours under these conditions. Low molecular weight fragments were not considered here, as their sedimentation is minimal over the course of the experiment.

3.5.3 Calculations and data analysis

For the analysis of sedimentation data, the partial-specific volume, as well as solvent density and viscosity of all FLC samples were calculated individually using the software SEDNTERP version 2.0 Beta (Laue 1992). Details of all fit parameters used for analysis are provided in the Supplementary information (Tab. 8.4). The sedimentation data analysis was carried out with the software SEDFIT version 16.1c using the $c(s)$ model (Schuck 2000; Schuck et al. 2002). A resolution of 0.1 S was applied for curve fitting, and the root mean square deviation (RMSD) was less than 1% of the total signal for all sedimentation data, except for sample P020 after 5 and 15 hours of incubation with TCEP. Both time-invariant (TI) and radial-invariant (RI) noise parameters were fitted in SEDFIT. Trial fits with the RI parameter disabled produced identical low-S and high-S regions, confirming that RI-noise modelling did not introduce artifacts. Significant aggregation and sedimentation of aggregates during the acceleration of the rotor to the final speed of 60,000 rpm resulted in a notable loss of signal, thereby affecting the signal-to-noise ratio. For these measurements, the achieved RMSD values were approximately 2% of the total signal. Sample loss was calculated by comparing the absorption signal from wavelength scans at the respective detection wavelength before measurement with the plateau heights recorded in early sedimentation profiles for each sample. Despite the low ionic strength of the buffer (30 mM Tris-HCl, pH 7.4), no significant primary-charge effect was observed in the sedimentation behavior of the FLCs. The measured s-values for monomeric and dimeric FLCs closely match values reported in the literature under different buffer conditions, as well as values obtained in this study under higher ionic strength, supporting the robustness of our sedimentation analysis. For further analysis and graphical representation fitted sedimentation data were exported to the software GUSSI (Brautigam 2015) and DataGraph version 5.3β, copyright 2020 (North Carolina, USA). The $c(s)$ distributions obtained show the number and s-values of the molecular species modelled as constitutes of the analysed samples. The s-values obtained from $c(s)$ analysis were corrected to standard conditions (20°C in water) and are reported as $s_{20,w}$ values. Default subtraction of TI and RI noise was applied in GUSSI. Integration limits including all detected peaks of the distribution were used to determine the weight-average s-values of a sample. This approach does not require baseline resolved signals of single species in the distribution and provides a mean value reflecting the overall

oligomerization state of the FLC samples. Within these global integration limits, individual ranges for fragments, monomers, dimers, and tetramers were selected for each sample, as far as possible.

3.5.4 Circular dichroism spectroscopy

The extent of secondary structure changes in FLCs upon TCEP treatment over various incubation times was determined by circular dichroism (CD) spectroscopy. FLC samples, prepared at an initial concentration of 35 µM in 10 mM sodium phosphate buffer at pH 7.4, were incubated with 7 mM TCEP at 37°C. To minimize aggregation, samples were not agitated, which allowed a more controlled analysis of structural changes. Aliquots were taken at 1.25 h, 5 h and 24 h and subsequently diluted to a final FLC concentration of 9.23 µM for CD spectroscopy. Since the final concentration of each sample was calculated and achieved through dilution, potential variations due to aggregation cannot be ruled out. Therefore, ellipticity values were not normalized to molar ellipticity to account for any inconsistencies that might arise from such aggregation effects. Far-UV CD spectra were measured using a Jasco (Hachioji, Tokyo, Japan) J-810 spectropolarimeter at room temperature across the wavelength range of 190 nm to 260 nm. Measurements were performed in quartz glass cuvettes with 1 mm optical path length, a scanning speed of 50 nm/min, 1 nm bandwidth, a digital integration time of 2 seconds and a resolution of 0.5 nm. Each spectrum was baseline corrected and represents the average of 15 accumulations.

3.5.5 Differential scanning fluorimetry

Differential scanning fluorimetry (DSF) can be used to assess the thermal stability of a sample across various conditions, enabling the detection of shifts in melting temperature that indicate structural unfolding. For analysis of the thermal stability of the FLCs a CFX Opus 96 Real-Time PCR System (Bio-Rad, California, USA) was used. All assays were performed at a sample concentration of 35 µM in a 30 mM Tris-HCl buffer at pH 7.4. To destabilize the disulfide bonds of FLCs, 7 mM TCEP was added to each preparation. For stability assessment at high ionic strength, the experiments were repeated with 0.1 M and 1 M NaCl. All measurements were performed in triplicate (n = 3), with a total reaction volume of 25 µL per well. Real-time unfolding of FLCs was monitored using the SYPRO Orange fluorescent dye (Sigma-Aldrich, S5692). A 10 mM stock solution was diluted 1:1,000 in the reaction mixture, resulting in a final working concentration of 10 µM. Samples were pipetted into low-profile, thin-walled Hard-Shell 96-well PCR plates (#HSP9601) and sealed with Microseal 'B' adhesive PCR plate sealing film (#MSB-1001). Melting curves were measured from 10°C to 95°C, with a temperature increment of 0.5°C per cycle every 15 seconds.

3.6 Results

3.6.1 SV-analysis of the size distribution of FLC samples

Purified FLC samples were subjected to SV analysis to determine their oligomeric state, expressed as *s*-value distribution. As described before, FLCs showed significant differences in size distributions under neutral buffer conditions (Sternke-Hoffmann et al. 2023). Briefly, determined *s*-values could be assigned predominantly to monomeric and dimeric FLC species in agreement with literature values, i.e., ~2.4 S for monomers and ~3.65 S for dimers (Klein et al. 1977). As also illustrated in Figure 3.1 (distributions without TCEP; black), FLC samples showed distinct species distributions, with λ-FLC P001 being particularly notable as the only sample with no detectable monomeric species, consisting almost entirely of dimers. Other samples showed either a higher proportion of monomers or dimers or, in the case of sample P005, an almost even distribution. In samples P007, P013, and to a lesser extent P016, the signals for monomers and dimers could not be distinctly resolved, resulting in one asymmetric peak with a left-skewed distribution and a variably pronounced shoulder. This suggests that the *s*-values of monomers and dimers in these samples are sufficiently close to hinder clear separation or that a dynamic, non-covalent equilibrium exists between species, preventing distinct detection over the several-hour measurement. In all distributions, additional signals of varying intensity were detected around ~0.1 S. These signals could potentially be artifacts resulting from the calculation of $c(s)$ distributions using maximum entropy regularization (Schuck 2016). Alternatively, they may reflect the presence of non- or slowly sedimenting solvent components or proteolytic fragments present in the samples. Additionally, samples P004 and P020 exhibit signals around ~5 S, which may correspond to impurities such as human serum albumin (HSA) or potentially represent trimeric or tetrameric FLC species, as described in the literature (Sakai et al. 2023). While this signal was weakly pronounced in sample P004, it was most prominent in sample P020, where it accounted for 8.8% of the total sample.

3.6.2 Changes in FLC size distribution after disulfide bond reduction

Building on previous SV experiments, 7 mM TCEP was added to the buffer (30 mM Tris-HCl, pH 7.4) to disrupt the disulfide bonds of FLCs. Given that this process reduces both intra- and intermolecular disulfide bonds, it is to be expected that both the tertiary and quaternary structures will be impaired. As demonstrated, these conditions are sufficient to destabilize the FLC structure to a degree that initiates self-assembly (Džupponová and Žoldák 2023). Since TCEP is acidic when dissolved in water, stock solutions were adjusted to pH 7.4 to maintain neutral pH conditions in samples after TCEP addition. The samples were incubated for 1.25 h, 5 h, and 15 h under reducing conditions at 37°C with shaking at 600 rpm. The size-distribution analysis captures changes induced by the onset of aggregation, regardless of the specific type of aggregation involved. Figure 3.1 presents selected $c(s)$ distributions, chosen based on their distinct species composition or individual response to the reducing conditions. The remaining distributions are included in the Supplementary information (Fig. 8.1), along with the corresponding raw data (Fig. 8.2A+B).

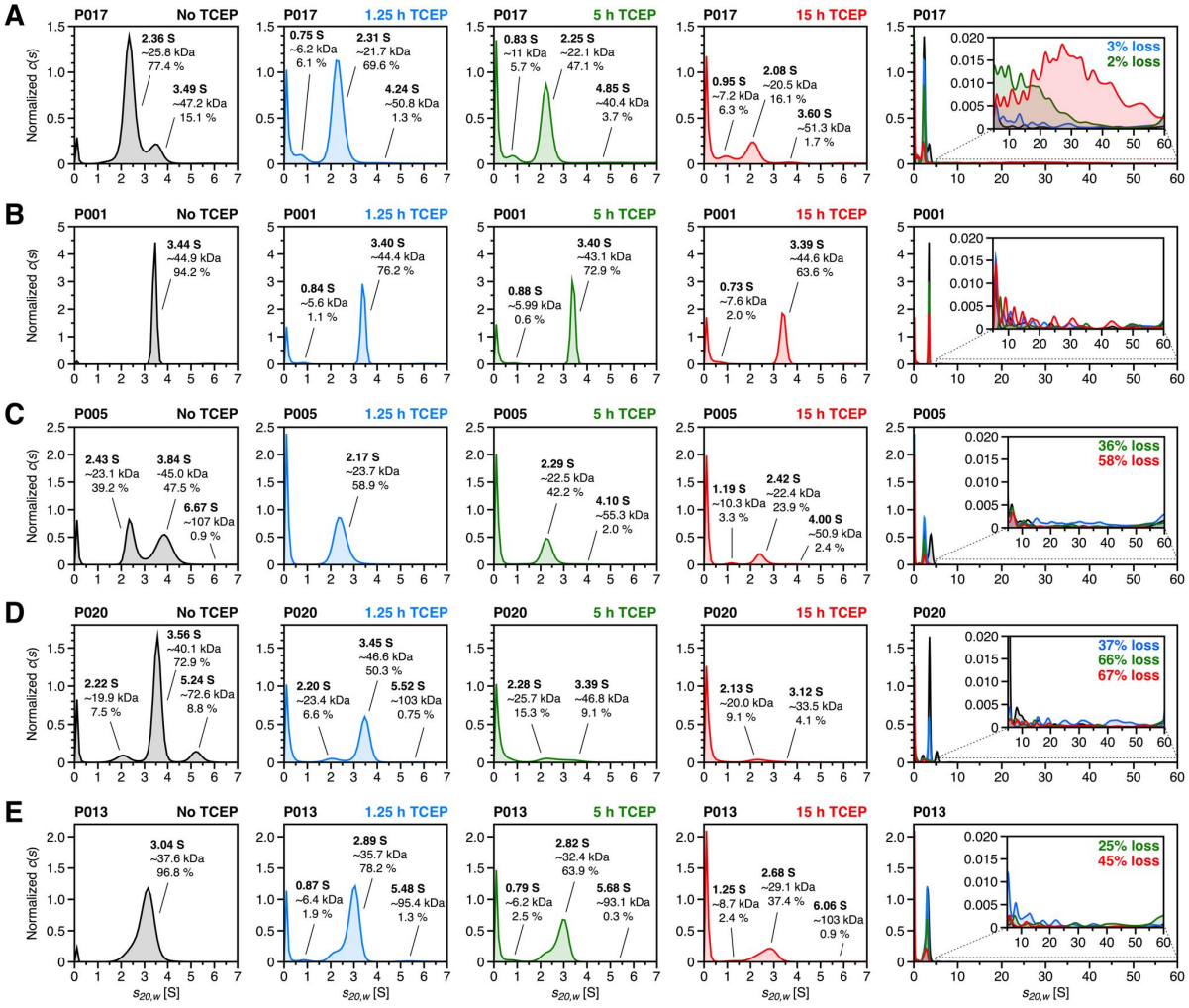

Figure 3.1: Influence of disulfide bond reduction on the monomer-dimer distribution of FLCs. The *c*(*s*) distributions of purified patient samples (**A**) P017, (**B**) P001, (**C**) P005, (**D**) P020 and (**E**) P013 are shown. Samples were prepared at a concentration of 35 µM in 30 mM Tris-HCl, pH 7.4 (black). To induce disulfide bond reduction, 7 mM pH-adjusted TCEP was added, followed by incubation at 37°C with shaking at 600 rpm for periods of 1.25 h (blue), 5 h (green), and 15 h (red). After incubation, 390 µL of each sample was transferred to the sample sector of standard aluminum double-sector cells, and sedimentation analysis was performed at 60,000 rpm and 20°C.

By comparing the *c*(*s*) distributions across different incubation times, the changes in molecular species in FLCs can be tracked throughout the aggregation process. After 1.25 h of incubation, the dimeric species in samples P017 (Fig. 3.1A) and P005 (Fig. 3.1C) almost completely dissociate. In samples with a higher initial dimer content, such as P001 (Fig. 3.1B), P020 (Fig. 3.1D) and P013 (Fig. 3.1E), a continuous decrease in dimer levels is observed with increasing incubation time. In sample P020, dimers exhibit substantial dissociation after 15 hours of incubation. Similarly, sample P013 shows a shift in the *s*-values towards monomeric species with increasing incubation time, indicating that dimeric components progressively dissociate over time. Notably, only sample P001 retains a significant proportion of dimers after 15 hours of incubation. This observation suggests that the remaining dimeric species in sample P001 are likely not covalently linked but instead stabilized by

non-covalent interactions, which remain unaffected by the reduction of disulfide bonds. Over time, the proportion of monomeric species also decreases, accompanied by a decline in *s*-value by an average of 0.2 S. This change could indicate structural changes, possibly due to the unfolding of monomers after the reduction of intramolecular disulfide bonds, which could explain the observed variations in sedimentation behavior. Unexpectedly, no increase in monomeric species was observed following the dissociation of dimers, particularly noticeable in sample P001. The exception was sample P005, where the proportion of monomers increased from ~39% to 59% after an incubation time of 1.25 h. These findings suggest that most monomers dissociating from reduced dimers exhibit distinct stability characteristics compared to free monomers, directing them immediately into the aggregation pathway. In addition to the redistribution of monomeric and dimeric species, an increase in signal at approximately 0.1 S is observed with prolonged incubation times. To confirm that the low-*S* signals represent genuine sample components rather than artifacts of maximum-entropy regularization, sedimentation data was re-analyzed with several minimum *s*-value limits (s_{min}) both with and without Bayesian modification to suppress baseline correlation. As shown in Supplementary information (Fig. 8.3), half-peaks appear only when s_{min} exceeds 0 S, whereas setting s_{min} to 0 S and applying Bayesian modification recovers the complete peak at ~0.1 S, indicating that these low molecular weight species are intrinsic to the samples and not mathematical artifacts (Schuck 2016). Since all measurements were performed under identical buffer conditions, the observed increase in signal cannot be attributed to solvent components. Instead, it may be associated with the degradation of monomeric FLCs, as indicated by their decreasing *s*-values, resulting in the formation of low molecular weight fragments. Additionally, the formation of a new species with an *s*-value of approximately 1 S was observed in samples P017 (Fig. 3.1A), P006 and P016 (Fig. 8.1B+D), and to a lesser extend in sample P005 (Fig. 3.1C), with increasing TCEP incubation time. In contrast to the previously identified low molecular weight fragments, this signal may indicate an alternative degradation mechanism occurring at a specific site within the protein sequence of FLCs.

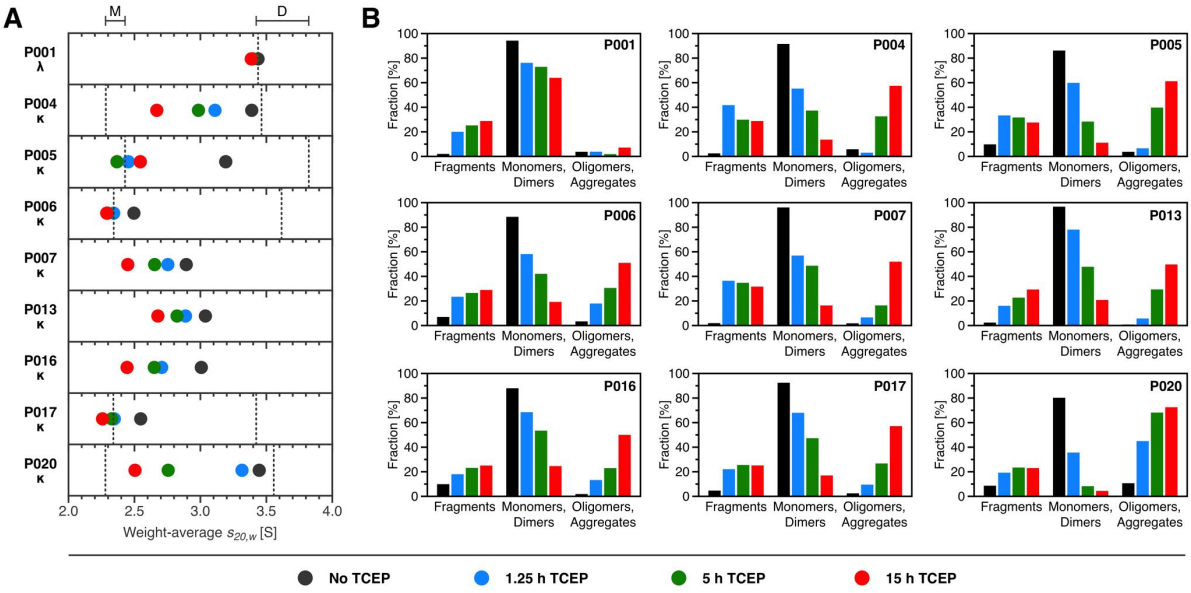

Figure 3.2: Shifts in monomeric and dimeric weight-average *s*-values and in time-dependent size distributions during TCEP incubation. (**A**) Illustration of the changes in weight-average *s*-values for all patient samples, derived from the analysis of sedimentation data. To track changes in monomeric and dimeric species over the incubation period, the sedimentation range from 1.6 to 4.7 S was integrated to calculate the weight-average *s*-values for both species combined. Dashed lines indicate *s*-values for individually identified monomers and dimers, with 'M' and 'D' above representing their average *s*-value range across samples. (**B**) Percentage of all species over the entire *s*-value range. A distinction was made between fragments (0 to 1.6 S), monomers and dimers (1.6 to 4.7 S) as well as oligomers and aggregates (4.7 S to end of distributions). In addition to the proportions of aggregates determined by integration, the previously calculated loss of sample during sedimentation was also incorporated into analysis.

The redistribution of molecular species in all samples triggered by the reduction of disulfide bonds is shown in Figure 3.2B. By integrating respective single peaks of the *c*(*s*) distribution, the mass fractions of the corresponding molecular species present can be determined. For this, identical integration ranges were applied to all samples: 0 S to 1.6 S for fragments, 1.6 S to 4.7 S for monomers and dimers, and 4.7 S till the end of distribution range for oligomers and aggregates. The time-dependent shifts in the weight-average *s*-values of monomers and dimers during TCEP incubation are summarized in Figure 3.2A. To provide a unified representation of the changes in sample compositions, monomeric and dimeric species were evaluated with common integration boundaries between 1.6 and 4.7 S. Additionally, Figure 3.3 visualizes the time-dependent increase in TCEP-induced aggregation of the FLCs over the course of experiments, based on the calculated fractions.

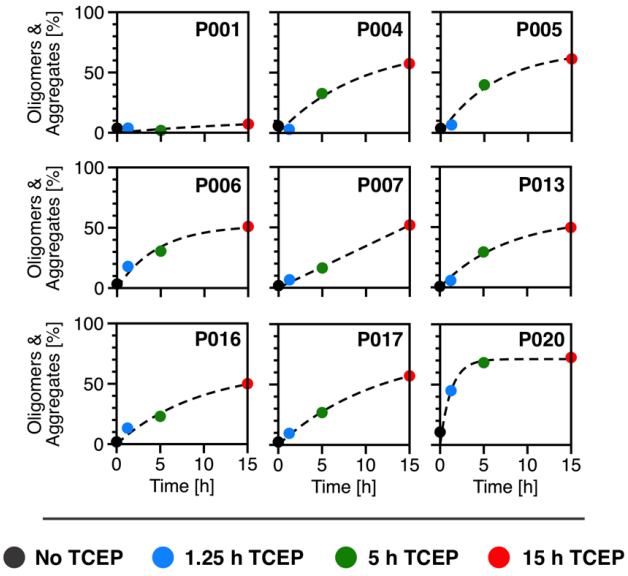

Figure 3.3: Time-dependent progression of TCEP-induced aggregation. Signal percentage of oligomers and larger aggregates (4.7 S – 60 S) out of the total signal, calculated from the *c*(*s*) distributions for each patient sample. The progression of TCEP-induced aggregation is shown as a function of incubation time. Data points represent aggregate content of the samples without TCEP (black), and after 1.25 h (blue), 5 h (green) and 15 h (red) of incubation. An exponential growth function ($Y = A(1-e^{-kx})$) was applied to illustrate differences in aggregation trends among samples over incubation time.

Incubation with TCEP revealed that patient samples P006, P016 and P017 exhibited a pronounced fragmentation pattern that intensified with increased incubation time. Notably, all three patient samples originate from the IGKV1-33 germline sequence, as previously identified (Sternke-Hoffmann et al. 2023). Figure 3.4 shows all three IGKV1-33 FLCs in comparison, both without TCEP and after 15 hours of TCEP incubation. Along with the non-specific low molecular weight fragments observed across all patient samples, a defined fragment appeared at approximately 1 S. Prior to TCEP treatment, the monomer peak of sample P006 shows a left shoulder between 1 and 2 S, suggesting a potential fragmentation state after purification. However, this fragment does not remain consistent throughout the incubation series, likely undergoing further degradation until stabilizing as a fragment around 1 S, similar to those observed in samples P016 and P017. Fragmentation of FLCs may have been induced by a range of factors. Current knowledge suggests that kinetically unstable and partially unfolded dimers exhibit a higher susceptibility to proteolytic digestion, leading to the cleavage of FLC domains into individual fragments that may possess amyloidogenic properties (Glenner et al. 1970; Morgan and Kelly 2016). As detected by mass spectrometry (MS) analysis of the nine samples, various cathepsins were co-purified during FLC extraction from patients urine (Dupré et al. 2021; Sternke-Hoffmann et al. 2023). However, without the addition of TCEP, the FLC samples appeared to be stable over time, consistent with previous studies using the same set of FLCs (Sternke-Hoffmann et al. 2020, 2023). Given that the fragments at ~1 S are undetectable under non-reducing conditions, it can be assumed that the corresponding cleavage sites are exposed by the addition of TCEP. Furthermore, TCEP-induced fragmentation has been observed in other proteins, where TCEP facilitated non-specific cleavage near cysteine residues over longer incubation times (Liu et al. 2010). Whether this

fragmentation behavior is caused by TCEP or arises from proteolytic activity, and whether it represents a characteristic feature across all IGKV1-33-derived LCs requires further investigation.

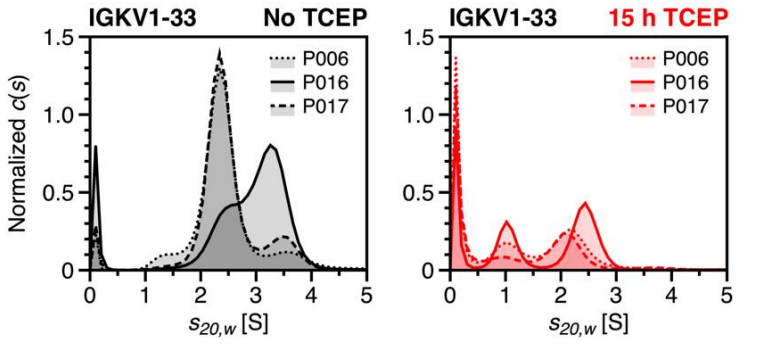

Figure 3.4: Fragmentation of IGKV1-33-derived FLCs after incubation with TCEP. Fragmentation patterns of FLCs derived from the IGKV1-33 germline sequence. The *c*(*s*) distributions of samples P006 (dotted line), P016 (solid line) and P017 (dashed line) are shown before TCEP addition (black) and after 15 h incubation with TCEP (red). To provide a more detailed comparison, only the range between 1 S and 5 S is displayed.

3.6.3 TCEP-induced changes in secondary structure of FLCs

To investigate possible changes within the secondary structure of FLCs caused by disulfide bond reduction through TCEP treatment, FLC samples were analyzed by CD spectroscopy. Figure 3.5 presents CD spectra for the nine FLC samples, both untreated and following incubation with TCEP at intervals of 1.25 h (blue), 5 h (green) and 24 h (red). In general, all FLC samples exhibit distinct β-sheet secondary structure motifs characteristic of LCs and other immunoglobulin domains (Brahms et al. 1977; Bork et al. 1994; Poshusta et al. 2013; Andrich et al. 2017). To monitor TCEP-induced changes across incubation periods, the zero-crossing of ellipticity in the range of ~200 – 210 nm was selected as a reference point. This point lies between the characteristic positive (~195 nm) and negative (~218 nm) bands typically observed in β-sheet-rich proteins such as FLCs (Greenfield 2006), and consistently appeared across all samples and time points. While not a structure-specific feature, the zero-crossing reflects the spectral balance of overlapping secondary structure contributions. Importantly, it remained robust despite minor differences in protein concentration or aggregation, making it a reliable and structurally meaningful marker for comparative analysis. Each sample exhibited varying levels of structural deviation from their initial structure after TCEP-induced disulfide bond reduction. Samples P001, P004 and P006 demonstrated minimal shifts at the zero-crossing point after 1.25 h incubation time, indicating an isosbestic point and limited structural disruption. In contrast, samples P005, P007, P017 and P020 displayed deviations from their initial structure, with zero-crossing shifts reaching up to 5 nm within the first 1.25 h of incubation, most notably in samples P005 and P020. These two samples also exhibited the highest aggregation levels after 15 h of incubation (Fig. 3.2B), suggesting a correlation between early structural loss and an increased aggregation propensity. Aside from sample P017 after 15 h incubation, post-incubation spectra across samples were generally similar in shape, with changes primarily attributable to aggregate formation and corresponding variations in effective sample concentration. Quantitative

deconvolution was not attempted because reliable interpretation requires a high tension (HT) voltage below 700 V for wavelengths under 200 nm (Fig. 8.4), as well as a homogeneous, non-scattering sample. These criteria were not met by several spectra in this heterogeneous sample set. The zero crossings determined for all spectra are summarized in the Supplementary information (Tab. 8.5).

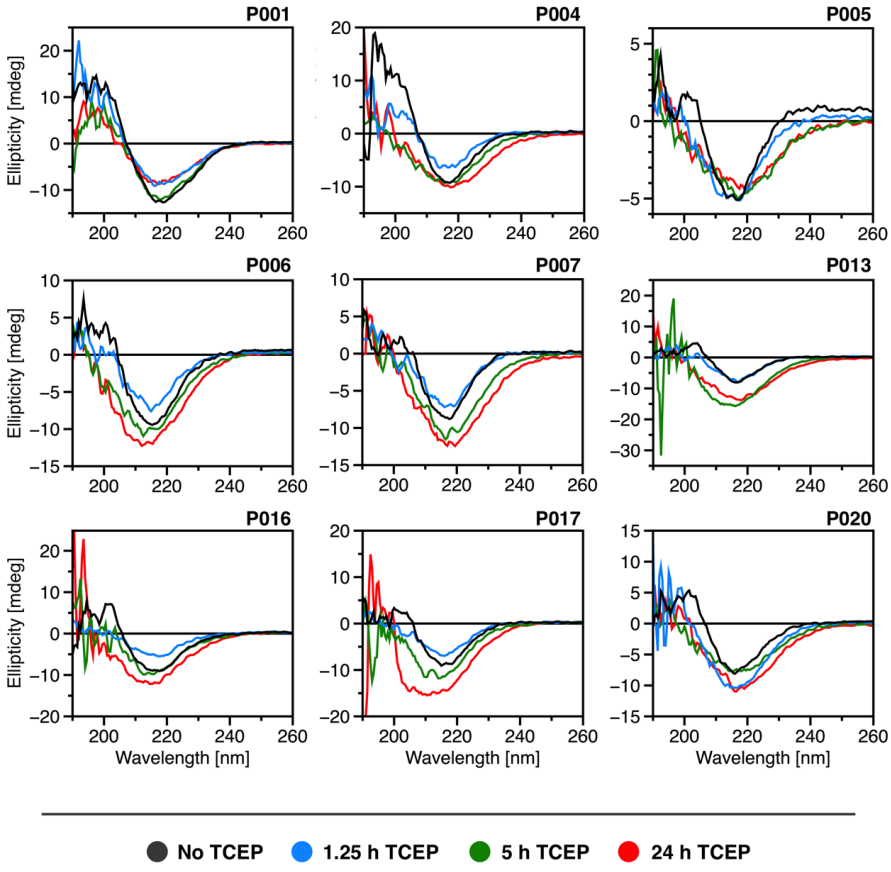

Figure 3.5: Secondary structure shifts after TCEP-induced reduction of disulfide bonds. Shown are the CD spectra of all nine FLCs before TCEP treatment (black), as well as after 1.25 h (blue), 5 h (green) and 24 h (red) incubation time. A sample concentration of 35 µM was incubated in 10 mM sodium phosphate buffer, pH 7.4 at 37°C. Aliquots were taken after specified time points and diluted to a final concentration of 9.23 µM for CD measurements. Corresponding HT voltage records are provided in the Supplementary information (Fig. 8.4).

3.6.4 Modulating effects of the molecular species distribution of FLCs

Distinct salt concentrations across renal compartments are crucial for maintaining normal kidney function by enabling water and electrolyte homeostasis through active and passive transport mechanisms (Gallardo and Vio 2022). Ionic strength is known to significantly influence protein stability by modulating secondary and tertiary structures through both hydrophobic interactions (Von Hippel and Wong 1965; Damodaran and Kinsella 1981) and electrostatic forces, including charge repulsion and ion pairing, which are key determinants of folding energetics (Dill 1990). As a result, the dynamic osmotic gradient in the kidney may play a key role in the formation of nephrotoxic FLC

aggregates. Previous studies have shown that varying salt concentrations can either promote or inhibit aggregate formation, depending on the specific FLC involved (Baden et al. 2009). To evaluate the relationship between ionic strength and FLC stability, patient samples were incubated with 0.1 M and 1 M sodium chloride (NaCl), and SV experiments were repeated under these conditions. Figure 3.6A displays the *c*(*s*) distributions of samples P006, P007, P017 and P020, illustrating the effects of ionic strength on FLC species distribution. Individual *c*(*s*) distributions with additional labeling are provided in the Supplementary information (Fig. 8.5), along with a summary plot illustrating changes in weight-average *s*-values as a function of ionic strength (Fig. 8.6). For samples P006, P017 and P020, an increase in ionic strength correlates with a higher degree of oligomerization. While this observation applies only to the proportion of dimers in sample P017, the addition of NaCl also results in an increase in tetrameric species around 5 S in samples P006 and P020, with the effect being particularly pronounced in P020. Based on the observed signal increase, it can be assumed that the signal at ~5 S in sample P020 is unlikely linked to an HSA impurity, as previously hypothesized, but is more likely attributable to tetrameric FLC species. The most significant increase is observed at 0.1 M NaCl, whereas this signal decreases partly at 1 M NaCl. The addition of NaCl also results in sharper peaks, which is at least partly due to the reduced diffusion in the increasingly viscous salt solutions. For sample P007, the addition of NaCl facilitates the separation of the main signal, suggesting that a dynamic equilibrium between monomeric and dimeric species becomes kinetically stabilized. The increased ionic strength likely slows the interconversion between these states on the timescale of the experiment, allowing for clearer resolution of distinct species in the *c*(*s*) distribution. Nevertheless, the *s*-values for monomers and dimers remain relatively close to each other, preventing complete signal separation.

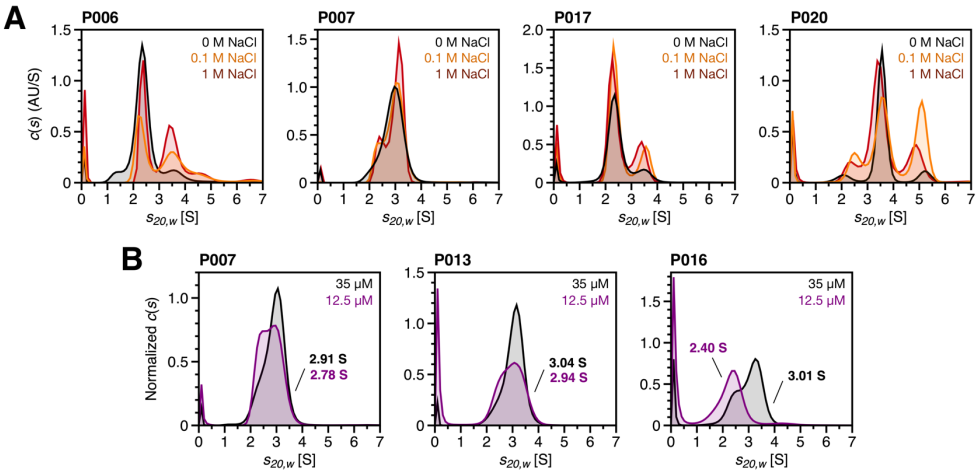

Figure 3.6: Modulation of the molecular species distribution of FLCs. (**A**) Effect of varying salt concentrations on the molecular species present in patient samples. The *c*(*s*) distributions of samples P006, P007, P017 and P020 are shown. A 30 mM Tris-HCl buffer at pH 7.4 was prepared without NaCl (0 M, black) and with the addition of 0.1 M (orange) or 1 M NaCl (red). To reach equilibrium, the samples were incubated for 24 h at 25°C prior to measurement. (**B**) Concentration-dependent dynamic equilibrium between monomers and dimers. The *c*(*s*) distributions of samples P007, P013 and P016 at a concentration of 12.5 µM (purple) are compared with those obtained at 35 µM (black). Corresponding raw data of the *c*(*s*) distributions are included in the Supplementary information (Fig. 8.7 & 8.8).

Depending on the type of FLC dimerization, a similar effect can be achieved by decreasing the sample concentration (Fig. 3.6B). At a concentration of 35 µM, samples P007, P013 and P016 showed no distinct separation between monomeric and dimeric signals (Fig. 3.1E, Fig. 8.1C, D). However, measurements repeated at FLC concentrations of 12.5 µM demonstrated varying degrees of dynamic equilibrium between monomers and dimers, further supporting the presence of non-covalent dimerization. While for samples P007 and P013 the peak shoulder of the monomer became more defined, sample P016 showed an almost complete shift to monomeric *s*-values. This is also reflected in the respective *s*-value, which decreased by ~0.1 S for samples P007 and P013 and by ~0.6 S for sample P016 at a concentration of 12.5 µM. Notably, after dilution, sample P016 displays a single dominant peak at 2.40 S, which corresponds to the *s*-value range of FLC monomers. This supports the hypothesis that samples P007, P013 and P016 exhibit, at least partially, a dynamic monomer-dimer equilibrium indicative of non-covalent dimerization. The results suggest that at a concentration of 35 µM, signals within the distribution of samples P007, P013 and P016 likely do not correspond to distinct FLC species. Instead, these signals reflect a reaction boundary formed by the rapidly reversible interaction between monomers and dimers during sedimentation, resulting in an averaged mixed state of FLC monomers and dimers (Schuck 2010). Nonetheless, the reduction of intramolecular disulfide bonds during the TCEP experiment appears to contribute to the dissociation of non-covalently bound dimers, as indicated by the observed continuous decline in dimer content with increasing incubation time as shown in Figure 3.1E and Figure 8.1C, D.

3.6.5 Thermal stability of FLCs under reducing conditions

In order to evaluate the stability of FLCs under reducing conditions, thermal shift assays were conducted utilizing DSF (Fig. 3.7). This technique allows the detection of changes in stability by monitoring shifts in the melting temperature (T_m) of proteins. The melting temperatures of the FLC samples were initially determined under neutral buffer conditions with 30 mM Tris-HCl, pH 7.4. The measurement was then repeated with the addition of 7 mM pH-adjusted TCEP to destabilize intra- and intermolecular disulfide bonds. The influence of TCEP-induced aggregation was considered negligible in the DSF measurements, as the samples were not pre-incubated, and the thermal scans began immediately after TCEP addition. This minimized the time available for aggregation to occur before reaching the unfolding transition. This assumption is supported by our SV-AUC and CD results (Fig. 3.3 and 3.5), which show that significant aggregation requires extended incubation under reducing conditions.

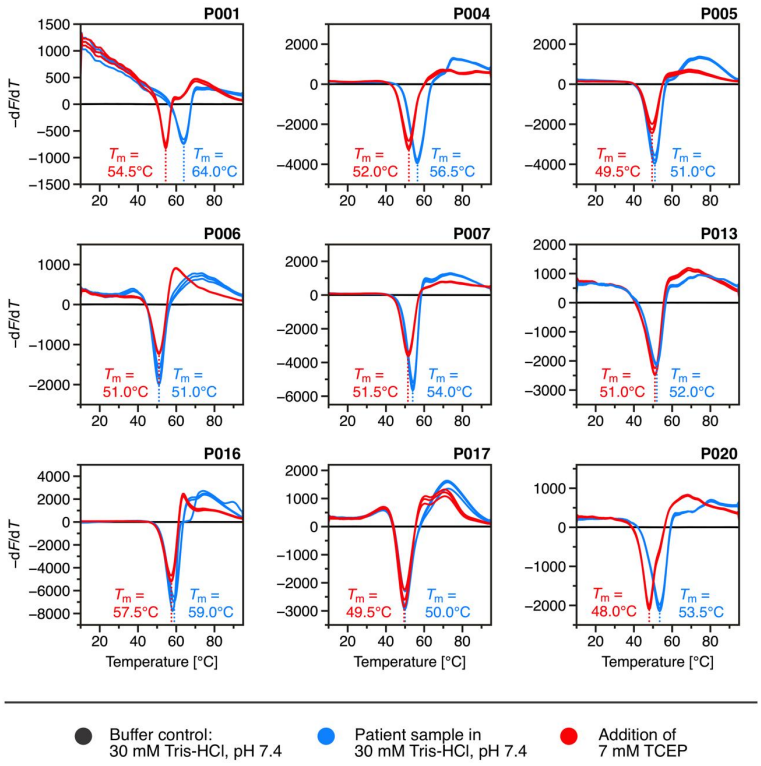

Figure 3.7: Influence of intra- and intermolecular disulfide bonds on melting temperatures of FLCs. The negative derivative fluorescence-temperature plots (−d*F*/d*T*) for all nine patient samples are shown. Samples were prepared at a concentration of 35 µM in 30 mM Tris-HCl, pH 7.4 (blue), with corresponding buffer control (black). To induce disulfide bond destabilization, 7 mM pH-adjusted TCEP (red) was added. Thermal denaturation was monitored using 10 µM SYPRO Orange in a total volume of 25 µL per well, measured in triplicate (n = 3). All replicates are shown individually, and consistent curve shapes and T_m values were observed across replicates.

The results indicate that observed differences in melting temperature induced by the reduction of disulfide bonds correlate with the propensity of FLCs to form dimers and higher oligomers. As expected for a κ-FLC, sample P006 shows the lowest degree of oligomerization, with 78.3% monomer and 9.7% dimer. After the addition of TCEP, no change was observed in the previously determined melting temperature of 51°C. In contrast, sample P004, consisting of 6.3% monomers and 84.7% dimers, showed a melting temperature shift of 4.5°C. Similarly, sample P020, consisting of 7.5% monomers, 72.9% dimers, and 8.8% tetramers, exhibited a 5.5°C difference between its two determined melting temperatures. Notably, both samples show an unusual high degree of dimerization for κ-type FLCs, which may already indicate a pathological deviation (Kaplan et al. 2011). As typical for λ-FLCs, sample P001 predominantly exists as a dimer (94.2%) and show no detectable monomeric signal. A temperature difference of 9.5°C was observed for P001, representing the largest deviation among the patient samples before and after disulfide bond reduction. This could be explained by the fact that, while κ-FLC dimerization often involves non-covalent interactions, λ-FLCs favors dimerization over covalent disulfide bonds (Sölling 1976). Although baseline separation of monomers and dimers was not achieved for samples P007, P013, and P016, their *c*(*s*) distributions nevertheless reveal dimeric species, as illustrated by their weight-average *s*-values (Fig. 3.2A). These findings suggest a dynamic monomer-dimer equilibrium driven by non-covalent interactions. Thermal shift data (Fig. 3.7) further

support this interpretation: despite measurable dimer fractions, only minimal ΔT_m values were observed in samples P006 (0°C), P017 (0.5°C), P013 (1°C), as well as P005 and P016 (1.5°C). Such minor shifts may indicate that these dimers are stabilized primarily by non-covalent interactions rather than by covalent bonds. Notably, sample P016 retains a relatively high melting temperature of 57.5°C after TCEP treatment, implying that some structural stabilization mechanisms remain active despite the reducing conditions. Since non-covalent dimerization would likely persist in the presence of TCEP, it is conceivable that this form of dimerization contributes to the thermal stability observed in P016. Alternatively, sequence-specific features or mutations unique to P016 may account for its above-average thermostability, even in the reduced state. In some measurements, particularly in sample P001, a distinct pre-transition fluorescence signal was observed. As no precipitation or signal loss was detected by SV-AUC, this signal was attributed to interactions with the fluorescent dye with native LCs, partially unfolded species, or other components such as LC fragments. Notably, this pattern was not consistent across all FLC samples and replicates confirmed a high degree of reproducibility.

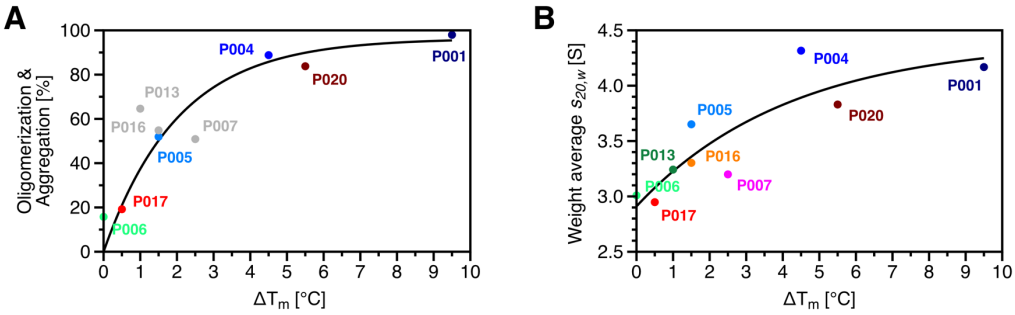

Figure 3.8: Correlation between oligomerization and the TCEP-induced melting-temperature shift (ΔT_m). (**A**) Oligomerization as a function of ΔT_m, obtained by integrating each $c(s)$ distribution from 2.93 S to 60.976 S, representing all species larger than monomer and low molecular weight fragments. The calculation is independent of that in Figure 3.2, although both analyses draw on the same dataset. Due to monomer and dimer peak overlap in samples P007, P013 and P016, the same limits were applied for consistency. These data points (grey) were excluded from the fit analysis. (**B**) Relationship between ΔT_m and weight-average s-values calculated by integration of the full $c(s)$ distribution range from 0 S to 60.976 S, including all detected species, such as fragments, monomers, and oligomers. DSF measurements were conducted without pre-incubation following TCEP addition, to isolate the effect of inter- and intramolecular disulfide bond reduction on thermal stability. Because DSF scans began immediately after TCEP addition and lasted only ~1 h, additional aggregation or fragmentation during the measurement is negligible. Fragment peaks in the $c(s)$ distribution profiles therefore reflect the samples' initial heterogeneity, not TCEP-induced degradation. Consequently, the full $c(s)$ range was used for calculation of weight-average s-values to capture the complete molecular composition and its relation to thermal stability.

Figure 3.8A presents the relationship between melting temperature shifts and oligomerization, demonstrating the correlation between both variables. As oligomerization increases across FLC samples, shifts in melting temperature before and after TCEP treatment become more pronounced, reaching a maximum shift of approximately 10°C for sample P001, which consists entirely of dimers. In Figure 3.8B, shifts in melting temperature are presented as a function of the weight-average s-values of FLCs. This value, averaged over the total distribution, provides an additional measure of the oligomerization states, allowing an inclusion of samples P007, P013 and P016. It remains uncertain

whether oligomerization beyond dimers would confer greater thermostability, with melting temperature shifts exceeding the highest detected shift of 10°C. The findings demonstrate that oligomerization significantly enhances the thermostability of FLCs. Samples with a high monomer content display only minor shifts in melting temperature after TCEP treatment, further suggesting that the stabilizing effects of the intramolecular disulfide bonds are minimal. Instead, stability appears to be predominantly driven by covalent dimerization or oligomerization rather than solely through disulfide bonds.

Table 3.1: Melting temperatures of FLCs at different buffer conditions.

				+ 0.1 M NaCl			+ 1 M NaCl		
Sample ID	T_m (°C)	T_m ^{TCEP} (°C)	ΔT_m (°C)	T_m (°C)	T_m ^{TCEP} (°C)	ΔT_m (°C)	T_m (°C)	T_m ^{TCEP} (°C)	ΔT_m (°C)
P001	64.0	54.5	9.5	61.0	53.0	8	61.0	51.5	9.5
P004	56.5	52.0	4.5	55.5	50.5	5	51.0	47.5	3.5
P005	51.0	49.5	1.5	49.5	48.0	1.5	47.5	46.5	1
P006	51.0	51.0	0	51.0	50.5	0.5	51.0	51.0	0
P007	54.0	51.5	2.5	53.0	50.5	2.5	51.5	50.0	1.5
P013	52.0	51.0	1.0	50.0	49.0	1.0	48.0	48.0	0
P016	59.0	57.5	1.5	59.0	57.0	2	60.0	59.0	1
P017	50.0	49.5	0.5	50.0	49.5	0.5	51.0	50.0	1
P020	53.5	48.0	5.5	51.5	46.5	5	51.0	45.5	5.5

$\Delta = T_m - T_m^{TCEP}$

The SV experiments indicate that sample P001 is unique among the samples in retaining dimeric structures after 15 hours of incubation. This dimerization may result from non-covalent interactions, which could also influence the thermostability of the sample as assumed for samples P007, P013 and P016. Given that the lowest melting temperature measured after TCEP addition was 48°C (in sample P020), it remains possible that the melting point of sample P001 could similarly decrease if complete loss of dimeric structure occurs. Consequently, the persistence of dimerization, even in reducing conditions, could play a critical role in maintaining the higher thermal stability observed in sample P001. Obtained melting temperatures and their respective shifts after disulfide bond reduction are summarized in Table 3.1. Corresponding thermal denaturation profiles for all patient samples are provided in the Supplementary information (Fig. 8.9). In addition to measuring the melting temperatures under standard conditions, the impact of ionic strength on the thermal stability of FLCs was evaluated by adding 0.1 M and 1 M NaCl. DSF measurements were repeated under otherwise identical conditions. Thermal denaturation profiles and corresponding negative derivative fluorescence-temperature plots for all measurements are provided in the Supplementary information (Fig. 8.10 and 8.11). All melting temperatures, including those from the NaCl conditions, are compiled in Table 3.1. For most FLC samples, the addition of NaCl resulted in a concentration-dependent decrease in T_m, both before and after TCEP treatment, suggesting that higher ionic strength may generally destabilizes these structures. However, this effect was not uniform across all samples. FLCs with more monomeric distributions, such as P006 and P017, showed minimal changes in T_m, while

more oligomeric samples, including P001, P004, and P020, exhibited more pronounced T_m reductions. This suggests that oligomeric FLCs may be more sensitive to changes in electrostatic interactions. Notably, samples derived from the IGKV1-33 germline again showed consistent behavior across different conditions.

3.7 Discussion

The biophysical characterization of FLCs purified from the urine of multiple myeloma patients aims to provide deeper insight into the relationship between their structural stability and aggregation propensity. Despite ongoing research, their behavior remains largely unpredictable, with tissue damage often detected only at advanced disease stages. It is estimated that between 25% to 75% of patients with multiple myeloma will develop kidney failure over the course of the disease (Yadav et al. 2015; Kundu et al. 2022). Moreover, approximately 25% of patients already show advanced kidney injury at the time of initial diagnosis (Bladé et al. 1998). To date, no confirmed correlation exists between the severity of tissue damage and the molecular properties of FLCs. However, pathogenesis is assumed to be influenced by protein-dependent factors intrinsic to monoclonal FLCs that predispose them to misfolding and aggregation (Basnayake et al. 2011). These factors may be determined by the individual amino acid sequence or may arise later through post-translational modifications (PTMs) and mutations that compromise structural integrity. Once initiated, the microenvironment – including the biochemical and physiological characteristics of the tissue, as well as the presence of specific interaction partners – may further promote aggregation (Bliznyukov et al. 2005). This complexity must be carefully considered when analysing FLCs.

To examine the effects of disulfide bond reduction on FLC species distribution and aggregation dynamics, nine purified FLC samples were incubated under reducing conditions for different periods of time. TCEP, which selectively and irreversibly reduces both inter- and intramolecular disulfide bonds within minutes (Burns et al. 1991), was used to induce destabilization. The reduction of disulfide bonds with TCEP is an established, but deliberately harsh, *in vitro* stress protocol for probing protein stability and triggering aggregation (Li et al. 2018; Sequeira et al. 2019; Melnikova et al. 2019; Džupponová and Žoldák 2023). Because this condition does not reproduce the complexity of physiological environments, the size, morphology, and surface chemistry of the resulting aggregates may differ from those that form naturally. Accordingly, the present data define one mechanistic limit – rapid aggregation after loss of disulfide bond stabilization – rather than a direct replica of *in vivo* aggregation pathway. The progression of changes in FLC species distribution following disulfide bond destabilization was monitored in a series of SV experiments. This approach enabled an analysis of structural stability and aggregation behavior as a function of incubation time in the presence of TCEP. Although the aggregates observed in this study were generated experimentally using reducing conditions, our use of the term ‘aggregation’ is not restricted to this specific pathway. Rather, it refers more generally to irreversible, misfolding-driven assemblies of potential pathological relevance. TCEP addition resulted in a time-dependent redistribution of molecular species in all samples, with disulfide bond reduction acting as a trigger for the observed aggregation process. Significant differences were observed among the samples in both the proportions of aggregates formed and the rates at which

these species developed. In conclusion, after 15 hours of incubation sample P001 exhibited the lowest aggregate proportion (~7%), while sample P020 demonstrated the highest level of aggregation (~73%). The remaining samples showed an average aggregate content of approximately 55% after the same incubation period. These findings indicate that the λ-FLC P001 demonstrates the highest stability, whereas P020 is the most susceptible to aggregation among κ-FLCs. However, this apparent relationship between aggregation stability and propensity does not correlate with patient clinical data (Tab. 8.1), nor with the documented degree of renal damage at the time of sample collection (Sternke-Hoffmann et al. 2020). The KDIGO (Kidney Disease: Improving Global Outcomes) nomenclature of chronic kidney disease (CKD) categorizes patients into five stages based on their glomerular filtration rate (GFR), ranging from normal kidney function (stage G1) to renal failure (Levey et al. 2020). Patient characteristics reveal that P020 shows only a mild decline in kidney function (G2), while patient P001 has progressed to moderate impairment (G3A). Similarly, patients P006 and P017 display distinct levels of kidney function despite comparable aggregation levels after 15 hours of TCEP incubation. While patient P017 presents normal kidney function (G1), patient P006 show an advanced renal impairment (G4). Therefore, it must be assumed that the specific type of aggregate, rather than the overall quantity, may play an important role in tissue damage. Since protein concentration is a well-established factor in driving self-assembly, it is likely that distinct FLCs exhibit unique concentration thresholds where they achieve peak aggregation levels. Additionally, factors beyond the structural destabilization of FLCs – such as the microenvironment – likely contribute to the formation of nephrotoxic aggregates as the disease progresses (Bliznyukov et al. 2005).

The SV experiments demonstrated different levels of resistance to reducing conditions among the dimeric FLC species. In most samples, a substantial loss of dimer was observed within 1.25 hours of TCEP incubation. However, samples P001, P004 and P020 showed greater resistance, with a pronounced dimer signal still present after 1.25 hours of incubation. Notably, sample P001 maintained a dimer signal of approximately 64% of total sample even after 15 hours of incubation. This suggests that TCEP-resistant dimers may exhibit sequence-specific features that contribute to a buried disulfide bond within the three-dimensional structure, limiting solvent accessibility and thereby preventing dissociation. Another possibility is that non-covalent interactions could stabilize the dimeric structure following disulfide bond reduction. However, this would be unexpected for sample P001, as covalent disulfide bonds are typically the primary stabilizing interactions facilitating dimer formation in λ-FLCs (Kaplan et al. 2011). No direct correlation was identified between the degree of dimerization and aggregation tendency. However, findings indicated that monomers dissociating from dimers lack stability in isolation and immediately transition into the aggregation pathway. It has been demonstrated that dimers formed under specific stress conditions exhibit structural differences from their native counterparts (Knight et al. 2022). Monomeric units within stress-induced dimers showed an increasingly non-native structural profile compared to native dimers. Consequently, it can be assumed that monomers resulting from forced dimer dissociation may also structurally differ from native monomers, potentially explaining the observed variation in stability. Given that the FLC samples analyzed are pathological, it should be considered that some dimers may inherently be stress-induced, having formed due to disease-associated alterations within the patients.

Previous studies on V_L and C_L domain fragments of FLCs have demonstrated that the reduction of disulfide bonds does not affect the secondary structure or folding state of the domains (Goto and Hamaguchi 1979; Frisch et al. 1996). However, after extended incubation with TCEP, a decrease of

approximately 0.2 S in the *s*-value of the monomeric signal was detected in the *c*(*s*) distribution, suggesting an altered sedimentation behavior. This shift could reflect partial unfolding of the monomer upon the reduction with TCEP, as both the V_L and C_L domains of FLCs contain intramolecular disulfide bonds. Supporting this interpretation, CD spectra obtained before and after TCEP treatment revealed secondary structure changes, further implying structural differences. A possible connection between TCEP-induced secondary structure changes and FLC aggregation was observed by comparing sedimentation and CD spectroscopy data. The results indicate that an early loss of secondary structure following TCEP reduction may be associated with an increased aggregation tendency of FLCs. Prolonged TCEP incubation also resulted in the formation of low molecular weight fragments, with an increase in the corresponding signal at approximately 0.1 S observed following the addition of reducing agent. This increase tends to correlate with the duration of incubation. Therefore, it must be considered that the observed decrease in monomeric *s*-value may also be associated with a loss in molecular mass.

Although disulfide bonds have been shown to have only a minor influence on the overall structure of FLCs, they remain essential for their stability (Goto and Hamaguchi 1979). Studies using a V_L domain fragment have demonstrated that the intramolecular disulfide bond contributes to folding stability by lowering the entropy of the unfolded state (Frisch et al. 1996). It is assumed that this decrease in entropy limits the conformational freedom of the unfolded state, thereby favouring the native folding of the domain. Consequently, while the disulfide bond is not strictly required for correct folding, it enhances stability and facilitates faster achievement of the native folding state (Frisch et al. 1996). The effect of disulfide bonds on the stability of the nine FLCs examined in this study was assessed through DSF. Measured melting temperatures of FLCs without TCEP addition aligned with previously determined values obtained using differential scanning calorimetry (DSC) and nanoDSF (Sternke-Hoffmann et al. 2023). Sample P006, which exhibited the lowest dimer proportion at approximately 10%, showed no change in melting temperature following disulfide bond reduction. In contrast, sample P001, consisting entirely of dimers, displayed a substantial decrease in melting temperature of nearly 10°C upon disulfide bond reduction. The remaining samples also showed a correlation between the reduction-induced decrease in melting temperature and the degree of oligomerization, which was also expressed by the $s_{20,w}$ of the total *c*(*s*) distribution. This trend is further supported by the response of FLCs to changes in ionic strength. Samples with a higher degree of oligomerization, such as P001, P004, and P020, exhibited more pronounced decreases in melting temperature upon addition of NaCl, both with and without TCEP. In contrast, monomeric or less oligomeric samples, including P006 and P017, remained largely unaffected, showing minimal or no changes in T_m. These findings suggest that intermolecular interactions stabilizing oligomeric assemblies are particularly sensitive to electrostatic screening effects at higher ionic strength. The resulting destabilization likely lowers the energy barrier for thermal unfolding. This observation further reinforces the link between quaternary structural organization and thermal stability and supports the broader conclusion that FLC oligomerization modulates sensitivity to environmental stressors.

In addition to an increase in low molecular weight fragments with a *s*-value of approximately 0.1 S during TCEP incubation, another signal at around 1 S was detected in the samples P006, P016 and P017, suggesting further fragmentation. Notably, these three samples share the genetic origin from the germline sequence IGKV1-33, potentially indicating a sequence-specific predisposition to

fragmentation (Sternke-Hoffmann et al. 2023). For the other FLCs, however, no correlation between germline sequence and species distribution was found. The underlying cause of the observed release of low molecular weight fragments as well as fragments associated with IGKV1-33 FLCs remains inconclusive. However, FLCs remain stable over extended incubation times in the absence of TCEP, with no fragmentation detected. Physiologically, fragment formation is often the result of proteolytic cleavage by endoproteases. Endoproteolysis, in turn, is influenced by the kinetic stability of dimeric structures, as the dimeric state protects FLCs from proteolytic cleavage (Morgan and Kelly 2016). While fragments from the V_L domain usually predominate in pathological aggregates (Glenner et al. 1970), aggregates consisting primarily C_L domain fragments have also been documented (Olsen et al. 1998). Unlike the V_L domain, the C_L domain appears to be able to resist further endoproteolytic cleavage (Solomon et al. 1998). MS analysis identified traces of various cathepsins across all nine patient samples (Dupré et al. 2021). These enzymes co-purified with FLCs from patients urine samples due to their similar molecular weight of 20 to 35 kDa (Turk 2001; Yuzhalin et al. 2018). However, as cathepsin levels were often near the detection threshold, their concentrations were insufficient for visualization in $c(s)$ distributions or on sodium dodecyl sulphate-polyacrylamide gel electrophoresis (SDS-PAGE). Given that samples are stable without TCEP addition, it can be assumed that disulfide bond reduction exposes previously inaccessible regions that are susceptible to cathepsin cleavage. Cathepsins show the highest activity in a reducing environment at a low pH of around 5 (Turk et al. 2012; Yadati et al. 2020). Whether cathepsins remain active under the experimental conditions used in this work and contribute to observed fragmentation is currently under further investigation. Breaks within the peptide backbone may occur in patients but only become apparent during experimental destabilization. Studies have shown that in addition to reducing disulfide bonds, TCEP itself can induce peptide bond cleavage (Liu et al. 2010). Under certain conditions, an unspecific side reaction can lead to the cleavage at cysteine residues, potentially causing TCEP-induced protein fragmentation, particularly during extended incubation periods. Given that fragmentation observed in the IGKV1-33 samples occur after prolonged TCEP incubation, this mechanism cannot be ruled out. This raises questions about specific characteristics in IGKV1-33 sequences that could underlie this distinctive fragmentation pattern. However, the evidence for two distinct fragmentation mechanisms suggests that identified fragments may result from an interplay between these processes.

3.8 Conclusion

The purification of FLCs from patient urine represents a non-invasive sampling method, yielding high FLC concentrations with sufficient purity for detailed biophysical and biochemical analyses. In search for prognostic markers to predict renal complications in monoclonal gammopathies, such as MM, this study emphasizes the critical role of disulfide bonds in preserving the structural integrity of FLCs and mitigating their tendency to form nephrotoxic aggregates. In summary, loss of disulfide bonds caused a redistribution of molecular species and aggregation as observed by SV-AUC after different TCEP-incubation periods. FLC dimers were differently resistant to dissociation, possibly due to non-covalent interactions or variations in cysteine accessibility to the reducing agent. Varying incubation times revealed that, in most cases, dimers do not dissociate into stable monomers but instead accumulate

directly into higher-order oligomers and aggregates. Prolonged reducing conditions led to FLC degradation, as evidenced by an increase in low molecular weight fragments that were detectable at approximately 0.1 S but did not sediment adequately at 60,000 rpm. A simultaneous decrease in monomeric *s*-value with increasing TCEP incubation times suggested potential unfolding, further supported by CD spectroscopy, which revealed secondary structure changes. Notably, FLCs derived from the IGKV1-33 gene exhibited unique fragmentation behavior under reducing conditions, while FLCs from other germline sequences did not demonstrate a connection between germline origin and molecular properties. A correlation between the oligomerization state and the melting temperature shift upon TCEP treatment further highlights the critical role of disulfide bonds in stabilizing FLCs, particularly in promoting dimerization through covalent bonding. While the *in vitro* behavior of purified FLCs offers valuable insights, its correlation with *in vivo* behavior across diverse patient tissue environments remains uncertain, as no direct correlation to patient-specific clinical data was observed. It is important to acknowledge that the clinical data available in this study represent only a single time point corresponding to sample collection at initial diagnosis, leaving both the pathological changes preceding diagnosis and the subsequent disease progression unexamined. To address these limitations, future studies should prioritize longitudinal monitoring of FLC levels in both serum and urine over the course of disease progression, with particular attention to their changes in relation to renal damage. Numerous additional factors likely influence the pathological behavior of disease associated FLCs, potentially evolving alongside disease progression. Tracking changes in patient characteristics over time may improve the interpretability of biophysically determined FLC properties and their pathological roles within the clinical context. Rather than expanding the sample size, future studies could focus on a selected cohort of patients with periodic sampling throughout disease progression. This approach would enhance the precision and relevance of the findings, supporting validation of the *in vitro* characteristics of FLCs described here as potential prognostic markers.

4

Reduction-associated fragmentation of FLCs

4.1 Abstract

Fragmentation of immunoglobulin free light chains (FLCs), particularly the release of isolated variable domain fragments, is associated with diseases such as light chain amyloidosis and multiple myeloma, where it can promote aggregation and amyloid formation. The underlying cause of fragmentation observed in patient-derived FLCs under reducing conditions during sedimentation velocity analysis remained unresolved. Preliminary mass spectrometry data revealed trace amounts of several cathepsin species in all FLC preparations. To investigate whether this fragmentation could arise from co-purified cathepsins, intrinsic protease activity was quantified using a fluorescence-based cathepsin D/E substrate assay, and proteolytic susceptibility was tested by controlled digestion with human liver-purified cathepsin D. All FLC samples exhibited detectable cathepsin activity under acidic conditions, whereas activity at physiological pH was markedly reduced and developed slowly over prolonged incubation time. Cathepsin activity persisted under reducing conditions, as indicated by substrate turnover in the presence of TCEP. Controlled digestion revealed pronounced sample-dependent responses. In sample P016, cathepsin D induced extensive formation of a defined fragment, whereas in sample P001, fragmentation occurred primarily after disulfide bond reduction and independently of cathepsin D addition. Fragmentation detected by SDS-PAGE was more extensive than that observed during sedimentation velocity experiments under comparable conditions. Overall, the results do not identify a single unifying mechanism of FLC fragmentation but instead provide a foundation for future investigations of the molecular basis of this process.

Keywords: Patient-derived immunoglobulin free light chains (FLCs), Fragmentation, Cathepsins, Proteolysis, Substrate specific fluorescence assay, Tris-Tricin SDS-PAGE

4.2 Introduction

Fragmentation of FLCs is of particular relevance in diseases such as AL amyloidosis and MM, where V_L domain fragments are associated with increased amyloidogenicity and aggregation propensity, indicating that fragmentation can alter the pathological behavior of FLCs and contribute to disease progression (Glenner et al. 1970; Morgan and Kelly 2016; Rennella et al. 2019; Lavatelli et al. 2024). In Chapter 3, fragmentation was detected under reducing conditions during SV-AUC analysis. However, the molecular cause of this fragmentation could not be determined. Despite its clinical relevance, the mechanisms underlying FLC fragmentation remain incompletely understood but may involve enzymatic proteolysis of destabilized FLC species (Morgan and Kelly 2016). In the context of the experimental setup, studies have shown that the reducing agent TCEP can promote peptide backbone cleavage at cysteine residues as a side reaction, resulting in chemical fragmentation (Liu et al. 2010). Discriminating between these possibilities therefore requires experimental approaches that investigate whether proteolytic activity is present in FLC preparations, remains active under relevant conditions, and is capable of generating fragmentation patterns comparable to those observed experimentally.

Proteases of the cathepsin family represent a plausible class of candidate enzymes in this context. Cathepsins are lysosomal proteases involved in intracellular protein turnover and antigen processing, with activity typically favored by acidic environments (Sun et al. 2013; Yadati et al. 2020). Although primarily localized within endo-lysosomal compartments, several cathepsins retain activity at neutral pH and have been implicated in pathological protein degradation processes beyond their intracellular environment (Yadati et al. 2020). Given that FLCs are filtered and processed by the kidneys and may encounter lysosomal compartments during tubular reabsorption, cathepsins exposure is likely (Sun et al. 2013; Fox et al. 2016). Consistent with this, prior MS analysis detected trace amounts of different cathepsin species in patient-derived FLC preparations (Tab. 4.1), suggesting co-purification during isolation from patients urine (Sternke-Hoffmann et al. 2023). Cathepsin D and L (CtsD, CtsL) can generate defined ~12 kDa fragments from LCs, with cleavage constrained by disulfide bonding patterns and local structural accessibility (Čaval et al. 2021). Other studies reported that certain pathogenic FLCs display substantial resistance to proteolytic degradation and fail to release V_L domain fragments (Sirac et al. 2021), underscoring that susceptibility to proteolysis is highly clone-dependent and that cathepsin-mediated cleavage is not a universal outcome. Beyond their intracellular roles, altered cathepsin expression and activity has been linked to CKD and fibrotic remodeling, and inhibition of CtsD with pepstatin A has been shown to attenuate kidney fibrosis in experimental models (Fox et al. 2016).

The experiments presented in this chapter aim to assess whether cathepsin activity is detectable in patient-derived FLC preparations, whether it remains enzymatically active under relevant experimental conditions, and whether it is sufficient to reproduce fragmentation patterns observed under reducing conditions.

4.3 Methods

4.3.1 Cathepsin D and E activity assay

To investigate whether proteolytic activity contributes to the formation of low-S FLC fragments after reduction, patient-derived FLC preparations were examined for intrinsic cathepsin activity potentially resulting from co-purification during extraction from patient urine. Preliminary MS analysis identified varying traces of different cathepsin species in all purified FLC samples (Tab. 4.1). To determine whether these co-purified proteases retain their enzymatic activity under the experimental conditions, cathepsin activity was quantified using a fluorescence-based assay. Measurements were performed using a CLARIOstar multi-mode plate reader (BMG Labtech, Ortenberg, Germany) and flat-bottom, half-area 96-well microplates with a high-binding surface (#3601, Corning, NY, USA), sealed with SealPlate film (#Z369667, Sigma-Aldrich). Assays were conducted in either 0.1 M sodium acetate buffer (pH 4.5) or 30 mM Tris-HCL buffer (pH 7.4) with FLC concentrations of 35 µM. A fluorogenic cathepsin D and E (CtsD/E) substrate (BML-P145-0001, Enzo Life Sciences, Farmingdale, NY, USA; Lot-Nr.: 01202304) was added to a final concentration of 20 µM. Negative control reactions contained substrate and buffer only. As a positive control, CtsD purified from human liver (BML-SE199-0025, Enzo Life Sciences, Farmingdale, NY, USA; Lot-Nr.: 06242118 & M43FZ59) was assayed under identical buffer and substrate conditions at a final concentration of 6 ng/µL. Further reactions included the addition of the aspartic proteinase inhibitor pepstatin A at final concentrations of 20 µM or pH-adjusted TCEP at a final concentration of 7 mM. All reactions were performed in a final volume of 100 µL and set up in triplicate (n = 3). Fluorescence measurements were conducted at 37°C with continuous shaking at 600 rpm in double-orbital mode prior to each measurement cycle. Fluorescence intensity was recorded from the bottom of the plate every 80 s for a duration of 4.5 h or 18 h using an excitation wavelength of 330 nm and an emission wavelength of 410 nm.

Table 4.1: Traces of cathepsins identified by MS analysis. MS/MS count denotes the number of spectra assigned to each protein. Entries shown in grey indicate proteins detected by only a single peptide and are therefore not considered validated. Data adapted from Sternke-Hoffmann et al. 2023.

Protease	P001	P004	P005	P006	P016	P017	P020
Cathepsin Z	7	6	10	12	9	9	7
Cathepsin D	3	2	11	6	2	13	8
Cathepsin B	1	1	7	3	5	7	8
Cathepsin L2	0	0	1	1	0	0	4
Pro-Cathepsin H	0	0	8	1	7	0	1
Pro-Cathepsin L	0	0	1	1	0	0	1
Cathepsin S	0	0	0	0	0	0	0

4.4.2 Analysis of CtsD-mediated fragmentation

To test whether proteolytic activity is sufficient to induce fragmentation patterns comparable to those observed after reduction in Chapter 3, patient-derived FLC samples were subjected to controlled proteolytic digestion using CtsD as a representative lysosomal protease. CtsD purified from human liver was added to FLC samples to amplify proteolytic activity beyond intrinsic levels. Fragmentation experiments were conducted in either 30 mM Tris-HCL buffer (pH 7.4) or 0.1 M sodium acetate buffer (pH 4.5). To evaluate whether cathepsin activity is retained under reducing conditions and to further investigate the protective role of FLC disulfide bonds against proteolysis, 3 mM TCEP adjusted to the corresponding buffer pH was added where indicated. In contrast to the reduction conditions used in Chapter 3, the TCEP concentration was deliberately lowered to minimize possible TCEP-induced fragmentation effects. All reactions were performed at an FLC concentration of 35 µM in a total reaction volume of 100 µL, resulting in a CtsD concentration of 6 ng/µL, in addition to any intrinsic proteolytic activity present in the samples. Preparations were then incubated for 1 h at 37°C with continuous shaking at 600 rpm. Subsequently, proteolytic fragmentation was analyzed by Tris-Tricine SDS-PAGE. Gel preparation and electrophoretic separation were performed using Mini-PROTEAN Tetra handcast systems and vertical electrophoresis chambers equipped with PowerPac Basic power supplies (Bio-Rad Laboratories, California, USA). Prior to electrophoresis, either reducing or non-reducing Laemmli sample buffer was added (Laemmli 1970), and samples were heated at 95°C for 5 min. A Spectra Multicolor Low Range Protein Ladder (1.7 to 40 kDa; #26628, Thermo Fisher Scientific, Waltham, MA, USA) was used as a molecular-weight standard. Electrophoresis was carried out at a constant voltage of 40 mA per gel for approximately 1 to 1.5 h. Following separation, gels were stained either with Coomassie brilliant blue followed by destaining or with the single-step gel dye *Der Blaue Jonas* (#GRP1, German Research Products, Haag, Germany), which does not require a destaining step. Gel images were acquired using a ChemiDoc MP imaging system (Universal Hood III; Bio-Rad Laboratories) and analyzed with Image Lab software version 5.1.

4.4 Results

4.4.1 Cathepsin D and E activity assay

To test whether patient-derived FLC preparations contain enzymatically active proteases co-purified during urine extraction, intrinsic cathepsin activity was quantified using a fluorogenic CtsD/E substrate assay as described in Section 4.3.1. Given the acidic pH optimum of cathepsins, initial measurements were performed in 0.1 M sodium acetate buffer at pH 4.5.

As shown in Figure 4.1, all FLC samples displayed a pronounced increase in fluorescence signal within the first hour of measurement, reaching plateau levels of ~700 arbitrary units after ~30 min. This signal increase was absent in buffer controls and is indicative of proteolytic activity under acidic conditions. While minor differences in kinetic profiles and plateau intensities were observed between samples, replicates showed a high level of consistency, suggesting sample-specific but reproducible protease activity, in agreement with prior MS findings (Sternke-Hoffmann et al. 2023). In the positive control containing purified human liver CtsD, fluorescence saturation was already present at the earliest time points, consistent with rapid substrate turnover occurring prior to data acquisition.

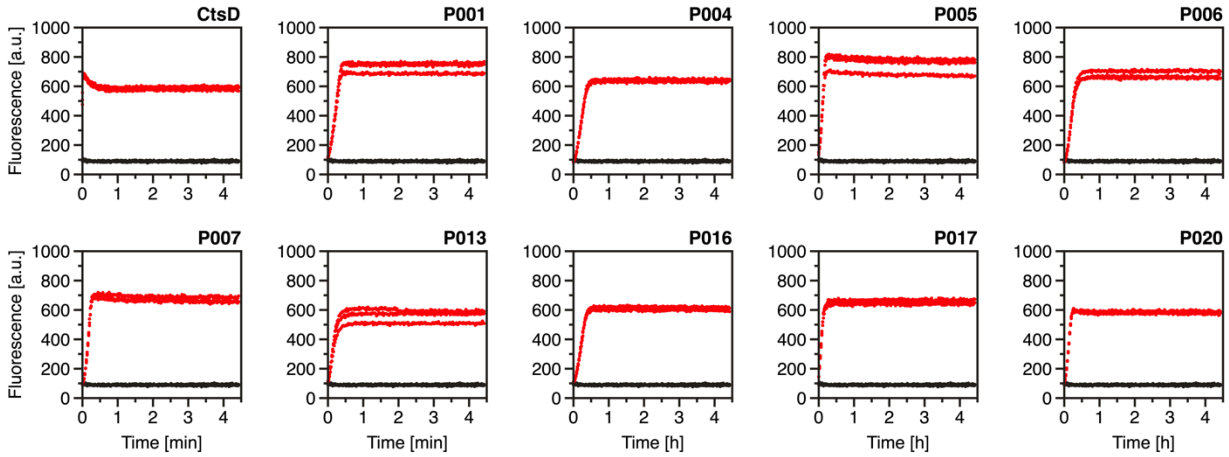

Figure 4.1: CtsD/E activity in patient-derived FLC samples at pH 4.5. Samples were prepared with FLC concentrations of 35 µM in 0.1 M sodium acetate buffer at pH 4.5 (red), with corresponding buffer-only controls (black). A fluorogenic CtsD/E substrate was added to a final concentration of 20 µM in a total reaction volume of 100 µL per well. Assays were performed in triplicate (n = 3) at 37°C with continuous shaking at 600 rpm. Human liver-purified CtsD at a concentration of 6 ng/µL served as positive control. Fluorescence intensity was detected at an excitation wavelength of 330 nm and an emission wavelength of 410 nm. Fluorescence was monitored over 4.5 h.

To assess cathepsin activity under physiological pH conditions, measurements were repeated in 30 mM Tris-HCl buffer at pH 7.4 (Fig. 4.2). Under these conditions, fluorescence signals were substantially reduced for most FLC samples and developed more slowly over an extended measurement period of 18 h. Samples P001, P007, P013, and P017 displayed only minimal signal increases without reaching a plateau. In contrast, sample P016 displayed slower but otherwise comparable kinetics to those observed at acidic conditions, reaching a plateau after ~3 h and showing

increased variability between replicates. Samples P004, P005, P006, and P020 showed sustained fluorescence increases throughout the measurement, similar to the CtsD control, with signals approaching plateau after 18 h.

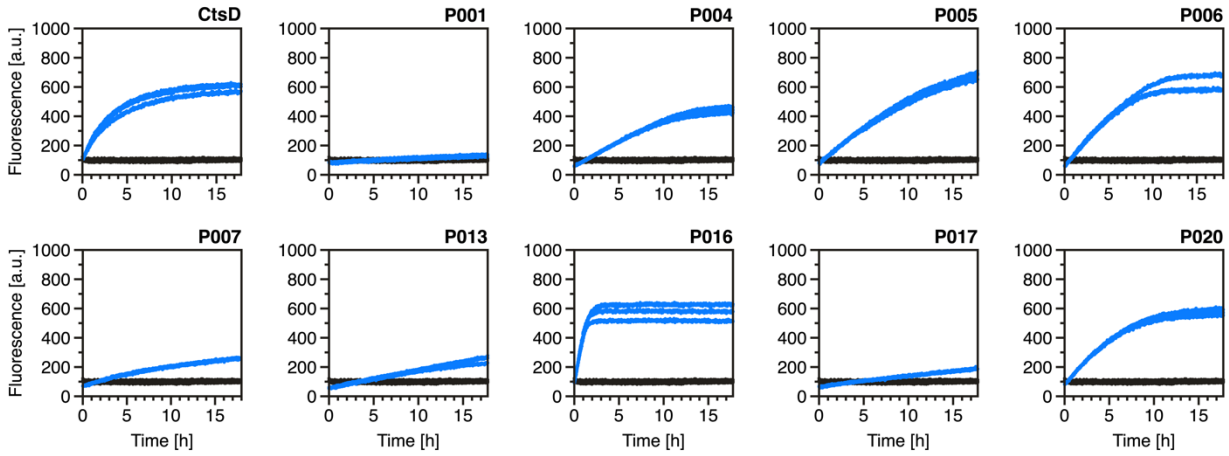

Figure 4.2: CtsD/E activity in patient-derived FLC samples at pH 7.4. Samples were prepared with FLC concentrations of 35 µM in 30 mM Tris-HCl buffer at pH 7.4 (blue), with corresponding buffer controls (black). A fluorogenic CtsD/E substrate was added to a final concentration of 20 µM in a total reaction volume of 100 µL per well. Assays were performed in triplicate (n = 3) at 37°C with continuous shaking at 600 rpm. Human liver-purified CtsD at a concentration of 6 ng/µL served as positive control. Fluorescence intensity was detected at an excitation wavelength of 330 nm and an emission wavelength of 410 nm. Fluorescence was monitored over 18 h.

To confirm that the observed fluorescence signals were attributable to protease activity, measurements at pH 4.5 were repeated in the presence of the proteinase inhibitor pepstatin A (Fig. 4.3). The addition of papstatin A resulted in a pronounced reduction of fluorescence signals for nearly all FLC samples, bringing signal intensities close to buffer control levels. The CtsD positive control was likewise inhibited, displaying only a minor fluorescence increase after ~4.5 h. Exceptions were samples P016 and P020, which retained activity, suggesting incomplete inhibition or alternative substrate interactions. Replicates remained highly consistent, supporting that the detected activity predominantly originated from co-purified cathepsins such as CtsD and CtsE, in accordance with the substrate specificity of the assay.

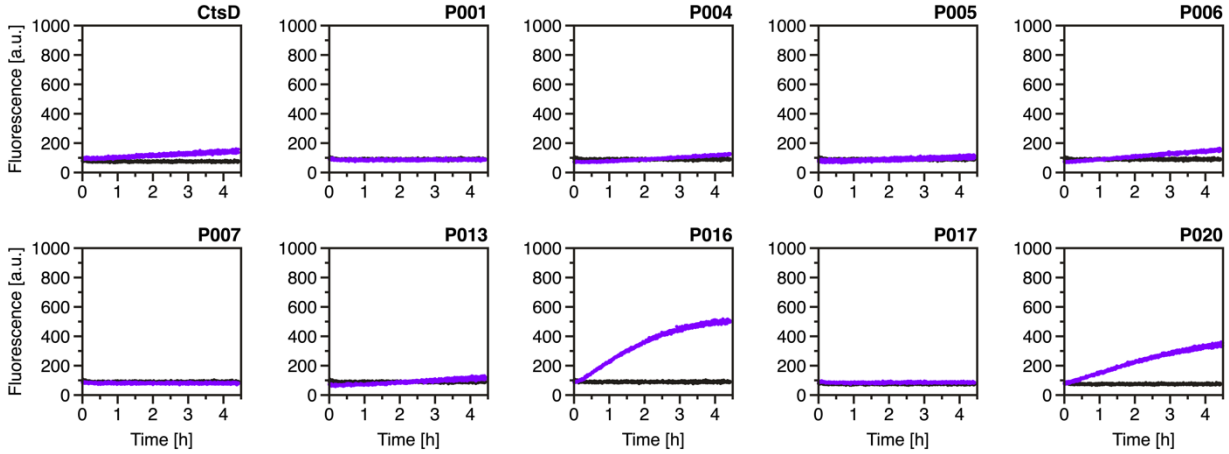

Figure 4.3: CtsD/E activity in patient-derived FLC samples at pH 4.5 in the presence of pepstatin A. Samples were prepared with FLC concentrations of 35 µM with the addition of 20 µM pepstatin A in 0.1 M sodium acetate buffer at pH 4.5 (purple), with corresponding buffer controls (black). A fluorogenic CtsD/E substrate was added to a final concentration of 20 µM in a total reaction volume of 100 µL per well. Assays were performed in triplicate (n = 3) at 37°C with continuous shaking at 600 rpm. Human liver-purified CtsD at a concentration of 6 ng/µL served as positive control. Fluorescence intensity was detected at an excitation wavelength of 330 nm and an emission wavelength of 410 nm. Fluorescence was monitored over 4.5 h.

To evaluate whether cathepsin activity persisted under reducing conditions relevant to the fragmentation behavior observed in Chapter 3, assays were repeated at pH 4.5 in the presence of 7 mM TCEP (Fig. 4.4). Samples P001 and P005, analyzed alongside a CtsD control, displayed fluorescence kinetics comparable to those observed at pH 4.5 in the absence of reducing agent. These results demonstrate that CtsD retains proteolytic activity under reducing conditions, confirmed by hydrolysis of the CtsD/E-specific fluorogenic substrate.

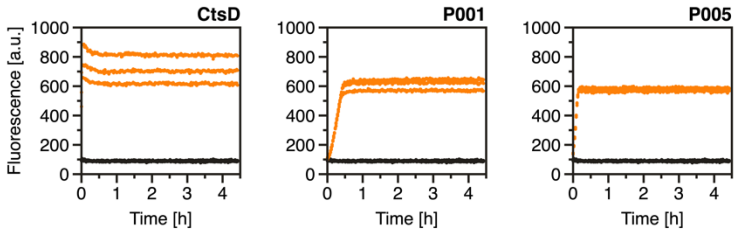

Figure 4.4: CtsD/E activity at pH 4.5 in the presence of TCEP. Samples were prepared with FLC concentrations of 35 µM with the addition of 7 mM TCEP in 0.1 M sodium acetate buffer at pH 4.5 (orange), with corresponding buffer controls (black). A fluorogenic CtsD/E substrate was added to a final concentration of 20 µM in a total reaction volume of 100 µL per well. Assays were performed in triplicate (n = 3) at 37°C with continuous shaking at 600 rpm. Human liver-purified CtsD at a concentration of 6 ng/µL served as positive control. Fluorescence intensity was detected at an excitation wavelength of 330 nm and an emission wavelength of 410 nm. Fluorescence was monitored over 4.5 h.

4.4.2 Analysis of CtsD-mediated fragmentation

To further examine whether enhanced proteolytic activity is sufficient to induce the fragmentation of patient-derived FLCs, samples were subjected to controlled digestion with CtsD and analyzed by Tris-Tricine SDS-PAGE, as described in Section 4.3.2. Representative results for samples P001 and P016 are shown in Figure 4.5.

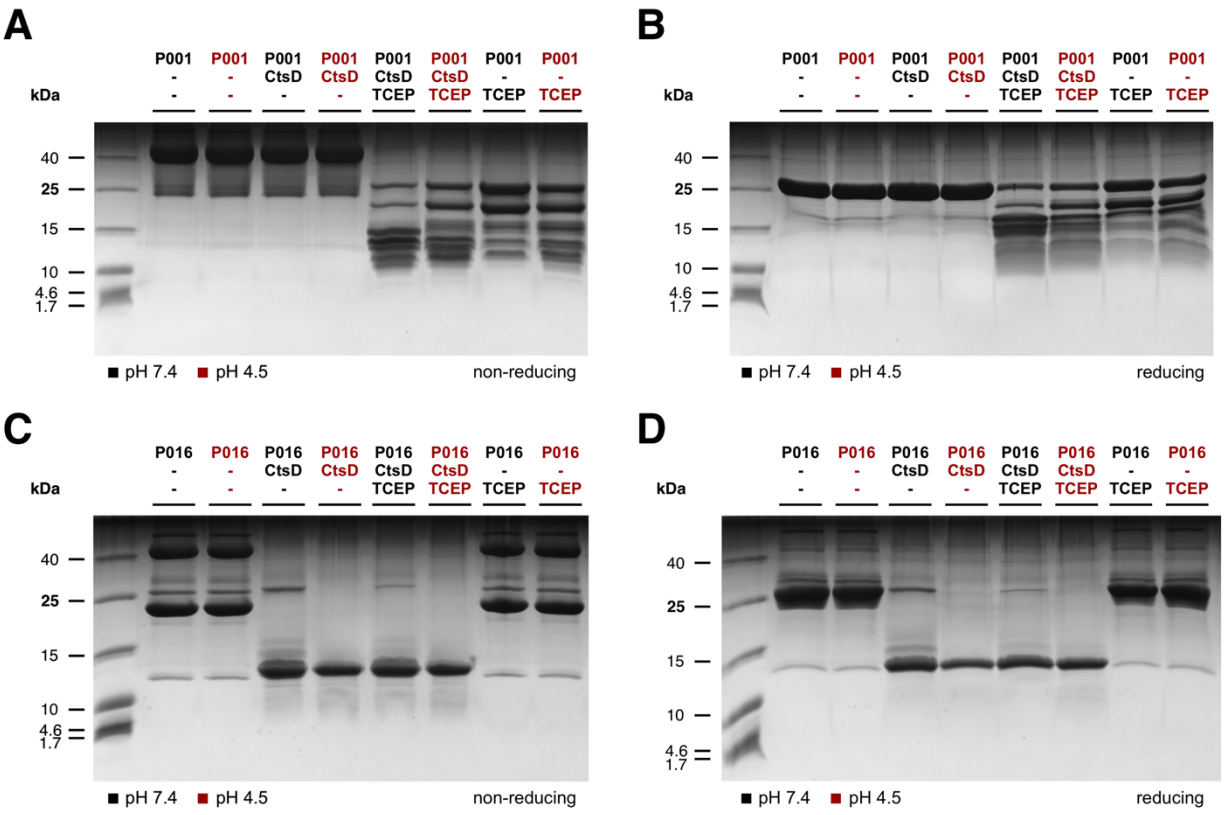

Figure 4.5: CtsD-mediated fragmentation of FLC samples P001 and P016. Proteolytic fragmentation was analyzed by Tris-Tricine SDS-PAGE using non-reducing (**A**, **C**) or reducing (**B**, **D**) sample buffer. FLCs were incubated at concentrations of 35 µM in either 30 mM Tris-HCl buffer at pH 7.4 or 0.1 M sodium acetate buffer at pH 4.5 in a total reaction volume of 100 µL. Where indicated, CtsD purified from human liver was added to a final concentration of 6 ng/µL. For destabilization of disulfide bonds, 3 mM TCEP was added. Samples were incubated for 1 h at 37°C with shaking at 600 rpm prior to electrophoretic analysis.

Following incubation under indicated buffer conditions, samples were prepared for SDS-PAGE using either non-reducing (Fig. 4.5A, C) or reducing (Fig. 4.5B, D) Laemmli sample buffer. Under non-reducing sample preparation conditions and across both buffers, samples P001 and P016 displayed dominant bands corresponding to monomeric and dimeric FLC species. Only faint additional bands in the range of approximately 10-15 kDa were detected (Fig. 4.5A, C). Upon preparation with reducing sample buffer, dimeric species collapsed into a dominant band at approximately 25 kDa (Fig. 4.5B, D), likely corresponding to reduced monomeric FLC species.

In sample P016, incubation with CtsD resulted in pronounced fragmentation (~10-15 kDa), characterized by complete loss of bands corresponding to intact monomeric and dimeric FLC species. This effect was observed at both pH values and remained reproducible when TCEP was present during incubation. In contrast, incubation with TCEP alone did not result in fragmentation in P016, and banding patterns remained comparable to those observed in samples incubated without reducing agent. Sample P001 demonstrated a distinct behavior. Incubation with CtsD alone did not result in detectable fragmentation. However, extensive fragmentation was observed following incubation with TCEP, both in the presence and absence of exogenous CtsD. Under these conditions, multiple bands in the molecular range of 10-25 kDa were detected. Because similar fragmentation patterns were observed in the absence of CtsD, these results do not support a dominant role for CtsD in the fragmentation of sample P001 under the applied conditions. Notably, fragmentation of P001 observed following reduction was less prominent in the corresponding SV-AUC experiments. This discrepancy suggests that the combination of disulfide bond reduction and denaturing conditions during SDS-PAGE, including sample heating to 95°C during preparation, promotes fragmentation as a consequence of FLC destabilization. Taken together, these experiments demonstrate pronounced sample-specific susceptibility to reduction and proteolysis but do not allow a clear attribution of fragment formation to CtsD-mediated proteolysis.

4.5 Discussion

The experiments presented in this chapter investigated whether proteolytic activity from cathepsins co-purified with patient-derived FLCs could account for the fragmentation observed under reducing conditions during SV-AUC analysis in Chapter 3. It is important to mention, that outside of reducing conditions, no evidence of proteolytic degradation was detected in any of the FLC samples. Based on long-term experience, all FLCs remained stable across a wide range of storage and handling conditions, including prolonged storage at 4°C and extended exposure at RT, without signs of spontaneous fragmentation or progressive degradation (Sternke-Hoffmann et al. 2020; Sternke-Hoffmann 2021; Sternke-Hoffmann et al. 2023; Tucholski et al. 2025).

Fluorescence-based CtsD/E substrate assays confirmed proteolytic activity in all FLC preparations under acidic conditions, consistent with prior MS detection of different cathepsin species (Tab. 4.1; Sternke-Hoffmann et al. 2023) and with the known lysosomal pH optimum of cathepsins around pH 4-5 (Yadati et al. 2020; Čaval et al. 2021). Inhibition with papstatin A markedly reduced substrate turnover in most samples, including CtsD controls, supporting the specificity of the detected signals. Residual activity observed in samples P016 and P020 may reflect incomplete inhibition or alternative substrate interactions. At physiological pH, enzymatic activity was substantially reduced and developed slowly over extended measurement periods, consistent with previous reports (Yadati et al. 2020). Proteolytic activity persisted under reducing conditions, indicating that TCEP does not eliminate cathepsin catalysis, in line with the reducing environment of lysosomal compartments (Hafner Česen et al. 2016).

Controlled digestion experiments with purified human liver CtsD produced distinct, sample-dependent outcomes. In sample P016, CtsD exposure resulted in the formation of a defined fragment species, whereas in sample P001, fragmentation occurred predominantly following disulfide bond reduction and independently of CtsD addition. Overall, fragmentation detected by Tris-Tricine SDS-PAGE was more pronounced than that observed by SV-AUC under comparable conditions, highlighting the influence of analytical context. Denaturing steps in electrophoretic analysis, including SDS exposure and heat treatment, likely further destabilize reduced FLC species and promote additional fragmentation of otherwise intact molecules, consistent with prior observations (Miekka 1983).

Based on these data, FLC fragmentation observed after disulfide bond destabilization cannot be attributed to a single mechanism, such as proteolysis caused by residual cathepsins (Morgan and Kelly 2016) or TCEP-induced chemical cleavage (Liu et al. 2010). Although CtsD/E specific proteolytic activity was detectable in all samples, the degree and intensity of fragmentation were highly sample dependent and variably influenced by CtsD addition or reducing conditions alone. The discrepancy between fragmentation patterns observed by SDS-PAGE and SV-AUC further highlights the impact of analytical context and sample handling on fragmentation outcomes. Importantly, these experiments demonstrated that cathepsins retain proteolytic activity beyond their acidic pH optimum and under reducing conditions, which was substantially inhibited by pepstatin A. However, because intrinsic cathepsin contributions under TCEP-only conditions cannot be excluded, future studies should incorporate protease inhibition strategies to better distinguish between proteolytic and reduction-induced fragmentation.

5

Recombinant expression of a patient-derived FLC in *E. coli*: a folding pathway analysis

5.1 Abstract

The recombinant expression of patient-derived proteins is an essential tool for investigating their structure, function, and *in vitro* behavior under defined and reproducible conditions. This is particularly valuable when working with clinical samples, where both sample scarcity and biological variability often complicate analysis. In this chapter, *Escherichia coli* was evaluated as a host system for recombinant production of the patient-derived monoclonal free light chain (FLC) P006, with the aim of generating structurally native-like material. Initial inclusion-body expression and redox-mediated *in vitro* refolding yielded tag-free, sequence-authentic recombinant light chains (rLCs) in high quantity but with non-native, disordered secondary structures, as revealed by circular dichroism (CD) spectroscopy, along with SV-AUC profiles showing the corresponding effects of non-native conformations on molecular species distribution. Neither optimization of the initial literature-adapted refolding protocol nor systematic evaluation of additional literature-based strategies succeeded in the recovery of a native-like conformation. To address these limitations, a periplasmic expression approach was tested to utilize the oxidizing folding environment and the assistance of periplasmic chaperones. Additionally, the co-expression of Skp facilitated disulfide bond formation and secondary-structure recovery, resulting in CD spectra closely resembling the patient-derived sample. However, low yields, likely influenced by incomplete periplasmic export, limited oxidative folding capacity, and partial inclusion-body formation, limited further biophysical characterization. Collectively, these findings demonstrate that folding environment and redox balance are principal determinants of structural integrity, solubility, and molecular heterogeneity in FLC folding, underscoring the value of periplasmic expression as a foundation for future optimization through improved chaperone support, leader-sequence engineering, and refined redox-folding strategies.

Keywords: Monoclonal light chains, Recombinant protein expression, redox-mediated refolding, Periplasmic folding, Secondary structure recovery, Molecular species distribution

5.2 Introduction

5.2.1 Recombinant model systems for structural and mechanistic studies

The advent of recombinant DNA technology in the 1970s (Jackson et al. 1972; Cohen et al. 1973) revolutionized biomedical and industrial biotechnology by enabling the efficient and reproducible synthesis of biologically active proteins in engineered host systems (Tripathi and Shrivastava 2019; Ojima-Kato 2024). This innovation formed the basis for modern drug development, structural biology, and mechanistic studies. Today, recombinant expression is essential for the large-scale production of biopharmaceuticals such as monoclonal antibodies, hormones, coagulation factors, and vaccines using diverse expression platforms, including bacteria, yeast, filamentous fungi, insect and mammalian cells, as well as transgenic plants (Rosano and Ceccarelli 2014; Tripathi and Shrivastava 2019; Schütz et al. 2023). Choosing an appropriate expression system requires consideration of the target protein's properties, including its native cellular localization, size and molecular weight, domain structure, and potential dependence of PTMs or co-factors required for proper folding and structural stabilization (Rosano and Ceccarelli 2014; Schütz et al. 2023). Among available hosts, *Escherichia coli (E. coli)* remains the most commonly used due to its rapid growth rate, low cultivation costs, genetic manipulability, and availability of genetically engineered strains and plasmid systems (Schütz et al. 2023; Ojima-Kato 2024; Rosano and Ceccarelli 2014). Widely used expression platforms such as the T7-based pET system in *E. coli* BL21 (DE3) allow high cell densities and efficient, high-throughput production of recombinant proteins (Ojima-Kato 2024). Continuous improvements in vector design, host engineering, and fermentation strategies have further increased recombinant yield and scalability. However, challenges persist when expressing eukaryotic proteins that rely on complex folding pathways or PTMs (including disulfide bonds), which often leads to misfolding, the formation of inclusion bodies (IBs), or low overall protein yields (Structural Genomics Consortium et al. 2008; Rosano and Ceccarelli 2014). These challenges often reflect fundamental differences in redox states, pH, folding pathways, and cofactor availability between microbial hosts and the native microenvironment of the target protein (Bhatwa et al. 2021). For FLCs, where patient-derived material is heterogeneous and limited, recombinant expression provides a crucial model system for investigating how sequence variations and structural features influence toxicity and aggregation behavior. Such systems enable controlled experiments that link the molecular properties of FLCs to their disease-related mechanisms and allow for both mechanistic and structural analyses (e.g., Stevens et al. 1995; Wall et al. 1999; Khurana et al. 2001; Mclaughlin et al. 2006; Martin and Ramirez-Alvarado 2010; Poshusta et al. 2013). In this context, the recombinant production of patient-derived FLCs in *E. coli* requires an understanding of how the distinct folding compartments, with their respective redox conditions, influence structure formation and how they can be utilized for the recovery of native-like FLCs.

5.2.2 The *E. coli* expression environment

Protein folding in *E. coli* occurs in two spatially and chemically distinct compartments, with a highly reducing cytoplasm and a periplasmic space that promotes oxidation and disulfide bond formation (Castillo-Corujo et al. 2024). This redox contrast shapes the folding landscape of recombinant proteins and determines whether cysteine-rich or structurally complex molecules can achieve their native conformation *in vivo*. A schematic overview of the major folding routes, quality-control systems, and disulfide bond pathways is shown in Figure 5.1. In the cytoplasm, disulfide formation is actively prevented by the thioredoxin (Trx) and glutaredoxin (Grx) reductase systems, which maintain cysteine residues in a reduced state (Bessette et al. 1999; Baneyx and Mujacic 2004; Castillo-Corujo et al. 2024). The macromolecular concentration in this compartment can exceed 300-400 mg/mL, and new polypeptide chains are released from the ribosome approximately every 20-40 seconds (Baneyx and Mujacic 2004; Uversky 2014; Gomes and Faísca 2019; Matamouros et al. 2023). This high degree of molecular crowding increases intermolecular encounters, which can promote aggregation when folding intermediates fail to mature efficiently (Sabate et al. 2010; Hartl et al. 2011). Under these conditions, recombinant proteins, particularly those with multiple cysteines or complex topologies, often fail to achieve their native conformation and instead accumulate as IBs. IBs represent dense cytoplasmic or periplasmic aggregates mainly composed of misfolded or partially folded proteins and reflect a disruption of protein homeostasis, through saturation of the folding and quality-control capacity (Baneyx and Mujacic 2004; Bhatwa et al. 2021). Although commonly associated with bacterial expression, similar aggregates occur across eukaryotic systems as part of conserved stress responses (Bhatwa et al. 2021). In *E. coli*, IB formation is typically triggered when recombinant expression outpaces the cell's folding capacity (e.g., DnaK-DnaJ-GrpE) and quality-control machinery (e.g., ClpB disaggregase), causing newly synthesized polypeptide chains to expose hydrophobic segments that drive self-association and aggregation (Baneyx and Mujacic 2004; Bhatwa et al. 2021). The lack of eukaryotic PTM pathways, including glycosylation or regulated disulfide bond formation, further increases the misfolding tendency of complex proteins (Bhatwa et al. 2021). While IBs can streamline purification by concentrating the target protein into an easily isolated fraction, the recovery of native, functional protein depends on successful *in vitro* refolding to recreate native intermolecular interactions and disulfide bonding patterns, which remains technically challenging (Atroshenko et al. 2024).

In contrast, the *E. coli* periplasm provides an oxidizing environment that supports disulfide bond formation through the disulfide bond protein (Dsb) oxidoreductase network (Walker and Gilbert 1994; Denoncin and Collet 2013). Additional periplasmic folding mediators such as the seventeen-kilodalton protein (Skp, OmpH), survival protein A (SurA), and FK506-binding protein A (FkpA), which are part of the outer membrane protein (OMP) biogenesis network, assist in folding and prevent the off-pathway aggregation of translocated polypeptides (Schäfer et al. 1999; Schiffrin et al. 2017; Karyolaimos and De Gier 2021). Expression in the periplasm therefore enables folding in an oxidative environment which often improves solubility and structural integrity.

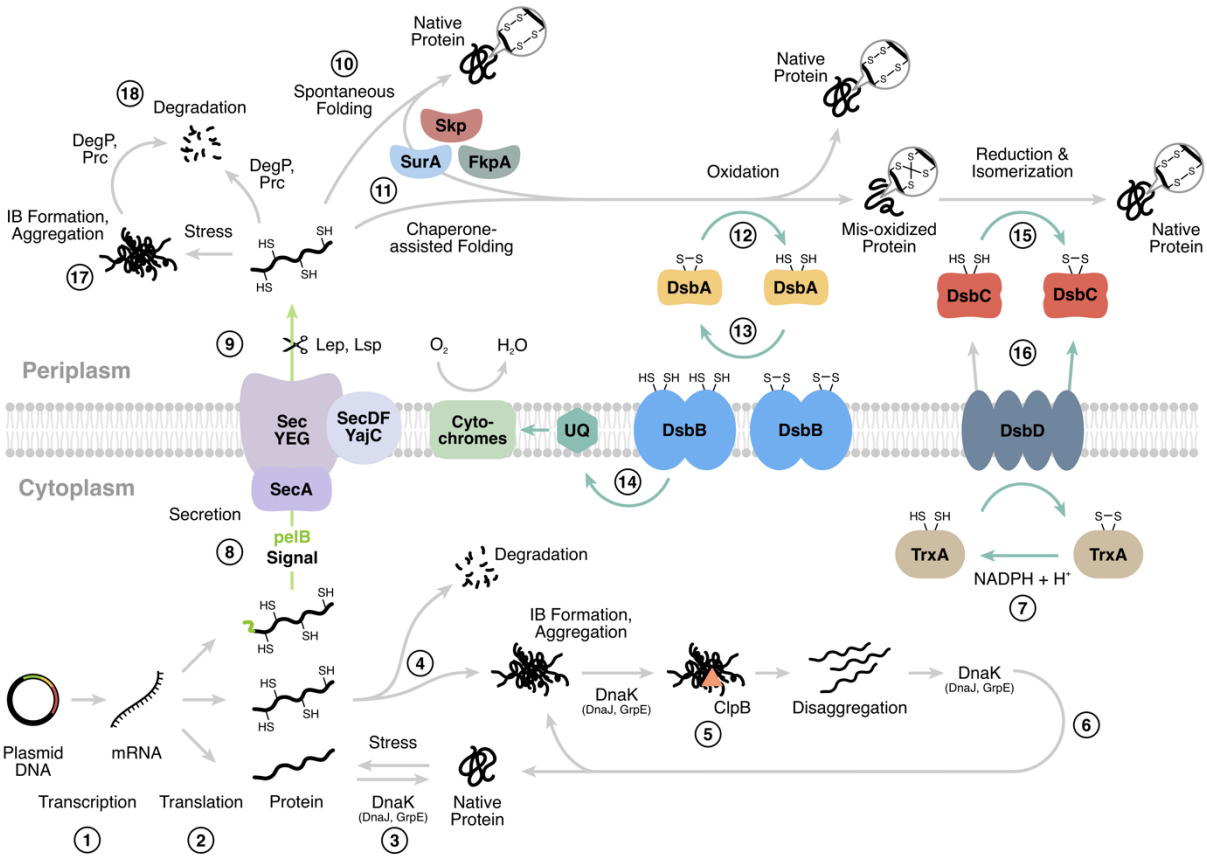

Figure 5.1: Schematic overview of cytoplasmic and periplasmic *de novo* folding pathways in *E. coli*. Grey arrows indicate potential reaction products, blue arrows the electron flow, and the green arrow the translocation pathway from cytoplasmic to periplasmic environments. (**1**) Plasmid-derived DNA is transcribed into mRNA, (**2**) which is translated into nascent polypeptide chains. (**3**) Cytoplasmic proteins that do not require disulfide bonds, fold with assistance from the DnaK-DnaJ-GrpE system. (**4**) In contrast, proteins that depend on disulfide bonds for stability and native conformation, such as most periplasmic or secreted proteins, cannot fold correctly in the reducing cytoplasm, often leading to the accumulation of non-native intermediates, aggregation, IB formation, or degradation. (**5**) Aggregated species are resolubilized by ClpB in cooperation with DnaK-DnaJ-GrpE. (**6**) Iterative chaperone cycles of binding and release can drive substrates toward the native conformation. (**7**) The reducing cytoplasmic environment is maintained by thioredoxin 1 (TrxA). (**8**) Proteins with an N-terminal signal sequence (e.g., pelB) are exported to the periplasm through the Sec translocon. (**9**) After post-translational secretion, Lep/Lsp peptidases remove the signal sequence. (**10**) In the oxidizing periplasm, non-native chains may fold spontaneously, (**11**) or fold with assistance from periplasmic chaperones such as Skp, SurA, and FkpA. (**12**) Disulfide bond formation is mediated by the Dsb system: DsbA introduces disulfides via its highly reactive Cys30 residue, while (**13**) DsbB reoxidizes DsbA through sequential thiol-disulfide exchange reactions using its two periplasmic cysteine pairs and (**14**) transfers electrons to membrane quinones (ubiquinone (UQ) in aerobic conditions and menaquinone (MQ) in anaerobic conditions), which subsequently enter the corresponding respiratory chain (under aerobic conditions via cytochromes, where O_2 serves as the terminal electron acceptor and is reduced to H_2O). (**15**) Incorrect disulfide pairing is corrected by the isomerase DsbC, which reshuffles disulfides via mixed-disulfide intermediates. (**16**) DsbC is maintained in a reduced, active form by DsbD, which relays electrons from cytoplasmic NADPH via TrxA. (**17**) Periplasmic stress (heat, oxidative imbalance, incorrect S-S pairing) can generate misfolded or aggregated species, which are counteracted by DegP (chaperone/protease switching temperature-dependently) and Prc. (**18**) Misfolded or terminally damaged proteins are degraded to prevent accumulation and enable amino-acid recycling. Figure adapted from Sevier and Kaiser 2002; Miot and Betton 2004; Choi and Lee 2004; Baneyx and Mujacic 2004; Messens and Collet 2006; Dutton et al. 2008; Kolaj et al. 2009; Berkmen 2012; De Geyter et al. 2016; Saez et al. 2017; Mamipour et al. 2017; Liu and Huang 2018; Sandomenico et al. 2020.

However, secretion efficiency remains limited by protein size, folding complexity, and the capacity of the bacterial export machinery, frequently resulting in low yields due to inefficient translocation to the periplasm, degradation, or unintended extracellular secretion (Baneyx and Mujacic 2004; Karyolaimos and De Gier 2021). These differences between the cytoplasmic and periplasmic compartments illustrate how the cellular redox landscape regulates folding efficiency and structural fidelity of recombinant proteins in *E. coli*. This is an important consideration for recombinant FLC production, where correct disulfide bond formation determines whether FLCs fold properly *in vivo* or require *in vitro* refolding approaches to restore their native structure.

5.2.3 Principles of protein folding and secondary structure formation

Protein folding is a cooperative and hierarchical process in which newly synthesized, linear polypeptide chains acquire their functional, three-dimensional conformation. This occurs through the ordered development of secondary and tertiary structures, followed by quaternary assembly through intermolecular interactions, ultimately resulting in a bioactive native state (Hartl et al. 2011; Iram and Naeem 2014; Adamcik and Mezzenga 2018; Gomes and Faísca 2019). The amino acid sequence intrinsically contains the information needed for self-assembly, directing the formation of α-helices and β-sheets that define early folding intermediates (Anfinsen 1973). These motifs subsequently organize into compact tertiary structures and, for multimeric proteins such as hemoglobin, into higher-order quaternary complexes (Gomes and Faísca 2019). This folding process is often conceptualized as a progressive descent down a funnel-shaped free-energy landscape (Fig. 5.2A), in which unfolded, high-entropy polypeptides form native intramolecular contacts as Gibbs free energy (ΔG) decreases (Hartl et al. 2011; Liu et al. 2012; Iram and Naeem 2014; Adamcik and Mezzenga 2018; Gomes and Faísca 2019).

Folding is driven by the balance of non-covalent interactions, including hydrophobic effects, van der Waals contacts, hydrogen bonds, and electrostatic forces (Iram and Naeem 2014; Gomes and Faísca 2019). Although individually weak (Fig. 5.2B), these interactions collectively determine the thermodynamic stability of the folded state and shape the free-energy landscape that governs productive folding. The rapid burial of non-polar residues away from the solvent, known as hydrophobic collapse, is considered a principal driving force that promotes compaction and the formation of stable secondary-structure motifs (Hartl et al. 2011; Gomes and Faísca 2019). This collapse is modulated by the balance of order- and disorder-promoting residues within the polypeptide sequence (Fig. 5.2C), which influences how efficiently secondary-structure elements can form and stabilize (Gomes and Faísca 2019). The resulting native state is further maintained by the cooperative interplay of the non-covalent forces together with covalent stabilizers such as disulfide bonds in oxidizing environments (Nick Pace et al. 2014). Small single-domain proteins typically exhibit cooperative two-state folding with a defined transition midpoint, whereas larger or multi-domain proteins often form partially folded molten-globule intermediates (Jackson 1998; Iram and Naeem 2014; Gomes and Faísca 2019). While the structure-function paradigm assumes that biological activity depends on a defined conformation, intrinsically disordered proteins (IDPs) lack sufficient hydrophobic residues to stabilize a fixed fold and instead remain flexible, adopting structure only

upon binding with interaction partners, which is described as disorder-function paradigm (Uversky 2014; Theillet et al. 2014; Gomes and Faísca 2019). Under suboptimal conditions, folding intermediates may accumulate and expose hydrophobic surfaces that promote self-association and aggregation (Fink 1998; Hartl et al. 2011). These aggregation-prone species can cause loss of function, mistrafficking, degradation, or conversion into amyloid and amorphous assemblies, processes underlying many protein folding disorders, including neurodegenerative and systemic amyloidosis (Gomes and Faísca 2019; Willbold et al. 2021). Maintaining a balanced physicochemical environment and an efficient network of molecular chaperones, disulfide isomerases, and quality-control systems is therefore essential for productive folding and cellular proteostasis.

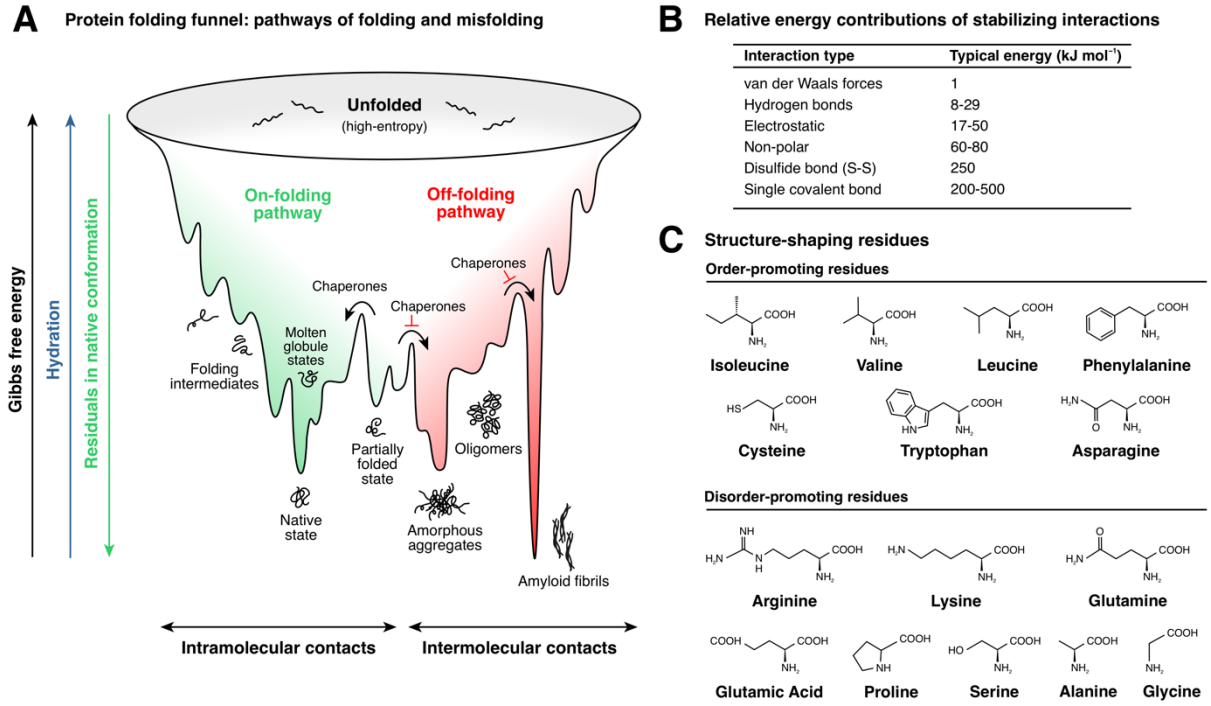

Figure 5.2: Competing pathways and determinants of protein folding. (**A**) Schematic representation of the protein-folding energy landscape. Unfolded polypeptides descend the funnel as ΔG decreases and native intramolecular contacts form. On-pathway intermediates fold cooperatively towards the native state, whereas off-pathway intermediates become kinetically trapped, leading to amorphous aggregates, or ordered amyloid fibrils. Folding speed and efficiency depend on the ruggedness of the energy surface, kinetic barriers, and the physicochemical environment, including redox conditions and chaperone activity. (**B**) Relative energy contributions of stabilizing interactions during protein folding. Protein stability arises from numerous weak, cooperative interactions that guide compaction and structure formation. (**C**) Order-promoting residues (e.g., Ile, Val, Leu, Phe, Cys, Trp, Tyr, Asn) support hydrophobic-core formation, whereas disorder-promoting residues (e.g., Arg, Lys, Glu, Pro, Ser, Gln, Gly, Ala) enhance flexibility and solvent exposure (Gomes and Faísca 2019). Figure adapted from Hartl et al. 2011; Liu et al. 2012; Iram and Naeem 2014; Adamcik and Mezzenga 2018; Gomes and Faísca 2019.

5.2.4 Disulfide bonds and redox-controlled folding

Cysteine residues play essential roles in protein chemistry, including catalytic activity, metal coordination, redox regulation, and structural stabilization through the formation of disulfide bonds (Bechtel and Weerapana 2017). Disulfide bonds arise post-translationally through the oxidation of two thiol groups (–SH), linking cysteine residues via a covalent bond that often influences protein stability, function, and redox responsiveness (Berkmen 2012). The processes of disulfide bond formation (oxidation), breaking (reduction), and reshuffling (isomerization) are illustrated in Figure 5.3 and represent central redox-controlled mechanisms that shape protein folding pathways (Fabianek et al. 2000; Berkmen 2012; Denoncin and Collet 2013). Depending on their molecular context, disulfide bonds can stabilize tertiary structure, regulate conformational changes in response to redox signals, or mediate electron transfer during catalysis. Structural disulfides decrease conformational entropy and enhance stability, whereas regulatory and catalytic disulfides participate dynamically in electron-exchange reactions that modulate protein activity (Berkmen 2012; Bechtel and Weerapana 2017). An accurate pairing of cysteines during protein folding is critical because incorrect oxidation or crosslinking leads to off-pathway intermediates that accumulate or aggregate (Zhang et al. 2011; Bhatwa et al. 2021).

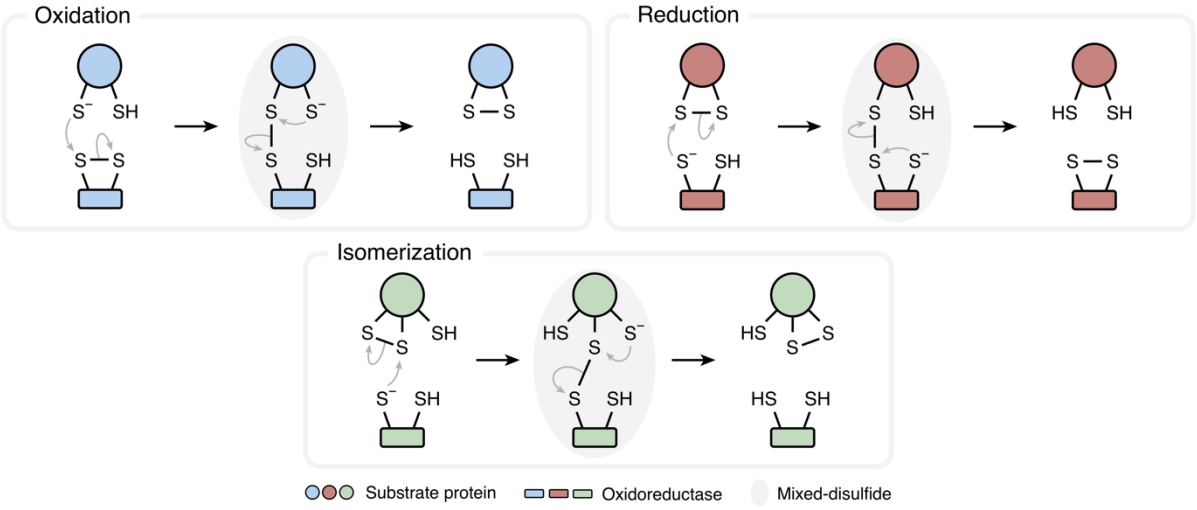

Figure 5.3: Disulfide bond oxidation, reduction, and isomerization. Schematic representation of thiol-disulfide exchange reactions in which active-site cysteines of oxidoreductases form a transient mixed-disulfide with a substrate protein, resulting in oxidation (blue; e.g., DsbA), reduction (red; e.g., TrxA), and isomerization (green; e.g., DsbC) of disulfide bonds. A deprotonated cysteine thiolate acts as the nucleophile, first attacking a disulfide to generate a mixed-disulfide intermediate and then resolving it in a second step, thereby transferring a disulfide to the substrate, removing it, or reshuffling non-native linkages within or between polypeptide chains. Electron flow is indicated by grey arrows and mixed-disulfide states by grey areas. Figure adapted from Sevier and Kaiser 2002b; Berkmen 2012; Fujimoto et al. 2019.

The significance of correct disulfide pairing for protein structure was demonstrated in the seminal work of Anfinsen and colleagues (Haber and Anfinsen 1961; Anfinsen 1973). In this experiments, fully unfolded and reduced ribonuclease A (RNaseA) regained its native conformation and enzymatic

activity when exposed to air. This demonstrated that all information required for native folding is contained in the amino acid sequence itself and that the presence of a simple electron acceptor such as molecular oxygen is sufficient to promote spontaneous disulfide bond formation *in vivo* (Haber and Anfinsen 1961; Berkmen 2012). In biological systems, disulfide bond formation is catalyzed by oxidoreductases that mediate electron exchange between cysteine residues of the substrate and their own active-site Cys-X_A-X_B-Cys motifs (Frand et al. 2000; Berkmen 2012; Bechtel and Weerapana 2017). During catalysis, a transient mixed-disulfide forms between enzyme and substrate, enabling controlled oxidation, reduction, or isomerization depending on the redox potential of the enzyme and its environment (Frand et al. 2000; Berkmen 2012). The redox activity of an oxidoreductase depends on the relative stability of its oxidized and reduced state, the chemistry of its active-site cysteines, and the redox conditions of its compartment. Consequently, a single enzyme can switch roles, as seen with Trx, which acts as a reductase in the cytoplasm but functions as an oxidase in the periplasm once it is no longer maintained in a reduced state by cytoplasmic reductase systems (Fabianek et al. 2000; Berkmen 2012; Denoncin and Collet 2013). The stability and reactivity of disulfide bonds are determined by their redox potential, which is influenced by thiol pK_a, solvent exposure, the entropic cost of constraining the backbone, and deviations from ideal bound geometry. Within a given environment, disulfide redox potentials span a broad range from roughly −95 mV to −470 mV, and even small deviations from the preferred dihedral angle (± 90°) can shift the potential by 10-100 mV and thereby alter disulfide stability (Bechtel and Weerapana 2017). Intramolecular disulfides within preorganized tertiary structures are entropically favored and stable (Creighton and Goldenberg 1984), whereas intermolecular disulfides between unstructured chains often promote aggregation (Mitra and Sarkar 2022). Structural disulfides are particularly important for extracellular proteins, which function in a more oxidizing environment (approximately +140 mV) than intracellular compartments (Jones et al. 2000).

In eukaryotes, disulfide formation occurs mainly in the ER, where it is tightly regulated to prevent non-specific oxidation and ensure correct folding before secretion (Feige and Hendershot 2011). During oxidative folding, members of the protein disulfide isomerase (PDI) family transfer disulfides to substrate proteins and are reoxidized by ER oxidoreductin 1 (Ero1), which transfers electrons to molecular oxygen, producing hydrogen peroxide (H_2O_2) as a by-product. This enzymatic relay maintains an oxidizing but flexible ER redox potential between −150 mV and −180 mV, with a glutathione ratio of ~1:1 to 3:1, allowing both disulfide formation and isomerization of mispaired cysteines (Bechtel and Weerapana 2017). Analogous oxidoreductase systems, such as MIA40/Erv1 in the mitochondrial intermembrane space (Deponte and Hell 2009) and DsbA/DsbB in the bacterial periplasm (Dutton et al. 2008) reflect the evolutionary conservation of oxidative folding pathways.

Maintaining accurate disulfide pairing is essential for protein homeostasis, as both excessive oxidation and reduction can lead to misfolding and aggregation, including aberrant modifications such as cysteinylation or glutathionylation that alter native disulfide patterns (Grek et al. 2013; Musaogullari and Chai 2020). Such dysregulation is implicated in diseases including Creutzfeldt-Jakob disease (CJD), amyotrophic lateral sclerosis (ALS), and various cancers. In the prion protein (PrP), reduction of its single disulfide destabilizes the α-helical fold and promotes β-sheet-rich aggregation. In superoxide dismutase 1 (SOD1), loss of the stabilizing disulfide accelerates fibrillation, while PDI upregulation in tumors supports increased folding demand and confers resistance to apoptosis (Bechtel and Weerapana 2017). In immunoglobulins and FLCs, precise disulfide pairing ensures

structural stability, HC linkage (Liu and May 2012) or covalent dimerization via the conserved C-terminal cysteine (Kaplan et al. 2011). Oxidative stress in MM or AL amyloidosis (Shi et al. 2010; Pick et al. 2023; Kul and Ozturk Kurt 2024) can disrupt these bonds, leading to destabilization, aggregation, and proteolytic cleavage into amyloidogenic fragments (Tucholski et al. 2025). A detailed understanding of redox-controlled folding is therefore essential not only for reproducing native-like FLCs in recombinant systems but also for elucidating how redox imbalance drives misfolding, aggregation, and structural heterogeneity in disease.

5.2.5 Aims and scope

The objective of this work was to establish a recombinant *E. coli*-based system for producing patient-derived FLCs in a native-like conformation that reproduces their secondary structure, disulfide connectivity, and molecular species distribution. Such systems enable controlled studies of folding and aggregation under defined and reproducible conditions while preserving the molecular authenticity of FLCs, including intra- and intermolecular disulfide bonding patterns. On a biomedical level, understanding how sequence-dependent differences affect folding efficiency, redox sensitivity, and aggregation tendency is key to identify molecular factors that influence FLC pathogenicity and clinical outcome in disorders such as MM and AL amyloidosis. Most recombinant FLC models have focused on the isolated V_L domain, which has frequently been identified as the predominant component in amyloid deposits and can be expressed in *E. coli* either in the cytoplasm or periplasm (Stevens et al. 1995; Khurana et al. 2001; Sikkink and Ramirez-Alvarado 2008; Blancas-Mejia et al. 2009; Martin and Ramirez-Alvarado 2010; Poshusta et al. 2013; Piehl et al. 2017; Hand et al. 2018; Misra et al. 2019; Misra and Ramirez-Alvarado 2021; Rottenaicher et al. 2021). To extend this approach towards a more physiologically complete model, the full-length sequence of the patient-derived FLC P006 was selected for recombinant expression. Previous studies have shown that full-length FLCs can also be produced in *E. coli* as cytoplasmic IBs, requiring subsequent *in vitro* refolding under controlled redox conditions to recover their native structure (Buchner and Rudolph 1991; Rognoni et al. 2013; Kazman et al. 2020; Nikolaou et al. 2022; Sakai et al. 2023). However, refolding full-length FLCs is generally more demanding than V_L fragments due to their higher number of cysteine residues and the need for correct intramolecular pairing across both domains. To systematically evaluate these folding environments for full-length FLC expression, two strategies were implemented:

i. Cytoplasmic expression followed by *in vitro* refolding of IBs under different redox conditions to investigate disulfide bond formation and redox-dependent folding.

ii. Periplasmic expression using a chaperone-assisted system that exploits the oxidizing periplasmic compartment to promote native disulfide bond formation *in vivo*.

These strategies provided a framework to evaluate how redox potential, chaperone assistance, and refolding conditions influence yield, solubility, and structural authenticity of recombinant light chains (rLCs). The resulting rLC species were characterized using CD spectroscopy and SV-AUC. CD

spectroscopy revealed the secondary structure composition and folding quality of rLCs, whereas SV-AUC quantified their oligomeric state, hydrodynamic properties, and conformational heterogeneity. Comparing these datasets across different folding environments enabled direct evaluation of how oxidative and reductive conditions shape FLC conformation, stability, and aggregation propensity. This study aimed to identify experimental conditions that best reproduce native-like FLCs and to further investigate the relationship between redox balance, disulfide chemistry, and structural stability. The biochemical and biophysical insights obtained here provided the foundation for subsequent studies using *Pichia pastoris*, a eukaryotic host that more closely recapitulates the folding environment of human plasma cells and enables direct comparison of redox-controlled folding mechanisms relevant to FLC-associated disease (Chapter 6).

5.3 Methods

The Methods in this chapter focus on the recombinant expression of the patient-derived FLC sample P006 in the *E. coli* host system. Detailed protocols for the biophysical techniques applied during downstream characterization of rLC6, including CD spectroscopy and AUC, are described in other chapters, and are cross-referenced where applicable.

5.3.1 Expression strategy and vector design

The aim of this study was to establish an expression system capable of producing rLCs in a native-like conformation comparable to their patient-derived counterparts. For this purpose, the full-length sequence of patient sample P006, comprising both the V_L and C_L domains, was expressed in *E. coli*. However, as commonly observed for disulfide-bonded eukaryotic proteins, high level cytoplasmic expression in *E. coli* often leads to the formation of IBs containing unfolded or misfolded protein species. The recovery of native protein therefore requires complete denaturation and reduction of the IBs, followed by refolding of the recombinant proteins under carefully controlled redox conditions to allow native secondary structure formation and disulfide bond assembly. In the case of FLCs, this process may also involve covalent dimerization through the C-terminal cysteine residue. To achieve this, the codon-optimized P006 gene was synthesized (Thermo Fisher Scientific, Waltham, MA, USA) and cloned into the pET-16b expression vector. The nucleotide sequences of the optimized gene insert and the final expression construct are provided in the Supplementary information (Tab. 8.6 and 8.7). Additionally, a schematic representation is shown in Results Figure 5.4A.

5.3.2 PCR amplification and vector linearization

The P006 gene insert was amplified by polymerase chain reaction (PCR) using primers designed to provide complementary overlaps for subsequent assembly into the linearized pET-16b expression vector. A complete list of all primers used is provided in Table 5.1. PCR amplification and vector

linearization were performed using the CloneAmp HiFi PCR Premix (Lot-Nr. 2202799A; #639298; Takara Bio, Kusatsu, Japan). Each reaction had a final volume of 50 µL, consisting of 25 µL 2× CloneAmp HiFi PCR Premix, 2.5 µL of each primer (10 µM working solution; final concentration 0.5 µM each), 1 ng of template plasmid DNA (pET-16b, 5,597 bp; reactions tested with 1 ng and 0.5 ng), and nuclease-free dH_2O. PCR was carried out on a T100 Thermal Cycler (#1861096; Bio-Rad, Hercules, CA, USA) using the following program: initial denaturation at 98°C for 30 s; 35 cycles of 98°C for 30 s, 56°C for 30 s, and 72°C for 3:30 min; followed by a final extension at 72°C for 10 min and hold at 4°C. For amplification of the P006 gene insert, annealing temperatures of 56°C, 58°C, and 60°C were tested, with optimal amplification of the expected 669 bp product observed at 60°C (Fig. 5.4B). Linearization of the pET-16b vector was performed at an annealing temperature of 56°C (Fig. 5.4C). PCR products (insert and vector) were analyzed by agarose gel electrophoresis. 1% (w/v) agarose gels were prepared by dissolving 0.55 g agarose in 55 mL 1× Tris-Acetate-EDTA (TAE) buffer by heating in a microwave until fully dissolved. After cooling to ~60°C, 5 µL of 10,000× GelRed Nucleic Acid Gel Stain (#41003; Biotium, Fremont, CA, USA) was added before casting the gel in a Sub-Cell GT Gel Caster (#1704412; Bio-Rad, Hercules, CA, USA). Samples were mixed with 6× Gel Loading Dye, Purple (Lot-Nr. 10250207; #B7024S; New England Biolabs, Ipswich, MA, USA) and electrophoresed in 1× TAE buffer at 120 V for ~1 h using the Sub-Cell GT system (Bio-Rad, Hercules, CA, USA). For size estimation, a GeneRuler 100 bp Plus DNA Ladder (Thermo Fisher Scientific, Waltham, MA, USA) was used for the gene insert (Fig. 5.4B), and a GeneRuler 1 kb DNA Ladder (Thermo Fisher Scientific, Waltham, MA, USA) was used for the vector (Fig. 5.4C). DNA bands were visualized using a G:Box gel documentation system (Syngene International Ltd, Cambridge, UK). Selected bands were excised and purified using the NucleoSpin Gel and PCR Clean-up Mini Kit (#740609.50; Macherey-Nagel, Düren, Germany) and stored at −20°C until further use.

Table 5.1: Primer sets used for the assembly of the pET-16b-P006 fusion construct for the expression of rLC6 in *E. coli*

Primer	Sequence (5' to 3')
pET-16b Forward	TAACTAGCATAACCCCTTGG
pET-16b Reverse	CATGGTATATCTCCTTCTTAAAG
P006+pET-16b Forward	AGGAGATATACCATGGATCTGCAAATGACCCAGAGTCC
P006+pET-16b Reverse	GGGTTATGCTAGTTAACATTCACCACGATTAAAGCTTTTG

5.3.3 Vector assembly, transformation, and verification

Final assembly of the linearized pET-16b vector and the P006 gene insert was performed with the In-Fusion Snap Assembly Master Mix (Lot-Nr. 2211576A and 2211579A; #638947; Takara Bio, Kusatsu, Japan) according to the manufacturer's instructions. Briefly, insert and vector DNA were combined at a molar ratio of 2:1, with the insert ranging between 10-200 ng and the linearized vector between 50-200 ng. To this mixture, 4 µL of 5× In-Fusion Master Mix and 4.5 µL of nuclease-free dH_2O were added, resulting in a final reaction volume of 20 µL. The assembly reaction was incubated for 15 min

at 50°C in an Eppendorf ThermoMixer Model C. The assembled constructs were then transformed either into chemically competent *E. Coli* Stellar cells (#636763; Takara Bio, Kusatsu, Japan) or into laboratory-prepared *E. coli* BL21 (DE3) competent cells using a standard heat-shock transformation protocol. Briefly, 50 µL of frozen competent cells were thawed on ice, after which 1-2.5 µL of the assembly mix was added. The mixture was incubated on ice for 30 min, heat-shocked at 42°C for 45 s and incubated on ice for additional 2 min. Afterwards, 450 µL of pre-warmed (37°C) 2×YT medium (prepared according to the manufacturer's instructions) was added, and the cultures were incubated at 37°C with shaking at 800 rpm for 1 h. Aliquots of 100 µL were plated on 2×YT agar plates containing 100 µg/mL ampicillin (1:1,000 dilution from a 100 mg/mL stock solution) and incubated overnight at 37°C. On the following day, three single colonies were picked and inoculated into 2×YT medium supplemented with 100 µg/mL ampicillin. Cultures were grown overnight at 37°C with shaking at 160 rpm. Glycerol stocks were prepared by mixing 500 µL of culture with 500 µL of sterile 50% (v/v) glycerol solution and stored at −80°C. The remaining culture was used for plasmid isolation using the NucleoSpin Plasmid Mini Kit (#740588.50; Macherey-Nagel, Düren, Germany). Purified plasmid DNA was verified by Sanger sequencing (Microsynth Seqlab, Göttingen, Germany) to confirm correct construct assembly.

5.3.4 Recombinant expression of rLC6 in *E. coli*

For large-scale expression, preculture was prepared in 2×YT medium and supplemented with 100 µg/mL ampicillin. A glycerol stock of the verified construct was used to inoculate the preculture, which was incubated overnight at 37°C with shaking at 160 rpm. The following day, large-scale expression was carried out in sterile 2 L baffled shaking flasks containing a maximum volume of 500 mL 2×YT medium supplemented with ampicillin (100 µg/mL). Cultures were inoculated at a 1:100 (v/v) ratio from the preculture and grown at 37°C with shaking at 160 rpm until an OD_{600} of 0.8 was reached. Expression of rLC6 was induced by adding isopropyl β-D-1-thiogalactopyranoside (IPTG) to a final concentration of 1 mM (1:1,000 dilution from a 1 M stock) and incubation continued for 4 h under the same conditions. Alternatively, after induction the expression temperature was reduced to 20°C and incubation was continued overnight for 16-20 h. Cells were harvested by centrifugation at 5,000 × *g* for 15 min at 4°C, washed once with 30 mM Tris-HCl (pH 7.4), and stored at −20°C until further use.

5.3.5 Protocol 1: Isolation of IBs and redox-mediated renaturation of rLCs

Adapted from Buchner and Rudolph (1991)

The initial purification and refolding procedure was performed using a method – adapted with minor modifications – from Buchner and Rudolph (*Nat. Biotechnol.*, 1991). Originally developed for a murine Fab fragment, Buchner and Rudolph's strategy is broadly applicable to disulfide-bonded proteins expressed as IBs in *E. coli*. Briefly, harvested cells were resuspended on ice in a pre-cooled lysis buffer containing 30 mM Tris-HCl (pH 7.4), 20 mM EDTA, and one tablet of cOmplete Mini EDTA-free

protease inhibitor cocktail (#11836170001, Merck Millipore, Darmstadt, Germany). Cell disruption was performed using a high-pressure homogenizer (Constant Systems Ldt., Daventry, UK) operated at 2.9 kbar pressure. The lysate was centrifuged for 60 min at 25,000 × *g* and 4°C. The supernatant was discarded and the pellet, containing the protein in form of insoluble IBs, was washed twice by resuspension in 50 mM Tris-HCl (pH 7.4) containing 20 mM EDTA, followed by centrifugation under the same conditions. The washed pellets were stored at −20°C until further use. IBs were solubilized by resuspension in 0.1 M Tris-HCl (pH 8.5) containing 6 M guanidine hydrochloride (GdnHCl), 2 mM EDTA, and 0.3 M dithiothreitol (DTT), and incubated for 1 or alternatively 2 h on a tube roller at room temperature. The solubilization volume was kept between 2 and 5 mL to allow subsequent 100-fold dilution in renaturation buffer. After solubilization, the suspension was centrifuged for 60 min at 25,000 × *g* and 4°C, and the pellet was discarded, since the solubilized IB proteins were present in the supernatant. Renaturation was initiated by slowly diluting the solubilized protein solution 100-fold into renaturation buffer containing 0.1 M Tris-HCl (pH 8.5), 6 M GdnHCl, 2 mM EDTA, and 0.2 M oxidized glutathione (GSSG). Residual DTT (final concentration 3 mM after dilution) was not removed prior to renaturation, as it was utilized to reduce GSSG to reduced glutathione (GSH), thereby establishing the GSH/GSSG redox equilibrium as described by Buchner and Rudolph. The addition of 0.4 M L-arginine to suppress aggregation was also tested. The reaction was incubated for 2 or 3 h at room temperature with gentle mixing. Following renaturation, the sample was dialyzed overnight at 4°C against 0.1 M Tris-HCl (pH 8.5) containing 2 mM EDTA to remove GSSG, GSH, DTT, and GdnHCl, using 35 mm SnakeSkin Dialysis Tubing with a 10 kDa MWCO (#88245, Thermo Fisher Scientific, Waltham, MA, USA). To maintain the concentration gradient and dialysis efficiency, the dialysis buffer was replaced twice with fresh buffer during this period. Aggregates arising from covalent side reactions were removed by centrifugation at 10,000 rpm for 1 h at 4°C, followed by sterile filtration using a Filtropur S polyethersulfone syringe filter with a pore size of 0.2 µm (#83.1826.001, Sarstedt, Nümbrecht, Germany). The state of purification was monitored after each step by SDS-PAGE, with detailed protocols for sample preparation and gel electrophoresis provided in the Methods of Chapter 6.5. To remove the redox buffer and concentrate the rLCs before final SEC purification, the solution was subjected to buffer exchange into 50 mM Tris-HCl (pH 8.5) using Amicon Ultra-15 centrifugal filter units with PLGC Ultracel-PL membrane and a NMWL of 10 kDa (#UFC901024; MilliporeSigma, Burlington, MA, USA). As a final purification step, samples were fractionated by SEC using an ÄKTA pure protein purification system (GE Healthcare, IL, USA) operated with Unicorn software (v6.3). Separation was performed on either a Superdex 75 10/300 GL Tricorn column (#17517401; Cytiva, Marlborough, MA, USA), or a HiLoad 16/600 Superdex 75 pg column (#28989333; Cytiva, Marlborough, MA, USA), both operated at a flow rate of 0.5–1 mL/min. Both columns provide a separation range of 3-70 kDa. Prior to loading, protein solutions were concentrated by ultrafiltration as described previously. Elution was carried out with 30 mM Tris-HCl (pH 7.4) and collected fractions were analyzed by SDS-PAGE to assess sample composition and purity. Fractions with comparable purity and molecular composition were pooled, aliquoted, snap-frozen in liquid nitrogen, and stored at −80°C until further use. Alternatively, samples were lyophilized prior to storage using an RVC 2-18 Rotary Vacuum Concentrator (Martin Christ Freeze Dryers, Osterode am Harz, Germany).

5.3.6 Protocol 2: Dropwise dilution refolding of rLCs in GSH/GSSG redox-shuffle buffer

Adapted from Rognoni et al. (2013)

A refolding protocol for full-length FLCs expressed without protein tags was described by Rognoni et al. (2013) which was adapted with minor modifications. The protocol follows the same general strategy as described by Buchner and Rudolph (1991), but differs in several steps, including extended solubilization time, a dropwise dilution into redox-shuffle buffer, and an additional purification step via anion-exchange chromatography (AEC). Briefly, cells from 1 L of expression culture were harvested by centrifugation at 7,000 × *g* for 10 min, and the resulting cell pellet was resuspended in 70 mL of ice-cold 50 mM Tris-HCl buffer (pH 8.0) containing 1 mM EDTA and 1 mM phenylmethylsulfonyl fluoride (PMSF). Cell disruption was performed as described previously using a high-pressure homogenizer. The lysate was centrifuged for 15 min at 30,000 × *g* and 4°C and the pellet was washed twice with 50 mM Tris-HCl (pH 8.0) containing 1 mM EDTA and 1 mM PMSF. IBs were then solubilized in 15 mL of 50 mM Tris-HCl (pH 8.0) supplemented with 1 mM EDTA, 1 mM PMSF, 6 M GdnHCl, and 5 mM β-mercaptoethanol, followed by incubation at 4°C for 5 h with gentle agitation. Samples were centrifuged at 30,000 × *g* for 15 min at 4°C, and the supernatant containing the solubilized rLCs was collected. Refolding was initiated by adding the protein solution dropwise into 300 mL of refolding redox shuffle buffer composed of 50 mM Tris-HCl (pH 8.0), 1 mM EDTA, 1 mM PMSF, 5 mM GSH, and 0.5 mM GSSG, resulting in a 20-fold dilution. The mixture was incubated overnight at 4°C with gentle agitation. Subsequently, the sample was centrifuged for 15 min at 30,000 × *g* and 4°C. The supernatant was dialyzed overnight at 4°C against 50 mM Tris-HCl (pH 8.0), as described previously. After refolding and dialysis, the sample was further purified by AEC. For this purpose, a self-packed column containing Q Sepharose Fast Flow resin (#17051004; Cytiva, Marlborough, MA, USA) was used. Elution was performed with 50 mM Tris-HCl (pH 8.0), 1 mM EDTA, 1 mM PMSF, and 1 M NaCl, applying a linear gradient from 0-100% over 30 min with the same buffer lacking NaCl. The flow rate during loading and elution was maintained at 2 mL/min. Final purification was carried out by SEC as described in Section 5.3.5, except that 50 mM Tris-HCl (pH 8.0) was used as elution buffer instead of 30 mM Tris-HCl (pH 7.4). An additional Protein L affinity chromatography step was tested to selectively isolate correctly folded rLCs, as described in Section 5.3.8. Samples were either snap-frozen in liquid nitrogen and stored at −80°C for long time storage or kept at 4°C for further analysis.

5.3.7 Protocol 3: Urea based solubilization and spontaneous refolding of rLCs

Adapted from Poshusta et al. (2013)

A mechanistically different approach for the purification and refolding of rLCs from IBs was described by Poshusta et al. (2013). In contrast to the GdnHCl solubilization and redox-shuffle methods, this strategy relied on a milder solubilization using urea and the spontaneous refolding during dialysis, without additional redox agents. Although only the V_L domains of FLCs were expressed and refolded in that study, the protocol was adapted and tested for full-length rLCs. A stepwise optimization strategy was applied, with each iteration incorporating minor modifications aimed at improving the

recovery of native rLCs. Briefly, harvested cell pellets were resuspended in 6 mL of lysis buffer containing 10 mM Tris-HCl (pH 7.4), 20 mM EDTA and one tablet of cOmplete Mini EDTA-free protease inhibitor cocktail (#11836170001, Merck Millipore, Darmstadt, Germany). Cell disruption was performed as described previously using a high-pressure homogenizer. The lysate was centrifuged at 8,000 × *g* for 20 min at 4°C, and the pellet containing the IBs was washed three times with 10 mM Tris-HCl (pH 7.4), 1% (v/v) Triton-X 100, and 0.5 M urea, followed by centrifugation at the same conditions. To solubilize the IB-associated rLCs, the washed pellet was resuspended in solubilization buffer composed of 10 mM Tris-HCl (pH 7.4) and 6 M urea and incubated on ice for 30 min. After solubilization, the sample was centrifuged at 20,000 × *g* for 1 h at 4°C, and the supernatant containing solubilized rLCs was collected. The sample was dialyzed overnight at 4°C against 10 mM Tris-HCl (pH 7.4). This dialysis step was reported to provide a suitable environment for the formation of intramolecular disulfide bonds without the need for additional redox agents. The following day, the dialyzed sample was sterile-filtered through a Filtropur S polyethersulfone syringe filter with a pore size of 0.2 µm (#83.1826.001, Sarstedt, Nümbrecht, Germany) and subsequently subjected to SEC for final purification as described previously but with the use of 10 mM Tris-HCl (pH 7.4) as elution buffer. An additional Protein L affinity chromatography step was tested to selectively isolate correctly folded rLCs, as described in Section 5.3.8. Samples were either snap-frozen in liquid nitrogen and stored at −80°C for long time storage or kept at 4°C for further analysis.

5.3.8 Protein L affinity chromatography

Protein L affinity chromatography was performed using Pierce Protein L Agarose resin (#20510, Thermo Fisher Scientific, Waltham, MA, USA) according to the manufacturer's instructions. Briefly, 2 mL of slurry (corresponding to 1 mL of settled resin) was equilibrated to room temperature and loaded onto an Econo-Pac chromatography column (#7321010, Bio-Rad Laboratories, California, USA) for gravity flow purification. The column was equilibrated with 10 mL of binding buffer (0.1 M sodium phosphate, 0.15 M sodium chloride, pH 7.2). Recombinant and patient-derived LC samples were prediluted 1:1 in binding buffer prior to affinity chromatography to maintain ionic strength and pH for optimal binding. After sample application, the flow-through was collected for subsequent analysis. In some cases, the flow-through was reapplied to the column to maximize potential binding. The column was then washed with 10 mL binding buffer, and bound LCs were eluted with 5-10 mL of elution buffer (0.1 M glycine, pH 2.5). Eluted fractions (1 mL) were immediately neutralized with 100 µL of 1 M sodium phosphate (pH 8.5). Fractions were screened for LC content by SDS-PAGE. After use, the column was regenerated with 10-15 mL of elution buffer, followed by washing with dH_2O containing 0.02% sodium azide and approximately 5 mL were left in the sealed column for storage at 4°C.

5.3.9 Protocol 4: Chaperone-assisted expression of rLCs in the periplasmic space of *E. coli*

Developed in collaboration with Dr. Hamed Shaykhalishahi

Since recovery from IBs did not yield a native-like secondary structure for rLC6, an alternative strategy was applied. To avoid cytoplasmic IB formation, the expression was directed to the periplasm, which provides an oxidizing folding environment that facilitates native disulfide bond formation. Therefore, the rLC6 gene insert was linked to an N-terminal signal peptide (pelB leader sequence) to enable periplasmic export. In addition, the construct contained a second T7 expression cassette encoding the periplasmic chaperone Skp to support folding in the periplasm. A C-terminal *hexa*histidine (6xHis) tag was included to allow purification by Ni-NTA affinity chromatography. The plasmid carried a chloramphenicol resistance marker, and cultures were maintained under chloramphenicol selection (1:1,000 dilution from a 34 mg/mL stock solution). The expression vector pCHAP (pET-derived, chaperone-assisted periplasmic expression) was generated as described in Section 5.3.2 and 5.3.3. Briefly, the codon-optimized gene insert for patient sample P006 was cloned into the linearized pCHAP vector using primers providing complementary overlaps. All primers used for cloning are listed in Table 5.2, and the nucleotide sequence of the final construct is provided in the Supplementary information (Tab. 8.8), with a schematic representation of the expression construct shown in Figure 5.19. For purification, a standard cold osmotic shock protocol was applied to selectively release periplasmic proteins while minimizing cytoplasmic contamination. Cell pellets were resuspended in 100 mL of cold TES buffer containing 200 mM Tris-HCl (pH 8.0), 5 mM EDTA and 200 g/L (w/v) sucrose. After incubation on ice for 30 min with gentle inversions every 5 min to prevent sedimentation, the sample was centrifuged at 8,000 × *g* for 10 min at 4°C. The supernatant was discarded, and the pellet fraction was rapidly resuspended in Milli-Q H_2O (35 mL per liter of initial culture) at 4°C supplemented with a protease inhibitor tablet. After a further 30 min incubation on ice, centrifugation at 23,000 × *g* for 30 min at 4°C was performed to remove cellular debris. The resulting supernatant contained the soluble periplasmic fraction, including rLC6, which was sterile-filtered through a Filtropur S polyethersulfone syringe filter with a pore size of 0.2 µm (#83.1826.001, Sarstedt, Nümbrecht, Germany). Affinity purification via immobilized metal affinity chromatography (IMAC) was carried out on a HisTrap HP 5 mL Ni-NTA column (Cytiva, Marlborough, MA, USA). The column was equilibrated and loaded using a flowrate of 2 mL/min. Elution was performed with 50 mM Tris-HCl (pH 8.0) containing 250 mM imidazole. After overnight dialysis at 4°C against 50 mM Tris-HCl (pH 8.0), SEC was carried out as described previously in Section 5.3.5 but with 50 mM Tris-HCl (pH 8.0) as elution buffer. After SEC, fractions were pooled according to their molecular composition which was further analyzed by SDS-PAGE and samples were either snap-frozen in liquid nitrogen and stored at −80°C for long time storage or kept at 4°C for further analysis. Since final sample concentrations were too low for analysis, the samples were concentrated and buffer-exchanged by ultrafiltration, before characterized by CD spectroscopy.

Table 5.2: Primer set used for cloning of the pCHAP-P006 fusion construct for the periplasmic expression of rLC6 in *E. coli*

Primer	Sequence (5' to 3')
pCHAP Forward	TTGTACACGGCCGCATAATC
pCHAP Reverse	CGCCAGCAGAAATGCGATATTCTTCTTCATGGTATATCTCCT
pCHAP+P006 Forward	ATATCGCATTTCTGCTGGCGAGCATGTTTGTTTTTAGCATTGCA
	ACCAATGCATATGCCAGCGATCTGCAAATGACCCAGAGTCCGA
pCHAP+P006 Reverse	ATGCGGCCGCAAGCTTTATCAATGGTGATGGTGATGGTGATGG
	TGACATTCACCACGATTAAAGCTTTTGGT

5.4 Results

5.4.1 Construction and validation of the pET-16b-P006 expression vector

The recombinant construct pET-16b-P006 was designed for the expression of the patient-derived FLC P006 in *E. coli*. As expression strategy, the well-established approach of IB purification was selected. Although IB formation is frequently exploited to obtain large amounts of recombinant protein, this strategy remains challenging for proteins that are difficult to refold, and the recovery of correctly folded material is often inefficient. The accumulation of proteins in insoluble aggregates can arise from different factors, including high expression rates, intrinsic folding kinetics of the protein, or, in the case of FLCs, the inability to form disulfide bonds in the reducing cytoplasmic environment (Baneyx and Mujacic 2004; De Marco 2009). In IBs, proteins are typically present in unfolded or misfolded states. Nevertheless, through carefully controlled solubilization and refolding steps during purification, rLCs can be recovered in their native conformation, including the correct formation of both intra- and intermolecular disulfide bonds (Buchner and Rudolph 1991; Rognoni et al. 2013; Poshusta et al. 2013). A schematic representation of the expression vector is shown in Figure 5.4A. Assembly of the vector was carried out as described in Section 5.3.2 and 5.3.3. PCR amplification of the codon-optimized gene insert yielded the expected 669 bp product (Fig. 5.4B), and the pET-16b vector was successfully linearized to its expected size of 5.6 kb (Fig. 5.4C).

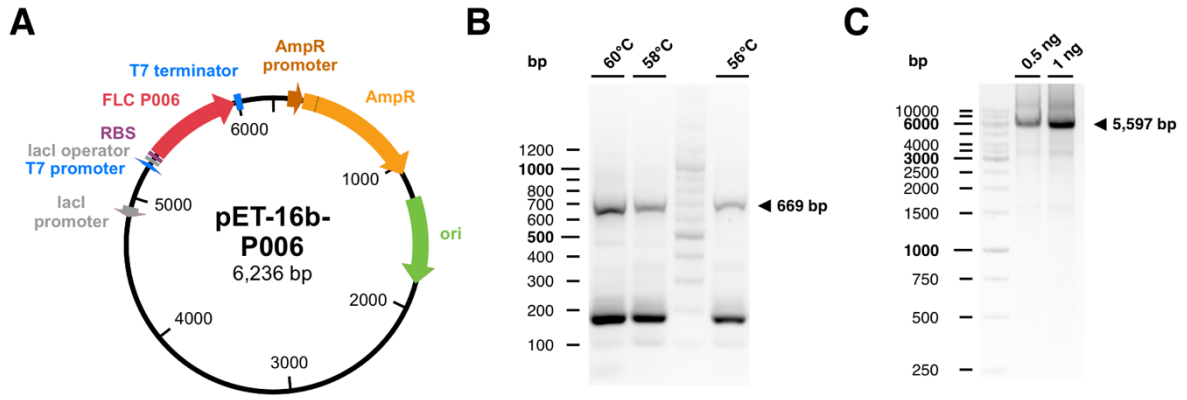

Figure 5.4: Vector design and assembly of pET-16b-P006 for the recombinant expression of rLC6 in *E. coli*. (**A**) Schematic representation of the pET-16b-P006 expression construct showing its key features: the P006 FLC gene insert (red), the T7 promoter and terminator enabling IPTG-inducible expression (blue), and the ampicillin resistance gene (AmpR; yellow) with its corresponding promoter (orange). The total length of the construct is 6,236 bp. (**B**) Agarose gel analysis of P006 gene amplification using primers containing vector-overlap sequences (Tab. 5.1: P006+pET-16b Forward & Reverse). PCR reactions were performed at annealing temperatures of 60°C, 58°C, and 56°C; optimal amplification was obtained at 60°C. The expected product size including primer overhangs was 669 bp. A GeneRuler 100 bp Plus DNA Ladder was used as molecular size marker. (**C**) Linearization of the pET-16b vector prior to gene insert assembly, yielding the expected 5,597 bp product. A GeneRuler 1 kb DNA Ladder was used as a size marker. After gel purification, the linearized vector and the amplified P006 insert were assembled using the In-Fusion Cloning Kit to generate the final pET-16b-P006 construct for expression of rLC6 in *E. coli*.

Following assembly, the pET-16b-P006 expression construct was transformed into either BL21 (DE3) or Stellar competent *E. coli* cells. Colonies were grown in 2×YT medium supplemented with ampicillin, and glycerol stocks were prepared for storage at −80°C. Plasmid DNA isolated from these cultures was verified by Sanger sequencing to confirm correct construct assembly. To verify construct functionality, a small-scale expression test was performed as described in Section 5.3.4. SDS-PAGE analysis revealed a distinct band at ~25 kDa after IPTG induction, corresponding to the predicted molecular weight of rLC6 (Fig. 5.5). No comparable band was observed in the non-induced control, confirming successful expression of rLC6, and thereby verifying construct functionality. The glycerol stocks generated from this test expression were subsequently used for expression and purification according to the protocols described in Section 5.3.5, 5.3.6, and 5.3.7.

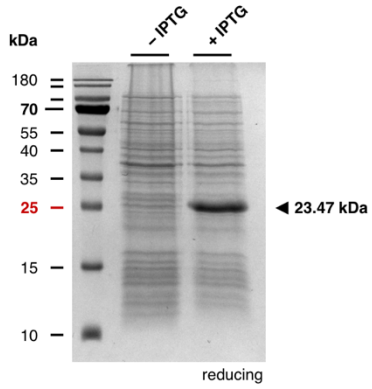

Figure 5.5: Expression test of pET-16b-P006 in *E. coli*. SDS-PAGE analysis of 2×YT cultures before (–IPTG) and after (+IPTG) induction with IPTG. The –IPTG sample was collected immediately prior to induction at an OD_{600} of 0.8. Expression was induced with 1 mM IPTG, and the +IPTG sample was taken 4 h post-induction, immediately before cell harvest. To ensure comparability, sample volumes were normalized to cell density (–IPTG: 121.95 µL; +IPTG: 70.42 µL). All samples were prepared in reducing Laemmli loading buffer. The predicted molecular weight of rLC6 is 23.47 kDa, as indicated by the arrow next to the corresponding band, which is consistent with the expected size.

5.4.2 Protocol 1: Isolation of IBs and redox-mediated renaturation of rLCs

Adapted from Buchner and Rudolph (1991)

In order to recover rLC6 in its native form from IBs, a classical refolding protocol described by Buchner and Rudolph (1991) was applied with minor modifications, as described in Section 5.3.5. In this approach, IBs were solubilized under denaturing conditions, and the unfolded protein was subsequently refolded by controlled dilution into a redox buffer establishing the GSH/GSSG equilibrium required for productive disulfide bond formation. The progression of purification and refolding was monitored by SDS-PAGE at each step as shown in Figure 5.6. After cell lysis by high-pressure homogenization, the total lysate displayed a distinct band at ~25 kDa, corresponding to the theoretical molecular weight of the LC monomer (Fig. 5.6A). Following centrifugation, the majority of rLC6 was detected in the pellet fraction, while only minor traces were present in the supernatant. This distribution is consistent with the accumulation of rLC6 in insoluble IBs, which remain in the pellet fraction after cell disruption. Compared with the total cell lysate before centrifugation, the pellet fraction already displayed a high degree of purity after the initial separation step. After IB preparation, stepwise solubilization was performed as described in Section 5.3.5 (Fig. 5.6B). The washed pellet fraction is shown under non-reducing (lane 1) and reducing (lane 2) conditions. Following solubilization, rLC6 was recovered in the supernatant fraction (lane 3), while insoluble impurities were removed by centrifugation and remained in the pellet fraction (lane 4). Lanes 5 and 6 show the undiluted supernatant and pellet fractions, respectively. The smeared and distorted appearance of the band in lane 5 likely results from high GdnHCl concentration (6 M) present in the undiluted sample, which interferes with the integrity of the SDS-PAGE matrix.

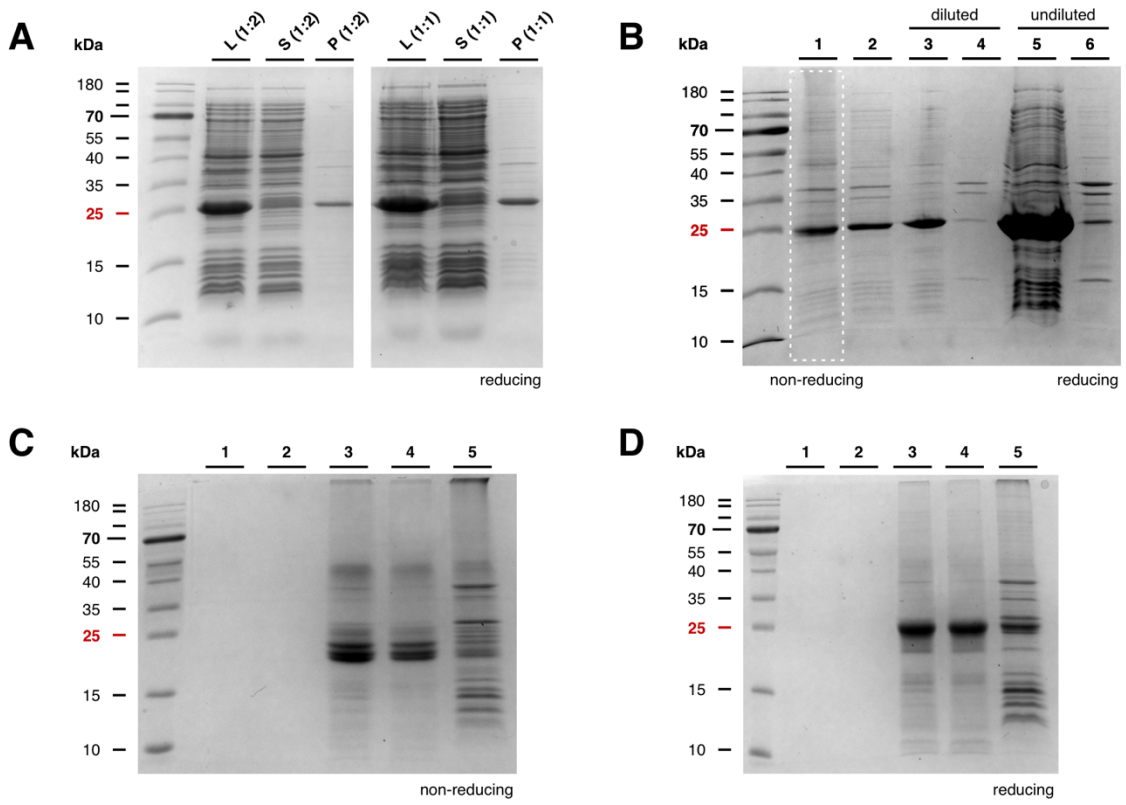

Figure 5.6: Protocol 1. Recovery of rLC6 from IBs. SDS-PAGE analysis of the samples collected during stepwise recovery of rLC6 from IBs after recombinant expression in *E. coli*. **(A)** After cell lysis by high-pressure homogenization and centrifugation for 60 min at 25,000 × *g* and 4°C, total cell lysate (L), supernatant (S), and pellet (P) fractions were collected. Each fraction is shown undiluted and at 1:2 dilution. All samples were prepared in reducing Laemmli loading buffer. The majority of overexpressed rLC6 (~25 kDa band) was detected in the pellet fraction containing the IBs. **(B)** Samples collected during IB solubilization and subsequent refolding were analyzed under reducing and non-reducing conditions, as indicated by the dotted line. (1, 2) Pellet after washing (non-reducing and reducing), (3) solubilized sample, 1:10 dilution, (4) pellet after solubilization, 1:10 dilution, (5) solubilized sample, undiluted, (6) pellet after solubilization, undiluted. Dilution for lanes 3 and 4 was performed in 0.1 M Tris-HCl (pH 8.5). The prominent band at ~25 kDa corresponds to rLC6, observed in both solubilized and refolded states. **(C, D)** Samples collected following renaturation and dialysis were analyzed under (**C**) non-reducing and (**D**) reducing conditions. (1) refolded protein after dialysis overnight at 4°C, (2) flow-through after centrifugal ultrafiltration, (3) concentrated sample (reduced from 200 mL to 1 mL total volume), (4) sample after centrifugation at 10,000 rpm for 1 h at 4°C and sterile filtration (0.2 µm), (5) pellet after centrifugation. The major band at ~25 kDa corresponds to rLC6. The clarified sample reached a concentration of 2.58 mg/mL.

After successful solubilization, rLC6 was present in a soluble but denatured state. Figures 5.6C and 5.6D show the SDS-PAGE analysis of rLC6 after refolding under non-reducing and reducing conditions. Due to 100-fold dilution of the solubilized protein into renaturation buffer, no detectable band was observed in the diluted refolded sample (lane 1) or in the flow-through after centrifugal ultrafiltration (lane 2). Following ultrafiltration, which reduced the total volume to 1 mL and yielded a final concentration of 2.58 mg/mL, a clear band at ~25 kDa was detected in both non-reducing and reducing gels. In the non-reducing SDS-PAGE (Fig. 5.6C), several closely spaced bands were observed around ~25 kDa, likely corresponding to rLC6 monomers with heterogeneous disulfide-bonding patterns or partially oxidized species. Such band heterogeneity under non-reducing conditions can

arise from disulfide scrambling or incomplete denaturation during sample preparation (Zhang et al. 2019). Similar migration patterns were observed for patient-derived FLCs previously and were therefore expected as well for the recombinant sample under non-reducing conditions. Upon reduction (Fig. 5.6D), these multiple bands collapsed into a single species at ~25 kDa, consistent with the fully reduced monomer. This supports the conclusion, that the observed band heterogeneity under non-reducing conditions likely originated from disulfide rearrangements rather than the presence of distinct structural isoforms. In addition, faint bands at ~50 kDa were observed in lanes 3 and 4, particularly under non-reducing conditions, consistent with rLC6 dimers formed through disulfide-linked C-terminal cysteines. Lane 4 shows the clarified sample after the final centrifugation and sterile filtration step, while lane 5 represents the pellet fraction of aggregated material removed during centrifugation. The aggregation of rLC6 during the refolding step becomes evident when compared with Figure 5.6A. In Figure 5.6C and 5.6D, residual material remained in the gel pockets (lanes 3–5), most likely representing high molecular weight species too large to enter the gel matrix during electrophoresis. Under reducing conditions (Fig. 5.6D, lane 5), the pocket band appeared only faint, while a clear band at ~25 kDa was observed, corresponding to monomeric rLC6 that was released from aggregates upon reduction.

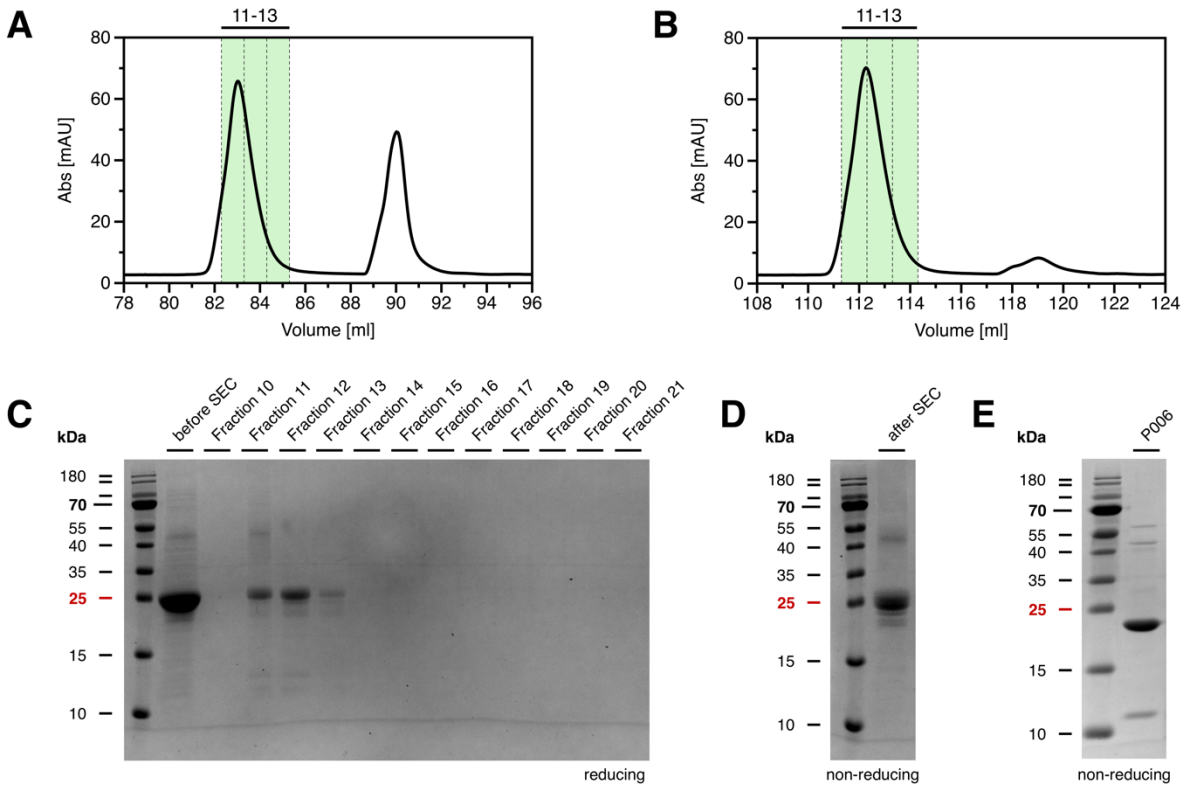

Figure 5.7: Protocol 1. SEC fractionation of rLC6 after renaturation. Following renaturation, rLC6 was concentrated to a final volume of 1 mL (2.58 mg/mL) by ultrafiltration and applied to a Superdex 75 10/300 GL Tricorn column in two 500 µL injections (**A**, **B**). Eluted fractions were analyzed by SDS-PAGE under reducing conditions to identify rLC6 (**C**). Fractions with comparable molecular composition were pooled and stored at 4°C for short term use or at −80°C for long-term storage. (**D**) Pooled SEC fractions 11-13 analyzed under non-reducing conditions. (**E**) Respective patient-derived FLC sample P006 shown for comparison.

A final purification step by SEC was performed as described in Section 5.3.5, using a Superdex 75 10/300 GL Tricorn column. The refolded sample, concentrated to a total volume of 1 mL after ultrafiltration, centrifugation, and sterile filtration, was applied to the column in two 500 µL injections. Both chromatograms are shown in Figures 5.7A and 5.7B, and collected fractions were analyzed by reducing SDS-PAGE (Fig. 5.7C). rLC6 was detected primarily in fractions 11-13, with fraction 12 containing the highest concentration of protein, as indicated by the prominent band at ~25 kDa. The second peak in the chromatogram (fractions 17-19) did not contain detectable rLC6 and most likely corresponded to buffer components and salts eluting at the column's total volume (V_t). Fractions 11-13 were pooled according to their molecular composition. The pooled sample is shown in Figure 5.7D, where the band at ~25 kDa corresponds to monomeric rLC6, and the faint band at ~50 kDa likely represents dimeric species. For comparison, Figure 5.7E shows the corresponding patient-derived FLC P006, which also exhibited a faint band consistent with a FLC dimer, while the monomer band appeared at a comparatively lower molecular weight range. This difference may reflect an alternative folding state in the patient-derived FLC that influences electrophoretic migration. In addition, a band between 10-15 kDa was observed in the patient sample, which may represent a lower molecular weight fragment likely generated by proteolytic digestion due to the presence of cathepsins in the patient samples, as discussed in Chapter 3 and 4.

After purification, rLC6 was subjected to biophysical characterization. As a first step, the refolding efficiency of Protocol 1 was assessed by analyzing the secondary structure of rLC6 using CD spectroscopy in comparison with the corresponding patient-derived sample P006. CD spectroscopy was performed as described in Section 3.4.4, with a sample concentration of 8 µM in 10 mM Tris-HCl (pH 7.4). Figure 5.8A and 5.8B presents the secondary structure analysis of rLC6 obtained using Protocol 1. The HT signals of rLC6 and P006 overlapped across the far-UV range (Fig. 5.8A), indicating comparable optical transmission, and allowing for a reliable direct comparison of their CD spectra. However, as shown in Figure 5.8B, significant differences in the secondary structure were observed between rLC6 and P006. While P006 and the other patient-derived FLC samples (e.g., Fig. 3.5) exhibited secondary structures dominated by distinct β-sheet motifs, with a minimum at approximately 217 nm, typical for immunoglobulin domains (Brahms et al. 1977; Bork et al. 1994; Poshusta et al. 2013; Andrich et al. 2017), rLC6 showed a minimum around 200 nm, which is consistent with a largely unstructured or disordered, random coil conformation (Greenfield 2006; Zerfaß et al. 2017). These results suggest that the refolding conditions applied in Protocol 1 did not succeed in restoring the native conformation of the patient-derived FLC. To rule out potential experimental errors and to test possible improvements in rLC6 recovery, the refolding protocol was repeated four additional times, resulting in five independent rLC6 preparations in total. While the second preparation strictly followed the initial protocol, subsequent preparations included minor modifications to enhance the recovery of native secondary structure. In preparation 3, the solubilization step was extended to 2 h, and the solubilized sample volume was reduced to 2 mL before dilution into the renaturation buffer. In preparation 4, the renaturation step was prolonged to 3 h. In preparation 5, 0.4 M L-arginine was added to the renaturation buffer to suppress aggregation of unstable off-pathway intermediates. Additionally, preparations 3 and 4 were lyophilized instead of being snap-frozen in liquid nitrogen before long-term storage at −80°C.

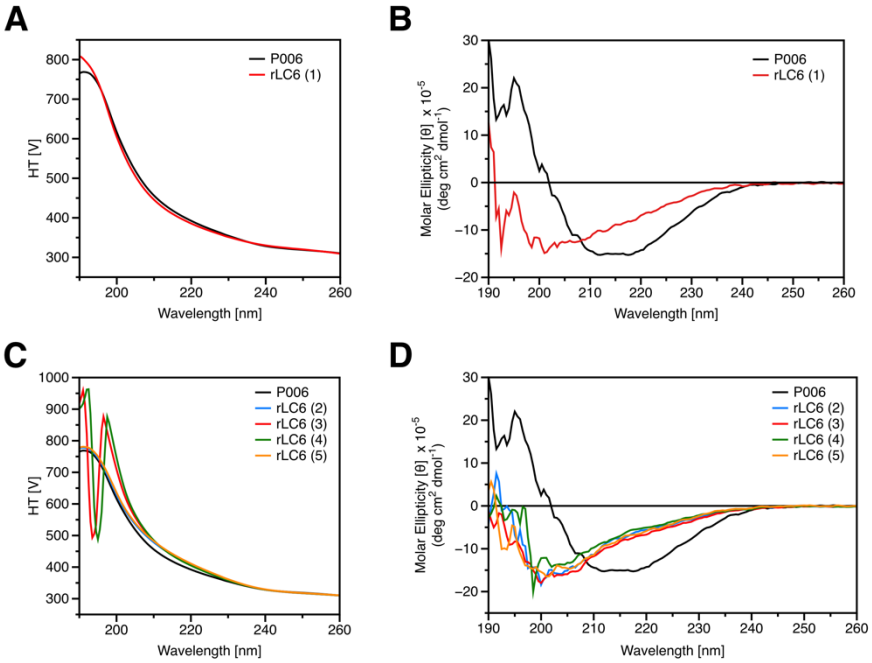

Figure 5.8: Protocol 1. CD spectroscopy analysis of rLC6. The refolding efficiency of rLC6 using Protocol 1 was assessed by CD spectroscopic secondary structure analysis. (**A**, **B**) First preparation of rLC6 (red) compared with the patient-derived sample P006 (black). (**A**) HT voltage signals, and (**B**) CD spectra. (**C**, **D**) Four additional rLC6 preparations (blue, red, green, yellow) compared with P006 (black). (**C**) HT voltage signals, and (**D**) CD spectra. All measurements were performed at a sample concentration of 8 µM in 10 mM Tris-HCl buffer (pH 7.4). All data was baseline corrected and 15 accumulations per sample were recorded. CD spectra are shown as molar ellipticity, calculated from raw ellipticity (millidegrees) normalized to protein concentration and path length.

As shown in Figure 5.8D, none of the additional attempts produced a native-like secondary structure, and all rLC6 preparations exhibited spectra comparable to the initial refolding experiment. Notably, the two lyophilized rLC6 preparations showed a pronounced drop in the HT voltage signal between 190 and 200 nm. This effect was absent in non-lyophilized samples and is therefore most likely caused by lyophilization-induced aggregation or buffer changes upon reconstitution. This shift in the HT voltage was also reflected in a reduced signal-to-noise ratio of the corresponding CD spectra (Fig. 5.8D, rLC6 (3) and (4)), although the overall spectral features remained consistent with those of the non-lyophilized preparations.

To further characterize the molecular composition of rLC6 after refolding, the first preparation was analyzed by SV-AUC as previously described in Chapter 3. The resulting $c(s)$ distribution under native conditions is shown in Figure 5.9A. The corresponding sedimentation profiles are provided in the Supplementary information (Fig. 8.12).

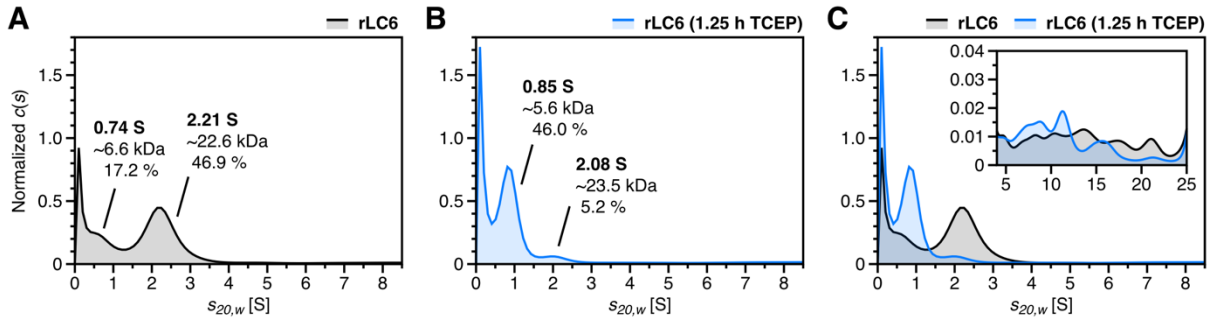

Figure 5.9: Protocol 1. SV-AUC analysis of rLC6 and the effect of disulfide bond reduction by TCEP. The *c*(*s*) distributions obtained from SV-AUC experiments are shown. (**A**) rLC6 under native conditions. (**B**) rLC6 after addition of 7 mM pH-adjusted TCEP and incubation for 1.25 h at 37°C with shaking at 600 rpm. (**C**) Overlay of the *c*(*s*) distributions of rLC6 and rLC6 after TCEP treatment. All samples were prepared at a concentration of 35 µM in 30 mM Tris-HCl (pH 7.4). For each measurement, 390 µL of sample were loaded into the sample sector of standard aluminum double-sector centerpieces, and SV analysis was carried out at 60,000 rpm and 20°C.

Approximately half of the sample corresponded to a species consistent with the LC monomer (2.21 S). In addition, a second species was detected at 0.74 S, reminiscent of FLC fragments previously observed during the analysis of the patient samples (e.g., Fig. 3.4). This signal converged with a sharp peak at ~0.1 S, which had also been observed in reduction experiments, where it increased with longer TCEP incubation time and was interpreted as a low molecular weight fragment. To assess the stability of the molecular species distribution as a function of disulfide bonding, rLC6 was analyzed after incubation with 7 mM TCEP for 1.25 h (Fig. 5.9B) as described in Chapter 3. After TCEP-treatment, the sample displayed a peak at 0.85 S accounting for 46% and a peak at 2.08 S, accounting for 5.2% of the total sample. Compared to rLC6 under native conditions (Fig. 5.9C), the overall signal distribution shifted towards lower *s*-values, consistent with the observations made for patient-derived FLC samples.

Measured *c*(*s*) distributions of rLC6 were then compared with those of the corresponding patient-derived sample P006, presented in the Supplementary material in Section 8.1.2. Figure 5.10A shows the overlay of rLC6 and P006 under native conditions. Compared to rLC6, P006 displayed a slightly higher *s*-value for the monomer (2.35 S vs. 2.21 S) together with a sharper overall peak, consistent with a more homogeneous molecular species. In addition, P006 exhibited a distinct signal at 1.36 S, likely corresponding to a fragmented species, as well as a dimeric species at 3.65 S that accounted for ~10% of the sample. In contrast, rLC6 showed no dimeric signal and instead displayed a broader monomer peak together with a fragment-like signal at a lower *s*-value (0.74 S), indicating a different fragmented species compared to P006. After incubation of P006 with TCEP for 1.25 h, the differences between reduced P006 and native rLC6 became less pronounced (Fig. 5.10B). The monomeric peak of reduced P006 shifted to 2.27 S, closely matching the 2.21 S monomer peak of rLC6. At the same time, the fragment distribution of P006 shifted toward a lower *s*-value (~0.7 S), resembling the fragment-like signal already observed in rLC6. Importantly, the dimeric species present in native P006 decreased after TCEP treatment, further aligning the molecular species distribution of reduced P006 with that of native rLC6.

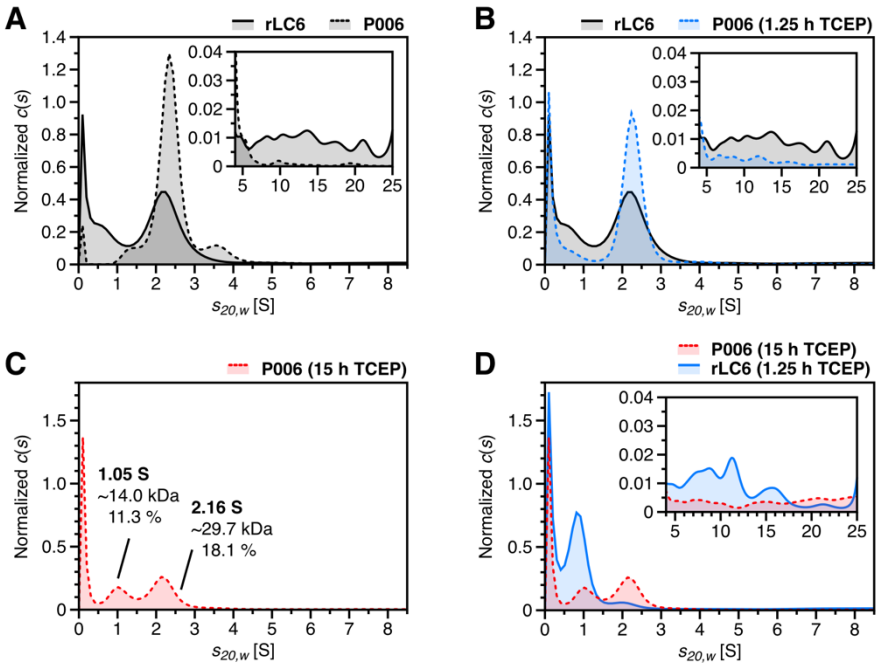

Figure 5.10: Protocol 1. SV-AUC comparison of rLC6 and P006. The *c*(*s*) distributions of rLC6 and P006 obtained from SV-AUC experiments are shown. The *c*(*s*) data for P006 are reproduced from Chapter 3. (**A**) Comparison of rLC6 and P006 in their native states. (**B**) Comparison of native rLC6 with P006 after 1.25 h of incubation with TCEP. (**C**) P006 after 15 h of TCEP incubation. (**D**) Comparison of rLC6 after 1.25 h of TCEP incubation with P006 after 15 h of TCEP incubation. All samples were prepared at a concentration of 35 µM in 30 mM Tris-HCl (pH 7.4). For each measurement, 390 µL of sample were loaded into the sample sector of standard aluminum double-sector centerpieces, and SV analysis was carried out at 60,000 rpm and 20°C.

This trend became even more apparent when comparing both samples in a reduced state (rLC6 after 1.25 h and P006 after 15 h of TCEP incubation), as shown in Figure 5.10C and 5.10D. Both distributions showed a shift of the monomer to lower *s*-values (P006: 2.16 S vs. rLC6: 2.08 S), an increase in fragment species (P006: 1.05 S vs. rLC6: 0.85 S), and a pronounced rise of low molecular weight signals around 0.1 S compared with their respective native states. Taken together, these results indicate that rLC6 is already destabilized under native conditions, resembling the partially reduced profile of P006 after short-term TCEP incubation. The absence of a stable dimer fraction, the broader and less defined signal of the monomeric species, and the altered fragment distribution collectively indicate that the refolding conditions were insufficient to re-establish the stabilizing disulfide bond pattern of the patient-derived FLC. Consequently, rLC6 likely represents a *pre-reduced-like* state in which native disulfide pairing is disrupted, leading to structural stabilization. While the CD data (Fig. 5.8) support this interpretation, it should be noted that disulfide reduction alone, as shown in Chapter 3 (Fig. 3.5), does not necessarily cause complete loss of β-sheet structure but rather decreases its stability and cooperativity. The observed random-coil-like profile of rLC6 therefore suggests additional misfolding.

5.4.3 Protocol 2: Dropwise dilution refolding of rLCs in GSH/GSSG redox-shuffle buffer

Adapted from Rognoni et al. (2013)

To further explore redox-mediated refolding strategies beyond the protocol of Buchner and Rudolph (1991), a method described by Rognoni et al. (2013) was tested for the recovery of full-length rLCs in *E. coli*. This protocol follows the same refolding concept but differs in several steps, including extended solubilization time, dropwise dilution into a redox-shuffle buffer, and an additional AEC step. Since these adjustments were expected to enhance folding efficiency and purity, the protocol was selected for evaluation. Protocol 2 was performed as described in Section 5.3.6 and samples were collected throughout the preparation for SDS-PAGE analysis to monitor purification efficiency (Fig. 5.11B), including the supernatant after the first centrifugation, the resuspended pellet before washing, and the supernatant after both washing steps.

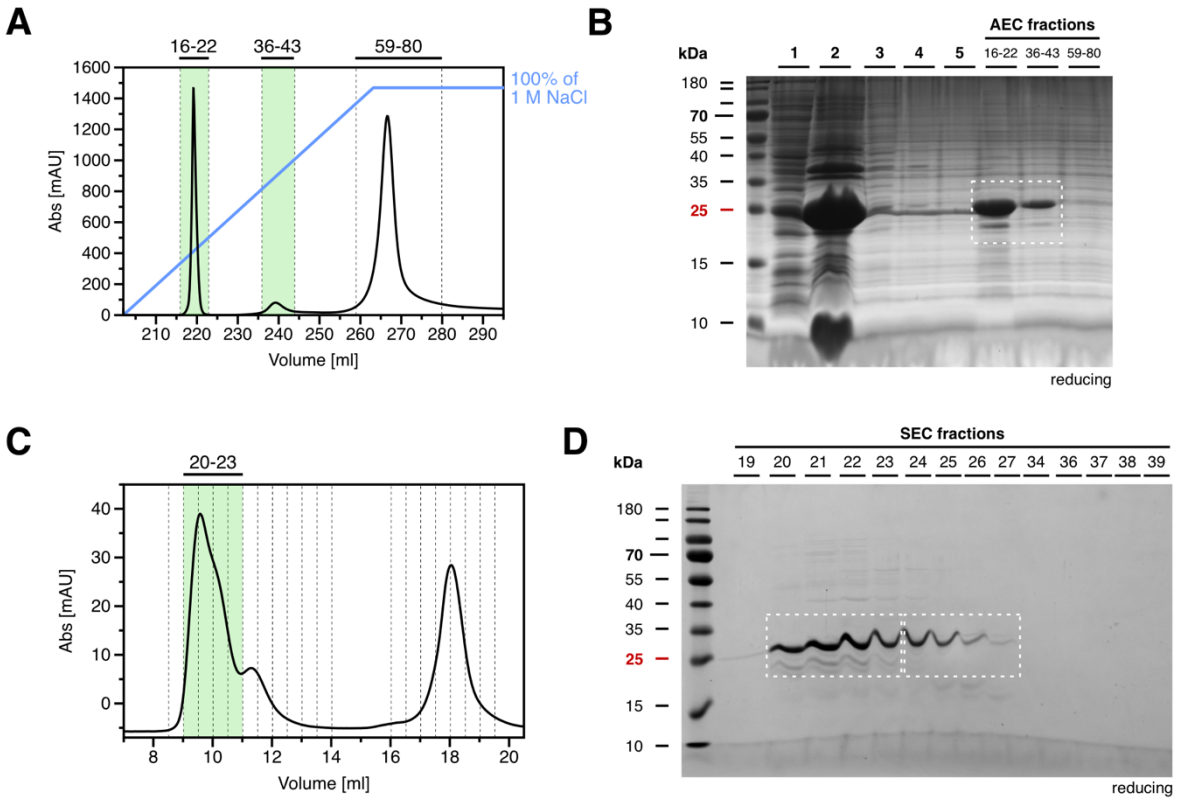

Figure 5.11: Protocol 2. AEC and SEC purification of rLC6 after renaturation. Shown are the AEC and SEC chromatograms, together with the SDS-PAGE analysis of collected fractions. (**A**) AEC chromatogram after rLC6 renaturation. Elution via NaCl gradient indicated in blue (started at 0% at ~202 mL to 100% (1 M NaCl final concentration) at ~262 mL, 2 mL/min). (**B**) Reducing SDS-PAGE analysis of (1) centrifugation step 1; (2) resuspended pellet before washing; (3,4) supernatant after first and second washing step; (5) AEC flow-through; (6) AEC fractions 16-22 (peak 1); (7) AEC fractions 36-43 (peak 2); (8) AEC fractions 59-80 (peak 3). Fractions 16-22 and 36-43 were pooled for further purification, as indicated by the dotted line. (**C**) SEC chromatogram of pooled AEC fractions 16-22 and 36-43 and (**D**) SDS-PAGE analysis of collected SEC fractions. Fractions 20-23 and 24-27 were pooled for further characterization, as indicated by the dotted lines.

IB-associated rLC6 was primarily detected in the pellet fraction after cell lysis, consistent with previous observations, and the washing steps only led to minor sample loss. After IB preparation, refolding, and dialysis, rLC6 was purified by AEC (Fig. 5.11A). Three elution peaks were observed, the first peak appeared at ~250 mM NaCl, the second between 600-700 mM, and the third at 1 M NaCl. SDS-PAGE analysis revealed only minor traces of rLC6 in the AEC flow-through, while the majority of rLC6 eluted in the first two peaks (Fig. 5.11B). Following AEC, the first two elution peaks (fractions 16-22 and 36-43) containing rLC6 were pooled and subjected to final purification by SEC. The SEC chromatogram (Fig. 5.11C) and the corresponding SDS-PAGE analysis of the eluted fractions (Fig. 5.11D) are shown. The chromatogram displayed a main peak eluting at approximately 9 mL, accompanied by a pronounced right-skewed shoulder. rLC6 was primarily detected in fractions 20-27, covering both main peak and its shoulder. Whether the right-skewed shoulder and the second AEC peak reflected the presence of rLC6 dimers could not be determined, as SDS-PAGE analysis was performed under reducing conditions. Based on molecular composition and band intensity, fractions 20-23 and 24-27 were pooled separately. The pooled samples were either snap-frozen in liquid nitrogen for long-term storage at −80°C or kept at 4°C for further analysis.

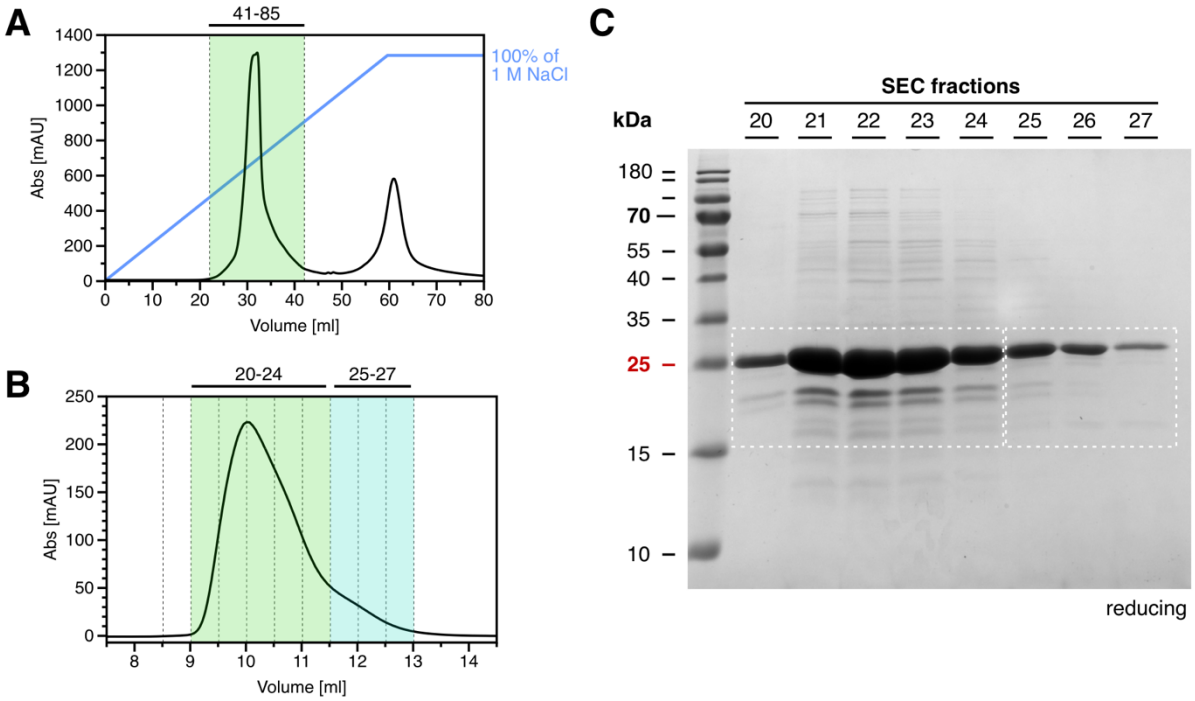

Figure 5.12: Protocol 2. Second preparation of rLC6. Shown are the AEC and SEC chromatograms, as well as SDS-PAGE analysis of collected fractions. (**A**) AEC chromatogram after rLC6 renaturation. Elution via NaCl gradient indicated in blue (started at 0% at ~0 mL to 100% (1 M NaCl final concentration) at ~60 mL, 2 mL/min). (**B**) SEC chromatogram of pooled AEC fractions 41-85 and (**C**) SDS-PAGE analysis of collected SEC fractions. Fractions 20-24 and 25-27 were pooled for further characterization, as indicated by the dotted lines.

A second rLC6 purification using Protocol 2 is shown in Figure 5.12. In contrast to the first preparation, AEC yielded a single broad elution peak between 300-600 mM NaCl (Fig. 5.12A). The broadening of the peak compared to the first preparation may indicate increased sample

heterogeneity. The entire peak (fractions 41-85) was pooled and subjected to SEC fractionation. Since rLC6 was not detectable in the late-eluting peak at 1 M NaCl during the first preparation, this region was not considered for further analysis. The SEC chromatogram (Fig. 5.12B) displayed a major peak at ~9 mL with a right-skewed shoulder, similar to the first preparation but less pronounced. SDS-PAGE analysis of the eluted fractions (Fig. 5.12C) confirmed rLC6 as the dominant species, primarily detected in fractions 20-27. Based on molecular composition and band intensities, fractions 20-24 and 25-27 were pooled separately. The overall yield of rLC6 was comparable to that of the first preparation, and pooled fractions were either snap-frozen in liquid nitrogen for storage at −80°C or kept at 4°C for further analysis. Despite differences in the AEC elution profile and minor variations in the SEC peak shape, both preparations yielded a consistent distribution of rLC6 across fractions. In the first preparation, pooled fractions 20-23 (rLC6 (1)) yielded a concentration of 1.04 mg/mL, while in the second preparation, pooled fractions 20-24 (rLC6 (2)) and 25-27 (rLC6 (3)) yielded 1.02 mg/mL and 0.88 mg/mL, respectively. In contrast to Protocol 1, the concentrations obtained with Protocol 2 were sufficiently high to allow further analysis without the need for additional concentration by ultrafiltration.

Following SEC, purified rLC6 samples were analyzed by CD spectroscopy to assess their secondary structure (Fig. 5.13). The folding efficiency of Protocol 2 was evaluated by comparing the spectra of rLC6 with those of the patient-derived sample P006, as well as with rLC6 obtained using Protocol 1. From the first preparation, the pooled SEC fractions 20-23 (green), and from the second preparation, both pooled fractions 20-24 (blue) and 25-27 (red) were analyzed. Figure 5.13A shows the HT voltage signals of all measurements. All three rLC6 preparations were analyzed in 10 mM sodium phosphate buffer, whereas P006 was measured in 10 mM Tris-HCl buffer, both at pH 7.4. Accordingly, all rLC6 samples displayed consistently lower HT voltage values across the far-UV wavelength range compared to sample P006, consistent with the lower far-UV absorbance of sodium phosphate relative to Tris-HCl (Pain 2004). While sodium phosphate buffers are generally preferred because they remain optically transparent down to ~185 nm, Tris-HCl exhibits stronger absorbance below 200 nm, which increases HT voltage and reduce spectral accuracy, particularly at higher buffer concentrations or pH values (Greenfield 2006). Nevertheless, low concentration Tris-HCl buffers (e.g., 10 mM) used with a 1 mm pathlength cuvette are widely considered acceptable. Figure 5.13B shows the CD spectra for all rLC6 preparations in comparison with P006. The spectra of the three rLC6 preparations closely overlapped, with minima around 205-208 nm and a tendency towards a signal around 217 nm. This high degree of consistency across preparations indicates that Protocol 2 reproducibly yielded rLC6 with comparable secondary structure content. Nevertheless, all rLC6 samples remained clearly distinct from P006. Thus, rLC6 obtained with Protocol 2 retained a largely disordered or partially folded character. For subsequent AUC analysis, the sample rLC6 (1) from the first preparation was selected.

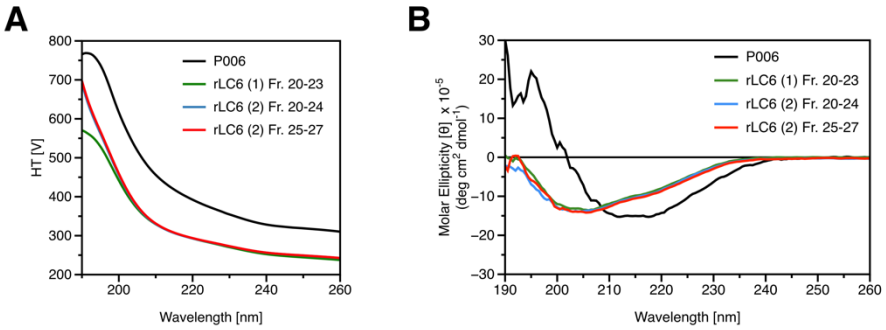

Figure 5.13: Protocol 2. CD spectroscopy analysis of rLC6. Refolding efficiency of rLC6 using Protocol 2, adapted from Rognoni et al. (2013), was assessed by secondary structure analysis via CD spectroscopy. From the first preparation (rLC (1)), the pooled SEC fractions 20-23 (green) were analyzed. From the second preparation (rLC (2)), pooled SEC fractions 20-24 (blue) and 25-27 (red) were analyzed. (**A**) HT voltage signals of the analyzed rLC6 samples compared with the patient-derived sample P006 (black). (**B**) Corresponding CD spectra of rLC6 samples in comparison with P006 (black). All measurements were performed at a protein concentration of 8 µM in 10 mM sodium phosphate buffer (pH 7.4). All data was baseline corrected and 15 accumulations per sample were recorded. CD spectra are shown as molar ellipticity, calculated from raw ellipticity (millidegrees) normalized to protein concentration and path length.

The hydrodynamic properties and molecular composition of rLC6, obtained using Protocol 2, were further analyzed by SV-AUC. Measurements were performed at a sample concentration of 35 µM in 30 mM Tris-HCl (pH 7.4). The sedimentation profile and the corresponding $c(s)$ distribution of rLC6 (1) are shown in Figure 5.14A and 5.14B. Under native conditions, the $c(s)$ distribution of rLC6 (1) showed a dominant peak at 3.17 S (~36% of the total signal) together with a well-resolved shoulder at 4.61 S (~20% of the total signal). Additionally, a broad, right-skewed tail extended up to ~30 S indicated the presence of higher-order oligomeric species. When compared directly to the patient-derived sample P006 (Fig. 5.14B), the sedimentation behavior of rLC6 showed pronounced differences. The main peak at 3.17 S was too large to correspond to the P006 monomer (2.35 S) yet too small to represent its dimer (3.65 S), while the second peak at 4.61 S exceeded the expected range for the dimer by approximately 1 S. Whether these signals represent dimers and tetramers of rLC6 in a partially folded or misfolded state remains unclear. Only a faint, left-skewed shoulder around 2.2 S hinted at the possible presence of monomers. Compared to the first rLC6 preparation using Protocol 1 (Fig. 5.9A), which predominantly yielded monomeric species and low molecular weight fragments resembling those in the destabilized patient sample P006, Protocol 2 resulted in a sample with a high degree of oligomerization. The nature of these oligomers remains unresolved, but they differ significantly from both P006 and rLC6 obtained using Protocol 1. These findings suggest that the refolding conditions used in Protocol 2 likely promote self-association rather than native folding, consistent with the results from CD spectroscopy.

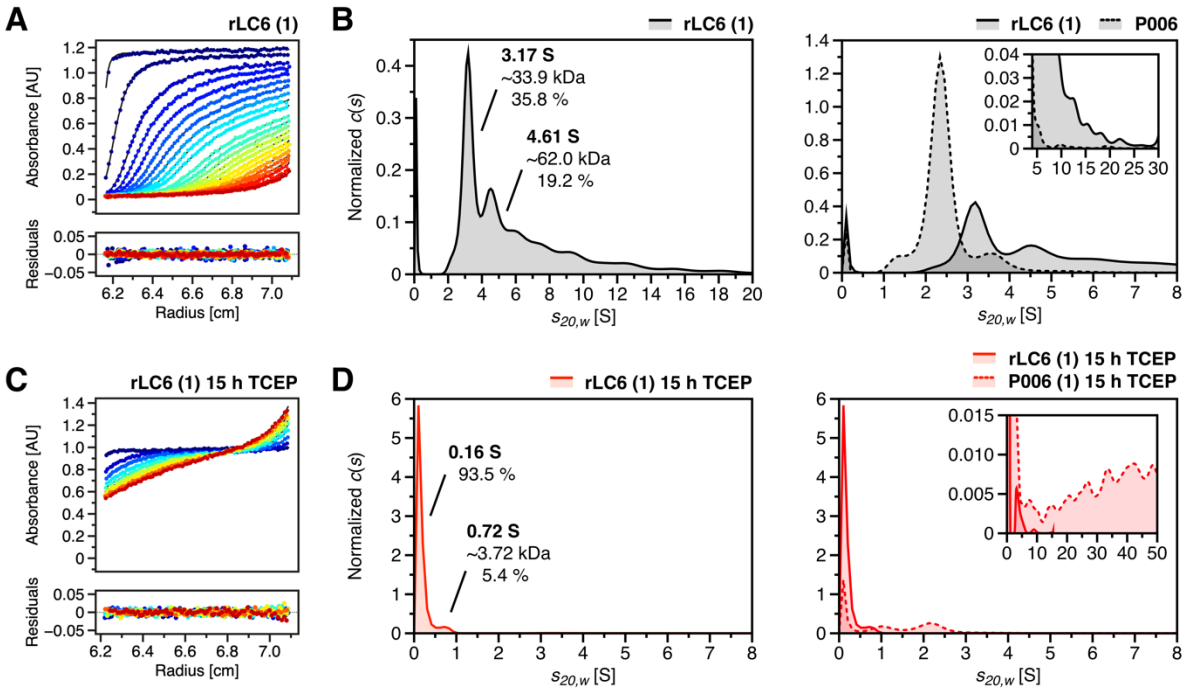

Figure 5.14: Protocol 2. SV-AUC analysis of rLC6. The *c*(*s*) distributions obtained from SV-AUC experiments are shown. (**A**) Sedimentation profile of rLC6 obtained using Protocol 2, with (**B**) the corresponding *c*(*s*) distribution and comparison with patient-derived sample P006. (**C**) Sedimentation profile of rLC6 after 15 h of incubation with 7 mM TCEP, with (**D**) the corresponding *c*(*s*) distribution and comparison with P006 after 15 h TCEP-incubation. SV experiments were performed in 30 mM Tris-HCl buffer (pH 7.4) at a protein concentration of 35 µM. For each measurement, 390 µL of sample were loaded into the sample sector of standard aluminum double-sector centerpieces, and measurements were carried out at 60,000 rpm and 20°C.

To further analyze the stability of these species, rLC6 obtained using Protocol 2 was treated with 7 mM TCEP for 15 hours and analyzed by SV-AUC in comparison with P006. The sedimentation profile and the corresponding *c*(*s*) distribution of the reduced sample are shown in Figure 5.14C and 5.14D. Both the sedimentation profile and the *c*(*s*) distribution showed a pronounced loss of sedimenting material, with the *c*(*s*) distribution dominated by a single sharp peak at 0.16 S (~94% of the total sample), consistent with the low molecular weight fragments previously observed during extended TCEP incubation of patient samples (e.g., Fig. 3.1). A minor peak at 0.72 S was also detected, likely reflecting a larger fragment. In contrast to P006, which forms aggregates under the same reducing conditions (Fig. 8.1B), rLC6 showed no signs of aggregation. Instead, the majority of the sample shifted toward smaller species, suggesting that degradation, rather than aggregation, was the dominant outcome of reduction. Since a minor drop in sedimentation plateau was only mildly noticeable after 15 h of TCEP treatment (Fig. 5.14C), this indicates that no substantial material was lost to rapidly sedimenting aggregates. Taken together, these results support the conclusion that rLC6 obtained using Protocol 2 adopts a non-native, unstable conformation that is highly sensitive to reduction, ultimately leading primarily to fragmentation and degradation.

5.4.4 Protocol 3: Urea based solubilization and spontaneous refolding of rLCs

Adapted from Poshusta et al. (2013)

To evaluate an alternative strategy for the recovery of native rLCs from IBs, a protocol described by Poshusta et al. (2013) was adapted. Unlike Protocol 1 and 2, which relied on solubilization using GdnHCl and refolding via controlled dilution into a redox buffer, this method used urea-based solubilization followed by the spontaneous refolding during dialysis into a physiological buffer, without the addition of redox agents. While GdnHCl is a strong ionic chaotrope that fully denatures proteins while shielding electrostatic interactions and thereby minimizing charge-charge effects during refolding, urea is a neutral denaturant that primarily disrupts hydrogen bonds and hydrophobic interactions but leaves electrostatics intact. These mechanistic differences result in distinct folding landscapes and stability profiles (Monera et al. 1994). Thus, while the GdnHCl-based protocol ensured complete unfolding but required controlled redox dilution for refolding, the urea-based protocol allowed gentler unfolding and enabled spontaneous refolding during dialysis.

After cell lysis and centrifugation, the pellet fraction containing the IBs was washed extensively to reduce impurities, solubilized in 6 M urea, and then dialyzed into physiological buffer, as described in Section 5.3.6. After dialysis, the refolded samples were clarified by sterile filtration and subjected to SEC. During purification, samples were collected after cell lysis, during the washing steps, and from the refolded sample before SEC (Fig. 5.15B, lanes 1-4). The chromatogram shown in Figure 5.15A represents a preparation obtained after all additional modifications of the protocol were implemented. Following SEC, eluted fractions were analyzed by SDS-PAGE to assess rLC6 content. The overall rLC6 concentrations were sufficiently high to allow the analysis of individual fractions, rather than combining them. Fraction 22, with a concentration of 1.33 mg/mL in a total volume of 2 mL, was selected for subsequent characterization by CD and AUC analysis. Remaining fractions were snap-frozen in liquid nitrogen and stored at −80°C until further use.

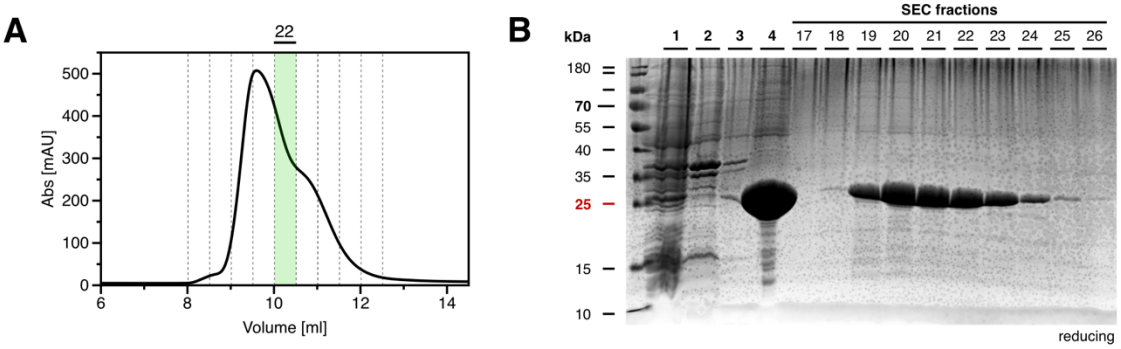

Figure 5.15: Protocol 3. SEC fractionation of rLC6 after renaturation. Following renaturation, rLC6 was concentrated by ultrafiltration, sterile-filtered, and applied to a Superdex 75 10/300 GL Tricorn column for SEC fractionation. (**A**) SEC chromatogram of rLC6 showing the main elution peak. Fraction 22 was used for subsequent analysis (green). (**B**) SDS-PAGE analysis under reducing conditions of samples collected prior to SEC (lane 1: supernatant after cell lysis; lane 2: pellet after initial washing step; lane 3: pellet after final washing step; lane 4: undiluted sample after refolding) and SEC fractions 17-26. rLC6 was primarily detected in fractions 19-24, with fraction 22 used for subsequent characterization by CD and AUC analysis.

Figure 5.16 shows the secondary structure analysis of three different rLC6 preparations obtained using Protocol 3. The individually pooled SEC fraction 22 is labelled rLC6 (2) and highlighted in green. All three rLC6 preparations were analyzed in 10 mM Tris-HCl buffer, pH 7.4. The HT voltage signals of the rLC6 preparations (Fig. 5.16A) were slightly elevated compared to those of the patient-derived sample P006, but overall indicated sufficient optical transmission to enable a reliable comparison of the CD spectra (Fig. 5.16B). All three preparations of rLC6 displayed spectra similar to those obtained with Protocol 1, but with the minimum shifted from ~200 nm to ~205-208 nm, as also observed in Protocol 2. This shift may indicate that Protocol 2 and 3 yielded rLC6 in a more partially folded state compared to Protocol 1, yet still distinct from the characteristic β-sheet signature of FLCs. While the overall spectral profile suggested a predominantly disordered conformation, the subtle differences observed also raised the possibility that the samples obtained with Protocol 2 and 3 contained a mixture of folding states, with only a fraction of rLC6 adopting a native-like conformation. Nevertheless, the dominant signal remained consistent with a largely disordered state, demonstrating that the dialysis-based refolding of Protocol 3 was insufficient to restore a native-like secondary structure.

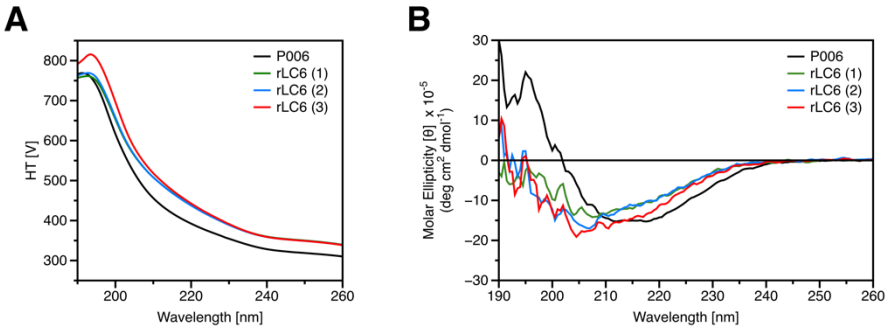

Figure 5.16: Protocol 3. CD spectroscopy analysis of rLC6. The refolding efficiency using the protocol adapted from Poshusta et al. (2013) was evaluated by secondary structure analysis via CD spectroscopy. Shown are (**A**) high-tension (HT) voltage signals, and (**B**) CD spectra of three independent rLC6 preparations (green, blue, red) compared with the patient-derived sample P006 (black). Fraction 22 from the preparation shown in Figure 5.15 is shown in blue (rLC6 (2)). Measurements were performed at a protein concentration of 8 µM in 10 mM Tris-HCl buffer (pH 7.4). Data were baseline corrected, and 15 accumulations per sample were recorded. CD spectra are shown as molar ellipticity, calculated from raw ellipticity (millidegrees) normalized to protein concentration and path length.

To analyze the molecular composition of rLC6 obtained using Protocol 3, the samples were subjected to SV-AUC. Figure 5.17 shows the sedimentation profiles (Fig. 5.17A, C, E) and the corresponding *c*(*s*) distributions (Fig. 5.17B, D, F) for the three analyzed preparations. Sample rLC6 (2) corresponds to SEC fraction 22 shown in Figure 5.15. All preparations displayed similar sedimentation profiles, with reproducible *s*-values that could be assigned to different molecular species. On average, the monomer sedimented at 2.09 ± 0.10 S, the dimer at 3.19 ± 0.07 S, and a third species, which most likely reflects a tetramer, at 4.64 ± 0.14 S. The consistency of these values across preparations indicated comparable conformational states, in agreement with the CD spectroscopic analysis (Fig. 5.16). Notably, the tetrameric species showed the highest variability in terms of *s*-value, suggesting a broader structural heterogeneity. In addition, all samples showed a right-skewed

shoulder in the 6-7 S range, consistent with higher-order oligomers beyond the tetramer. A similar signal broadening was also observed for the monomer of rLC6 (1) in the range of 1-1.5 S (Fig. 5.17B), which most likely reflects fragmentation, as described previously. Also, rLC6 (2) displayed an additional, baseline-resolved peak around 0.62 S, which also indicates the presence of a fragment species. In the third preparation, no fragment species was observed. Compared to the patient-derived sample P006, rLC6 samples consistently exhibited lower *s*-values, with average decreases of 0.26 S for the monomer and 0.46 S for the dimer. Moreover, a tetrameric species reproducibly observed in rLC6 preparations across different protocols (i.e., Fig. 5.17D, F and Fig. 5.14B) was absent in P006. In context of the CD data, these differences support the conclusion that rLC6 obtained using Protocol 3 adopts a non-native conformation largely dominated by unstructured random coil motifs, resulting in a distinct distribution of molecular species.

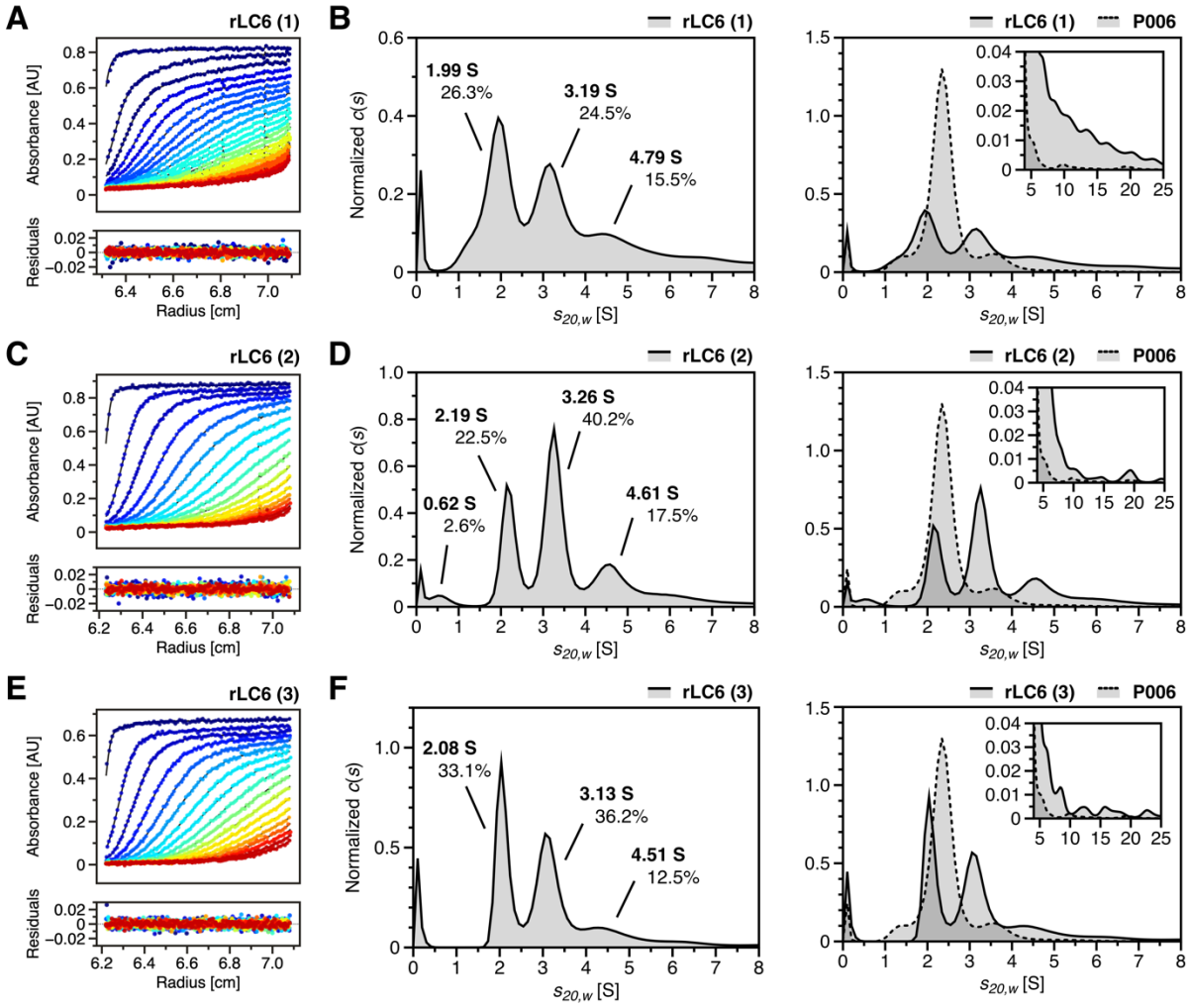

Figure 5.17: Protocol 3. SV-AUC analysis of rLC6. SV experiments were performed under native conditions in 30 mM Tris-HCl buffer (pH 7.4) at a protein concentration of 35 µM. (**A**, **C**, **E**) Sedimentation profiles of three independent rLC6 preparations obtained using Protocol 3, and (**B**, **D**, **F**) the corresponding *c*(*s*) distributions with additional comparison with patient-derived sample P006. For each measurement, 390 µL of sample were loaded into the sample sector of standard aluminum double-sector centerpieces, and measurements were carried out at 60,000 rpm and 20°C.

In summary, the adapted Protocol 3, based on urea solubilization and spontaneous refolding of rLC6 during dialysis without additional redox agents, yielded consistent results across independent preparations and provided sufficient material for downstream analyses. CD spectroscopy confirmed that rLC6 did not adopt a native-like secondary structure but instead adopted a conformation dominated by random coil motifs, closely resembling rLC6 from Protocol 1 and 2. Notably, both Protocols 2 and 3 yielded rLC6 preparations with a CD spectral minimum around 205-208 nm, suggesting a shared, partially ordered conformation distinct from the completely unfolded-like spectrum observed in Protocol 1, which displayed a minimum at ~200 nm. This shift may reflect the formation of residual secondary structure elements or intermediate folding states of rLC6. Importantly, unlike Protocol 2, which led to broad, heterogeneous oligomerization and lacked a clearly defined monomer peak, Protocol 3 consistently produced distinct, stable peaks corresponding to monomeric, dimeric, and tetrameric species. This suggests that the refolding conditions in Protocol 3 allowed for at least partially folded, stable monomers to form, representing a key difference from the loss of monomer observed in Protocol 2. Although the oligomeric distribution generated by Protocol 3 was more defined than in Protocol 2, it still diverged from the native sedimentation profile of the patient-derived sample P006. These differences likely arise from persistent deviations in folding, intermolecular interactions, or the nature of stabilizing forces (e.g., covalent versus non-covalent), which continue to prevent the formation of native-like assemblies.

5.4.5 Evaluation of Protein L as a tool for selective purification of rLC6

Since rLC6 obtained using Protocol 2 and 3 exhibited CD spectral features suggestive of mixed folding states, it was tested whether correctly folded species could be selectively isolated using Protein L affinity chromatography. Originally isolated from the cell wall of *Peptostreptococcus magnus*, Protein L binds with high affinity to the folded framework region of κ-type LC V_L domains (Akerström and Björck 1989). While strong binding has been reported for the VκI, VκIII and VκIV subgroups, only weak or no affinity was observed for VκII and λ-type LCs (Nilson et al. 1993). Unlike Protein A and G, which exclusively interact with IgG HCs (Akerström and Björck 1989; Zheng et al. 2012), Protein L directly binds to the V_L domain of κ-type LCs and is therefore also applicable to single-chain antibody fragments (scFv). This makes it a potential tool for selectively isolating native or partially folded FLC and rLC species from heterogeneous samples. To evaluate the potential of Protein L for this purpose, gravity flow chromatography was performed as described in Section 5.3.8. Figure 5.18 summarizes the results of three Protein L binding experiments performed with rLC6 obtained with Protocol 2 (Fig. 5.18A), rLC6 obtained with Protocol 3 (Fig. 518B), and the patient-derived sample P006 (Fig. 5.18C). SDS-PAGE was performed under reducing conditions and only the first elution fractions are shown, as no significant protein was detected beyond.

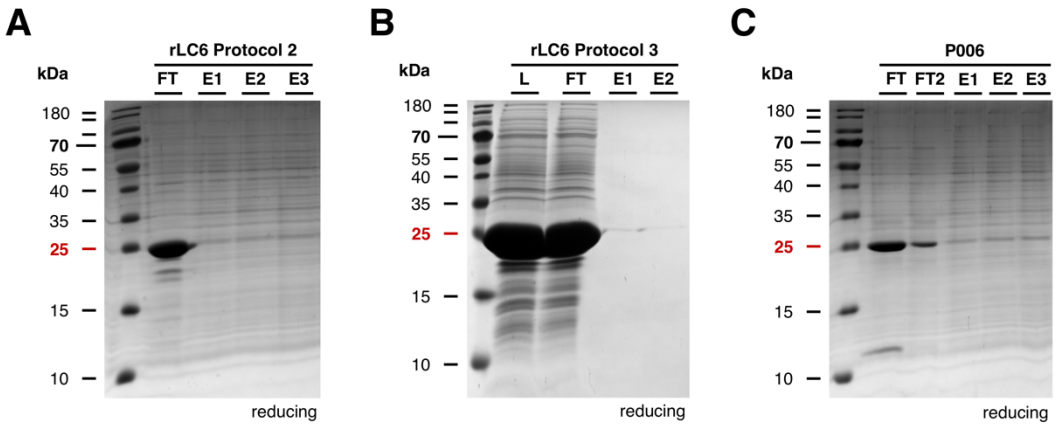

Figure 5.18: Protocol 2 & 3. Protein L affinity chromatography of rLC6 and P006. The SDS-PAGE analysis of three Protein L binding experiments is shown. (**A**) rLC6 obtained with Protocol 2, showing flow-through (FT) and elution fractions (E1-E3). (**B**) rLC6 obtained with Protocol 3, showing the sample before loading (L), the flow-through (FT) and the elution fractions (E1, E2). (**C**) Patient-derived sample P006, showing the flow-through (FT), reloaded flow-through (FT2), and elution fractions (E1-E3). Only the first elution fractions are shown as example, no significant amounts of rLC6 or P006 were detected. SDS-PAGE was performed under reducing conditions.

The experiments revealed little to no affinity of rLC6 obtained using Protocol 2 and 3 for Protein L (Fig. 5.18A, B). The majority of rLC6 was found in the flow-through, and comparison with the loaded sample (Fig. 5.18B) showed nearly identical SDS-PAGE profiles, confirming that rLC6 did not bind to the Protein L column. Only minor traces of rLC6 were observed in the elution fractions, which were insufficient for meaningful concentration or further analysis. To determine whether the absence of binding was caused by misfolding or epitope disruption in rLC6, a control experiment was performed with the patient-derived sample P006 (Fig. 5.18C). Surprisingly, P006 also exhibited minimal Protein L binding, with the majority of material recovered in the flow-through. Reloading of the sample showed no improvement, and the elution fractions again showed only faint traces of P006, likely due to non-specific retention rather than affinity. P006 was classified as a κ-type LC of the VκI subgroup using the ANARCI web tool (Dunbar and Deane 2016) and was therefore expected to demonstrate a high binding affinity to Protein L. While structural epitope disruption caused by somatic mutations or partial unfolding within the framework region of the V_L domain could explain the absence of binding in rLC6, as at least partially expected, this result was unexpected for P006. Previous studies have reported that Protein L can show reduced binding to free κ-type LCs compared to intact IgG or scFv constructs, likely explained by HC pairing contributions to a more accessible conformation of the VL domain for Protein L interaction (Akerström and Björck 1989). However, it has also been reported that isolated VκI fragments can retain comparable binding affinities to those of intact IgG molecule (Nilson et al. 1992, 1993), suggesting that additional structural or conformational factors may influence the interaction of FLCs with Protein L.

5.4.6 Protocol 4: Chaperone-assisted expression of rLCs in the periplasmic space of *E. coli*

Developed in collaboration with Dr. Hamed Shaykhalishahi

To establish an oxidative *in vivo* folding system, the P006 gene was cloned into the pCHAP vector kindly provided by Dr. Hamed Shaykhalishahi. This construct directs rLC6 into the periplasm via an N-terminal pelB leader sequence, where the oxidizing environment facilitates folding and disulfide bond formation. In addition, the vector encodes the periplasmic chaperone Skp to further promote proper folding, and a C-terminal 6xHis tag to enable downstream purification by IMAC. A schematic representation of the construct is shown in Figure 5.19A. Assembly of the construct was performed as described in Section 5.3.2 and 5.3.3. Linearization of the pCHAP vector yielded the expected band at ~4.3 kb when using 1 ng of template DNA, accompanied by minor PCR by-products. In contrast, the reaction with 0.5 ng template did not produce the expected product but instead resulted in a smear and prominent primer-dimer formation (Fig. 5.19B). PCR amplification of the codon-optimized gene insert with primers providing overlaps for the assembly into the pCHAP vector (Table 5.2) produced the expected 753 bp fragment (Fig. 5.19C). Amplification was successful at both tested annealing temperatures (58°C and 60°C), producing very strong and distinct bands. Final assembly of the linearized pCHAP vector with the P006 gene insert was carried out using the In-Fusion Snap Assembly Kit according to the manufacturer's instructions.

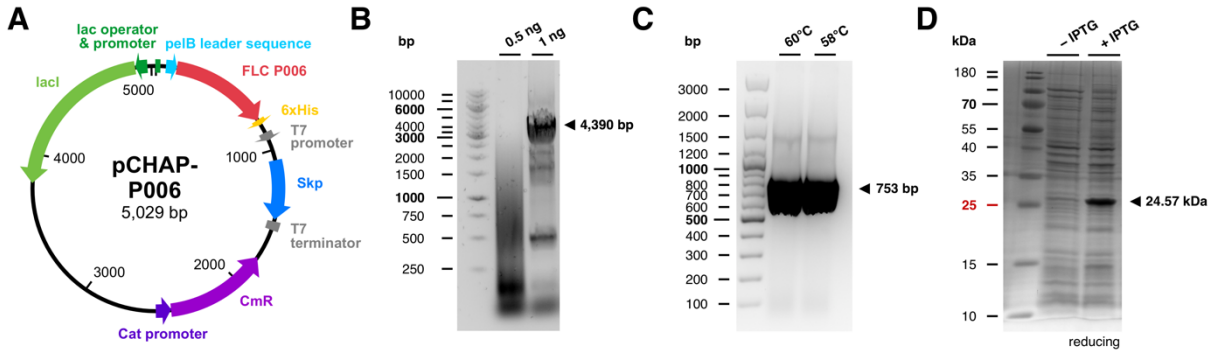

Figure 5.19: Protocol 4. Vector design, assembly, and validation of pCHAP-P006 for periplasmic expression of rLC6 in *E. coli*. (**A**) Schematic representation of the pCHAP-P006 construct, highlighting key vector features: the P006 gene insert (red), the N-terminal pelB leader sequence for periplasmic export (light blue), the co-expressed periplasmic chaperone Skp (blue), and the C-terminal 6xHis tag (yellow). The plasmid also carries a chloramphenicol resistance marker (purple) with its Cat promoter (dark purple). The total construct length comprises 5,029 bp. (**B**) Agarose gel of the linearized pCHAP vector (expected size 4,390 bp). GeneRuler 1 kb DNA Ladder was used as a marker. (**C**) PCR amplification of the codon-optimized P006 insert with primers containing vector-overlap sequences (Tab. 5.2). PCR reactions at 58°C and 60°C both yielded the expected 753 bp fragment. GeneRuler 100 bp Plus DNA Ladder was used as a marker. Linearized vector and P006 insert were purified and assembled using the In-Fusion Cloning Kit. (**D**) Test expression of pCHAP-P006 in *E. coli*. SDS-PAGE analysis of cultures before (–IPTG) and after (+IPTG) induction. The –IPTG sample was collected at an OD_{600} of 0.8; expression was induced with 1 mM IPTG, and the +IPTG sample was taken 4 h after expression. Sample volumes were normalized to cell density as described before. A distinct band at ~25 kDa (arrow) corresponds to rLC6, consistent with its predicted molecular weight (24.57 kDa).

The resulting constructs were transformed into *E. coli* BL21 (DE3) competent cells via heat-shock transformation, plated on 2×YT agar containing 34 µg/mL chloramphenicol, and incubated overnight at 37°C. The next day, single colonies were picked from the plate, inoculated in 2×YT medium, and grown overnight. Glycerol stocks were prepared, and plasmid DNA was purified and verified by Sanger sequencing to confirm correct construct assembly. To validate construct functionality, a small-scale expression test was performed as described in Section 5.3.4. Following IPTG induction, SDS-PAGE analysis revealed a distinct band at ~25 kDa (Fig. 5.19D), consistent with the predicted molecular weight of rLC6 including the 6xHis tag (24.57 kDa, 221 aa). This band was absent in the non-induced control, confirming successful expression of rLC6.

After large-scale expression, cells were harvested by centrifugation and subjected to cold osmotic shock as described in Section 5.3.9, allowing the release of rLC6 from the periplasm while minimizing cytoplasmic contamination. Since a C-terminal 6xHis tag was included in this strategy, the supernatant following osmotic shock, which contained soluble, folded rLC6, was purified by IMAC. The Ni-NTA chromatogram (Fig. 5.20A) showed a single distinct elution peak, and the corresponding fractions (11-23) were pooled for subsequent SEC. The SEC chromatogram (Fig. 5.20B) displayed one major peak at ~9 mL with a right-skewed shoulder at ~11 mL, and a minor peak at ~14 mL. To confirm the presence of rLC6, fractions 18-30 covering all three peaks were analyzed by non-reducing SDS-PAGE (Fig. 5.20C). Distinct bands at ~25 kDa were detected in fractions 18-21, consistent with the expected molecular weight of rLC6 including the 6xHis tag (24.57 kDa). Additional bands at ~50 kDa were also observed, likely representing disulfide-linked rLC6 dimers, as disulfide bond formation is expected during periplasmic folding.

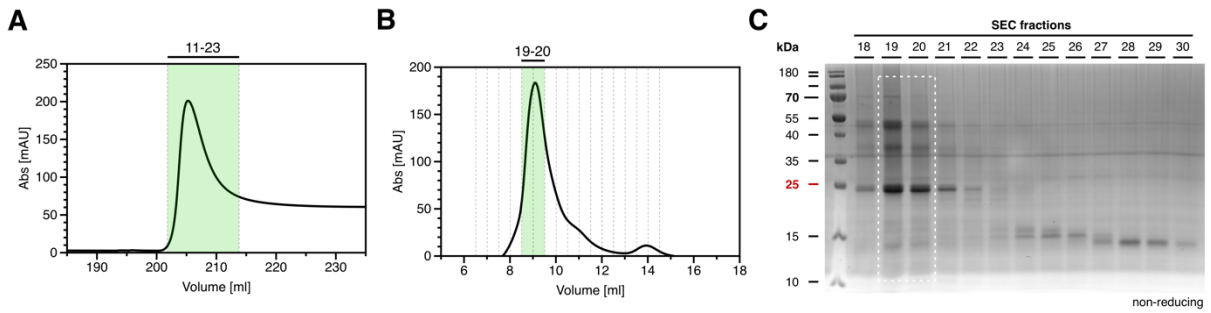

Figure 5.20: Protocol 4. Purification of periplasmic rLC6. The purification combining IMAC and SEC is shown. (**A**) Ni-NTA chromatogram of 6xHis-tagged rLC6. Fractions 11-23 (green area) were pooled for SEC. (**B**) SEC chromatogram of the IMAC-purified sample, showing a main peak at ~9 mL with a right-skewed shoulder. Fractions 19-20 (green area) were selected for downstream characterization based on SDS-PAGE analysis. Dotted lines indicate all collected fractions analyzed by SDS-PAGE. (**D**) Non-reducing SDS-PAGE of SEC fractions 18-30. Prominent rLC6 bands were observed in early fractions comprising the main peak, while later fractions showed bands at ~15 kDa.

While fractions 22 and 23 still contained minor amounts of rLC6, fractions 24-30 predominantly displayed bands at ~15 kDa. Because these species were recovered following IMAC purification, they are most consistently explained as His tag containing rLC6 fragments. Co-expressed Skp (~17 kDa) or other periplasmic *E. coli* proteins are unlikely contributors, as they do not carry a 6xHis tag and therefore would not be expected to bind efficiently to the IMAC resin. Based on these results,

fractions 19 and 20, which contained the most prominent monomeric and dimeric rLC6 signals, were pooled, buffer-exchanged into 10 mM Tris-HCl (pH 7.4) by ultrafiltration, and subsequently concentrated. The initial preparation of rLC6 using Protocol 4 yielded low protein recovery, resulting in a final concentration of approximately 0.1 mg/mL (~0.02 mg total), corresponding to ~2.5 µM rLC6 in a volume of ~200 µL, which was used for CD spectroscopic analysis to evaluate the refolding efficiency of Protocol 4. This preparation was performed before implementing the cold osmotic shock step, which was introduced subsequently to reduce cytoplasmic contamination and improved purification efficiency. In the final preparation, the concentration reached 0.942 mg/mL (0.188 mg total) in a comparable volume (~200 µL), corresponding to 38.35 µM rLC6.

Despite using 4 L of expression culture per preparation, the overall yield of periplasmic expression remained low in comparison with IB-based protocols. To address this limitation, a series of optimization experiments was performed in which parameters such as expression temperature and duration, IPTG concentration, and pre-induction cold shock were systematically varied (data not shown; available upon request). None of these approaches increased the proportion of soluble rLC6. Figure 5.21 illustrates how the solubility of rLC6 after expression was evaluated. Following expression, the harvested cells were lysed using a high-pressure homogenizer, as described for Protocols 1-3, to ensure efficient cell disruption. The lysate was centrifuged for 15 min at 20,000 × *g* and 4°C, and the resulting supernatant and pellet fractions were analyzed by SDS-PAGE to determine the subcellular distribution of rLC6. In this context, rLC6 detected in the supernatant corresponds to soluble, periplasmically folded protein, whereas rLC6 in the pellet indicates IB formation. As shown in Figure 5.21, the majority of rLC6 was located in the pellet fraction, while only faint bands were detected in the supernatant. This suggests that most of the protein remained accumulated in cytoplasmic or periplasmic IBs, and only a small fraction of rLC6 was present in a soluble, periplasmically folded form. While this observation could explain the low yields obtained in Protocol 4, none of the tested modifications of the expression parameters increased the proportion of soluble rLC6 or improved the overall recovery.

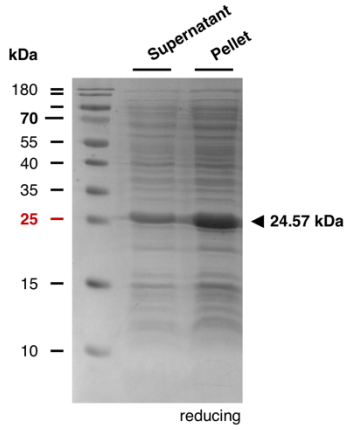

Figure 5.21: Protocol 4. SDS-PAGE analysis of rLC6 solubility after periplasmic expression. After expression, cells were lysed using a high-pressure homogenizer and the lysate was centrifuged for 15 min at 20,000 × *g* and 4°C, and the resulting supernatant and pellet fractions were analyzed to assess the solubility and subcellular distribution of rLC6. Together with the 6xHis tag, rLC6 has a predicted molecular weight of 24.57 kDa, indicated by the arrow next to the corresponding band, consistent with the expected size. All samples were prepared in reducing Laemmli loading buffer.

After each preparation using Protocol 4, the purified rLC6 samples were analyzed by CD spectroscopy at the available concentrations. The spectra were compared with the concentration-matched patient-derived sample P006 to evaluate the efficiency of Protocol 4 in recovering rLC6 in a native-like folding state. In the first preparation, the low protein yield (~0.1 mg/mL) limited the quality of the spectra; nevertheless, the data were sufficient to assess overall folding trends. Subsequent preparations yielded higher protein concentrations, which enabled more reliable secondary structure analysis. The results of the CD spectroscopic analysis of rLC6 obtained with Protocol 4 are shown in Figure 5.22.

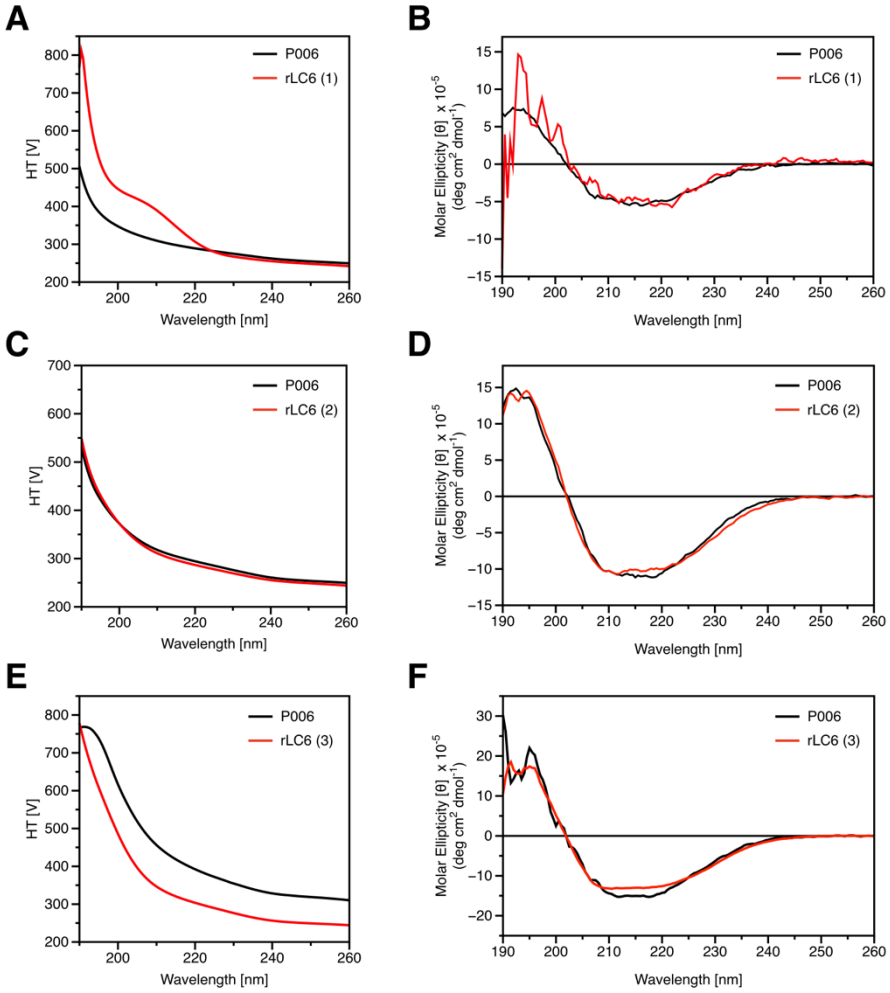

Figure 5.22: Protocol 4. CD spectroscopic analysis of rLC6. The refolding efficiency of rLC6 obtained using Protocol 4 was evaluated by CD spectroscopic analysis. CD spectra and corresponding HT voltage signals are shown. (**A**, **B**) First rLC6 preparation (red), recovered from the *E. coli* periplasm prior to implementation of the cold osmotic shock protocol, in comparison with the patient-derived sample P006. (**A**) HT voltage signals; (**B**) CD spectra. Due to the low yield, rLC6 (1) was analyzed at a concentration of approximately 2.5 µM. (**C-F**) Two independent rLC6 preparations obtained after implementing the cold osmotic shock step in Protocol 4, which enhanced purification efficiency and enabled higher sample concentrations. (**C, D**) CD analysis performed at 4 µM rLC6. (**E, F**) Final preparation measured at 8 µM. All measurements were performed in 10 mM Tris-HCl buffer (pH 7.4), with matched concentrations of the patient-derived reference sample P006, respectively. Measurements were baseline corrected and 15 accumulations per sample were recorded. CD spectra are shown as molar ellipticity, calculated from raw ellipticity (millidegrees), normalized to protein concentration and path length.

The figure displays the CD spectra (Fig. 5.22B, D, F) together with the corresponding HT voltage signals (Fig. 5.22A, C, E). In the first preparation (Fig. 5.22A, B), measured at a concentration of ~2.5 µM, the HT signal showed an unusual signal around 210 nm while reaching high voltage levels (~800 V around 190 nm), suggesting an unstable transmission. This artifact is most likely related to residual purification components (e.g., imidazole, EDTA) or other trace impurities. The CD spectrum displayed a comparatively low signal-to-noise ratio, which can be explained primarily by the low protein concentration but possibly also have been influenced by instrument re-adjustments performed between measurements. Nevertheless, the overall secondary structure trend was consistent with P006, which highlighted the potential of periplasmic expression. To improve purification and increase rLC6 yield, an additional osmotic shock step was subsequently included into Protocol 4. The second preparation of rLC6 (Fig. 5.22C, D), measured at a concentration of 4 µM, showed the closest overlap in HT signal with P006. The corresponding CD spectra also matched closely, suggesting a comparable overall secondary structure, which confirmed the results obtained at lower concentration.

Minor deviations were observed around 235 nm and 217 nm. As the signal region around 217 nm is a characteristic feature of the secondary structure of LCs, these differences may reflect slight concentration mismatches or subtle variations in local folding or structural dynamics. Despite these differences, the spectral profile of rLC6 remained highly consistent with P006, supporting the conclusion that Protocol 4 enabled the recovery of a largely native-like conformation. The third preparation (Fig. 5.22E, F) yielded sufficient material to perform CD analysis at 8 µM, matching the concentration used for rLCs produced with Protocol 1-3. Compared with concentration-matched sample P006, rLC6 showed a reduced HT signal, potentially reflecting improved optical conditions after instrument re-adjustments. The CD spectrum showed a modestly reduced signal intensity in the 210-220 nm range. Since this decrease appeared evenly distributed in the main signal are of ~210-220 nm, it is most likely attributable to a slight concentration mismatch rather than structural differences. Nonetheless, the overall spectral profile remained consistent with that of P006, reinforcing the findings of previous preparations and further supporting the successful recovery of a largely native-like conformation.

Taken together, the CD spectra of rLC6 at concentrations of ~2.5 µM (Fig. 5.22B), 4 µM (Fig. 5.22D) and 8 µM (Fig. 5.22E) closely resembled those of the patient-derived sample P006. This demonstrates that the periplasmic expression strategy of Protocol 4 effectively reproduced the secondary structure of the respective patient-derived sample. In contrast, rLC6 samples obtained using IB-based protocols consistently yielded random coil-dominated conformations that deviated significantly from P006. This suggests that only a fraction of the protein, if any, may have adopted a native-like fold, which motivated the Protein L binding experiments (Fig. 5.18). Protocol 4 provided the first clear evidence that rLC6 adopted a native-like secondary structure, highlighting the importance of the folding environment, chaperone assistance, and correct disulfide bond formation. Despite this structural consistency, Protocol 4's major limitation was its low yield, which prevented further biophysical characterization beyond CD spectroscopy.

5.5 Discussion

This chapter investigated different strategies for the recombinant expression and purification of patient-derived FLCs in the *E. coli* host system. The primary objective was to obtain rLCs in a native-like folding state comparable to their patient-derived counterparts. Establishing such a recombinant model system provides a homogeneous and reproducible source of FLCs suitable for detailed structural and biophysical analyses, which typically require high purity and concentration. *E. coli* was selected as a cost- and time-efficient platform suitable for testing different expression and refolding strategies. Several protocols for IB isolation and *in vitro* refolding, described in the literature (Buchner and Rudolph 1991; Rognoni et al. 2013; Poshusta et al. 2013), were adapted and evaluated, alongside a periplasmic secretion approach designed to allow *in vivo* folding under oxidizing conditions. Together, these complementary strategies enabled a comparative assessment of how the folding environment influences structural recovery, redox state, and conformational stability of rLCs.

5.5.1 Comparative analysis of rLC6 refolding pathways

Two mechanistically distinct expression routes were investigated. In cytoplasmic expression (Protocol 1-3), rLC6 accumulated in IBs and required solubilization under denaturing and reducing conditions, followed by *in vitro* refolding under defined redox conditions. In contrast, periplasmic expression (Protocol 4) directed rLC6 to the oxidizing periplasm via an N-terminal signal peptide, facilitating *in vivo* folding with assistance from the co-expressed chaperone Skp. Across the IB protocols, CD spectroscopy showed that rLC6 remained soluble but structurally non-native after refolding. Protocol 1 (adapted from Buchner and Rudolph 1991) produced a random-coil spectrum with a minimum near 200 nm (Fig. 5.8B), inconsistent with the β-sheet-rich profile typical of native LCs (Brahms et al. 1977; Bork et al. 1994; Poshusta et al. 2013; Andrich et al. 2017). Adjustments of solubilization and renaturation parameters, including the addition of L-arginine, did not improve folding efficiency, suggesting that redox balance was a dominant factor under the tested conditions rather than the specific procedural variations evaluated. Protocols 2 and 3 (adapted from Rognoni et al. 2013 and Poshusta et al. 2013) altered the refolding chemistry through different solubilization and redox-shuffle conditions. The resulting spectra shifted to ~205-208 nm (e.g., Fig. 5.13B, 5.16B), consistent with a partial recovery of secondary structure and intermediate-like conformations. In contrast, the periplasmic strategy (Protocol 4) produced CD spectra closely matching the patient-derived sample P006, indicating productive disulfide bond formation *in vivo* supported by Skp and the Dsb network (Schäfer et al. 1999; Berkmen 2012; Denoncin and Collet 2013). Although yields were low, these data indicate that native-like secondary structure was achieved under an oxidizing folding environment with chaperone support. The observed differences in refolding efficiency between FLC preparations likely arise from patient-specific sequence variations (Tab. 8.2) that modulate folding kinetics and the redox sensitivity of individual LCs (Welker et al. 2001; Poshusta et al. 2009). Establishing the IB workflow nevertheless provided a reproducible foundation for subsequent redox-folding experiments.

5.5.2 Redox-driven species distribution analyzed by SV-AUC

SV-AUC analysis provided quantitative insights into how the redox conditions applied during refolding influenced the molecular species distribution of rLC6. Clear differences in the relative abundance of monomeric, dimeric, and oligomeric species highlighted the sensitivity of cysteine reactivity and disulfide bond formation to small changes in redox balance. With Protocol 1, rLC6 sedimented predominantly as a monomer (2.21 S), accompanied by a minor fragmented species (0.74 S), in contrast to the patient-derived P006 monomer at 2.35 S (Fig. 5.9A). This difference in monomeric *s*-value, accompanied by noticeable peak broadening, reflects altered hydrodynamic properties and conformational heterogeneity, consistent with a less compact, destabilized structure as indicated by the random-coil CD spectrum. Short-term incubation with TCEP (1.25 h) was associated with rapid fragmentation of rLC6, whereas P006 remained largely intact under identical conditions (e.g., Fig. 5.10B). This difference is consistent with the absence of stabilizing intramolecular disulfide bonds and/or an increased susceptibility to reductant-associated cleavage near cysteine residues, as discussed previously (Liu et al. 2010). The lack of dimeric or higher-order species suggests that the GSH/GSSG-based refolding buffer shifted too far toward reduction. Under these conditions, free thiols, especially the reactive C-terminal Cys213, likely formed mixed disulfides with low molecular weight thiols, consistent with thiol capping that would prevent both intermolecular linkage and native intradomain pairing (Hochgräfe et al. 2007; Prade et al. 2021). Such capping would further hinder structural stabilization, yielding monomeric species resembling the partially reduced and destabilized monomers observed after short-term TCEP incubation in Chapter 3, which similarly displayed lower *s*-value, reduced β-sheet content, and an increased tendency toward fragmentation. Given that cysteinylation has been detected in patient-derived FLCs (Dupré et al. 2021), these findings provide a plausible *in vitro* analogue for redox-modified species that may also arise *in vivo* under oxidative stress (Lim et al. 2001; Migrino et al. 2010; Lu et al. 2017).

In Protocol 2, applying a more oxidizing redox environment during refolding produced the opposite outcome. SV-AUC revealed major peaks likely corresponding to disulfide-linked dimers (~3.17 S) and higher oligomers up to *s*-values of 30 S (Fig. 5.14B). Under these conditions, the C-terminal cysteine may have undergone premature oxidation, forming intermolecular disulfides before native intradomain pairing. The non-native spectral profile (Fig. 5.13B) is consistent with this interpretation, suggesting that native β-sheet structure was not restored and that mis-oxidized intramolecular disulfides may have contributed to structural heterogeneity and non-native assemblies. Protocol 3 yielded an improved but still non-native outcome, showing a more balanced monomer-dimer distribution and sharper sedimentation peaks, implying partial equilibration between oxidation and reduction (e.g., Fig. 5.17D, F). Nevertheless, all measured *s*-values remained below those of P006 (i.e., 2.35 S and 3.65 S for the native monomer and dimer), indicating that rLC6 retained a less compact conformation than the native FLC. This agrees with CD analysis (Fig. 5.16B) and is consistent with incomplete folding.

Taken together, these findings show that subtle deviations in the redox potential during refolding critically influence whether rLC6 adopts native-like or aberrant configurations. It remains uncertain whether non-covalent intermolecular interactions, such as electrostatic or hydrophobic contacts, contributed to the stabilization or association of these redox-defined species. As shown in Chapter 3, non-covalent dimerization can provide structural stabilization even in the absence of covalent

disulfide linkages. A disruption or imbalance of such interactions under overly reducing or overly oxidizing conditions may therefore further destabilize rLC6 and contribute to the structural heterogeneity observed across the refolding protocols. The absence of a native-like monomer-dimer distribution and the persistent redox-dependent heterogeneity of rLC6 further underscores the intrinsic sensitivity of LCs to cysteine chemistry. In contrast, periplasmic expression yielded soluble rLC6 with CD spectra closely matching P006, suggesting that the oxidizing periplasm provided the balanced redox milieu required for proper folding and disulfide bond formation. Here, Skp maintained folding intermediates in a soluble, competent state and prevented premature aggregation during oxidative folding (Schäfer et al. 1999). However, incomplete export of rLC6 to the periplasm (Fig. 5.21) and the limited oxidative folding capacity of *E. coli* (De Marco 2009; Schütz et al. 2023) likely resulted in low overall yield, restricting biophysical analysis to CD spectroscopy. Consequently, further characterization by SV-AUC could not be performed, leaving the precise molecular species distribution unresolved.

5.5.3 Redox-dependent folding imbalance and implications for FLC heterogeneity

The collective results emphasize that redox balance is a major determinant of structural outcome and species distribution in rLC6. The opposing outcomes of cytoplasmic and periplasmic expression highlight how the strongly reducing cytoplasm of *E. coli* is inherently unsuitable for correct disulfide bond formation, frequently resulting in IB accumulation of rLC6 (Bhatwa et al. 2021). In overly reducing environments, cysteine residues remain either reactive or become protected by the formation of mixed disulfides with small thiols, whereas excessive oxidation promotes uncontrolled intermolecular cross-linking and non-native disulfide pairing that drive aggregation (De Marco 2009; Hatahet and Ruddock 2009). Both extremes disturb the sensitive equilibrium required for efficient disulfide exchange and domain stabilization. These *in vitro* observations are consistent with aspects of the molecular heterogeneity observed in patient-derived FLCs, which typically contains mixtures of cysteinylated monomers and disulfide-linked dimers (Connors et al. 2007; Dupré et al. 2021). The refolding outcomes of rLC6 therefore provide a mechanistic model for how modest redox imbalances can generate structurally distinct, coexisting FLC populations *in vitro*, and potentially contribute to heterogeneity *in vivo*. Protocol 1 represents an over-reduced, monomeric state, while Protocol 2 reproduces an over-oxidized population characterized by excessive cross-linking. This redox-driven diversity may contribute to variable stability and aggregation behavior of monoclonal FLCs under pathological oxidative-stress conditions, particularly in tissues such as the kidney or heart during MM or AL amyloidosis (Kul and Ozturk Kurt 2024; Krata et al. 2018; Gyurászová et al. 2020).

Beyond being shaped by their redox environment, FLCs themselves can actively disrupt their local redox homeostasis (Shi et al. 2010; Basnayake et al. 2010; Migrino et al. 2010). Some monoclonal FLCs have been shown to generate ROS, particularly H_2O_2, through intrinsic physicochemical properties of their V_L domains (Wang and Sanders 2007; Migrino et al. 2010; Ying et al. 2019). In renal proximal-tubule cells, endocytosed FLCs activate the redox-sensitive JAK2/STAT1 pathway, inducing the expression of proinflammatory cytokines such as interleukin-1 beta (IL-1β) and profibrotic mediators including transforming growth factor-beta (TGF-β), which promotes inflammation and fibrosis

(Basnayake et al. 2010; Ying et al. 2019). In microvascular and cardiac models, amyloidogenic FLCs cause mitochondrial dysfunction, apoptosis, and enhanced superoxide ($O_2^{\bullet-}$) generation, which impair vascular relaxation and cellular integrity (Shi et al. 2010; Migrino et al. 2010; Ying et al. 2012). Clinically, patients with AL amyloidosis show increased systemic protein carbonylation (Migrino et al. 2010), which is an established marker for oxidative stress and underscores the link between circulating FLCs and systemic redox imbalance. Together, these findings support a self-perpetuating feedback loop in which FLCs both respond to and amplify oxidative stress, reinforcing tissue injury and potentially favouring pathogenic self-association pathways.

By contrast, periplasmic expression in *E. coli* provided an oxidizing folding environment sustained by the Dsb oxidoreductase network, in which the DsbA/DsbB pathway catalyzes disulfide bond formation and the DsbC/DsbD system mediates their reduction and isomerization (Denoncin and Collet 2013; Ke and Berkmen 2014). Alongside periplasmic chaperones such as Skp, which stabilize folding intermediates and prevent aggregation (Schäfer et al. 1999), these factors collectively recreate an oxidative folding pathway analogous to the eukaryotic PDI system (Tu and Weissman 2004). This environment enabled native disulfide assembly and secondary-structure formation of rLC6; however, further biophysical characterization was hindered by the low overall yield. Most of rLC6 still accumulated as IBs (Fig. 5.21), either in the cytoplasm, reflecting incomplete translocation to the periplasm, or within the periplasm itself, likely due to overloading of the folding machinery. Another possibility is the misdirected extracellular secretion of rLC6 into the culture medium (Walker and Gilbert 1994; Karyolaimos and De Gier 2021), which was not systematically analyzed and requires further investigations. Overall, these results indicate that the folding environment is a major determinant of both structural integrity and biochemical heterogeneity of rLCs. The parallels between bacterial redox-dependent folding behavior and oxidative modifications observed *in vivo* provide a mechanistic link between recombinant and patient-derived FLCs, suggesting that the redox imbalance in *E. coli* may, on a smaller scale, recapitulate aspects of oxidative processes that shape FLC variability in MM and AL amyloidosis.

5.5.4 Limitations and outlook

While periplasmic expression successfully produced rLC6 in a native-like conformation, the main limitation of Protocol 4 was the low protein yield, which restricted biophysical analysis to CD spectroscopy. Several factors potentially contribute to this low recovery: (i) the limited oxidative folding capacity of *E. coli* (Ke and Berkmen 2014; Rettenbacher and Von Der Haar 2022), (ii) incomplete export of rLC6 to the periplasm (Mergulhão et al. 2005; Hsu et al. 2016), (iii) periplasmic IB formation caused by overloading of the folding machinery (Baneyx and Mujacic 2004; Bhatwa et al. 2021), (iv) possible misdirection of rLC6 into the extracellular medium (Walker and Gilbert 1994; Karyolaimos and De Gier 2021), and (v) proteolytic degradation within the periplasm (Baneyx and Mujacic 2004; Mergulhão et al. 2005). Since FLCs are known to induce oxidative stress (Wang and Sanders 2007; Shi et al. 2010; Basnayake et al. 2010; Migrino et al. 2010; Ying et al. 2012, 2019), it remains unclear whether intracellular expression, degradation, or accumulation of FLCs affects the vitality or protein folding capacity of the bacterial host. It is plausible that FLC variants with higher

redox activity or aggregation propensity impose elevated stress levels on the cellular redox environment of the host system, thereby potentially limiting recombinant yield. As a result, recombinant models described in the literature may disproportionately represent FLCs with moderate reactivity or lower pathogenic potential, while highly redox-active species could be underrepresented due to unsuccessful expression. Moreover, information regarding FLC expression or refolding attempts that fail to yield the native conformation is rarely published (Atroshenko et al. 2024), which potentially obscure the actual frequency and underlying cause of such complications and thereby hindering efforts to correlate these outcomes with intrinsic physicochemical properties of FLCs. Further studies are therefore needed to determine whether the intrinsic redox activity of FLCs influences host metabolism, oxidative balance, or folding capability during recombinant production. In addition, the periplasmic space provides only a narrow and highly crowded environment, which can further hinder efficient folding and promote aggregation (Castillo-Corujo et al. 2024).

Future optimization should aim to enhance periplasmic folding efficiency and protein recovery. While attempts were made to slow the expression rate by reducing inducer concentration and cooling the cells on ice for different periods prior to induction, the extracellular secretion of rLC6 into the medium was not investigated. Additional strategies may include co-expression of extra disulfide isomerases, modulation of general periplasmic chaperone levels, or the use of alternative leader sequences to improve translocation efficiency (Bessette et al. 1999; Zhang et al. 2002; Berkmen 2012; De Marco 2009). Engineered *E. coli* strains offer an alternative approach to overcome the limitations of wild-type expression platforms by enabling oxidative folding directly within the cytoplasm (Bessette et al. 1999; Ponniah et al. 2010; Lobstein et al. 2012). Strains such as Origami (Novagen) feature mutations in *trxB* and *gor* genes, which disrupt the thioredoxin and glutathione reductase pathways responsible for keeping cysteines in a reduced state (Ponniah et al. 2010). More advanced systems, such as SHuffle, combine these mutations with cytoplasmic expression of DsbC, thereby providing both oxidative folding capacity and disulfide isomerase activity essential for native-like disulfide pairing (Lobstein et al. 2012). However, initial attempts to express rLC6 using the SHuffle strain resulted in IB formation at levels comparable to those observed during periplasmic expression (data not shown; available upon request). Further, the potential influence of the C-terminal 6xHis tag on covalent dimer formation remains uncertain, and relocation of the tag to the N-terminus could facilitate native dimer association and improve folding yield.

Despite these limitations, the *E. coli* expression studies provided valuable mechanistic insight into how redox potential influences FLC folding pathways and species heterogeneity. These findings established the experimental and conceptual foundation for Chapter 6, which investigates the recombinant FLC production in *Pichia pastoris*. As a eukaryotic host, *Pichia pastoris* offers an oxidizing ER and an efficient secretory pathway that support native disulfide bond formation, as well as other PTMs (if present in the FLC sample of interest), and higher overall yields than bacterial systems. Comparative analysis of rLC6 expressed in *E. coli* and *Pichia pastoris* will therefore help to further clarify how host-specific redox environments and folding machineries influence the expression and stability of challenging FLC variants, and how these parameters relate to self-association behavior, redox imbalance, and the formation of potentially nephrotoxic intermediates relevant to FLC-associated organ involvement during disease progression.

6

Recombinant expression and structural validation of a pathogenic patient-derived free light chain in *Pichia pastoris*

This chapter contains a research article that is currently under peer review. The original structure of the manuscript has been preserved to maintain its integrity and to ensure readability. Any overlap with other chapters is limited to essential background information.

6.1 Article information

Title: Recombinant expression and structural validation of a pathogenic patient-derived free light chain in *Pichia pastoris*
Journal: Protein Science
Status: Received: 08.02.2026 / Under Revision (as of 15.03.2026)

Authors: Florian T. Tucholski[†1], Shuang-Yan Wang[†2], Katharina Vormann[1,3], Andrea Janosch[1], Nils-Alexander Lakomek[1,3], Luitgard Nagel[1,3], Dieter Willbold[1,3], Rainer Haas[4], Alexander K. Buell[2*]
[†]Equal contributions, joint first authors; *Corresponding author

Affiliation: [1]Institut für Physikalische Biologie, Heinrich Heine University Düsseldorf, Germany
[2]Department of Biotechnology and Biomedicine, Technical University of Denmark, Søltofts Plads, Building 227, Kgs. Lyngby, Denmark
[3]Institute of Biological Information Processing (IBI-7: Structural Biochemistry), Research Center Jülich, Jülich, Germany
[4]Department of Hematology, Oncology and Clinical Oncology, Heinrich Heine University Düsseldorf, Germany

6.2 Declaration of contributions

A.K.B., R.H. L.N., D.W., N.-A.L.: Conceptualization; F.T.T., S.-Y.W., K.V.: Methodology, Investigation, Formal analysis; F.T.T., S.-Y.W., K.V., A.J.: Validation; F.T.T.: Visualization; A.K.B., R.H., D.W., L.N., N-A.L.: Supervision, Resources, Project administration; F.T.T., S.-Y.W., A.K.B.: Writing original draft; All authors: Writing, review, and editing; All authors read and approved the final manuscript.

6.3 Abstract

Immunoglobulin free light chains (FLCs) are unbound antibody components associated with disorders such as multiple myeloma and light chain amyloidosis, where they can contribute to progressive organ damage. Due to their unpredictable aggregation behavior, detailed biophysical and biochemical *in vitro* characterization of patient-derived FLCs, typically isolated from serum or urine, remains essential for understanding their pathogenicity. In addition, the recombinant expression of full-length FLCs and individual domains offer a valuable model system for investigating structural and functional properties under defined conditions. Compared to bacterial expression systems that often require refolding, the eukaryotic host *Pichia pastoris* provides distinct advantages for secretory expression and native-like disulfide formation. Leveraging this capability, we successfully expressed a full-length, patient-derived FLC in *Pichia pastoris*. The recombinant protein adopted a native-like secondary structure and exhibited biophysical properties closely resembling its urinary counterpart. Post-translational modification analysis confirmed the absence of detectable phosphorylation or glycosylation, supporting its fidelity as a clinically relevant model. Sedimentation velocity analysis confirmed identical monomeric species but revealed differences in higher-order oligomers, suggesting altered covalent and non-covalent interactions. Differential scanning fluorimetry detected variations in thermal stability upon disulfide bond reduction, further supporting these conclusions. Together, these findings establish *Pichia pastoris* as a reliable and valuable system for producing patient-derived FLCs, offering a clinically relevant platform for mechanistic investigations on how structural features and molecular interactions drive FLC stability and pathological aggregation.

Keywords: Multiple myeloma, Patient-derived immunoglobulin free light chain, Antibodies, *Pichia pastoris*, *Komagataella phaffii*, Recombinant protein expression, Protein purification, Oligomerization

6.4 Introduction

FLCs are antibody components unbound to their HC counterparts, and their overproduction by plasma cells in the bone marrow is a hallmark of various pathological conditions, including MM and AL amyloidosis (Merlini et al. 2018; Malard et al. 2024). Due to their derivation from a single neoplastic plasma cell, the resulting cell clones continuously produce large quantities of monoclonal FLCs with unique, patient-specific amino acid sequences (Morgan et al. 2019). When FLC production exceeds the kidneys' reabsorption capacity, elevated circulating FLC levels can promote aggregation, ultimately leading to organ damage, with the heart and kidneys being most commonly affected (Falk et al. 2016). Due to their structural heterogeneity and high aggregation propensity, FLCs pose significant diagnostic challenges, and the mechanisms underlying FLC aggregation remain an active area of research, both in the context of LCs and amyloidogenic proteins more broadly (Willbold et al. 2021).

In addition to studying FLCs directly isolated from patient samples, the recombinant expression of full-length FLCs and their individual domains, such as the V_L or C_L regions, has become an essential strategy for investigating their structural and pathological properties (Khurana et al. 2001; Blancas-Mejia et al. 2009; Martin and Ramirez-Alvarado 2010; Rognoni et al. 2013; Misra et al. 2019; Sakai et al. 2023). By developing recombinant model systems, researchers can increase the availability of well-characterized patient-derived samples, while enabling precise manipulation of structural properties, such as the role of disulfide bonds in monomer stability or their influence on oligomerization. Importantly, these recombinant systems not only provide access to highly patient-specific material but also support mechanistic studies crucial for understanding disease-related aggregation and FLC pathology. To achieve this, FLCs have been expressed in various host systems, with *Escherichia coli* (*E. coli*) being the most widely used. A key advantage of *E. coli* is its accessibility, enabling in some cases the efficient production of large quantities of FLCs with high purity in a time- and cost-efficient manner.

A major challenge, however, lies in the correct formation of both secondary and tertiary structures, the latter being stabilized by intra- and intermolecular disulfide bonds, during the refolding of recombinant FLCs. To circumvent this, researchers often focus on expressing and analyzing only fragments of the full-length FLC (V_L or C_L regions), as these are more amenable to proper refolding. The expression of FLCs in *E. coli* is frequently associated with the formation of IBs, which result from the aggregation of misfolded or partially folded proteins (Palmer and Wingfield 2012). This occurs due to the reducing conditions of the cytoplasm and the absence of significant levels of PTMs, both of which prevent the proper formation of intra- and intermolecular disulfide bonds that are crucial for stabilizing the FLC structure (Singh et al. 2015). A potential key advantage of IBs is that they enable efficient purification of the expressed protein to a high level of purity without requiring additional affinity tags for downstream processing. Nevertheless, protein recovery through solubilization and subsequent refolding into the native structure remains challenging, particularly for proteins with complex disulfide bonding patterns. Although oxido-shuffling systems can facilitate this process (Wang et al. 2006), complete recovery of the native protein is often not achieved. Consequently, recombinant FLCs may exhibit structural deviations from patient-derived samples, potentially affecting their biophysical and biochemical properties. An alternative approach is to direct protein

expression to the *E. coli* periplasm, where the oxidizing environment due to the presence of different oxidoreductases promotes the formation and isomerization of disulfide bonds (Berkmen 2012; Denoncin and Collet 2013). However, this method typically results in lower yields, as a significant portion of the expression product often remains in the cytoplasm (Schütz et al. 2023). Therefore, periplasmatic expression requires extensive optimization and fine-tuning depending on the protein of interest.

Human embryonic kidney cells (HEK293) provide human-like PTMs and are widely used for producing monoclonal antibodies (Chin et al. 2019). However, expression is usually limited to small-scale assays, as yields are low, production costs are high, and transient transfection requires large amounts of plasmid DNA (Tan et al. 2021; Veber et al. 2025). Although well established for biotherapeutics, successful expression of full-length, patient-derived, and aggregation-prone FLCs is limited, and the system is not routinely used for this purpose. Compared to *E. coli*, the eukaryotic expression system *Pichia pastoris* (*P. pastoris*), also known as *Komagataella phaffii*, offers several advantages. As a methylotrophic yeast, *P. pastoris* efficiently metabolizes methanol as a carbon source, enabling exceptionally high cell densities while supporting high-yield heterologous protein expression. This is primarily driven by the tightly regulated alcohol oxidase 1 (AOX1) promoter, which ensures strong transcriptional control in response to methanol availability (Daly and Hearn 2005; Ahmad et al. 2014). As a eukaryotic system, *P. pastoris* is also capable of performing PTMs, making it an ideal host for the production of proteins with complex disulfide bonding patterns in a correctly folded, soluble, and functional form (Daly and Hearn 2005). Furthermore, secretion signal sequences, such as the prepro-alpha mating factor (α-MF), direct the expressed protein into the culture medium, facilitating proper folding, promoting disulfide bond formation, and simplifying downstream purification (Zou et al. 2022). These features provide distinct advantages over bacterial systems and eliminate the need for complex refolding strategies. In this study, we produced a recombinant FLC based on sample P004, originally purified from the urine of a patient with MM. This sample is part of a set of FLCs that have undergone extensive characterization in prior studies by our laboratories (Sternke-Hoffmann et al. 2020; Dupré et al. 2021; Sternke-Hoffmann et al. 2023; Tucholski et al. 2025). Following expression and purification of the recombinant light chain P004 (rLC4), we conducted a series of experiments to assess whether rLC4 adopted the correct secondary structure and exhibited biophysical and biochemical properties comparable to the patient-derived sample. By demonstrating that *P. pastoris* enables the recombinant production of clinically relevant, patient-derived FLCs in their native conformation, this work provides a technical advance and a foundation for future mechanistic studies of pathogenic FLC aggregation.

6.5 Methods

6.5.1 Expression strategy for patient-derived FLCs

The κ-FLC P004, previously purified from the urine of a multiple myeloma patient, was part of an extensive characterization by MS (Dupré et al. 2021), and biochemical and biophysical analyses (Sternke-Hoffmann et al. 2020, 2023). The study was approved by the institutional ethics committee, and written informed consent was obtained from all patients whose samples were used. The study was conducted in accordance with the Declaration of Helsinki and is registered under study number 5926R (registration ID 20170664320). Based on these findings, P004 was selected for recombinant expression in *P. pastoris*. Its 698 bp nucleotide sequence was codon-optimized to enhance expression efficiency in the *P. pastoris* host system. Recombinant expression in *P. pastoris* was carried out using the pPICZα expression vector with A-version reading frame. The vector features an AOX1 promoter, enabling methanol-inducible expression of the gene of interest. An N-terminal α-MF secretion signal facilitates the secretion of the expression products into the surrounding medium, eliminating the need for additional cell lysis steps during purification. To further simplify the downstream purification process, a C-terminal 6xHis tag was incorporated into the construct, enabling efficient purification via IMAC. Notably, aside from the 6xHis tag, the fusion construct was designed to exclude extraneous amino acids, ensuring that no additional residues remain at the N- or C-terminus of the mature protein following cleavage of the α-MF secretion signal (Tab. 8.10). Gene synthesis including codon optimization was carried out by BioCat GmbH (Heidelberg, Germany).

6.5.2 Vector amplification in *E. coli*

For vector amplification, the pPICZαA vector containing the κ-FLC P004 gene insert was transformed into *E. coli* DH5α competent cells (#18265017, Thermo Fisher Scientific, Waltham, MA, USA). Briefly, 500 ng of the vector was gently mixed with DH5α cells to a total volume of 50 µL, followed by a 30-min incubation on ice. Heat shock was applied at 42°C for 45 s, after which the cells were cooled on ice for 2 min. Subsequently, 200 µL of pre-warmed super optimal broth with catabolic repression (SOC) medium (2% (w/v) tryptone, 0.5% (w/v) yeast extract, 10 mM NaCl, 2.5 mM KCl, 10 mM $MgCl_2$, 10 mM $MgSO_4$, 20 mM glucose) was added. The cells were incubated for 1 h at 37°C with shaking at 600 rpm. After incubation, either 50 µL or 150 µL of the transformed cells were plated onto low-salt LB agar plates (1% (w/v) tryptone, 0.5% (w/v) yeast extract, 0.5% (w/v) NaCl, 1.5% (w/v) agar) containing 50 µg/mL Gibco Zeocin Selection Antibiotic (#R25001, Thermo Fisher Scientific, Waltham, MA, USA). On the following day, isolated single colonies were selected and inoculated into 5 mL low-salt LB medium supplemented with 50 µg/mL Zeocin (1:2,000 dilution). The cultures were incubated at 37°C with agitation at 250 rpm overnight. Subsequently, 2 mL of the overnight culture were transferred to 100 mL of fresh low-salt LB medium containing Zeocin and incubated at 30°C with agitation at 160 rpm. The next day, cells were harvested by centrifugation at 4,600 × *g* for 20 min at 4°C. Plasmid DNA was then isolated from the cells using the GeneJET Plasmid Miniprep Kit (#K0502; Thermo Fisher Scientific, Waltham, MA, USA), following the manufacturer's protocol. The

concentration of the purified vector totaled 120.7 ng/μL with an A_{260}/A_{280} ratio of ~1.8, indicating high-purity DNA.

6.5.3 Vector linearization and transformation into *P. pastoris*

For transformation into *P. pastoris*, the vector was linearized using the Mssl (Pmel) restriction enzyme (#ER1341; Thermo Fisher Scientific, Waltham, MA, USA), which cleaves the vector at the GTTT^AAAC recognition site. Efficiency of linearization was confirmed by agarose gel electrophoresis using a gel with an agarose concentration of 1.5% (w/v). A GeneRuler 1 kb DNA Ladder (#SM0313; Thermo Fisher Scientific, Waltham, MA, USA), spanning 250 bp to 10,000 bp, was used as a molecular weight standard. To further concentrate the linearized vector, ethanol precipitation was performed. Sodium acetate (3 M, pH 5.2) was added to achieve a final concentration of 0.3 M, followed by the addition of three volumes of ice-cold 100% ethanol. Precipitation was carried out overnight at −20°C to maximize recovery. After centrifugation at 13,000 rpm for 30 min at 4°C, the precipitate was washed twice with 0.5 mL of ice-cold 75% (v/v) ethanol, air dried, and resuspended in 100 μL of competent *P. pastoris* X-33 cells (#C18000; Thermo Fisher Scientific, Waltham, MA, USA). The linearized vector was transformed using the *Pichia* EasyComp Transformation Kit (#K173001; Thermo Fisher Scientific, Waltham, MA, USA), and transformation was carried out according to the manufacturer's protocol. Following transformation, *P. pastoris* X-33 cells containing the expression vector were plated onto yeast extract peptone dextrose sorbitol (YPDS) agar plates (1% (w/v) yeast extract, 2% (w/v) peptone, 2% (w/v) D-glucose, 1 M sorbitol, 2% (w/v) agar) containing 100 μg/mL Zeocin, according to the protocol of the *Pichia* EasyComp Transformation Kit (#K173001; Thermo Fisher Scientific, Waltham, MA, USA). The plates were incubated at 30°C for 72 h, allowing colonies to grow to a sufficient size for selection (Fig. 8.13).

6.5.4 Colony selection and expression of rLC4

Following a three-day incubation period, nine isolated single colonies were selected for test expression. Each colony was individually inoculated into 5 mL of yeast extract peptone dextrose (YPD) medium supplemented with 100 μg/mL Zeocin and incubated for 16 h at 30°C with 160 rpm agitation. The following day, the overnight cultures were transferred to buffered glycerol-complex medium (BMGY; 1% (w/v) yeast extract, 2% (w/v) peptone, 100 mM potassium phosphate (pH 6.0), 1.34% (w/v) yeast nitrogen base (YNB), 4×10^{-5}% (w/v) biotin and 1% (v/v) glycerol) and incubated at 30°C with agitation at 160 rpm. Cell growth was monitored via optical density (OD_{600}) measurements, and cells were harvested by centrifugation (3,000 × *g* for 5 min at room temperature). BMGY medium was replaced with buffered methanol-complex medium (BMMY; 1% (w/v) yeast extract, 2% (w/v) peptone, 100 mM potassium phosphate (pH 6.0), 1.34% (w/v) YNB, 4×10^{-5}% (w/v) biotin and 0.5% (v/v) methanol), inducing protein expression at 26°C with shaking at 160 rpm. To maintain expression, 0.5% (v/v) methanol was added daily over a period of three days. Following expression, cells were removed by centrifugation at 3,000 × *g* for 10 min at room temperature. The supernatant was

supplemented with stock solutions of Tris-HCl (1.0 M, pH 8.0), NaCl (5.0 M), and imidazole (5.0 M) to final concentrations of 30 mM, 300 mM, and 20 mM, respectively. The mixture was then filtered through a Nalgene Rapid-Flow Sterile Disposable Filter Unit with 0.45 µm pore size (#567-0020; Thermo Fisher Scientific, Waltham, MA, USA) and incubated with Ni-IMAC MagBeads (#A50589, Thermo Fisher Scientific, Waltham, MA, USA) pre-equilibrated in Tris-buffered saline (TBS) buffer containing 30 mM Tris-HCl (pH 8.0), 300 mM NaCl, and 20 mM imidazole. Incubation was performed at room temperature with shaking at 160 rpm for 1 h. The beads were then washed twice with equilibration buffer, and bound protein was eluted using TBS buffer containing 30 mM Tris-HCl (pH 8.0), 300 mM NaCl, and 500 mM imidazole. Subsequently, all nine test expressions were analyzed for the presence of rLC4 by Tris-Glycine SDS-PAGE. The analysis was performed using Mini-PROTEAN TGX Precast Gels, with samples prepared in premixed 4× Laemmli protein sample buffer (#456-1093, #1610747; Bio-Rad Laboratories, Hercules, CA, USA) and 10× Bolt Sample Reducing Agent (#B0009, Thermo Fisher Scientific, Waltham, MA, USA). A Prestained Protein Marker, ranging from 10-180 kDa (#PL00001; Proteintech, Rosemont, IL, USA) was used as a molecular weight standard. For large-scale expression, the cryo-stock derived from the test expression of single colony #3 – identified as the highest yield clone – was used. The same protocol was followed, beginning with initial cell growth in YPD, followed by transition to BMGY at 30°C with agitation at 160 rpm. After further overnight growth in BMGY, the medium was replaced with BMMY to initiate protein expression at 26°C, with daily supplementation of 0.5% (v/v) methanol for three days. Additionally, 50 mL of fresh BMMY medium was added to each flask after two days. A total culture volume of 6 × 500 mL was prepared for large-scale expression.

6.5.5 Purification of rLC4

Purification was initiated by separation of the cells from the culture medium containing the expression product via centrifugation at 3,000 × *g* for 20 min at room temperature. To optimize the binding conditions for affinity purification utilizing the 6xHis tag, Tris-HCl, NaCl and imidazole were added to the culture medium to achieve a final concentration of 30 mM Tris-HCl (pH 7.4), 300 mM NaCl, and 20 mM imidazole, followed by another centrifugation step at 17,000 × *g* for 30 min at room temperature. Buffered medium was then filtered with Nalgene Rapid-Flow Sterile Disposable Filter Unit with 0.45 µm pore size (#567-0020; Thermo Fisher Scientific). Affinity purification was performed using either Pierce High Capacity Ni-IMAC MagBeads, EDTA compatible (#A50589; Thermo Fisher Scientific, Waltham, MA, USA), or HisPur Ni-NTA Resin (#88221; Thermo Fisher Scientific, Waltham, MA, USA) loaded onto a chromatography column compatible with peristaltic pump system. After binding of the target protein via the 6xHis tag, three washing steps were performed using TBS buffer containing 30 mM Tris-HCl (pH 7.4), 300 mM NaCl, and 20 mM imidazole to reduce non-specific binding to the column material. To elute the immobilized expression products, imidazole was increased to a concentration of 500 mM. Following IMAC, the collected flow-through, wash fraction and eluate were analyzed for the presence of rLC4 using SDS-PAGE, employing the same gel system, sample preparation and molecular weight marker as described above. To remove imidazole and concentrate rLC4, the eluate was subjected to buffer exchange using Amicon Ultra-15 centrifugal filter

units with PLGC Ultracel-PL membrane and a nominal molecular weight limit (NMWL) of 10 kDa (#UFC901024; MilliporeSigma, Burlington, MA, USA). The initial protein concentration of the eluate was determined using a NanoDrop Microvolume Spectro-photometer. The recombinant protein was concentrated in different batches to approximately 4.0 mg/mL and 5.7 mg/mL before undergoing final purification via SEC. An Äkta pure protein purification system (GE Healthcare, IL, USA) equipped with Unicorn software version 6.3 was used for SEC. Separation was performed using a Superdex 75 10/300 GL Tricorn column (GE Healthcare, IL, USA), suitable for resolving molecules ranging from 3 to 70 kDa. Following fraction collection, samples were analyzed by SDS-PAGE using self-cast Tris-Glycine or Tris-Tricine SDS-PAGE gels together with either a PageRuler Prestained Protein Ladder (10 to 180 kDa; #26616, Thermo Fisher Scientific, Waltham, MA, USA) or a Spectra Multicolor Low Range Protein Ladder (#26628; Thermo Fisher Scientific, Waltham, MA, USA) to assess purity. Fractions with similar molecular composition (fractions 19–25 and 26–30) were combined, reconcentrated using Amicon Ultra-15 centrifugal filter units, aliquoted and stored at −80°C until further use.

6.5.6 Immunodetection via Western blot

Following purification, immunological verification via Western blot analysis with an anti-6xHis tag antibody was performed to confirm the presence of rLC4. Aliquots of the pooled SEC fractions (19–25 and 26–30) were diluted in 30 mM Tris-HCl, pH 7.4, to a concentration of 35 µM (monomer equivalents). Protein concentration was calculated from the molar extinction coefficient of the full-length, 6xHis-tagged LC, obtained with ExPASy ProtParam (Gasteiger et al. 2005); the same calculation provided the theoretical molecular weight used for reference. Either self-cast Tris-Glycine or Tris-Tricine SDS-PAGE gels were used, employing the same protein ladders as previously described. A reducing sample buffer (Laemmli 1970) or a non-reducing sample buffer – to preserve intermolecular disulfide bonds – was added at a 1× working concentration, and samples were heated at 95°C for 5 min before loading a volume of 10 µL onto the gels. After electrophoretic separation, electrotransfer was performed using a Trans-Blot Turbo Transfer System (Bio-Rad Laboratories, Hercules, CA, USA). A standard Western blot sandwich was assembled with three sheets of Whatman cellulose blotting paper (pre-soaked in 1× Towbin buffer), a 0.2 µm Immun-Blot polyvinylidene fluoride (PVDF) membrane (activated in 100% ethanol), the SDS gel, and a final layer of three sheets of Whatman paper. Electrotransfer from SDS gel to membrane was carried out at 25 V and 1.0 A for a duration of 30 min. The transfer efficiency was verified using Ponceau S staining solution (#A40000279; Thermo Fisher Scientific, Waltham, MA, USA). After washing with distilled water, the membrane was blocked for 1 hour at room temperature with gentle agitation on a tube roller using 5 mL of 5% (v/v) skimmed milk in 1× Tris-buffered saline with Tween 20 (TBST; 20 mM Tris(hydroxymethyl)-aminomethane, 150 mM NaCl, 0.1% (v/v) Tween 20) to prevent non-specific antibody binding. The blocked membrane was incubated overnight at 4°C with gentle agitation on a tube roller with a mouse monoclonal anti-6xHis epitope tag antibody (HIS.H8; #MA1-21315, Thermo Fisher Scientific, Waltham, MA, USA), at a 1:1,000 dilution in 5 mL of 1× TBST buffer containing 5% (v/v) skimmed milk. The next day, the membrane was washed three times for 10 min with 1× TBST

buffer before incubation with an HRP-conjugated goat anti-mouse IgG (H+L) secondary antibody (#31430; Thermo Fisher Scientific, Waltham, MA, USA), diluted 1:10,000 in 5 mL of 1× TBST buffer containing 5% (v/v) skimmed milk for 1 hour at room temperature. After washing multiple times with 1× TBST buffer, the membrane was treated with SuperSignal West Pico PLUS chemiluminescent HRP substrate (#34577; Thermo Fisher Scientific, Waltham, MA, USA) according to the manufacturer's protocol for enhanced signal detection. Imaging was performed using a Universal Hood III ChemiDoc MP Imaging System (Bio-Rad Laboratories, Hercules, CA, USA) with Image Lab version 5.1 software.

6.5.7 PTM analysis

To evaluate whether the *P. pastoris* expression system introduces host-specific PTMs, both rLC4 and P004 were examined for phosphorylation and glycosylation. Phosphorylation screening was carried out via Western blot, following the previously described protocol with the exception that 3% (w/v) bovine serum albumin (BSA) was used for membrane blocking and antibody incubation instead of 5% (v/v) skimmed milk. As milk contains the phosphoprotein casein, BSA was used in 1× TBST buffer as a blocking solution to prevent cross-reaction with the phospho-specific antibody (Yang and Mahmood 2012). SDS-PAGE analysis was performed with both LC samples alongside a phosphoprotein standard bearing a well-defined phosphorylation pattern, serving as a positive control. To increase detection sensitivity, the highest possible protein concentrations were loaded. After electrotransfer, the corresponding SDS gel was stained with a Coomassie-based solution to visualize total protein content for direct comparison with the Western blot results. Detection was performed using a rabbit phospho-Serine/Threonine/Tyrosine-specific primary antibody (#61-8300; Thermo Fisher Scientific, Waltham, MA, USA) diluted 1:250 in 5 mL of 1× TBST buffer containing 3% (w/v) BSA resulting in a final concentration of 1 µg/mL, followed by incubation with a goat anti-rabbit IgG (H+L) HRP-conjugated secondary antibody (#31460; Thermo Fisher Scientific, Waltham, MA, USA) diluted 1:1,000 to a final concentration of 0.8 µg/mL in the same buffer. In addition to phosphorylation, both samples were analyzed for glycosylation patterns using the Protein Deglycosylation Mix II Kit (#P6044S; New England Biolabs, Ipswich, MA, USA), which enzymatically removes *N*- and *O*-linked glycans without causing protein degradation. The enzyme pre-mix includes PNGase F, *O*-Glycosidase, α2-3,6,8,9 Neuraminidase A, β1-4 Galactosidase S and β-N-acetylhexosaminidase$_f$. The deglycosylation reaction was performed under denaturing conditions for optimal enzymatic glycan removal following manufacturer's protocol. Briefly, up to 100 µg of protein was diluted with dH_2O to a total volume of 40 µL. After adding 5 µL of Deglycosylation Mix Buffer 2, the samples were reduced at 75°C for 10 min. After cooling down at room temperature, 5 µL of the enzyme mix (Protein Deglycosylation Mix II) was added and the samples were incubated for 25 min at room temperature, followed by a final incubation step at 37°C for 1 h. The glycoprotein fetuin from bovine serum, which contains sialylated *N*- and *O*-linked glycans, was included as a positive control. Upon completion of the reaction, deglycosylation products were analyzed via SDS-PAGE as previously described.

6.5.8 Circular dichroism spectroscopy

The secondary structure of rLC4 was analyzed using CD spectroscopy. To assess structural similarities and folding state, the results were compared with CD spectra of patient-derived FLC P004. Far-UV CD spectra were recorded over a wavelength range of 190 nm to 260 nm at room temperature using a J-810 spectropolarimeter (Jasco, Hachioji, Tokyo, Japan) equipped with the associated Spectra Manager software (version 2.15.01). All samples were diluted to a concentration of 12 µM in 10 mM Tris-HCl buffer (pH 7.4). The measurements were performed in quartz glass cuvettes with a 1 mm optical path length, employing a scanning speed of 50 nm/min, a bandwidth of 1 nm, a digital integration time of 2 s and a resolution of 0.5 nm. Baseline correction was performed by automatically subtracting the buffer spectrum, with a total of 15 accumulations recorded per sample. CD data were recorded as raw ellipticity values in millidegrees and converted to molar ellipticity by normalizing for sample concentration and path length. The secondary structures of rLC4 and P004 were further analyzed using the BeStSel algorithm (Micsonai et al. 2022). Graphical visualization was prepared using DataGraph version5.3β, copyright 2020 (Visual Data Tools, NC, USA).

6.5.9 Analytical ultracentrifugation

The distribution of molecular species, including monomeric and oligomeric forms, of rLC4 was analyzed by AUC to allow comparison with the patient-derived sample P004, as characterized in previous studies (Sternke-Hoffmann et al. 2020, 2023; Dupré et al. 2021; Tucholski et al. 2025). SV experiments were performed using a Beckman Optima XL-A ultracentrifuge (Beckman Coulter, Brea, CA, USA) equipped with UV/Vis absorbance optics. An An-60Ti 4-hole rotor (Beckman Coulter, Brea, CA, USA) was used, along with standard double-sector measuring cells featuring quartz glass windows and aluminum centerpieces with a 12 mm optical path length. All experiments were conducted using a sample concentration of 35 µM in 30 mM Tris-HCl (pH 7.4). Measurements with varying salt concentrations between 0.1 and 1 M showed no significant effect on the *s*-value (Tucholski et al. 2025), indicating that charge-charge interactions did not influence the data. For all SV experiments, the measuring cells were loaded with a reference volume of 400 µL and a sample volume of 390 µL. Sedimentation was carried out at a speed of 60,000 rpm and a temperature of 20°C in continuous mode, with a radial resolution of 0.003 cm, until all sample components were fully sedimented. The recorded sedimentation data were analyzed using the $c(s)$ model implemented in the software SEDFIT version 16.1c (Schuck 2000; Schuck et al. 2002). For curve fitting, a resolution of 0.1 S and a confidence level (*F*-ratio) of 0.95 were selected. The partial-specific volume of rLC4 ($\bar{v}$ = 0.724306 $cm^3\ g^{-1}$), as well as solvent density (ρ = 1.0004 g cm^{-3}) and viscosity (η = 0.0101244 P) were calculated using the software SEDNTERP version 2.0 Beta (Laue 1992). The quality of the fits was assessed based on the RMSD values, all of which were below 1% of the total signal. To obtain $s_{20,w}$ the *s*-values were standardized to water at 20°C using the software GUSSI (Brautigam 2015) and graphical visualizations were prepared using DataGraph version5.3β, copyright 2020 (Visual Data Tools, NC, USA).

6.5.10 Differential scanning fluorimetry

To assess differences in thermal stability of rLC4 and P004, DSF was used to enable the detection of shifts in melting temperature indicating structural unfolding. Analysis of thermal stability was performed using a CFX Opus 96 Real-Time PCR System (Bio-Rad, CA, USA). Thermal shift assays were performed at sample concentrations of 35 µM in 30 mM Tris-HCl buffer (pH 7.4). In order to analyze the stability of the LCs without the influence of the inter- and intramolecular disulfide bonds, the samples were additionally treated with 7 mM TCEP. Samples were transferred into low-profile, thin-walled Hard-Shell 96-well PCR plates (#HSP9601), sealed with Microseal 'B' adhesive PCR plate sealing film (#MSB-1001). Real-time unfolding of the samples was monitored using the SYPRO Orange fluorescent dye (Sigma-Aldrich, S5692). A 10 mM stock solution was diluted 1:1,000 in the reaction mixture, resulting in a final working concentration of 10 µM. All measurements were performed in triplicate (n = 3), with a total reaction volume of 25 µL per well. Thermal unfolding was performed in a temperature range between 10°C to 95°C, with a temperature increment of 0.5°C per cycle every 15 s.

6.6 Results

6.6.1 Expression and purification of rLC4

In order to enable the recombinant expression of κ-FLC P004 – previously purified from the urine of a multiple myeloma patient (Sternke-Hoffmann et al. 2020, 2023) – in *P. pastoris*, the corresponding gene was codon-optimized and cloned into the pPICZαA vector. A graphical representation of the vector map is provided in Figure 6.1A, with the complete nucleotide sequence of the construct available in the supporting information (Tab. 8.9).

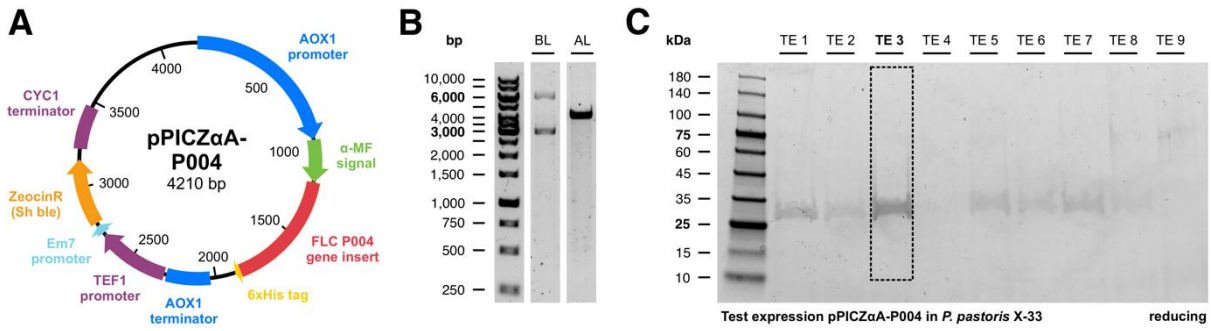

Figure 6.1: Vector design and expression strategy for patient-derived sample P004 in *P. pastoris*. (**A**) Schematic representation of the pPICZαA expression vector, with gene insert of patient sample P004 (red). The AOX1 promoter (blue) facilitates methanol-induced expression, while the α-MF secretion signal (green) directs the recombinant protein into the culture medium. A C-terminal 6xHis tag (yellow) was added for downstream purification. (**B**) Agarose gel analysis of the purified pPICZαA-P004 construct before (BL) and after (AL) linearization for transformation into *P. pastoris* X-33 competent cells. (**C**) Colony selection for recombinant production of P004. Nine TEs were performed, with seven showing varying levels of target protein expression. TE 3 was selected for large-scale production.

Following amplification of the pPICZαA vector carrying the κ-FLC P004 gene insert in *E. coli* DH5α competent cells, the vector was linearized using the MssI (PmeI) restriction enzyme for transformation into *P. pastoris* X-33 cells (Fig. 6.1B). After three days of growth on Zeocin-selective plates, individual colonies were screened for protein expression. Among nine test expressions (TE), seven showed detectable secretion of the desired recombinant protein. TE 3 exhibited the highest protein yield and was therefore selected for large-scale expression (Fig. 6.1C).

Following methanol-induced expression in *P. pastoris*, rLC4 was purified directly from the culture medium using IMAC via the 6xHis tag. SDS-PAGE analysis of the IMAC fractions confirmed the presence of expression products in the eluate, with minimal protein loss detected in flow-through and wash fractions (Fig. 6.2A). Further purification by SEC (Fig. 6.2B) resulted in an improved sample purity. To assess the distribution of molecular FLC species of rLC4, all collected SEC fractions (17–30) were analyzed by non-reducing SDS-PAGE (Fig. 6.2C), revealing the presence of monomers, dimers, and lower-molecular-weight fragments.

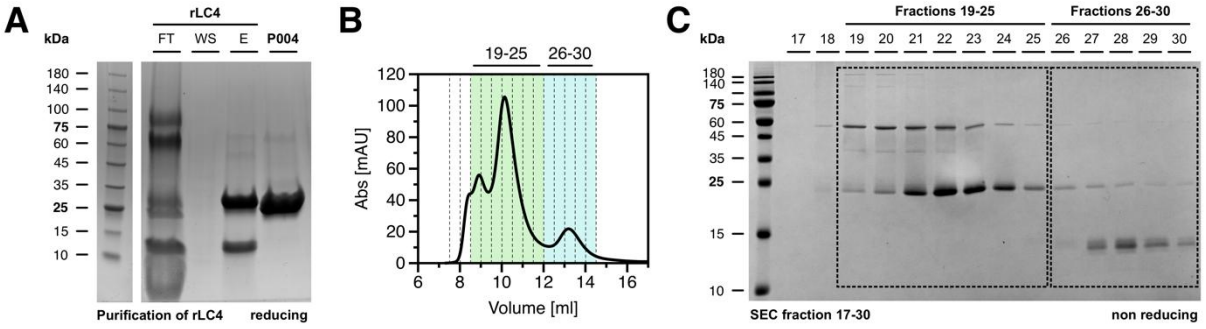

Figure 6.2: Purification workflow of rLC4: IMAC, SEC, and fraction analysis. Sequential purification steps for isolating rLC4 from BMMY culture medium post-expression. (**A**) SDS-PAGE analysis of the initial IMAC purification step, showing the flow-through (FT), wash step (WS) fraction, and eluate (E). As reference, the respective patient sample P004 was also loaded onto the gel alongside rLC4. (**B**) Representative SEC chromatogram, showing the collected fractions (dotted lines), with highlighted fractions 19–25 (green) and 26–30 (blue). (**C**) Non-reducing SDS-PAGE analysis of all collected fractions (17–30) to determine species distribution (e.g., monomers, dimers, and fragments), guiding the selection of fractions for pooling or exclusion.

Based on this distribution, fractions were pooled into two final samples (19–25 and 26–30) for subsequent characterization of rLC4, which were again analyzed via non-reducing Tris-Tricine SDS-PAGE to maintain intermolecular interactions (Fig. 6.3).

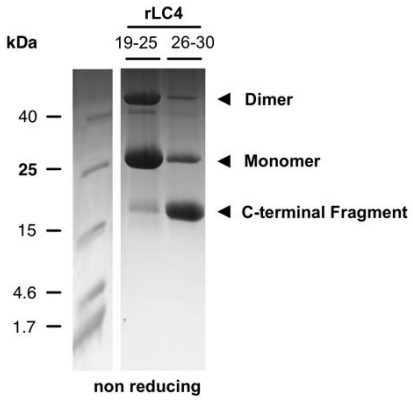

Figure 6.3: SDS-PAGE analysis of fully purified rLC4. A non-reducing SDS-PAGE gel displaying the two final pooled fractions (19–25 and 26–30) following SEC. The gel shows multiple bands, likely corresponding to different oligomeric states of rLC4, including monomers, dimers, and lower-molecular-weight fragments derived from the C-terminal C_L region, including the 6xHis tag. Additionally, an unidentified species appears below the putative dimer band, potentially representing an imperfect dimer formed by a full-length monomer and a low-molecular-weight fragment.

6.6.2 Immunodetection of rLC4 via Western blot analysis

To validate the purification state and assess the molecular species distribution of rLC4, Western blot analysis was performed on the final pooled SEC fractions 19–25 and 26–30. Samples were electrophoretically separated using both Tris-Tricine and Tris-Glycine SDS-PAGE, followed by immunodetection with an anti-6xHis monoclonal antibody in combination with an HRP-conjugated secondary antibody. Figure 6.4A presents the Western blot results from reducing Tris-Tricine SDS-PAGE, while Figure 6.4B displays results from Tris-Glycine SDS-PAGE under both reducing and non-reducing conditions. Under reducing conditions, both blots predominantly show a band at ~25 kDa, corresponding to monomeric rLC4 in both pooled fractions. Additionally, a band below 15 kDa is visible, likely representing lower-molecular-weight fragments. Since these fragments were detected via the 6xHis tag, they must originate from the C_L region at the C-terminus of the LC and therefore most likely reflect proteolytic degradation rather than incomplete expression. Western blot analysis under non-reducing conditions reveals dimeric rLC4 species at ~55 kDa (Fig. 6.4B). Interestingly, a faint dimer band persists even under reducing conditions. This could reflect oxidation during electrophoresis, as residual ammonium persulfate creates a pro-oxidative environment that common reducing agents cannot fully counteract, a phenomenon previously observed for cysteine-rich proteins (Achilli et al. 2018). However, it may also indicate that dimer formation in rLC4 is not solely dependent on disulfide bonds, as earlier studies on FLCs have suggested that additional non-covalent interactions, such as hydrophobic or electrostatic forces, can contribute to dimerization (Klein et al. 1977; Roussel et al. 1999). Notably, in the later SEC fractions (26–30) the band migrating near 25 kDa appears at a slightly lower apparent molecular weight than the corresponding band in the earlier fractions (19–25) under both reducing and non-reducing conditions (Fig. 6.4B). Because this band is recognized by the anti-6xHis antibody, it must contain the C-terminal 6xHis tag. Its lower mobility therefore likely represents a different species – such as a dimer of smaller C_L fragments – rather than a full-length monomer. This species also shows a faint band under reducing conditions. Additionally,

a distinct band around 40 kDa is observed, which does not correspond to the expected monomeric or dimeric species. This species may represent an imperfect dimer between a full-length monomer and a lower-molecular-weight fragment, although this interpretation remains speculative until further investigation, for example by MS analysis.

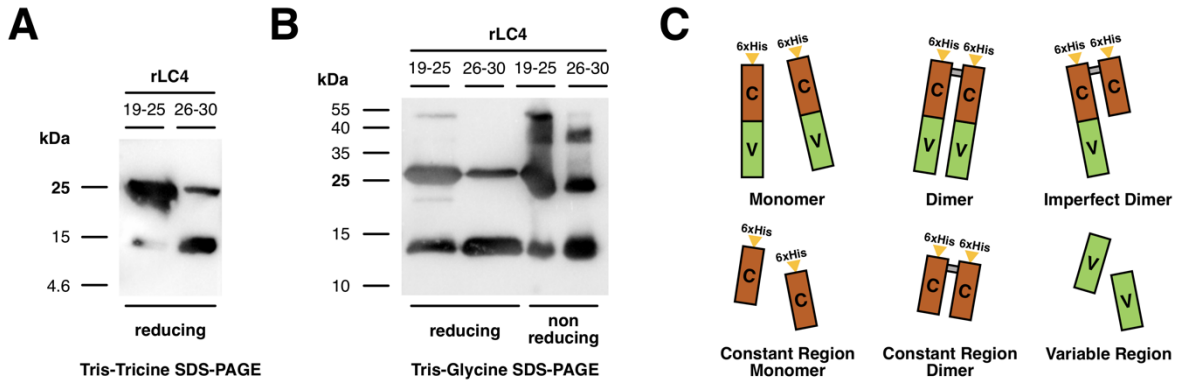

Figure 6.4: Western blot analysis of the pooled SEC fractions 19–25 and 26–30. Samples were prepared at a concentration of 35 µM in 30 mM Tris-HCl buffer (pH 7.4), and electrophoretic separation was performed using both Tris-Tricine and Tris-Glycine SDS-PAGE. Detection was carried out using an anti-6xHis monoclonal antibody in combination with an HRP-conjugated secondary antibody. (**A**) Tris-Tricine SDS-PAGE under reducing conditions. Monomeric rLC4 appears at approximately 25 kDa in both fraction collections, while lower-molecular-weight fragments are visible below 15 kDa. (**B**) Tris-Glycine SDS-PAGE under both reducing and non-reducing conditions. Under non-reducing conditions, dimeric species are observed at approximately 55 kDa. A faded dimer band is still detectable under reducing conditions. (**C**) Proposed distribution of rLC4 species following expression and purification from *P. pastoris*. Fragments of the V_L domain could correspond to the band between 10 and 15 kDa in the flow-through fraction from IMAC purification in Figure 6.2A, as these fragments lack the 6xHis tag and were not retained during purification.

6.6.3 Validation of PTM consistency

To further assess the suitability of rLC4 as a representative model for human FLCs, the recombinant LC was analyzed for potential PTMs that could be introduced by the *P. pastoris* expression system. Such unintended modifications may lead to structural alterations, thereby influencing the biophysical and biochemical properties of the protein and compromising comparability with the patient-derived sample. To investigate whether *P. pastoris* introduces phosphorylation, Western blot analysis was performed on both rLC4 and P004 using a phosphor-Serine/Threonine/Tyrosine-specific antibody (Fig. 8.18). No phosphorylation signals were detected in either sample under reducing or non-reducing conditions. Additionally, possible glycosylation of rLC4 and P004 was assessed using enzymatic deglycosylation of *N*- and *O*-linked glycans, followed by SDS-PAGE analysis (Fig. 8.19). No changes in band mobility were observed, indicating the absence of detectable glycosylation in both the recombinant and patient-derived LCs. These results suggest that rLC4 is free of expression system-specific PTMs and is structurally consistent with the native patient-derived protein.

6.6.4 Evaluation of rLC4 folding and structural similarity to P004

To further characterize rLC4 and compare it with the corresponding patient sample P004, their secondary structures were analyzed using CD spectroscopy. Figure 6.5A presents the CD spectra of rLC4 and P004. Measurements were performed at a concentration of 12 µM in 10 mM Tris-HCl buffer (pH 7.4), with baseline correction applied and 15 accumulations measured per sample. CD data were initially measured as ellipticity in millidegrees and subsequently normalized to calculate molar ellipticity values. Corresponding HT voltage records are provided in the Supplementary information (Fig. 8.14). Both rLC4 and P004 exhibit characteristic β-sheet secondary structure motifs, which are typical of LCs and immunoglobulin domains (Brahms et al. 1977; Bork et al. 1994; Poshusta et al. 2013; Andrich et al. 2017). The identical positions of the CD spectra minima, maxima and zero-crossing points indicate that the recombinant and the patient-derived LCs are structurally equivalent with respect to their secondary structure. This observation is further supported by the absence of detectable differences in PTMs between rLC4 and P004, confirming that expression in *P. pastoris* does not introduce structural artifacts that could alter secondary structure.

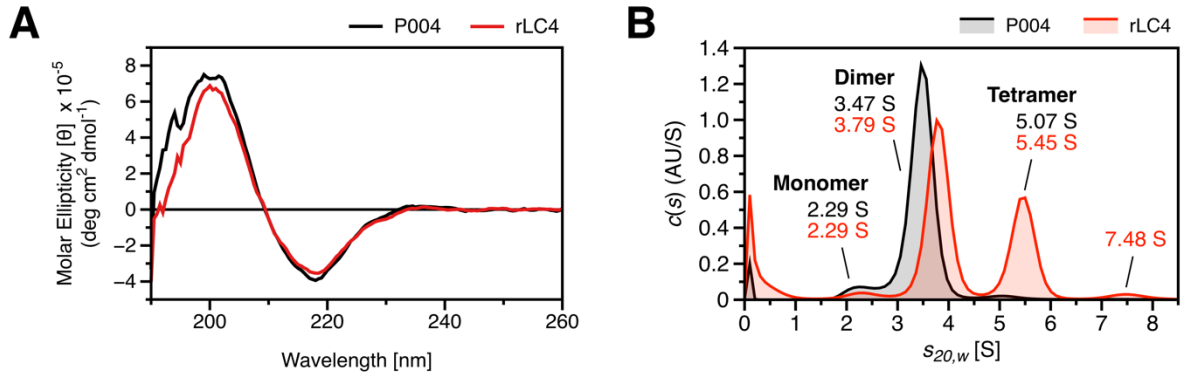

Figure 6.5: Characterization of rLC4 in comparison with the corresponding patient sample P004. (**A**) CD spectroscopic analysis of the secondary structure of rLC4 (red) and P004 (black). Measurements were conducted at a sample concentration of 12 µM in 10 mM Tris-HCl buffer (pH 7.4). Measurements were baseline corrected and a total of 15 accumulations per sample were recorded. (**B**) Sedimentation velocity analysis comparing the molecular species distribution of rLC4 and P004. Samples were prepared at a concentration of 35 µM in 30 mM Tris-HCl buffer (pH 7.4), and 390 µL of each sample was loaded into the sample sector of standard double-sector cells. Sedimentation velocity experiments were performed at 60,000 rpm and 20°C.

CD spectra of rLC4 and P004 were deconvoluted using the BeStSel web server to gain further insights into their secondary structure. The calculated compositions, shown in Table 6.1, confirm that both samples adopt a β-sheet-rich architecture, consistent with the established structure of immunoglobulin LCs (Brahms et al. 1977; Bork et al. 1994; Poshusta et al. 2013; Andrich et al. 2017). While antiparallel β-sheets dominate in both rLC4 and P004, the patient-derived sample exhibits a slightly higher proportion (68.4% vs. 62.0%). Conversely, rLC4 contains a greater fraction of parallel β-sheets (11.4% vs. 3.3%). The proportion of other secondary structure motives like unstructured regions and loops remains comparable between the two (28.3% in P004, 26.6% in rLC4), suggesting a similar degree of structural flexibility. No helical content was detected in either sample.

Table 6.1: Analysis of secondary structure motifs of rLC4 and P004 using the BeStSel web server. The secondary structure compositions of rLC4 and P004 are listed. CD spectra were uploaded as normalized molar ellipticity values for deconvolution and analysis. A graphical representation of the BeStSel analysis is provided in the Supplementary information (Fig. 8.15).

Secondary structure [%]	rLC4 [%]	P004 [%]
Helix	0.0	0.0
Antiparallel β-sheet	62.0	68.4
Parallel β-sheet	11.4	3.3
Turn	0.0	0.0
Others*	26.6	28.3

**Unstructured regions, loops, etc.*

Despite these minor variations in β-sheet subtypes suggested by the BeStSel analysis, the CD experiments confirm that the overall fold of rLC4 closely resembles that of the patient-derived LC, supporting its structural conservation. These subtle deviations may arise from variations in species distribution, particularly due to the presence of a truncated lower-molecular-weight fragment of the C_L region present in the recombinant sample. Since truncation could affect intramolecular disulfide bond formation, depending on the conservation of the relevant cysteine residue, structural perturbations in this region are expected. Whether these differences influence the aggregation propensity of rLC4 in comparison to P004 remains to be further investigated.

After confirming that rLC4 adopts a near-identical secondary structure to the patient-derived sample P004, its hydrodynamic properties were analyzed by SV analysis via AUC. Figure 6.5B shows the *s*-value distributions of rLC4 (red) and P004 (black). The corresponding sedimentation profiles for both measurements are provided in the supporting information (Fig. 8.16), along with individual plots of the respective *c*(*s*) distributions (Fig. 8.17). Total sedimentation of the samples was performed at 60,000 rpm at 20°C for approximately 5 hours. Based on their *s*-values, observed signals in the *c*(*s*) distribution could be reliably assigned to different FLC species, in agreement with reported literature values (i.e., monomer: ~2.4 S, dimer: ~3.65 S) (Klein et al. 1977). Both rLC4 and P004 share an identical *s*-value for their monomeric species (2.29 S), which supports the CD data that rLC4 has folded correctly and is highly similar to the patient sample (Fig. 6.5A). However, notable differences were observed in the sedimentation behavior of higher-order oligomers. The *s*-values for dimeric and tetrameric species in rLC4 were systematically higher than those in P004, with an average deviation of 0.35 S. This shift could reflect differences in intermolecular covalent or non-covalent interactions, potentially related to differences in folding environment, although other explanations cannot be excluded. Further analyses, such as MS, could provide additional insights. Additionally, rLC4 displayed an oligomeric species at 7.48 S, which was not detected in P004. As the glomerular filtration threshold in the kidneys typically ranges between 30 and 50 kDa (Graham and Karnovsky 1966), it is expected that – under normal kidney function – monomeric FLC species are freely filtered into the urine, while dimeric and higher-order oligomeric species may experience restricted filtration. However, as kidney damage advances, this threshold becomes less selective, allowing larger molecular species to pass into the urine (Roksnoer et al. 2016). Consequently, oligomeric FLC species are likely

excreted in urine only during advanced disease stages, when significant impairment of the filtration barrier has occurred. This could explain the absence of equivalent oligomers in the sample P004, a finding consistent with that patient's preserved renal function (Sternke-Hoffmann et al. 2020).

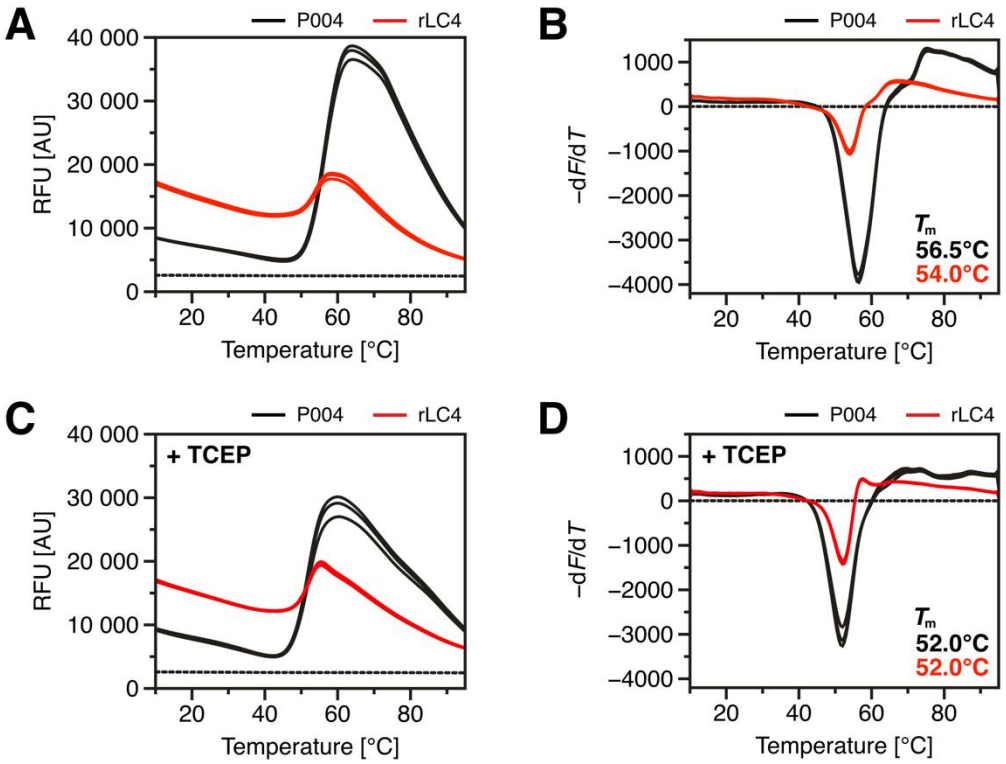

Figure 6.6: Comparison of melting temperatures of rLC4 and corresponding patient sample P004. Thermal denaturation was monitored using DSF with SYPRO Orange fluorescent dye at a 10 µM working concentration. Samples were prepared at 35 µM in 30 mM Tris-HCl buffer (pH 7.4), and measurements were performed in triplicate (n = 3). The patient sample P004 (black), rLC4 (red) and the buffer control (dotted black line) are shown. (**A**) Thermal denaturation profiles of rLC4 and P004 with (**B**) corresponding negative-derivative fluorescence-temperature plots (–dF/dT). (**C**) Thermal denaturation profiles of rLC4 and P004 in the presence of 7 mM TCEP with (**D**) corresponding negative-derivative fluorescence-temperature plots (–dF/dT).

Furthermore, T_m-values of rLC4 and P004 were analyzed under both neutral and reducing conditions using DSF. A series of thermal shift assays were performed to monitor structural unfolding in real time via fluorescence of the SYPRO Orange fluorescent dye. Figure 6.6 shows the thermal denaturation profiles of rLC4 and P004, along with the corresponding negative-derivative fluorescence-temperature plots ($-dF/dT$) to facilitate determination of the unfolding temperature. Thermal unfolding under neutral buffer conditions (30 mM Tris-HCl, pH 7.4) is shown in Figure 6.6A and 6.6B, while measurements in the presence of the reducing agent TCEP are shown in Figure 6.6C and 6.6D. Since measurements in the presence of TCEP did not require pre-incubation and were completed within approximately 1.5 hours, potential sample aggregation due to intra- and intermolecular disulfide bond reduction was considered negligible. Under neutral conditions, P004 shows a melting temperature of 56.5°C, while rLC4 has a slightly lower melting temperature of 54.0°C

(Fig. 6.6B). This temperature difference of 2.5°C may reflect structural differences in oligomerization and folding state, resulting in a higher thermostability of P004 compared to the recombinant LC. However, when disulfide bonds (both intra- and intermolecular) are disrupted, the melting temperatures of both samples become identical (Fig. 6.6C and 6.6D), suggesting that the observed difference under neutral conditions is primarily due to covalent disulfide bonding. These results align with the CD and AUC data, supporting the conclusion that rLC4 has adopted the correct secondary structure, with structural differences arising primarily from altered covalent and non-covalent interactions that govern oligomerization. SV analysis revealed that rLC4 exhibits a higher proportion of oligomeric species compared to P004, particularly species with increased *s*-values (5.45 S and 7.48 S). The DSF data further indicate that a significant fraction of these oligomers in rLC4 consists of non-covalently associated species. In addition to differences in melting temperature, the fluorescence signal intensity during thermal unfolding differed noticeably between the two samples. P004 exhibited a higher fluorescence signal upon unfolding, along with a lower pre-transition baseline. This may suggest a more compact folding state and greater hydrophobic surface exposure during denaturation. In contrast, rLC4 displayed lower overall fluorescence and an elevated pre-transition signal, signatures that may arise from partially exposed hydrophobic surfaces or greater conformational flexibility. These features could in part reflect contributions from truncated fragments, which present more hydrophobic surface area than the intact protein. Together, the data suggest that P004 species may be stabilized by intra- and intermolecular disulfide bonds, whereas rLC4 appears to form more dynamic, predominantly non-covalent oligomers. While P004 already displayed an unusually high dimer content for a κ-FLC (Kaplan et al. 2011), the exact factors influencing the formation of these higher-order species remain unclear and further investigations will be required to confirm the predominant stabilization mechanisms.

6.7 Discussion

In this study, a recombinant full-length LC, based on a FLC purified from the urine of a patient with MM, was successfully produced using the *P. pastoris* expression system. Compared to prokaryotic hosts such as *E. coli*, *P. pastoris* offers distinct advantages. Its intracellular folding environment supports the formation of native-like secondary structures and both intra- and intermolecular disulfide bonds, which are essential for achieving proper tertiary folding and maintaining the structural integrity. This eliminates the need for refolding strategies, such as oxido-shuffling or oxidative regeneration (Wingfield 1995), which often yield low amounts of correctly folded proteins and suffer from significant aggregation-related losses. Consequently, *E. coli* is frequently unsuitable for the expression of proteins that depend on disulfide bonding for their native folding (Daly and Hearn 2005). Moreover, *P. pastoris* secrets the expressed proteins directly into the culture medium, eliminating the need for cell lysis and thus simplifying downstream purification. This study highlights *P. pastoris* as a suitable and efficient platform for the expression of full-length FLCs, preserving their native structural and biophysical properties.

After expression and purification of rLC4 from the *P. pastoris* culture medium via IMAC and SEC, the final SEC fractions were analyzed by Western blot to validate their species composition utilizing

antibodies against the 6xHis tag. The analysis revealed a range of molecular species, including unexpected variants likely resulting from interactions with lower-molecular-weight fragments, primarily derived from the C-terminal C_L region. To assess whether *P. pastoris* introduced host-specific PTMs, both rLC4 and the patient-derived FLC P004 were screened for phosphorylation and glycosylation. No detectable modifications were found in either sample. This structural equivalence was further supported by CD spectroscopy, which confirmed that rLC4 adopted a native-like secondary structure with only minor deviations from the patient-derived sample P004, likely attributable to the presence of truncated C_L fragments. Subsequent SV analysis revealed identical monomeric *s*-values for both rLC4 and P004, but differences emerged in the distribution of higher-order oligomers. Specifically, the dimeric and tetrameric forms of rLC4 showed increased *s*-values by 0.32 S and 0.38 S, respectively, compared to those of P004. These differences may reflect subtle variations in intermolecular interactions, with the higher *s*-value of rLC4 suggesting an alternative non-covalent packing within its oligomeric assemblies. Both κ- and λ-FLCs can exist as monomers or dimers, with dimerization stabilized through covalent and non-covalent interactions (Klein et al. 1977; Roussel et al. 1999). λ-FLCs tend to form covalent dimers more readily, mediated by a conserved cysteine residue at the C-terminus. In contrast, κ-FLCs predominantly assemble through non-covalent interactions, often resulting in a heterogeneous mixture of monomers, and both covalently and non-covalently linked dimers (Caponi et al. 2018; Gudowska-Sawczuk and Mroczko 2019; Sarto et al. 2021). Higher-order assemblies such as tetramers have also been reported (Sölling 1976; Džupponová and Žoldák 2023; Sakai et al. 2023).

Both P004 and rLC4 contain five cysteine residues (Tab. 8.10). In P004, four of these participate in two conserved intramolecular disulfide bonds involving Cys23–Cys89 and Cys135–Cys195 (Dupré et al. 2021). The remaining unpaired cysteine at the C-terminus, Cys215, may either be cysteinylated or available for intermolecular disulfide bonding. Cysteinylation, also known as S-thiolation, is a reversible, non-enzymatic PTM involving a disulfide bond between an unpaired cysteine residue of a protein and a low molecular weight thiol (Thomas et al. 1994; Loi et al. 2015; Nakashima et al. 2018). While commonly associated with cellular redox regulation and protection from oxidative stress, cysteinylation can also interfere with disulfide-mediated dimerization, the formation of native disulfide bonds (Liu et al. 2009). Whether changes in intermolecular interactions contribute to the higher proportions of oligomeric species observed in rLC4 (i.e., 5.45 S and 7.48 S) remains uncertain. This could also be influenced by the progressive increase in glomerular filtration threshold due to renal damage (Graham and Karnovsky 1966; Roksnoer et al. 2016), where higher-order oligomeric FLC species are only released into the urine during advanced disease stages. This may explain their absence in sample P004 but does not exclude their presence in patient serum, cerebrospinal fluid, or synovial fluid. Finally, rLC4 and P004 were analyzed by DSF, and their melting temperatures were determined using a series of thermal shift assays. Under native conditions, rLC4 exhibited a melting temperature of 54.0°C, while P004 showed a slightly higher value of 56.5°C. This difference of 2.5°C may reflect subtle variations in molecular interactions between the species. Upon reduction of intra- and intermolecular disulfide bonds with TCEP, both samples displayed an identical melting temperature of 52.0°C, suggesting that disulfide bonding contributes to the observed thermal stabilization. Previous studies have demonstrated that intermolecular disulfide bonds, which mediate covalent oligomerization, contribute more significantly to the thermal stability of FLCs than intramolecular disulfide bonds, which primarily stabilize the monomeric structure (Tucholski et al.

2025). These observations are consistent with SV analysis, which revealed that rLC4 exhibits a higher proportion of oligomeric species compared to P004, particularly at increased *s*-values (i.e., 5.45 S and 7.48 S). In this context, the DSF data are consistent with the idea that a proportion of the rLC4 oligomers may be stabilized predominantly by non-covalent interactions, although confirmation will require further investigation. One possible factor that could influence this behavior is the presence of the C-terminal 6xHis tag, located near Cys215, which is involved in covalent dimer formation. However, this effect appears unlikely to arise from the expression vector or host system alone, as the patient-derived sample P004 already displays an unusually high proportion of dimers and higher-order species for a κ-FLC, which in itself may indicate a pathological alteration (Kaplan et al. 2011). The mechanisms regulating disulfide-linked dimer and oligomer formation remain incompletely understood but are thought to involve oxidoreductases whose activity depends on the redox potential of the surrounding microenvironment (Elkabetz et al. 2008; Feige et al. 2010). Oxidative stress, often elevated under pathological conditions, may alter redox homeostasis, and thus influence the dithiol-disulfide equilibrium of FLCs. Previous studies have reported elevated oxidative stress markers in affected patients (Brenner et al. 2004; Migrino et al. 2010; Cavallone et al. 2024), suggesting a potential connection between redox balance and FLC dimerization (Kaplan et al. 2014). However, whether shifts in FLC species distribution track with disease stage or clinical severity remains to be determined.

This study highlights that the balance between covalent and non-covalent oligomerization is an important consideration when establishing a reliable model system for investigating the pathology of patient-derived FLCs *in vitro*. Given that the cellular microenvironment, particularly oxidative stress and shifts in redox potential often caused by pathological changes, strongly influence the formation of distinct FLC species, it remains unclear whether conventional expression systems can fully replicate the molecular characteristics observed in patient samples. Even when the correct secondary structure is achieved, FLC behavior appears to be shaped by multiple additional factors that are often underexplored. Furthermore, this study raises the question of whether FLCs purified from patient urine fully capture the molecular heterogeneity of the pathological state *in vivo*. Our comparison between a recombinant LC and its urinary counterpart suggests that the distribution of molecular FLC species may vary across physiological compartments beyond the kidneys. For example, the FLC profile in serum may differ from that in urine, particularly as disease progression alter tissue environments and glomerular filtration dynamics. This underscores the need for longitudinal studies that not only quantify FLC concentrations in serum and urine, but also track the molecular composition and structural heterogeneity of FLC species over time and in close relation to disease progression. While this study did not employ MS, the structural and biophysical analyses presented here provide a robust foundation for future MS-based investigations. High-resolution MS could enable detailed mapping of disulfide bonding patterns, oxidative modifications, or subtle PTM differences that may influence FLC oligomerization and aggregation. In this context, rLC4 offers a validated platform to support mechanistic studies into how redox shifts, cysteinylation, or other covalent modifications contribute to disease progression. The findings presented here highlight the importance of selecting an appropriate expression system and conducting detailed biophysical characterization of full-length FLCs. A deeper understanding of the mechanisms driving both covalent and non-covalent oligomerization, and how these evolve during disease progression, could offer important insights into the structural transitions that promote aggregation and tissue damage in disorders such as MM and AL amyloidosis.

7

General discussion

7.1 Pathological heterogeneity of FLCs

PCDs such as MM and AL amyloidosis are characterized by pronounced clinical heterogeneity, ranging from asymptomatic disease to severe end-organ damage (Merlini et al. 2013; Cowan et al. 2022; Malard et al. 2024; Rajkumar 2024). This variability complicates clinical risk stratification at diagnosis and limits the ability to predict organ involvement over the course of disease (Van De Donk et al. 2021; Zorlu et al. 2025). In the patient cohort from which the FLC samples investigated in this thesis were derived, clinical metadata captured at diagnosis revealed a wide spectrum of serum FLC concentrations and renal function parameters (Tab. 8.1), reflecting substantial variation in both clonal burden and renal presentation (Sternke-Hoffmann et al. 2020). Given the small cohort size (n = 9) and the single diagnostic time point, these metadata are interpreted only descriptively and are not used to infer statistical associations within this thesis. Nevertheless, this heterogeneity is consistent with the understanding that renal impairment reflects an interplay of FLC burden, their intrinsic properties, and patient-specific factors (Leboulleux et al. 1995; Basnayake et al. 2011; Yadav et al. 2018; Taylor and Ryan 2019; Sternke-Hoffmann et al. 2020).

Renal impairment is among the most prevalent and severe complications of MM and is closely associated with morbidity and early mortality (Heher et al. 2013; Yadav et al. 2015; Leung and Rajkumar 2023). In FLC-mediated renal disease, elevated levels of monoclonal FLCs in the urine can promote cast formation and tubular injury, accompanied by inflammation, oxidative stress, and progressive fibrotic remodeling (Huang and Sanders 1997; Basnayake et al. 2010, 2011; Sirac et al. 2021; Malard et al. 2024). Clinically, monoclonal FLCs are routinely quantified to assess clonal burden and monitor treatment response (Katzmann et al. 2002; Bradwell et al. 2002; Siegel et al. 2009). However, patients with comparable FLC concentrations can present with markedly different degrees of renal impairment, consistent with prior observations that concentration alone does not capture the pathogenic potential of individual FLCs (Leboulleux et al. 1995; Basnayake et al. 2011; Andrich et al. 2017; Yadav et al. 2020; Sternke-Hoffmann et al. 2020).

At the molecular level, FLC pathogenicity is likely modulated by sequence-driven physicochemical and conformational properties, including disulfide connectivity, cysteine reactivity, and stability of molecular species, as well as by local environmental conditions that influence destabilization, self-assembly, fragmentation, and tissue deposition (Huang and Sanders 1997; Lim et al. 2001; Basnayake et al. 2011; Morgan and Kelly 2016; Džupponová and Žoldák 2023). Interactions with renal proteins such as UMOD further contribute to the complexity of cast nephropathy and tubular injury (Huang

and Sanders 1997; Lim et al. 2001; Basnayake et al. 2011). Previous studies of this set of samples support this interpretation by demonstrating substantial variability in biochemical and biophysical properties across samples, while reporting only inconsistent correlations between individual parameters and renal impairment (Sternke-Hoffmann et al. 2020; Dupré et al. 2021; Sternke-Hoffmann 2021; Sternke-Hoffmann et al. 2023).

Against this background, this thesis investigates pathological FLCs using complementary biophysical approaches that combine patient-derived samples with recombinant model systems. Analysis of urinary FLCs from MM patients captures native molecular heterogeneity and clinically relevant species distributions, while defined perturbations provide a tool for investigating stability and self-assembly pathways. In parallel, recombinant expression systems were established to reproduce patient-specific FLC sequences under controlled folding and redox environments, enabling systematic evaluation of how intrinsic sequence features together with environmental conditions shape molecular behavior. Within this framework, reductive perturbation was employed as one experimentally tractable tool to interrogate the sensitivity of FLC species to disulfide chemistry and cysteine reactivity (Bechtel and Weerapana 2017). Across patient-derived and recombinant systems, the results show that aggregation and fragmentation behavior cannot be attributed to a single determinant such as concentration, sequence family, or oligomeric state alone, but instead arise from the interplay between intrinsic molecular properties and environmental context.

7.2 Redox effects in patient-derived FLCs

Across all FLC samples examined, disulfide bond reduction was associated with the redistribution of molecular species. The direction and kinetics of these shifts differed substantially between patients, indicating that redox perturbation interacts with sample-specific molecular determinants. Notably, reduction of dimeric species did not result in detectable accumulation of reduced monomers as a stable population. Instead, the observations are consistent with the formation of highly unstable monomeric intermediates that, within the sensitivity and time resolution of the SV-AUC readout, do not manifest as a sustained increase in monomer signal and instead rapidly convert into non-native assemblies and higher-order species, indicating only transient monomer release before entry into aggregation-prone states.

Quaternary structure was not sufficient to predict behavior under reducing conditions. In a subset of samples, dimeric signals persisted under identical reducing conditions, consistent with sequence-dependent stabilization of dimeric species (Andrich et al. 2017; Zhao et al. 2018; Rennella et al. 2019). This may reflect limited solvent accessibility of intermolecular disulfide bonds (Natesan et al. 2023), rendering them more resistant to reduction, and/or persistent non-covalent interdomain interactions that stabilize dimeric species even when covalent linkage is perturbed. While disulfide-linked dimerization can increase the kinetic stability and proteolytic resistance of FLCs, it can also promote aggregation under destabilizing conditions, emphasizing that stabilization and pathogenic assembly are not mutually exclusive outcomes (Morgan and Kelly 2016; Morgan et al. 2019). In contrast, monomeric species detectable prior to reduction remained detectable over extended incubation,

suggesting that reduced monomers may form different conformational states with varying aggregation competence.

Redox perturbation of disulfide bonds primarily affects tertiary and quaternary structure and can alter hydrodynamic behavior even when substantial secondary structure remains intact (McAuley et al. 2008). Consistent with this, CD measurements indicated that reduction does not necessarily abolish native-like secondary structure, whereas SV-AUC revealed time-dependent changes in sedimentation behavior and the formation of higher-order species under prolonged reducing conditions. Prolonged reduction also appears to induce gradual changes within monomeric species, such as altered compactness or partial unfolding, resulting in progressive shifts in sedimentation behavior rather than abrupt dissociation events. Together, these observations support a model in which reduction transiently exposes partially destabilized intermediates that enter oligomerization and aggregation pathways rather than persisting as discrete monomeric species.

Reduction-associated fragmentation was consistently observed in a subset of FLCs sharing a common genetic origin, which increased over incubation time. In disease context, fragmentation, particularly the generation of V_L-domain-containing fragments, has been associated with AL amyloidosis and may increase amyloidogenic propensity by removing stabilizing interactions contributed by the C_L domain (Glenner et al. 1970; Morgan and Kelly 2016; Rennella et al. 2019; Kazman et al. 2021; Mazzini et al. 2022; Lavatelli et al. 2024).

Fragmentation observed under reducing conditions was further investigated, and intrinsic proteolytic activity, likely corresponding to co-purified cathepsins, was detected in all FLC preparations. Cathepsin activity persisted under acidic and reducing conditions, consistent with their native lysosomal environment (Yadati et al. 2020). At the same time, controlled digestion experiments revealed pronounced, sample-specific responses and demonstrated that fragmentation could occur in the presence of TCEP alone, without addition of CtsD, which supports the possibility of chemically induced cleavage associated with exposure to strong reductants (Liu et al. 2010). Moreover, denaturation and thermal stress introduced during sample preparation may have further contributed to backbone instability (Miekka 1983). Because pronounced fragmentation occurred only in a subset of samples under otherwise identical incubation conditions, intrinsic sample-specific properties likely modulate susceptibility. However, a reagent-associated contribution cannot be excluded on the basis of present data. Accordingly, fragmentation is treated as a reproducible reduction-linked process, while its precise molecular origin remains unresolved and will require additional investigations.

7.3 Patient material and model systems

Patient-derived samples capture the physiological complexity of disease, including sequence diversity, native PTMs, including cysteine-based modification patterns, and fragment formation. They also capture mixtures of covalent and non-covalent assemblies that may arise *in vivo* within the context of disease (Kaplan et al. 2011). This complexity strengthens biological relevance, but also limits mechanistic attribution. The ability to link specific molecular features to clinically relevant FLC behavior is constrained by co-purified proteases, compartment-specific selection effects between serum und urine, and clinical metadata that are restricted to a single time point at diagnosis. These

limitations are particularly relevant for MM-associated renal disease, where clinical risk is likely shaped by the interplay of systemic FLC burden, renal handling, and local microenvironmental conditions (Leboulleux et al. 1995; Basnayake et al. 2011; Yadav et al. 2018; Taylor and Ryan 2019; Sternke-Hoffmann et al. 2020).

Previous work on the same set of patient samples highlights this challenge. Across samples, most individual biochemical or biophysical parameters did not show consistent correlations with renal impairment, highlighting the multifactorial nature of disease progression. A potentially relevant observation is that FLCs from patients with the most severe renal impairment were among the least susceptible to trypsin digestion *in vitro* (Sternke-Hoffmann 2021). While trypsin digestibility is an indirect measure influenced by cleavage-site availability and structural accessibility, this observation is consistent with the hypothesis that proteolytic resistance could modulate persistence and tissue exposure, and it motivates further investigation with physiologically relevant proteases and defined model systems.

Accordingly, this thesis adopts a complementary strategy. Patient-derived material provides biological relevance and captures disease-associated heterogeneity, while controlled recombinant systems enable systematic manipulation of redox balance, folding environment, and molecular composition in order to test mechanistic hypotheses under defined conditions. Recombinant expression and refolding experiments emphasized the importance of redox balance in determining FLC species distributions. Even for identical primary sequences, varying redox conditions during expression, secretion, and refolding were associated with distinct molecular assemblies, consistent with altered cysteine reactivity and disulfide pairing. Deviations toward overly reducing or overly oxidizing environments disrupted productive disulfide pairing and increased structural heterogeneity, in line with established principles of oxidative protein folding and disulfide exchange. These findings mirror observations from patient-derived material, in which cysteine-modified monomeric variants coexist alongside covalently disulfide-linked dimers and non-covalent assemblies (Dupré et al. 2021; Sternke-Hoffmann et al. 2023; Tucholski et al. 2025). In proteomic terms, these coexisting species could be described as distinct proteoforms, or proteoform-like states, emphasizing that pathological FLC preparations behave as mixtures, whose composition depends on redox conditions and, in turn, influences the accessibility of self-assembly pathways.

7.4 Conclusions and outlook

Based on a small cohort sampled at diagnosis and analyses performed under controlled redox-stress conditions, the results indicate that pathological FLC preparations exist as redox-dependent mixtures of dynamically interconverting species. These include cysteine-modified monomeric variants, covalent dimers stabilized by intermolecular disulfide bonds, non-covalent assemblies maintained through electrostatic and hydrophobic interactions, and, under certain conditions, fragmented species. In this context, reduction does not merely induce a transition between dimers and monomers. Instead, it reshapes the accessible conformational assembly landscape by generating transient, destabilized intermediates that redistribute into oligomeric and higher-order species and, in a subset of samples, give rise to reproducible fragmentation patterns.

From a translational perspective, these findings motivate the concept that variant-resolved redox-responses could, in principle, complement concentration-based diagnostics. If reproducible redox-linked behaviors, such as susceptibility to destabilization-linked redistribution, oligomerization, or distinct fragmentation patterns under standardized conditions, are shown to associate with organ involvement in larger, longitudinal cohorts, they could contribute to improved risk stratification at diagnosis. Although clinical association cannot be established within the present cohort, the work identifies potential parameters for validation in larger and longitudinal studies.

Future investigations should prioritize time- and compartment-resolved sampling to track not only FLC concentrations but also molecular species distributions and cysteine-based modification patterns alongside clinical course. Combining SV analysis with MS-based approaches that are capable of resolving fragments, cysteine modifications, and disulfide connectivity would enable direct linkage of hydrodynamic signatures to molecular identities. In addition, controlled experiments designed to distinguish reductant-associated chemical cleavage from protease-dependent fragmentation will be essential to interpret fragmentation as a biologically meaningful consequence of destabilization rather than an experimental artefact.

Overall, the findings indicate that reductive perturbation is associated with the redistribution of FLC species in a sample-dependent manner, which is coupled to destabilization, assembly into higher-order species and, under certain conditions, fragmentation. Across both patient-derived and recombinant samples, the results indicate that redox conditions are a major determinant of FLC species distributions. By influencing the balance between cysteine-modified monomers, covalent dimers, and non-covalent assemblies, different redox conditions influence which self-assembly pathways become accessible under destabilizing conditions. These findings support the idea that organ involvement cannot be predicted based on concentration or oligomeric state alone. Instead, future work could follow an approach which combines sequence context, redox sensitivity, and variant-resolved species distributions to test whether such measures add value to risk assessment, particularly when connected to longitudinal, compartment-aware clinical sampling.

8

Supplementary information

8.1 General supplementary information

Table 8.1: Clinical characteristics of patient-derived FLC samples analyzed in this thesis. Patients were grouped according to CKD stage at the time of examination (Group I (CKD stage 1-2), Group II (CKD stage 3), and Group III (CKD stage 4-5). Data adapted from Sternke-Hoffmann et al. 2020.

Patient ID	Age (years)	Sex	Ig subtype	LC isotype	Serum FLC (mg/L)	Urine FLC (mg/L)	eGFR (mL/min/1.73 m²)	CKD stage
P001	47	male	IgG	λ	3.75	1.06	50	3
P004	72	male	IgG	κ	5.28	7.65	90	1
P005	65	female	IgG	κ	1.25	6.14	48	3
P006	66	female	IgG	κ	2.46	6.88	27	4
P007	54	male	IgG	κ	0.90	—	83	2
P013	65	male	—	κ	11.0	—	50	3
P016	59	male	—	κ	1.15	17.5	45	3
P017	72	female	IgG	κ	1.38	—	90	1
P020	64	female	—	κ	4.12	—	74	2

All patients were diagnosed with MM, and samples were collected at the time of diagnosis.

Table 8.2: Amino acid sequences of all patient-derived samples analyzed in this study. Data adapted from Dupré et al. 2021; Sternke-Hoffmann et al. 2023.

P001

GPDLTQPRSVSGSPGQSVTLSCTGTSSDVGGYNYVSWYQQHPGKAPKLMLYDVTKRPSGVPDRFSGSKSGTTASLTLSGLQAEDE
ADYYCCSYAGLDLFVLFGGGTKLTVLGQPKAAPSVTLFPPSSEELQANKATLVCLLSDFYPQVTVAWKADSSPVKAGVETTTPSK
QSNNKYAASSYLSLTPEQWKSHRSYSCQVTHEGSTVEKTVAPTECS

P004

EIVLTQSPGTLSLSPGERATLSCRASQSVSSSYLAWYQQKPGQAPRLLIYDASTRATGIPDRFSGSGSGADFLLTISSLEPEDFA
MYYCQQYGRSPYTFGPGTKVDIKRTVAAPSVFIFPPSDEQLKSGTASVVCLLNNFYPREAKVQWKVDNALQSGNSQESVTEQDSK
DSTYSLSSTLTLSKADYEKHKVYACEVTHQGLSSPVTKSFNRGEC

P005

DLQMTQSPSSLSASVGDRVSLTCRASESLSSYVNWYQQKPGKAPKLLLYTASSLQSGVPPRFSGSASGTDFTLTLSSLQPEDFAT
YYCQQSYSTPLTFGQGTRLELKRTVAAPSVFLFPPSDEQLKSGTASVVCLLNNFYPREAKVQWKVDNALQSGNSQESVTEQDSKD
STYSLSSTLTLSKADYEKHKVYACEVTHQGLSSPVTKSFNRGEC

P006

DLQMTQSPSSLSASVGDRVTLTCQASQDLAKYLNWYQQKPGKPPKLLLYDTSNLETGVPSRFSNGGGTDFTFTLNSLQPEDLATY
YCQQYDDFPLTFGPGTKVDLKRTVAAPSVFLFPPSDEQLKSGTASVVCLLNNFYPREAKVQWKVDNALQSGNSQESVTEQDSKDS
TYSLSSTLTLSKADYEKHKVYACEVTHQGLSSPVTKSFNRGEC

P007

DLQMTQSPSTLSASVGDRVTLTCRASQSLSSSLAWYQQKPGKAPKLLLYDASSLETGVPSRFSGSGSGTEFTLSLSSLQPDDFAT
YYCQHYNSYSLTFGQGTKVELKRTVAAPSVFLFPPSDEQLKSGTASVVCLLNNFYPREAKVQWKVDNALQSGNSQESVTEQDSKD
STYSLSSTLTLSKADYEKHKVYACEVTHQGLSSPVTKSFNRGEC

P013

DLQMTQSPSTLSASVGDAVTLTCRASQSLNVWLAWYQQKPGKPPKLLLYEASNLESGVPSRFSGSGSGTEFTLTLSSLQPDDFAT
YYCQQYNSYPYTFGQGAKLELKRTVAAPSVFLFPPSDEQLKSGTASVVCLLNNFYPREAKVQWKVDNALQSGNSQESVTEQDSKD
STYSLSSTLTLSKADYEKHKLYACEVTHQGLSSPVTKSFNRGEC

P016

DLQMTQSPSSLSASVGDRVTLTCQASRDLSNYLNWYQQKPGKAPMLLLYAASNLQTGVPSRFSGSGSGTDFTFTLSSLQPEDLAT
YYCQQYGNLPLTFGGGTKVELKGTVAAPSVFLFPPSDEQLKSGTASVVCLLNNFYPREAKVQWKVDNALQSGNSQESVTEQDSKD
STYSLSSTLTLSKADYEKHKVYACEVTHQGLSSPVTKSFNRGEC

P017

DLQMTQSPSSLSASVGDRVTLTCQASQDLGNYLNWYQQKPGKAPRLLLYDASDLEEGVPSRFSGSGSGTDFTFTLSSLQPEDFAT
YYCQQYHTLPPLTFGGGTKVDVKRSLAAPSVFLFPPSDEQLKSGTASVVCLLNNFYPREAKVQWKVDNALQSGNSQESVTEQDSK
DSTYSLSSTLTLSKADYEKHKVYACEVTHQGLSSPVTKSFNRGEC

P020

DLQMTQSPSTLSTSVGDRVTLTCRASQSLRTWLAWYQQKPGKAPKLLLYKASTLETGVPSRFSGSGSGTDFTLTLSSLQPEDFAT
YYCQQYNDYSGTFGQGTKLELKRTLAAPSVFLFPPSDEQLKSGTASVVCLLNNFYPREAKVQWKVDNALQSGNSQESVTEQDSKD
STYSLSSTLTLSKADYEKHKVYACEVTHQGLSSPVTKSFNRGEC

Table 8.3: Intrinsic physicochemical parameters derived from the primary sequences of patient-derived FLCs. Parameters were calculated from amino acid sequence using ProtParam (Walker 2005). CamSol represents the intrinsic solubility score. Data adapted from Sternke-Hoffmann 2021.

Patient ID	Isotype	Length (aa)	MW (kDa)	theor. pI	ε280 ($M^{-1}cm^{-1}$)	Instability index	Aliphatic index	CamSol
P001	λ	216	22,93	6.34	33,265	59.99	64.07	0.15
P004	κ	215	23,44	6.12	27,640	52.65	68.05	0.43
P005	κ	214	23,35	6.91	26,150	56.03	66.96	0.27
P006	κ	213	23,47	5.20	26,150	50.03	66.34	0.40
P007	κ	214	23,31	6.35	26,150	53.95	66.96	0.27
P013	κ	214	23,48	5.73	33,140	50.69	67.90	0.13
P016	κ	214	23,22	5.70	26,150	50.00	68.79	0.07
P017	κ	215	23,53	5.19	26,150	56.18	66.19	0.30
P020	κ	214	23,55	7.75	31,650	49.83	65.61	0.39

8.2 Tracking reduction-induced molecular changes in pathological free light chains by SV-AUC

8.2.1 Supplementary methods

Calculation and data analysis

Table 8.4: Fit parameters used to analyse SV-AUC sedimentation data.

Sample ID	$\bar{\nu}$ [$cm^3\ g^{-1}$]
P001	0.726160
P004	0.726223
P005	0.725521
P006	0.726200
P007	0.725071
P013	0.726996
P016	0.726208
P017	0.724235
P020	0.726701

Buffer solution	Density [g/cm^3]	Viscosity [*P*]
30 mM Tris-HCl, pH 7.4	1.0004	0.010124
+ 0.1 M NaCl	1.0045	0.010224
+ 1 M NaCl	1.0407	0.011091

8.2.2 Supplementary results

Changes in FLC size distribution after disulfide bond reduction

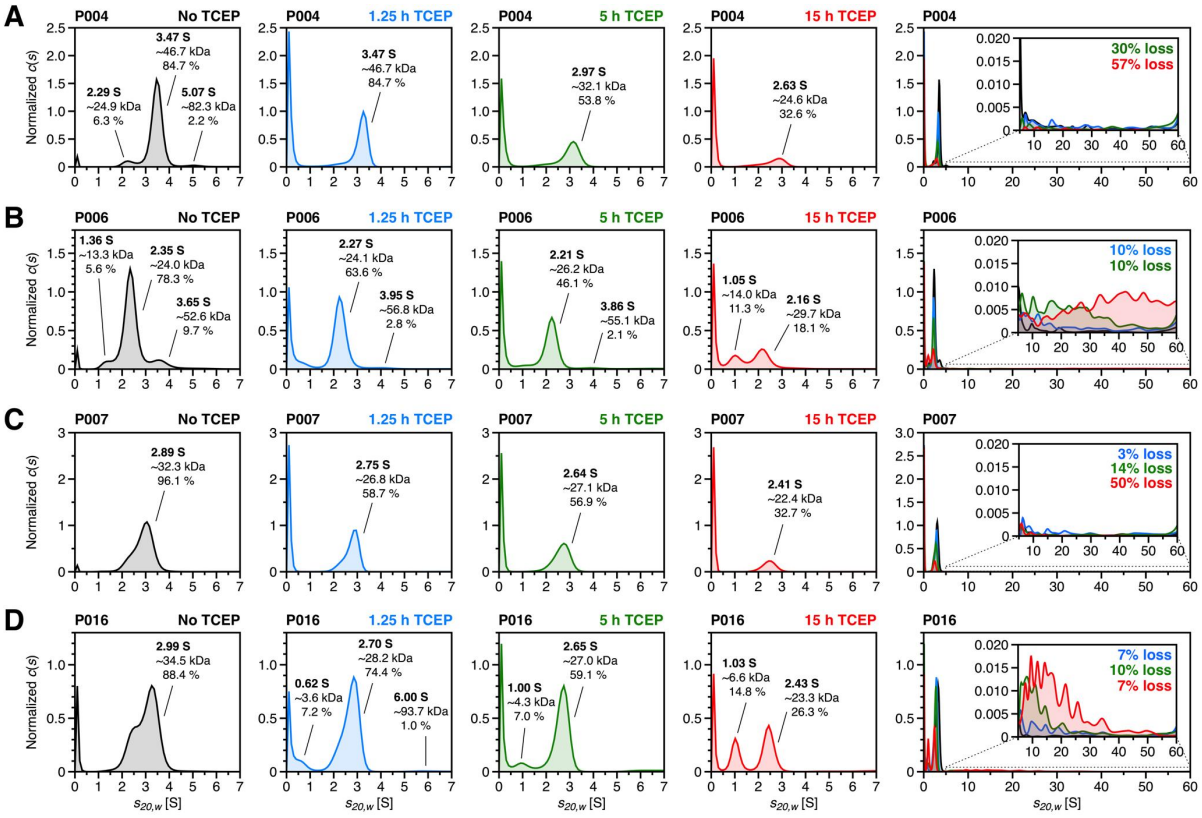

Figure 8.1: Influence of disulfide bond reduction on the monomer-dimer distribution of FLCs. The *c*(*s*) distributions of purified patient samples (**A**) P004, (**B**) P006, (**C**) P007, and (**D**) P016 are shown. Samples were prepared at a concentration of 35 µM in 30 mM Tris-HCl, pH 7.4 (black). To reduce disulfide bonds, 7 mM pH-adjusted TCEP was added, followed by incubation at 37°C with shaking at 600 rpm for periods of 1.25 h (blue), 5 h (green), and 15 h (red). After incubation, 390 µL of each sample was transferred to the sample sector of standard aluminum double-sector cells, and sedimentation analysis was performed at 60,000 rpm and 20°C.

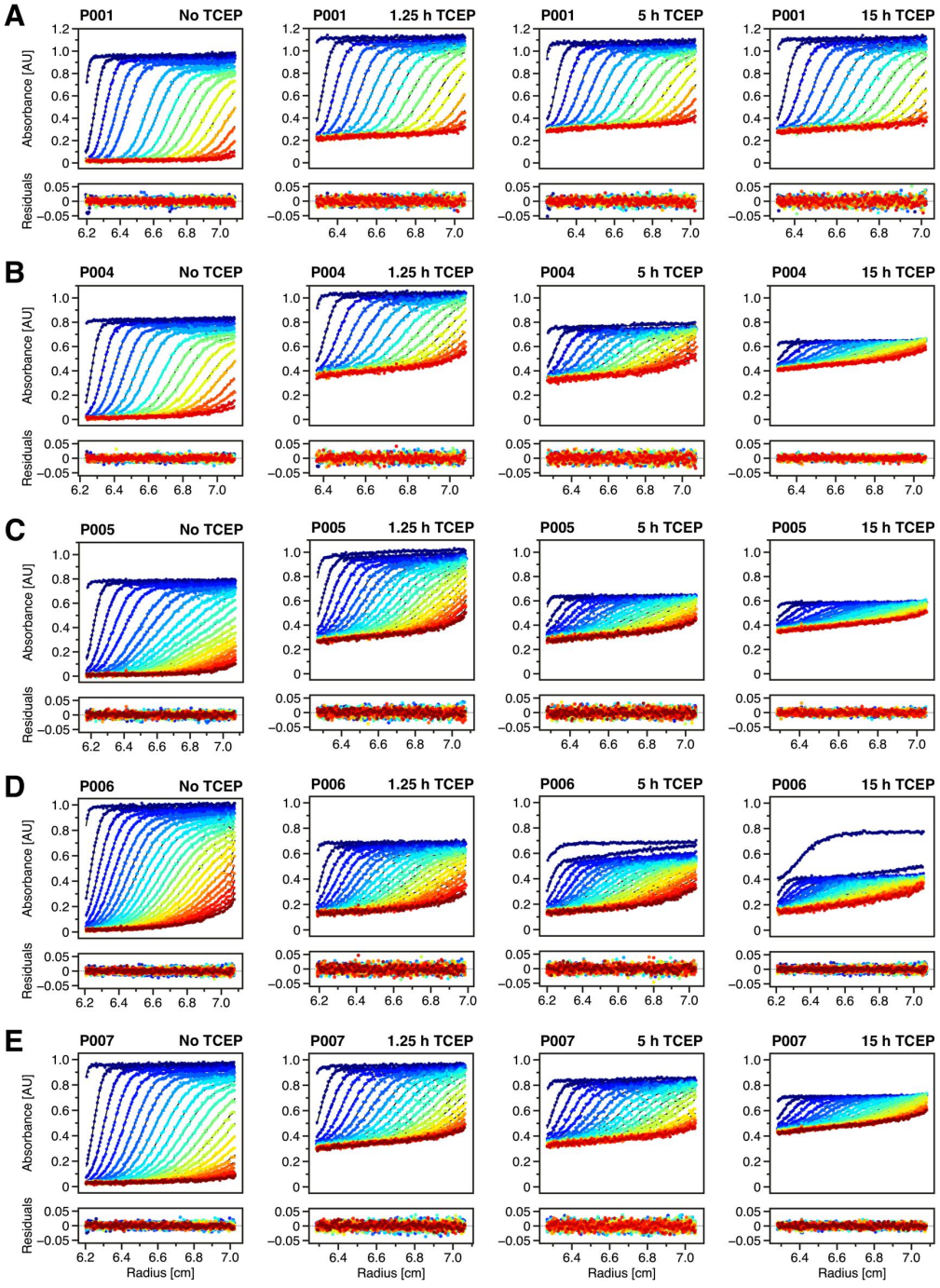

Figure 8.2A: Sedimentation profiles of FLC samples. Shown are the sedimentation profiles of patient samples (**A**) P001, (**B**) P004, (**C**) P005, (**D**) P006 and (**E**) P007, before and after TCEP treatment. A FLC concentration of 35 µM was measured in 30 mM Tris-HCl, pH 7.4. Disulfide bond destabilization was induced by the addition of 7 mM pH-adjusted TCEP, followed by incubation at 37°C and 600 rpm shaking for 1.25 h, 5 h and 15 h. A total of 70 scans were measured per sample, with every third scan displayed for clarity.

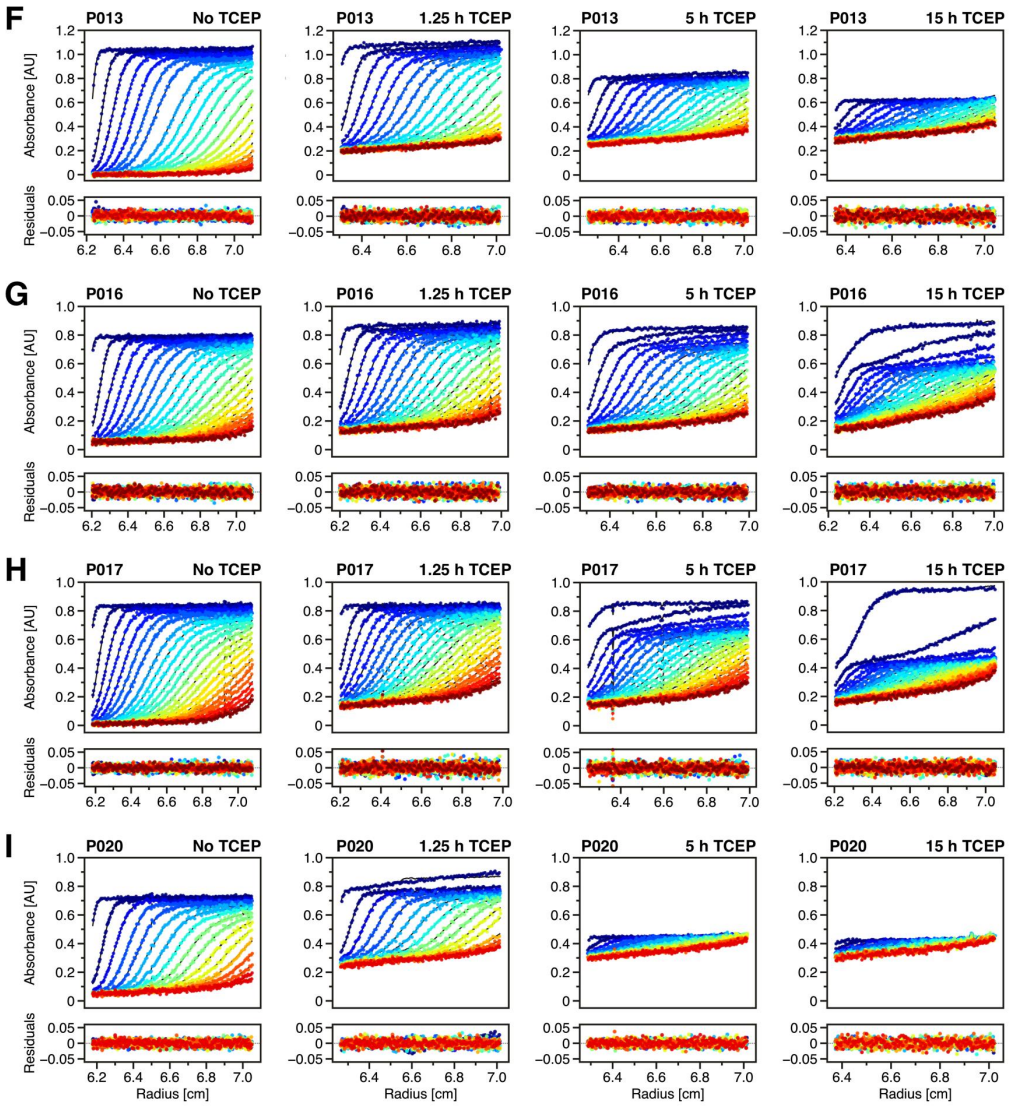

Figure 8.2B: Sedimentation profiles of FLC samples. Shown are the sedimentation profiles of patient samples (**F**) P013, (**G**) P016, (**H**) P017 and (**I**) P020, before and after TCEP treatment. A FLC concentration of 35 µM was measured in 30 mM Tris-HCl, pH 7.4. Disulfide bond destabilization was induced by the addition of 7 mM pH-adjusted TCEP, followed by incubation at 37°C and 600 rpm shaking for 1.25 h, 5 h and 15 h. A total of 70 scans were measured per sample, with every third scan displayed for clarity.

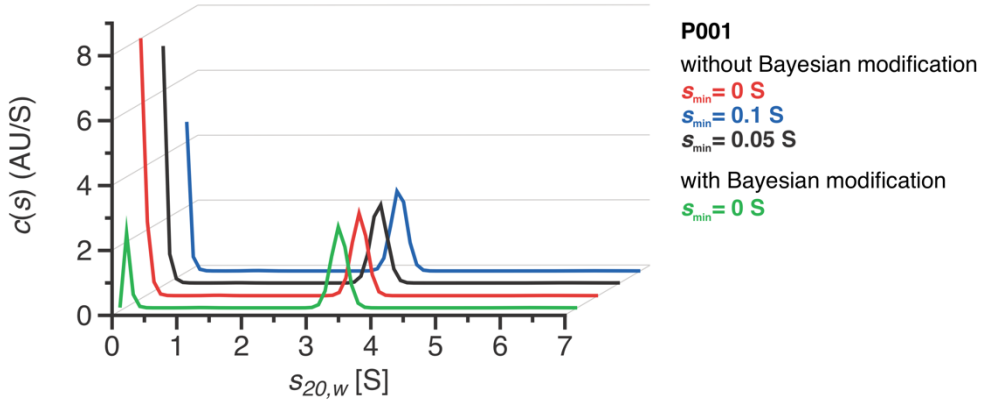

Figure 8.5: Effect of varying the minimum *s*-value limit (s_{min}) and of applying Bayesian modification on the detection of low-*S* species in sample P001. Plain maximum-entropy regularization was performed with s_{min} = 0 S (red), 0.05 S (black) and 0.1 S (blue); the same data were re-analyzed with Bayesian modification at s_{min} = 0 S (green). Half-peaks at s_{min} indicate that the lower boundary is constraining the fit, as described by Schuck (Schuck 2016): they grow taller as smin is lowered when baseline correlation is not suppressed. Setting s_{min} = 0 S and applying Bayesian modification removes this artifact and recovers the full peak that represents genuine low-*S* species (e.g., fragments or buffer components). The fragment peak at ~0.1 S is therefore a real, reproducible signal rather than a fitting artifact.

TCEP-induced changes in secondary structure of FLCs

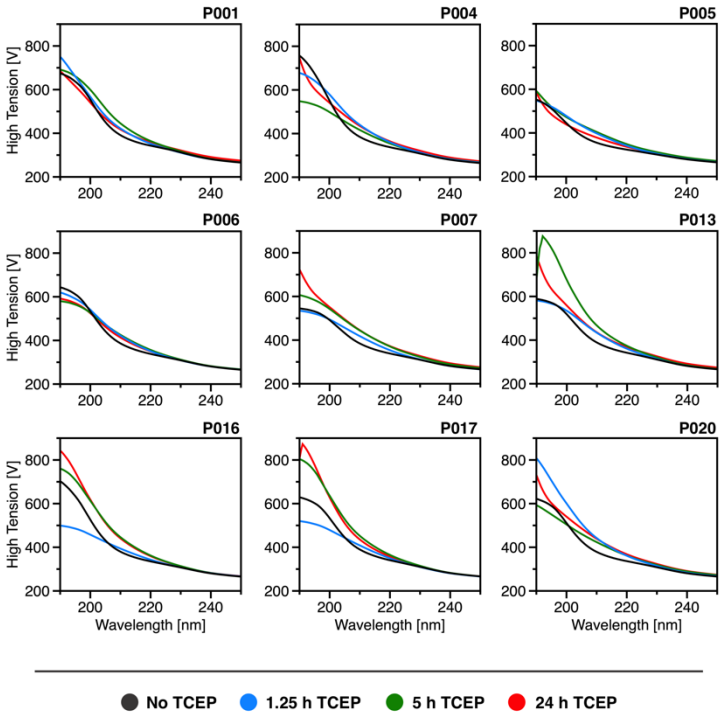

Figure 8.4: HT voltage records for the CD spectra of all nine FLC samples before and after TCEP treatment. For each sample, HT records are shown for the untreated state (black) and after incubation with 7 mM TCEP for 1.25 h (blue), 5 h (green) and 24 h (red) incubation time. Incubation was carried out with a sample concentration of 35 µM in 10 mM sodium phosphate buffer, pH 7.4 at 37°C. Aliquots were taken after specified time points and diluted to a final concentration of 9.23 µM for CD measurements.

Table 8.5: Position of zero-crossing of ellipticity (~200-210 nm) as function of TCEP incubation time.

Patient sample	Zero-crossing without TCEP [nm]	Zero-crossing after 1.25 h [nm]	Zero-crossing after 5 h [nm]	Zero-crossing after 15 h [nm]
P001	207.00	206.90	206.40	204.50
P004	207.00	206.70	198.00	199.70*
P005	205.10	200.20	196.00	197.70
P006	204.40	203.30	195.00	195.00
P007	206.00	199.40	198.90	200.00
P013	207.00	205.40	200.90	198.00*
P016	205.70	202.20	203.90	195.80*
P017	206.00	198.70	196.60*	200.00
P020	206.50	201.50	197.40	201.90

*HT values above 700 V at wavelength below 200 nm render the data unreliable

Modulating effects of the molecular species distribution of FLC

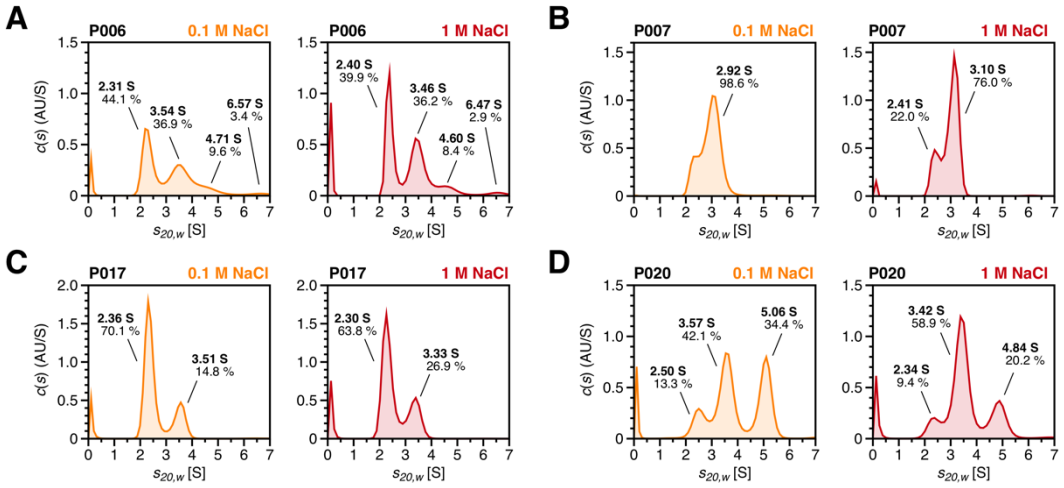

Figure 8.5: Effect of varying salt concentrations on the molecular species distribution of FLCs. Shown are the *c*(*s*) distributions for samples (**A**) P006, (**B**) P007, (**C**) P017, and (**D**) P020 with the addition of 0.1 M (orange) or 1 M (red) NaCl. A 30 mM Tris-HCl buffer at pH 7.4 and a FLC concentration of 35 µM was used. To reach equilibrium, the samples were incubated for 24 h at 25°C prior to measurement. After incubation, 390 µL of each sample was transferred to the sample sector of standard aluminum double-sector cells, and sedimentation analysis was performed at 60,000 rpm and 20°C.

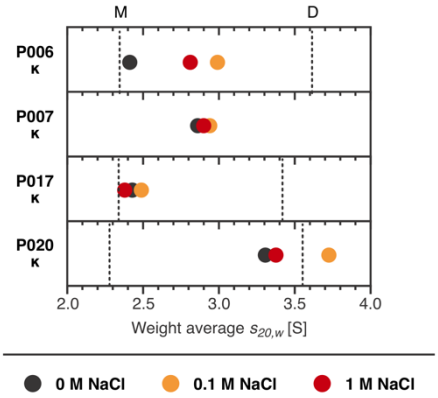

Figure 8.6: Salt-induced shifts in weight-average *s*-values of FLCs. Illustration of changes in weight-average *s*-values for samples P006, P007, P017, and P020, caused by the addition of 0.1 M (orange) or 1 M (red) NaCl. Corresponding weight-average *s*-values without NaCl addition are shown in black. The sedimentation range from 0 to 7 S was integrated to calculate the weight-average *s*-value, capturing the combined contribution of all species in this region and reflecting the overall distribution trend for each sample. Dashed lines labelled with 'M' and 'D' indicate *s*-values for individually identified monomers and dimers, representing their average *s*-value range across samples.

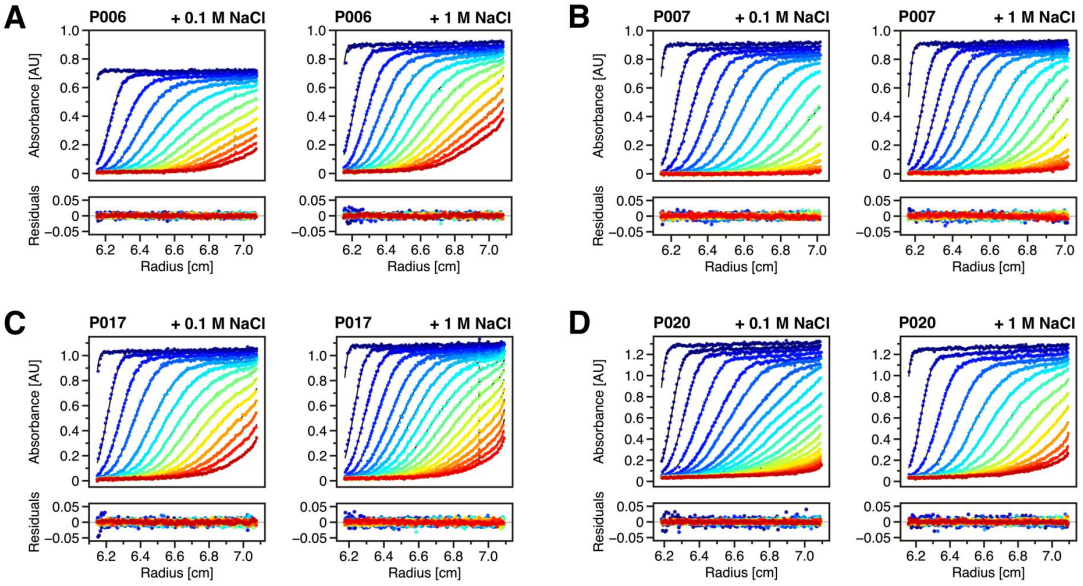

Figure 8.7: Sedimentation profiles of FLC samples with addition of 0.1 M and 1 M NaCl. The *c*(*s*) distributions of samples (**A**) P006, (**B**) P007, (**C**) P017 and (**D**) P020 are shown. A FLC concentration of 35 µM was measured prepared in 30 mM Tris-HCl buffer at pH 7.4, with the addition of 0.1 M or 1 M NaCl. To reach equilibrium, the samples were incubated for 24 h at 25°C prior to measurement. A total of 70 scans were measured per sample, with every third scan displayed for clarity.

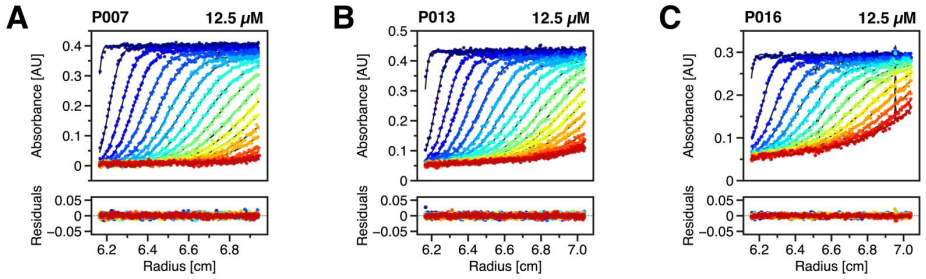

Figure 8.8: Sedimentation profiles of FLC samples at a concentration of 12.5 µM. The *c*(*s*) distributions of samples (**A**) P007, (**B**) P013 and (**C**) P016 are shown. All FLC samples were prepared at a concentration of 12.5 µM to investigate the presence of a dynamic monomer-dimer equilibrium. Samples were measured in 30 mM Tris-HCl buffer at pH 7.4. A total of 70 scans were measured per sample, with every third scan displayed for clarity.

Thermal stability of FLCs under reducing conditions

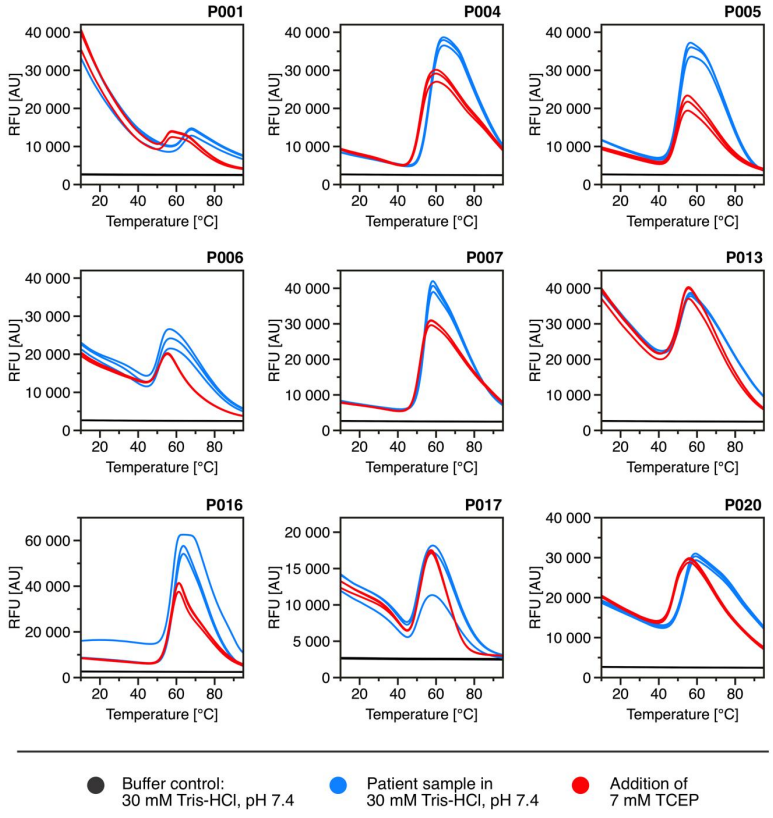

Figure 8.9: DSF data of all patient-derived FLCs. A sample concentration of 35 µM was prepared in 30 mM Tris-HCl, pH 7.4 (blue). To induce disulfide bond destabilization, 7 mM TCEP (red) were added in addition. Thermal denaturation was monitored using 10 µM SYPRO Orange in a total volume of 25 µL per well, measured in triplicate (n = 3). Presented are the thermal denaturation profiles for all nine FLC samples. Elevated pre-transition fluorescence suggests that SYPRO Orange binds to native LCs, unfolded species, or other sample components, such as LC fragments.

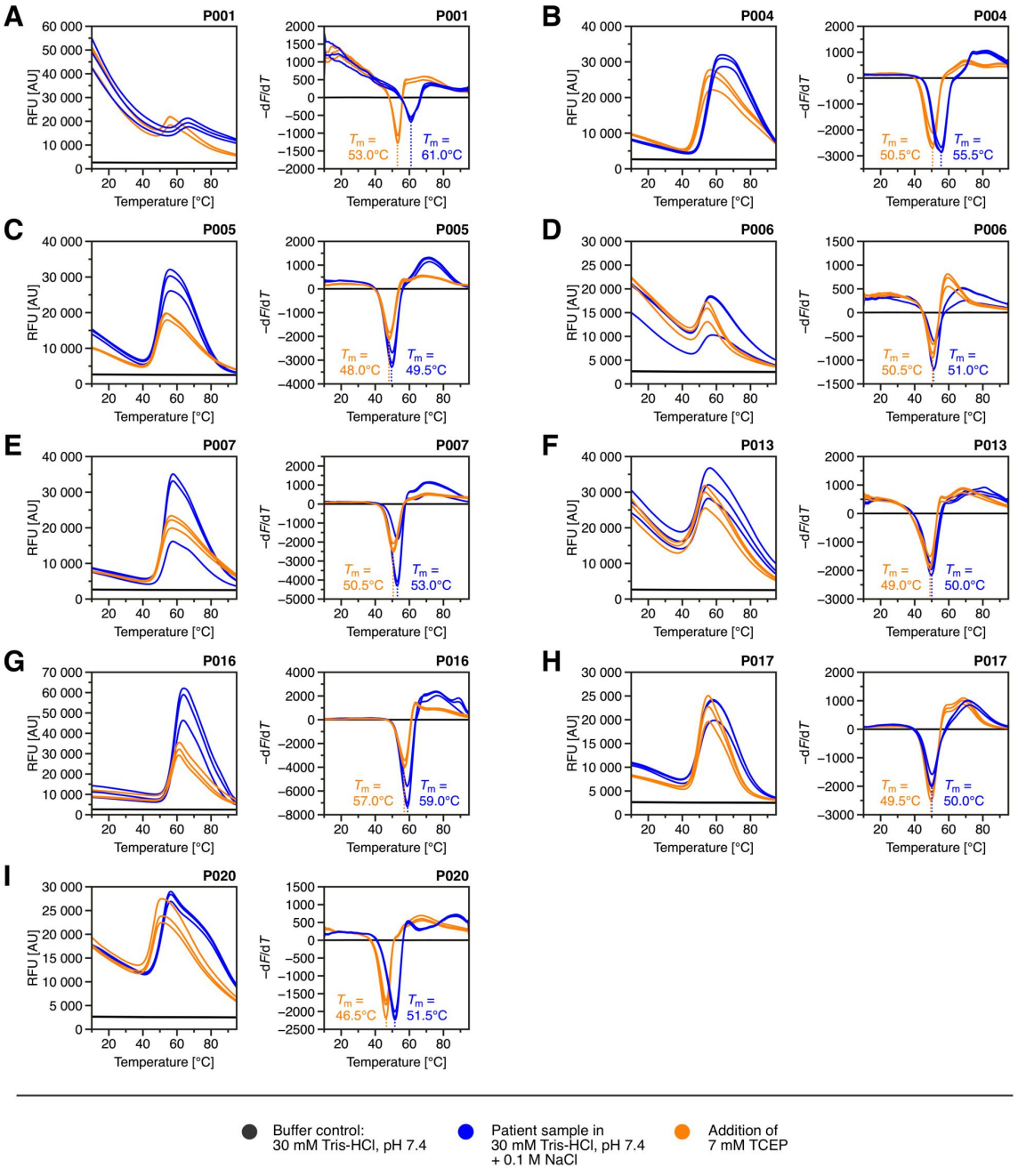

Figure 8.10: DSF data of all patient-derived FLCs with the addition of 0.1 M NaCl. A sample concentration of 35 µM was prepared in 30 mM Tris-HCl, pH 7.4 with the addition of 0.1 M NaCl (blue). To induce disulfide bond destabilization, 7 mM TCEP (orange) were added in addition. Thermal denaturation was monitored using 10 µM SYPRO Orange in a total volume of 25 µL per well, measured in triplicate (n = 3). The thermal denaturation profiles are presented alongside the corresponding negative derivative fluorescence-temperature plots (−d*F*/d*T*) for patient samples P001 (**A**), P004 (**B**), P005 (**C**), P006 (**D**), P007 (**E**), P013 (**F**), P016 (**G**), P017 (**H**) and P020 (**I**). Elevated pre-transition fluorescence suggests that SYPRO Orange binds to native LCs, unfolded species, or other sample components, such as LC fragments.

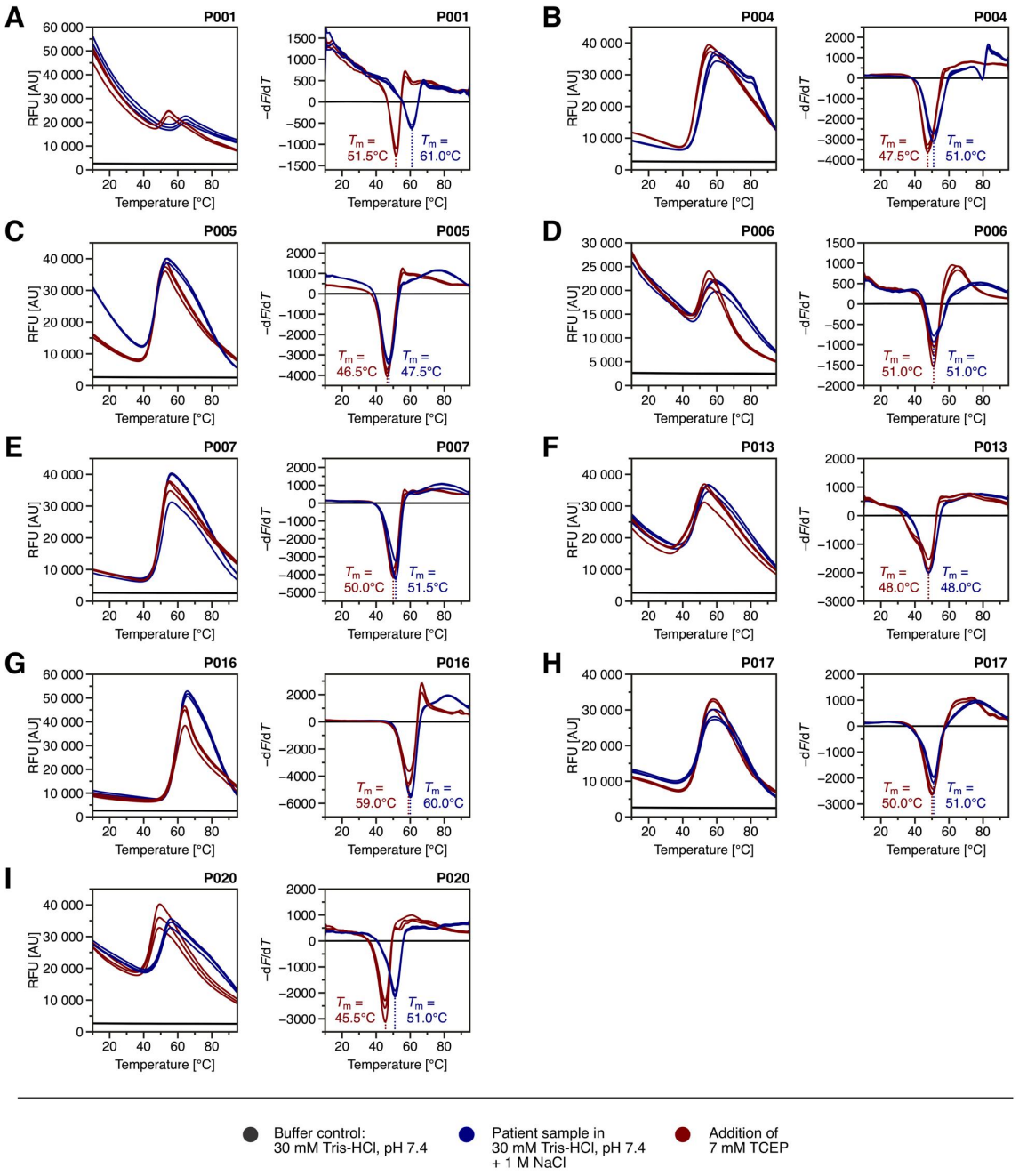

Figure 8.11: DSF data of all patient-derived FLCs with the addition of 1 M NaCl. A sample concentration of 35 µM was prepared in 30 mM Tris-HCl, pH 7.4 with the addition of 1 M NaCl (dark blue). To induce disulfide bond destabilization, 7 mM TCEP (dark red) were added in addition. Thermal denaturation was monitored using 10 µM SYPRO Orange in a total volume of 25 µL per well, measured in triplicate (n = 3). The thermal denaturation profiles are presented alongside the corresponding negative derivative fluorescence-temperature plots (−d*F*/d*T*) for patient samples P001 (**A**), P004 (**B**), P005 (**C**), P006 (**D**), P007 (**E**), P013 (**F**), P016 (**G**), P017 (**H**) and P020 (**I**). Elevated pre-transition fluorescence suggests that SYPRO Orange binds to native LCs, unfolded species, or other sample components, such as LC fragments.

8.3 Recombinant expression of a patient-derived FLC in *E. coli*: a folding pathway analysis

8.3.1 Supplementary methods

Table 8.6: Codon-optimized nucleotide sequence of the P006 gene insert. The sequence (639 bp) represents the coding region of the patient-derived FLC P006, optimized for expression of rLC6 in *E. coli*. The corresponding amino acid sequence is provided in the general Supplementary information (Tab. 8.2, P006).

```
GATCTGCAAATGACCCAGAGTCCGAGCAGCCTGAGCGCAAGCGTTGGTGATCGTGTTACCCTGACCTGTCAGGCAAGCCAGGATC
TGGCAAAATATCTGAATTGGTATCAGCAGAAACCGGGTAAACCGCCTAAACTGCTGCTGTATGATACCAGCAATCTGGAAACCGG
TGTTCCGAGCCGTTTTAGCAATGGTGGTGGCACCGATTTTACCTTTACACTGAATAGCCTGCAGCCGGAAGATCTGGCCACCTAT
TATTGTCAGCAGTATGATGATTTTCCGCTGACCTTTGGTCCGGGTACAAAAGTTGATCTGAAACGTACCGTTGCAGCACCGAGCG
TTTTTCTGTTTCCGCCTAGTGATGAACAGCTGAAAAGCGGCACCGCCAGCGTTGTTTGTCTGCTGAATAACTTTTATCCGCGTGA
AGCAAAAGTTCAGTGGAAAGTTGATAATGCACTGCAGAGCGGTAATAGCCAAGAAAGCGTTACCGAACAGGATAGCAAAGATAGC
ACCTATAGCCTGAGCAGCACCCTGACACTGAGCAAAGCAGATTATGAAAAACACAAAGTGTATGCCTGCGAAGTTACCCATCAGG
GTCTGAGCAGTCCGGTTACCAAAAGCTTTAATCGTGGTGAATGT
```

Table 8.7: Nucleotide sequence of the pET16-b-P006 expression construct. The construct was assembled for the recombinant expression of rLC6 in *E. coli*. The total vector length is 6,236 bp, and a schematic representation of the construct is shown in Figure 6.1A.

```
TTCTTGAAGACGAAAGGGCCTCGTGATACGCCTATTTTTATAGGTTAATGTCATGATAATAATGGTTTCTTAGACGTCAGGTGGC
ACTTTTCGGGGAAATGTGCGCGGAACCCCTATTTGTTTATTTTTCTAAATACATTCAAATATGTATCCGCTCATGAGACAATAAC
CCTGATAAATGCTTCAATAATATTGAAAAAGGAAGAGTATGAGTATTCAACATTTCCGTGTCGCCCTTATTCCCTTTTTTGCGGC
ATTTTGCCTTCCTGTTTTTGCTCACCCAGAAACGCTGGTGAAAGTAAAAGATGCTGAAGATCAGTTGGGTGCACGAGTGGGTTAC
ATCGAACTGGATCTCAACAGCGGTAAGATCCTTGAGAGTTTTCGCCCCGAAGAACGTTTTCCAATGATGAGCACTTTTAAAGTTC
TGCTATGTGGCGCGGTATTATCCCGTGTTGACGCCGGGCAAGAGCAACTCGGTCGCCGCATACACTATTCTCAGAATGACTTGGT
TGAGTACTCACCAGTCACAGAAAAGCATCTTACGGATGGCATGACAGTAAGAGAATTATGCAGTGCTGCCATAACCATGAGTGAT
AACACTGCGGCCAACTTACTTCTGACAACGATCGGAGGACCGAAGGAGCTAACCGCTTTTTTGCACAACATGGGGGATCATGTAA
CTCGCCTTGATCGTTGGGAACCGGAGCTGAATGAAGCCATACCAAACGACGAGCGTGACACCACGATGCCTGCAGCAATGGCAAC
AACGTTGCGCAAACTATTAACTGGCGAACTACTTACTCTAGCTTCCCGGCAACAATTAATAGACTGGATGGAGGCGGATAAAGTT
GCAGGACCACTTCTGCGCTCGGCCCTTCCGGCTGGCTGGTTTATTGCTGATAAATCTGGAGCCGGTGAGCGTGGGTCTCGCGGTA
TCATTGCAGCACTGGGGCCAGATGGTAAGCCCTCCCGTATCGTAGTTATCTACACGACGGGGAGTCAGGCAACTATGGATGAACG
AAATAGACAGATCGCTGAGATAGGTGCCTCACTGATTAAGCATTGGTAACTGTCAGACCAAGTTTACTCATATATACTTTAGATT
GATTTAAAACTTCATTTTTAATTTAAAAGGATCTAGGTGAAGATCCTTTTTGATAATCTCATGACCAAAATCCCTTAACGTGAGT
TTTCGTTCCACTGAGCGTCAGACCCCGTAGAAAAGATCAAAGGATCTTCTTGAGATCCTTTTTTTCTGCGCGTAATCTGCTGCTT
GCAAACAAAAAAACCACCGCTACCAGCGGTGGTTTGTTTGCCGGATCAAGAGCTACCAACTCTTTTTCCGAAGGTAACTGGCTTC
AGCAGAGCGCAGATACCAAATACTGTCCTTCTAGTGTAGCCGTAGTTAGGCCACCACTTCAAGAACTCTGTAGCACCGCCTACAT
ACCTCGCTCTGCTAATCCTGTTACCAGTGGCTGCTGCCAGTGGCGATAAGTCGTGTCTTACCGGGTTGGACTCAAGACGATAGTT
ACCGGATAAGGCGCAGCGGTCGGGCTGAACGGGGGGTTCGTGCACACAGCCCAGCTTGGAGCGAACGACCTACACCGAACTGAGA
TACCTACAGCGTGAGCTATGAGAAAGCGCCACGCTTCCCGAAGGGAGAAAGGCGGACAGGTATCCGGTAAGCGGCAGGGTCGGAA
CAGGAGAGCGCACGAGGGAGCTTCCAGGGGGAAACGCCTGGTATCTTTATAGTCCTGTCGGGTTTCGCCACCTCTGACTTGAGCG
TCGATTTTTGTGATGCTCGTCAGGGGGGCGGAGCCTATGGAAAAACGCCAGCAACGCGGCCTTTTTACGGTTCCTGGCCTTTTGC
TGGCCTTTTGCTCACATGTTCTTTCCTGCGTTATCCCCTGATTCTGTGGATAACCGTATTACCGCCTTTGAGTGAGCTGATACCG
CTCGCCGCAGCCGAACGACCGAGCGCAGCGAGTCAGTGAGCGAGGAAGCGGAAGAGCGCCTGATGCGGTATTTTCTCCTTACGCA
TCTGTGCGGTATTTCACACCGCATATATGGTGCACTCTCAGTACAATCTGCTCTGATGCCGCATAGTTAAGCCAGTATACACTCC
GCTATCGCTACGTGACTGGGTCATGGCTGCGCCCCGACACCCGCCAACACCCGCTGACGCGCCCTGACGGGCTTGTCTGCTCCCG
GCATCCGCTTACAGACAAGCTGTGACCGTCTCCGGGAGCTGCATGTGTCAGAGGTTTTCACCGTCATCACCGAAACGCGCGAGGC
AGCTGCGGTAAAGCTCATCAGCGTGGTCGTGAAGCGATTCACAGATGTCTGCCTGTTCATCCGCGTCCAGCTCGTTGAGTTTCTC
CAGAAGCGTTAATGTCTGGCTTCTGATAAAGCGGGCCATGTTAAGGGCGGTTTTTTCCTGTTTGGTCACTGATGCCTCCGTGTAA
GGGGGATTTCTGTTCATGGGGGTAATGATACCGATGAAACGAGAGAGGATGCTCACGATACGGGTTACTGATGATGAACATGCCC
```

GGTTACTGGAACGTTGTGAGGGTAAACAACTGGCGGTATGGATGCGGCGGGACCAGAGAAAAATCACTCAGGGTCAATGCCAGCG
CTTCGTTAATACAGATGTAGGTGTTCCACAGGGTAGCCAGCAGCATCCTGCGATGCAGATCCGGAACATAATGGTGCAGGGCGCT
GACTTCCGCGTTTCCAGACTTTACGAAACACGGAAACCGAAGACCATTCATGTTGTTGCTCAGGTCGCAGACGTTTTGCAGCAGC
AGTCGCTTCACGTTCGCTCGCGTATCGGTGATTCATTCTGCTAACCAGTAAGGCAACCCCGCCAGCCTAGCCGGGTCCTCAACGA
CAGGAGCACGATCATGCGCACCCGTGGCCAGGACCCAACGCTGCCCGAGATGCGCCGCGTGCGGCTGCTGGAGATGGCGGACGCG
ATGGATATGTTCTGCCAAGGGTTGGTTTGCGCATTCACAGTTCTCCGCAAGAATTGATTGGCTCCAATTCTTGGAGTGGTGAATC
CGTTAGCGAGGTGCCGCCGGCTTCCATTCAGGTCGAGGTGGCCCGGCTCCATGCACCGCGACGCAACGCGGGGAGGCAGACAAGG
TATAGGGCGGCGCCTACAATCCATGCCAACCCGTTCCATGTGCTCGCCGAGGCGGCATAAATCGCCGTGACGATCAGCGGTCCAG
TGATCGAAGTTAGGCTGGTAAGAGCCGCGAGCGATCCTTGAAGCTGTCCCTGATGGTCGTCATCTACCTGCCTGGACAGCATGGC
CTGCAACGCGGGCATCCCGATGCCGCCGGAAGCGAGAAGAATCATAATGGGGAAGGCCATCCAGCCTCGCGTCGCGAACGCCAGC
AAGACGTAGCCCAGCGCGTCGGCCGCCATGCCGGCGATAATGGCCTGCTTCTCGCCGAAACGTTTGGTGGCGGGACCAGTGACGA
AGGCTTGAGCGAGGGCGTGCAAGATTCCGAATACCGCAAGCGACAGGCCGATCATCGTCGCGCTCCAGCGAAAGCGGTCCTCGCC
GAAAATGACCCAGAGCGCTGCCGGCACCTGTCCTACGAGTTGCATGATAAAGAAGACAGTCATAAGTGCGGCGACGATAGTCATG
CCCCGCGCCCACCGGAAGGAGCTGACTGGGTTGAAGGCTCTCAAGGGCATCGGTCGAGATCCCGGTGCCTAATGAGTGAGCTAAC
TTACATTAATTGCGTTGCGCTCACTGCCCGCTTTCCAGTCGGGAAACCTGTCGTGCCAGCTGCATTAATGAATCGGCCAACGCGC
GGGGAGAGGCGGTTTGCGTATTGGGCGCCAGGGTGGTTTTTCTTTTCACCAGTGAGACGGGCAACAGCTGATTGCCCTTCACCGC
CTGGCCCTGAGAGAGTTGCAGCAAGCGGTCCACGCTGGTTTGCCCCAGCAGGCGAAAATCCTGTTTGATGGTGGTTAACGGCGGG
ATATAACATGAGCTGTAACTAGCATAACCCTCTTCGGTATCGTCGTATCCCACTACCGAGATATCCGCACCAACGCGCAGCCCGG
ACTCGGTAATGGCGCGCATTGCGCCCAGCGCCATCTGATCGTTGGCAACCAGCATCGCAGTGGGAACGATGCCCTCATTCAGCAT
TTGCATGGTTTGTTGAAAACCGGACATGGCACTCCAGTCGCCTTCCCGTTCCGCTATCGGCTGAATTTGATTGCGAGTGAGATAT
TTATGCCAGCCAGCCAGACGCAGACGCGCCGAGACAGAACTTAATGGGCCCGCTAACAGCGCGATTTGCTGGTGACCCAATGCGA
CCAGATGCTCCACGCCCAGTCGCGTACCGTCTTCATGGGAGAAAATAATACTGTTGATGGGTGTCTGGTCAGAGACATCAAGAAA
TAACGCCGGAACATTAGTGCAGGCAGCTTCCACAGCAATGGCATCCTGGTCATCCAGCGGATAGTTAATGATCAGCCCACTGACG
CGTTGCGCGAGAAGATTGTGCACCGCCGCTTTACAGGCTTCGACGCCGCTTCGTTCTACCATCGACACCACCACGCTGGCACCCA
GTTGATCGGCGCGAGATTTAATCGCCGCGACAATTTGCGACGGCGCGTGCAGGGCCAGACTGGAGGTGGCAACGCCAATCAGCAA
CGACTGTTTGCCCGCCAGTTGTTGTGCCACGCGGTTGGGAATGTAATTCAGCTCCGCCATCGCCGCTTCCACTTTTTCCCGCGTT
TTCGCAGAAACGTGGCTGGCCTGGTTCACCACGCGGGAAACGGTCTGATAAGAGACACCGGCATACTCTGCGACATCGTATAACG
TTACTGGTTTCACATTCACCACCCTGAATTGACTCTCTTCCGGGCGCTATCATGCCATACCGCGAAAGGTTTTGCGCCATTCGAT
GGTGTCCGGGATCTCGACGCTCTCCCTTATGCGACTCCTGCATTAGGAAGCAGCCCAGTAGTAGGTTGAGGCCGTTGAGCACCGC
CGCCGCAAGGAATGGTGCATGCAAGGAGATGGCGCCCAACAGTCCCCCGGCCACGGGGCCTGCCACCATACCCACGCCGAAACAA
GCGCTCATGAGCCCGAAGTGGCGAGCCCGATCTTCCCCATCGGTGATGTCGGCGATATAGGCGCCAGCAACCGCACCTGTGGCGC
CGGTGATGCCGGCCACGATGCGTCCGGCGTAGAGGATCGAGATCTCGATCCCGCGAAATTAATACGACTCACTATAGGGGAATTG
TGAGCGGATAACAATTCCCCTCTAGAAATAATTTTGTTTAACTTTAAGAAGGAGATATACCATGGATCTGCAAATGACCCAGAGT
CCGAGCAGCCTGAGCGCAAGCGTTGGTGATCGTGTTACCCTGACCTGTCAGGCAAGCCAGGATCTGGCAAAATATCTGAATTGGT
ATCAGCAGAAACCGGGTAAACCGCCTAAACTGCTGCTGTATGATACCAGCAATCTGGAAACCGGTGTTCCGAGCCGTTTTAGCAA
TGGTGGTGGCACCGATTTTACCTTTACACTGAATAGCCTGCAGCCGGAAGATCTGGCCACCTATTATTGTCAGCAGTATGATGAT
TTTCCGCTGACCTTTGGTCCGGGTACAAAAGTTGATCTGAAACGTACCGTTGCAGCACCGAGCGTTTTTCTGTTTCCGCCTAGTG
ATGAACAGCTGAAAAGCGGCACCGCCAGCGTTGTTTGTCTGCTGAATAACTTTTATCCGCGTGAAGCAAAAGTTCAGTGGAAAGT
TGATAATGCACTGCAGAGCGGTAATAGCCAAGAAAGCGTTACCGAACAGGATAGCAAAGATAGCACCTATAGCCTGAGCAGCACC
CTGACACTGAGCAAAGCAGATTATGAAAAACACAAAGTGTATGCCTGCGAAGTTACCCATCAGGGTCTGAGCAGTCCGGTTACCA
AAAGCTTTAATCGTGGTGAATGTTAACTAGCATAACCCCTTGGGGCCTCTAAACGGGTCTTGAGGGGTTTTTTGCTGAAAGGAGG
AACTATATCCGGATATCCCGCAAGAGGCCCGGCAGTACCGGCATAACCAAGCCTATGCCTACAGCATCCAGGGTGACGGTGCCGA
GGATGACGATGAGCGCATTGTTAGATTTCATACACGGTGCCTGACTGCGTTAGCAATTTAACTGTGATAAACTACCGCATTAAAG
CTTATCGATGATAAGCTGTCAAACATGAGAA

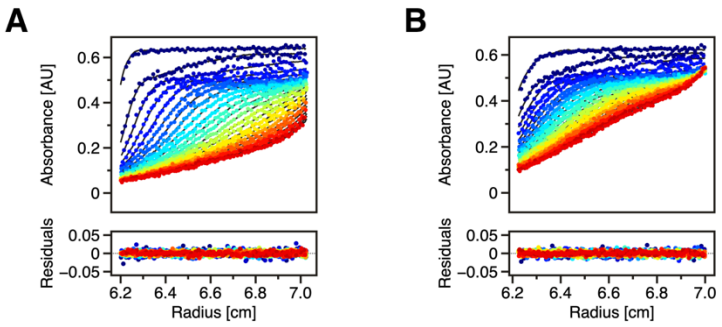

Figure 8.12: Protocol 1: Sedimentation profiles of rLC6. Shown are the sedimentation profiles of rLC6 obtained using Protocol 1. (**A**) rLC6 under native conditions and (**B**) rLC6 after 1.25 h of TCEP treatment. Samples were measured at a concentration of 35 µM in 30 mM Tris-HCl (pH 7.4). Disulfide bond reduction was induced by adding of 7 mM pH-adjusted TCEP, followed by incubation of the sample at 37°C and 600 rpm shaking for 1.25 h. A total of 70 scans were measured per sample, with every third scan displayed for clarity.

Table 8.8: Nucleotide sequence of the pCHAP-P006 expression construct. The construct was assembled for the recombinant expression of rLC6 in the periplasmic space of *E. coli*. The total vector length is 5,029 bp, and a schematic representation of the construct is shown in Figure 5.19A.

GGGGAATTGTGAGCGGATAACAATTCCCCTGTAGAAATAATTTTGTTTAACTTTAATAAGGAGATATACCATGAAGAAGAATATC
GCATTTCTGCTGGCGAGCATGTTTGTTTTTAGCATTGCAACCAATGCATATGCCAGCGATCTGCAAATGACCCAGAGTCCGAGCA
GCCTGAGCGCAAGCGTTGGTGATCGTGTTACCCTGACCTGTCAGGCAAGCCAGGATCTGGCAAAATATCTGAATTGGTATCAGCA
GAAACCGGGTAAACCGCCTAAACTGCTGCTGTATGATACCAGCAATCTGGAAACCGGTGTTCCGAGCCGTTTTAGCAATGGTGGT
GGCACCGATTTTACCTTTACACTGAATAGCCTGCAGCCGGAAGATCTGGCCACCTATTATTGTCAGCAGTATGATGATTTTCCGC
TGACCTTTGGTCCGGGTACAAAAGTTGATCTGAAACGTACCGTTGCAGCACCGAGCGTTTTTCTGTTTCCGCCTAGTGATGAACA
GCTGAAAAGCGGCACCGCCAGCGTTGTTTGTCTGCTGAATAACTTTTATCCGCGTGAAGCAAAAGTTCAGTGGAAAGTTGATAAT
GCACTGCAGAGCGGTAATAGCCAAGAAAGCGTTACCGAACAGGATAGCAAAGATAGCACCTATAGCCTGAGCAGCACCCTGACAC
TGAGCAAAGCAGATTATGAAAAACACAAAGTGTATGCCTGCGAAGTTACCCATCAGGGTCTGAGCAGTCCGGTTACCAAAAGCTT
TAATCGTGGTGAATGTCACCATCACCATCACCATCACCATTGATAAAGCTTGCGGCCGCATAATGCTTAAGTCGAACAGAAAGTA
ATCGTATTGTACACGGCCGCATAATCGAAATTAATACGACTCACTATAGGGGAATTGTGAGCGGATAACAATTCCCCATCTTAGT
ATATTAGTTAAGTATAAGAAGGAGATATACATATGAAAAAATGGCTGCTGGCAGCAGGTCTGGGTTTAGCACTGGCAACCAGCGC
ACAGGCAGCAGATAAAATTGCCATTGTTAATATGGGTAGCCTGTTTCAGCAGGTTGCACAGAAAACCGGTGTTAGCAATACCCTG
GAAAATGAATTTAAAGGTCGTGCAAGCGAACTGCAGCGTATGGAAACCGATCTGCAGGCAAAAATGAAAAAACTGCAGAGCATGA
AAGCAGGTAGCGATCGTACCAAACTGGAAAAAGATGTTATGGCACAGCGTCAGACCTTTGCGCAGAAAGCACAGGCATTTGAACA
GGATCGTGCACGTCGTAGCAATGAAGAACGTGGTAAACTGGTTACCCGTATTCAGACCGCAGTTAAAAGCGTTGCAAATAGCCAG
GATATTGATCTGGTTGTTGATGCAAATGCCGTTGCCTATAATAGCAGTGATGTGAAAGATATTACCGCAGACGTTCTGAAGCAGG
TCAAATAACCTAGGCTGCTGCCACCGCTGAGCAATAACTAGCATAACCCCTTGGGGCCTCTAAACGGGTCTTGAGGGGTTTTTTG
CTGAAACCTCAGGCATTTGAGAAGCACACGGTCACACTGCTTCCGGTAGTCAATAAACCGGTAAACCAGCAATAGACATAAGCGG
CTATTTAACGACCCTGCCCTGAACCGACGACCGGGTCGAATTTGCTTTCGAATTTCTGCCATTCATCCGCTTATTATCACTTATT
CAGGCGTAGCACCAGGCGTTTAAGGGCACCAATAACTGCCTTAAAAAAATTACGCCCCGCCCTGCCACTCATCGCAGTACTGTTG
TAATTCATTAAGCATTCTGCCGACATGGAAGCCATCACAGACGGCATGATGAACCTGAATCGCCAGCGGCATCAGCACCTTGTCG
CCTTGCGTATAATATTTGCCCATAGTGAAAACGGGGGCGAAGAAGTTGTCCATATTGGCCACGTTTAAATCAAAACTGGTGAAAC
TCACCCAGGGATTGGCTGAGACGAAAAACATATTCTCAATAAACCCTTTAGGGAAATAGGCCAGGTTTTCACCGTAACACGCCAC
ATCTTGCGAATATATGTGTAGAAACTGCCGGAAATCGTCGTGGTATTCACTCCAGAGCGATGAAAACGTTTCAGTTTGCTCATGG
AAAACGGTGTAACAAGGGTGAACACTATCCCATATCACCAGCTCACCGTCTTTCATTGCCATACGGAACTCCGGATGAGCATTCA
TCAGGCGGGCAAGAATGTGAATAAAGGCCGGATAAAACTTGTGCTTATTTTTCTTTACGGTCTTTAAAAAGGCCGTAATATCCAG
CTGAACGGTCTGGTTATAGGTACATTGAGCAACTGACTGAAATGCCTCAAAATGTTCTTTACGATGCCATTGGGATATATCAACG
GTGGTATATCCAGTGATTTTTTTCTCCATTTTAGCTTCCTTAGCTCCTGAAAATCTCGATAACTCAAAAAATACGCCCGGTAGTG
ATCTTATTTCATTATGGTGAAAGTTGGAACCTCTTACGTGCCGATCAACGTCTCATTTTCGCCAAAAGTTGGCCCAGGGCTTCCC
GGTATCAACAGGGACACCAGGATTTATTTATTCTGCGAAGTGATCTTCCGTCACAGGTATTTATTCGGCGCAAAGTGCGTCGGGT
GATGCTGCCAACTTACTGATTTAGTGTATGATGGTGTTTTTGAGGTGCTCCAGTGGCTTCTGTTTCTATCAGCTGTCCCTCCTGT
TCAGCTACTGACGGGGTGGTGCGTAACGGCAAAAGCACCGCCGGACATCAGCGCTAGCGGAGTGTATACTGGCTTACTATGTTGG
CACTGATGAGGGTGTCAGTGAAGTGCTTCATGTGGCAGGAGAAAAAAGGCTGCACCGGTGCGTCAGCAGAATATGTGATACAGGA

TATATTCCGCTTCCTCGCTCACTGACTCGCTACGCTCGGTCGTTCGACTGCGGCGAGCGGAAATGGCTTACGAACGGGGCGGAGA
TTTCCTGGAAGATGCCAGGAAGATACTTAACAGGGAAGTGAGAGGGCCGCGGCAAAGCCGTTTTTCCATAGGCTCCGCCCCCCTG
ACAAGCATCACGAAATCTGACGCTCAAATCAGTGGTGGCGAAACCCGACAGGACTATAAAGATACCAGGCGTTTCCCCTGGCGGC
TCCCTCGTGCGCTCTCCTGTTCCTGCCTTTCGGTTTACCGGTGTCATTCCGCTGTTATGGCCGCGTTTGTCTCATTCCACGCCTG
ACACTCAGTTCCGGGTAGGCAGTTCGCTCCAAGCTGGACTGTATGCACGAACCCCCCGTTCAGTCCGACCGCTGCGCCTTATCCG
GTAACTATCGTCTTGAGTCCAACCCGGAAAGACATGCAAAAGCACCACTGGCAGCAGCCACTGGTAATTGATTTAGAGGAGTTAG
TCTTGAAGTCATGCGCCGGTTAAGGCTAAACTGAAAGGACAAGTTTTGGTGACTGCGCTCCTCCAAGCCAGTTACCTCGGTTCAA
AGAGTTGGTAGCTCAGAGAACCTTCGAAAAACCGCCCTGCAAGGCGGTTTTTTCGTTTTCAGAGCAAGAGATTACGCGCAGACCA
AAACGATCTCAAGAAGATCATCTTATTAATCAGATAAAATATTTCTAGATTTCAGTGCAATTTATCTCTTCAAATGTAGCACCTG
AAGTCAGCCCCATACGATATAAGTTGTAATTCTCATGTTAGTCATGCCCCGCGCCCACCGGAAGGAGCTGACTGGGTTGAAGGCT
CTCAAGGGCATCGGTCGAGATCCCGGTGCCTAATGAGTGAGCTAACTTACATTAATTGCGTTGCGCTCACTGCCCGCTTTCCAGT
CGGGAAACCTGTCGTGCCAGCTGCATTAATGAATCGGCCAACGCGCGGGGAGAGGCGGTTTGCGTATTGGGCGCCAGGGTGGTTT
TTCTTTTCACCAGTGAGACGGGCAACAGCTGATTGCCCTTCACCGCCTGGCCCTGAGAGAGTTGCAGCAAGCGGTCCACGCTGGT
TTGCCCCAGCAGGCGAAAATCCTGTTTGATGGTGGTTAACGGCGGGATATAACATGAGCTGTCTTCGGTATCGTCGTATCCCACT
ACCGAGATGTCCGCACCAACGCGCAGCCCGGACTCGGTAATGGCGCGCATTGCGCCCAGCGCCATCTGATCGTTGGCAACCAGCA
TCGCAGTGGGAACGATGCCCTCATTCAGCATTTGCATGGTTTGTTGAAAACCGGACATGGCACTCCAGTCGCCTTCCCGTTCCGC
TATCGGCTGAATTTGATTGCGAGTGAGATATTTATGCCAGCCAGCCAGACGCAGACGCGCCGAGACAGAACTTAATGGGCCCGCT
AACAGCGCGATTTGCTGGTGACCCAATGCGACCAGATGCTCCACGCCCAGTCGCGTACCGTCTTCATGGGAGAAAATAATACTGT
TGATGGGTGTCTGGTCAGAGACATCAAGAAATAACGCCGGAACATTAGTGCAGGCAGCTTCCACAGCAATGGCATCCTGGTCATC
CAGCGGATAGTTAATGATCAGCCCACTGACGCGTTGCGCGAGAAGATTGTGCACCGCCGCTTTACAGGCTTCGACGCCGCTTCGT
TCTACCATCGACACCACCACGCTGGCACCCAGTTGATCGGCGCGAGATTTAATCGCCGCGACAATTTGCGACGGCGCGTGCAGGG
CCAGACTGGAGGTGGCAACGCCAATCAGCAACGACTGTTTGCCCGCCAGTTGTTGTGCCACGCGGTTGGGAATGTAATTCAGCTC
CGCCATCGCCGCTTCCACTTTTTCCCGCGTTTTCGCAGAAACGTGGCTGGCCTGGTTCACCACGCGGGAAACGGTCTGATAAGAG
ACACCGGCATACTCTGCGACATCGTATAACGTTACTGGTTTCACATTCACCACCCTGAATTGACTCTCTTCCGGGCGCTATCATG
CCATACCGCGAAAGGTTTTGCGCCATTCGATGGTGTCCGGGATCTCGACGCTCTCCCTTATGCGACTCCTGCATTAGGAAATTAA
TACGACTCACTATA

8.4 Recombinant expression and structural validation of a pathogenic patient-derived free light chain in *Pichia pastoris*

8.4.1 Supplementary methods

Table 8.9: Nucleotide sequence of the expression vector pPICZαA containing the P004 gene insert. The coding sequence of P004 (698 bp) was codon-optimized for efficient expression in *P. pastoris*. The complete expression construct comprises a total length of 4210 bp.

```
AGATCTAACATCCAAAGACGAAAGGTTGAATGAAACCTTTTTGCCATCCGACATCCACAGGTCCATTCTCACACATAAGTGCCAA
ACGCAACAGGAGGGGATACACTAGCAGCAGACCGTTGCAAACGCAGGACCTCCACTCCTCTTCTCCTCAACACCCACTTTTGCCA
TCGAAAAACCAGCCCAGTTATTGGGCTTGATTGGAGCTCGCTCATTCCAATTCCTTCTATTAGGCTACTAACACCATGACTTTAT
TAGCCTGTCTATCCTGGCCCCCCTGGCGAGGTTCATGTTTGTTTATTTCCGAATGCAACAAGCTCCGCATTACACCCGAACATCA
CTCCAGATGAGGGCTTTCTGAGTGTGGGGTCAAATAGTTTCATGTTCCCCAAATGGCCCAAAACTGACAGTTTAAACGCTGTCTT
GGAACCTAATATGACAAAAGCGTGATCTCATCCAAGATGAACTAAGTTTGGTTCGTTGAAATGCTAACGGCCAGTTGGTCAAAAA
GAAACTTCCAAAAGTCGGCATACCGTTTGTCTTGTTTGGTATTGATTGACGAATGCTCAAAAATAATCTCATTAATGCTTAGCGC
AGTCTCTCTATCGCTTCTGAACCCCGGTGCACCTGTGCCGAAACGCAAATGGGGAAACACCCGCTTTTTGGATGATTATGCATTG
TCTCCACATTGTATGCTTCCAAGATTCTGGTGGGAATACTGCTGATAGCCTAACGTTCATGATCAAAATTTAACTGTTCTAACCC
CTACTTGACAGCAATATATAAACAGAAGGAAGCTGCCCTGTCTTAAACCTTTTTTTTTATCATCATTATTAGCTTACTTTCATAA
TTGCGACTGGTTCCAATTGACAAGCTTTTGATTTTAACGACTTTTAACGACAACTTGAGAAGATCAAAAAACAACTAATTATTCG
AAACGATGAGATTTCCTTCAATTTTTACTGCTGTTTTATTCGCAGCATCCTCCGCATTAGCTGCTCCAGTCAACACTACAACAGA
AGATGAAACGGCACAAATTCCGGCTGAAGCTGTCATCGGTTACTCAGATTTAGAAGGGGATTTCGATGTTGCTGTTTTGCCATTT
TCCAACAGCACAAATAACGGGTTATTGTTTATAAATACTACTATTGCCAGCATTGCTGCTAAAGAAGAAGGGGTATCTCTCGAGA
AAAGAGAGGCTGAAGCTGAAATCGTTCTTACTCAATCTCCTGGTACTCTTAGTCTTAGTCCTGGTGAAAGAGCTACTCTTAGTTG
TAGAGCTTCTCAATCTGTTAGTTCTTCTTACTTGGCTTGGTATCAACAAAAACCAGGTCAAGCTCCAAGATTGTTGATCTATGAT
GCTTCTACTAGAGCTACTGGTATTCCAGATAGATTCTCTGGTTCTGGTTCTGGAGCTGACTTCTTGTTGACTATTAGTTCTCTTG
AACCAGAAGACTTCGCTATGTACTATTGTCAACAATATGGTAGATCTCCATACACCTTCGGTCCAGGTACTAAGGTTGATATTAA
AAGAACTGTTGCTGCTCCTTCTGTCTTCATCTTCCCACCATCTGATGAACAATTGAAATCTGGTACTGCTTCTGTTGTCTGTCTT
CTTAACAACTTCTATCCAAGAGAAGCTAAGGTTCAATGGAAAGTTGATAACGCTCTTCAATCTGGTAATTCTCAAGAATCTGTTA
CTGAACAAGATTCTAAGGATTCTACTTATTCTCTTAGTTCTACTCTTACTCTTAGTAAGGCTGATTATGAAAAGCATAAAGTCTA
TGCTTGTGAAGTTACTCATCAAGGTCTTAGTTCTCCAGTTACTAAATCCTTCAATAGAGGTGAATGTCATCATCATCATCATCAT
TGAGCGGCCGCCAGCTTTCTAGAACAAAAACTCATCTCAGAAGAGGATCTGAATAGCGCCGTCGACCATCATCATCATCATCATT
GAGTTTGTAGCCTTAGACATGACTGTTCCTCAGTTCAAGTTGGGCACTTACGAGAAGACCGGTCTTGCTAGATTCTAATCAAGAG
GATGTCAGAATGCCATTTGCCTGAGAGATGCAGGCTTCATTTTTGATACTTTTTTATTTGTAACCTATATAGTATAGGATTTTTT
TTGTCATTTTGTTTCTTCTCGTACGAGCTTGCTCCTGATCAGCCTATCTCGCAGCTGATGAATATCTTGTGGTAGGGGTTTGGGA
AAATCATTCGAGTTTGATGTTTTTCTTGGTATTTCCCACTCCTCTTCAGAGTACAGAAGATTAAGTGAGACCTTCGTTTGTGCGG
ATCCCCCACACACCATAGCTTCAAAATGTTTCTACTCCTTTTTTACTCTTCCAGATTTTCTCGGACTCCGCGCATCGCCGTACCA
CTTCAAAACACCCAAGCACAGCATACTAAATTTTCCCTCTTTCTTCCTCTAGGGTGTCGTTAATTACCCGTACTAAAGGTTTGGA
AAAGAAAAAAGAGACCGCCTCGTTTCTTTTTCTTCGTCGAAAAAGGCAATAAAAATTTTTATCACGTTTCTTTTTCTTGAAATTT
TTTTTTTTAGTTTTTTTCTCTTTCAGTGACCTCCATTGATATTTAAGTTAATAAACGGTCTTCAATTTCTCAAGTTTCAGTTTCA
TTTTTCTTGTTCTATTACAACTTTTTTTACTTCTTGTTCATTAGAAAGAAAGCATAGCAATCTAATCTAAGGGGCGGTGTTGACA
ATTAATCATCGGCATAGTATATCGGCATAGTATAATACGACAAGGTGAGGAACTAAACCATGGCCAAGTTGACCAGTGCCGTTCC
GGTGCTCACCGCGCGCGACGTCGCCGGAGCGGTCGAGTTCTGGACCGACCGGCTCGGGTTCTCCCGGGACTTCGTGGAGGACGAC
TTCGCCGGTGTGGTCCGGGACGACGTGACCCTGTTCATCAGCGCGGTCCAGGACCAGGTGGTGCCGGACAACACCCTGGCCTGGG
TGTGGGTGCGCGGCCTGGACGAGCTGTACGCCGAGTGGTCGGAGGTCGTGTCCACGAACTTCCGGGACGCCTCCGGGCCGGCCAT
GACCGAGATCGGCGAGCAGCCGTGGGGGCGGGAGTTCGCCCTGCGCGACCCGGCCGGCAACTGCGTGCACTTCGTGGCCGAGGAG
CAGGACTGACACGTCCGACGGCGGCCCACGGGTCCCAGGCCTCGGAGATCCGTCCCCCTTTTCCTTTGTCGATATCATGTAATTA
GTTATGTCACGCTTACATTCACGCCCTCCCCCCACATCCGCTCTAACCGAAAAGGAAGGAGTTAGACAACCTGAAGTCTAGGTCC
CTATTTATTTTTTTATAGTTATGTTAGTATTAAGAACGTTATTTATATTTCAAATTTTTCTTTTTTTTCTGTACAGACGCGTGTA
CGCATGTAACATTATACTGAAAACCTTGCTTGAGAAGGTTTTGGGACGCTCGAAGGCTTTAATTTGCAAGCTGGAGACCAACATG
TGAGCAAAAGGCCAGCAAAAGGCCAGGAACCGTAAAAAGGCCGCGTTGCTGGCGTTTTTCCATAGGCTCCGCCCCCCTGACGAGC
ATCACAAAAATCGACGCTCAAGTCAGAGGTGGCGAAACCCGACAGGACTATAAAGATACCAGGCGTTTCCCCCTGGAAGCTCCCT
CGTGCGCTCTCCTGTTCCGACCCTGCCGCTTACCGGATACCTGTCCGCCTTTCTCCCTTCGGGAAGCGTGGCGCTTTCTCAATGC
```

TCACGCTGTAGGTATCTCAGTTCGGTGTAGGTCGTTCGCTCCAAGCTGGGCTGTGTGCACGAACCCCCCGTTCAGCCCGACCGCT
GCGCCTTATCCGGTAACTATCGTCTTGAGTCCAACCCGGTAAGACACGACTTATCGCCACTGGCAGCAGCCACTGGTAACAGGAT
TAGCAGAGCGAGGTATGTAGGCGGTGCTACAGAGTTCTTGAAGTGGTGGCCTAACTACGGCTACACTAGAAGGACAGTATTTGGT
ATCTGCGCTCTGCTGAAGCCAGTTACCTTCGGAAAAAGAGTTGGTAGCTCTTGATCCGGCAAACAAACCACCGCTGGTAGCGGTG
GTTTTTTTGTTTGCAAGCAGCAGATTACGCGCAGAAAAAAAGGATCTCAAGAAGATCCTTTGATCTTTTCTACGGGGTCTGACGC
TCAGTGGAACGAAAACTCACGTTAAGGGATTTTGGTCATGAGATC

Table 8.10: Amino acid sequences of P004 and rLC4. Shown are the amino acid sequences of the patient-derived FLC P004 and the recombinant expression product rLC4. P004 consists of 215 amino acids, whereas rLC4 contains 310 amino acids, including an N-terminal 89-amino-acid α-MF secretion signal (shown in red), which is enzymatically cleaved after expression, and a C-terminal 6-amino-acid 6xHis tag (shown in yellow). The final rLC4 sequence comprises 221 amino acids.

P004

EIVLTQSPGTLSLSPGERATLSCRASQSVSSSYLAWYQQKPGQAPRLLIYDASTRATGIPDRFSGSGSGADFLLTISSLEPEDFA
MYYCQQYGRSPYTFGPGTKVDIKRTVAAPSVFIFPPSDEQLKSGTASVVCLLNNFYPREAKVQWKVDNALQSGNSQESVTEQDSK
DSTYSLSSTLTLSKADYEKHKVYACEVTHQGLSSPVTKSFNRGEC

rLC4

MRFPSIFTAVLFAASSALAAPVNTTTEDETAQIPAEAVIGYSDLEGDFDVAVLPFSNSTNNGLLFINTTIASIAAKEEGVSLEKR
EAEAEIVLTQSPGTLSLSPGERATLSCRASQSVSSSYLAWYQQKPGQAPRLLIYDASTRATGIPDRFSGSGSGADFLLTISSLEP
EDFAMYYCQQYGRSPYTFGPGTKVDIKRTVAAPSVFIFPPSDEQLKSGTASVVCLLNNFYPREAKVQWKVDNALQSGNSQESVTE
QDSKDSTYSLSSTLTLSKADYEKHKVYACEVTHQGLSSPVTKSFNRGECHHHHHH

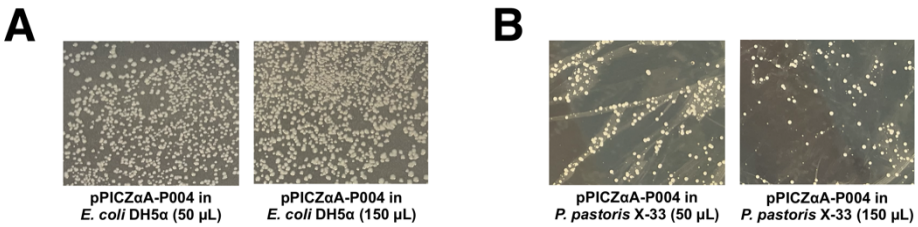

Figure 8.13: Selection of *E. coli* DH5α and *P. pastoris* X-33 transformants containing the pPICZαA expression construct carrying the P004 gene insert. Representative selection plates are shown for (**A**) *E. coli* DH5α and (**B**) *P. pastoris* X-33 transformed with the pPICZαA vector carrying the P004 gene insert. *E. coli* transformants were plated on low-salt LB agar supplemented with 50 µg/µL Zeocin and incubated overnight at 37°C. *P. pastoris* transformants were plated on YPDS agar supplemented with 100 µg/µL Zeocin and incubated at 30°C for three days. For each condition, either 50 µL or 150 µL of transformation culture was plated.

8.4.2 Supplementary results

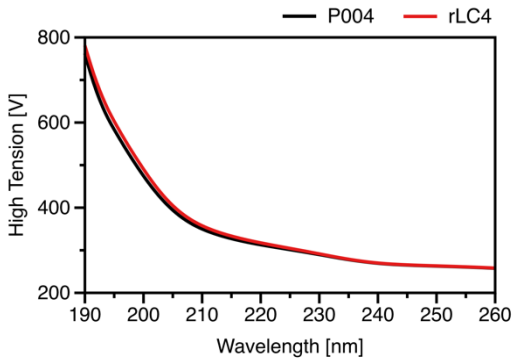

Figure 8.14: HT voltage records corresponding to the CD spectra of P004 and rLC4. HT voltage records are shown for rLC4 (red) and the patient-derived FLC P004 (black). Measurements were conducted at a sample concentration of 12 µM in 10 mM Tris-HCl buffer (pH 7.4).

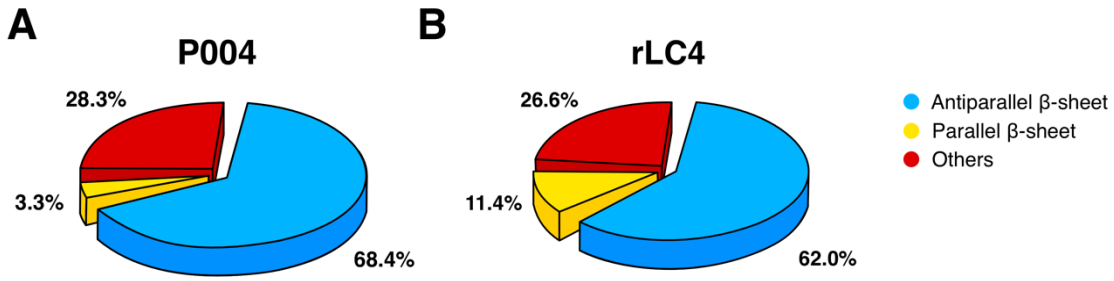

Figure 8.15: Secondary structure analysis of rLC4 and patient-derived sample P004 using the BeStSel web server. Secondary structure compositions of (**A**) P004 and (**B**) rLC4 were determined by deconvolution of CD spectra using the BeStSel web server. Distinct secondary structure elements are highlighted: antiparallel β-sheets (blue), parallel β-sheets (yellow) and other structural components including unstructured regions and loops (red). CD spectra were uploaded as normalized molar ellipticity values for computational analysis.

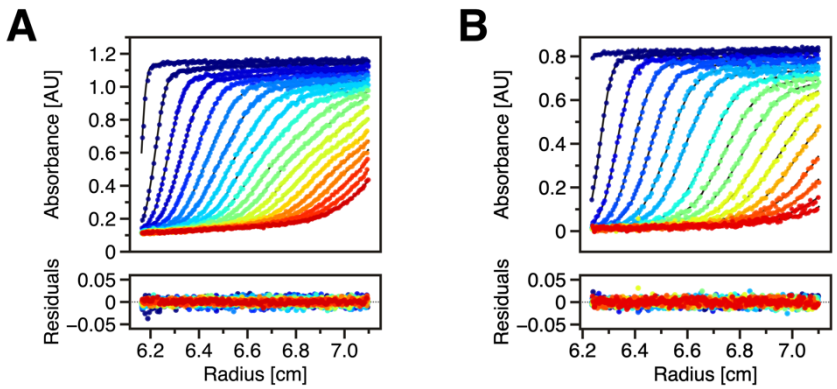

Figure 8.16: Sedimentation profiles from SV analysis of rLC4 and patient-derived sample P004. Shown are the sedimentation profiles of (**A**) rLC4 and (**B**) P004 determined by SV-AUC. SV experiments were performed at 60,000 rpm and 20°C. Complete sedimentation of the samples was achieved after approximately 5 h of centrifugation. A total of 70 scans were measured per sample, with every third scan displayed for clarity.

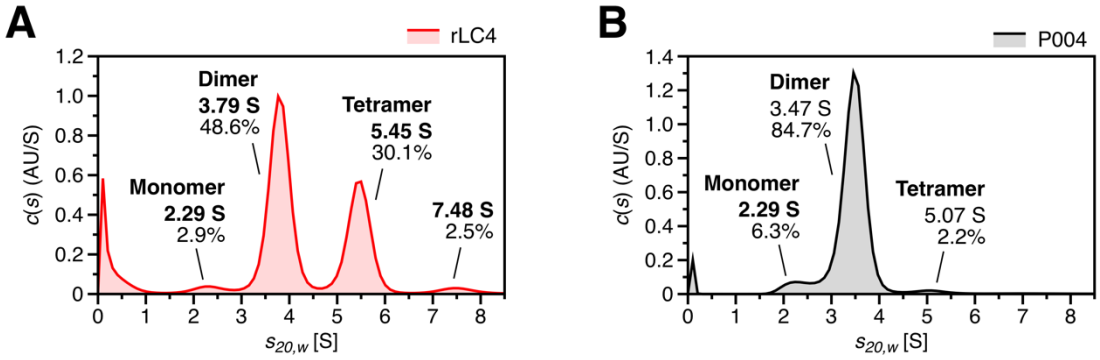

Figure 8.17: SV-AUC data of rLC4 and patient-derived sample P004. Shown are the *c*(*s*) distributions of (**A**) rLC4 and (**B**) P004 determined by SV-AUC. SV experiments were performed at 60,000 rpm and 20°C. Complete sedimentation of the samples was achieved after approximately 5 h of centrifugation.

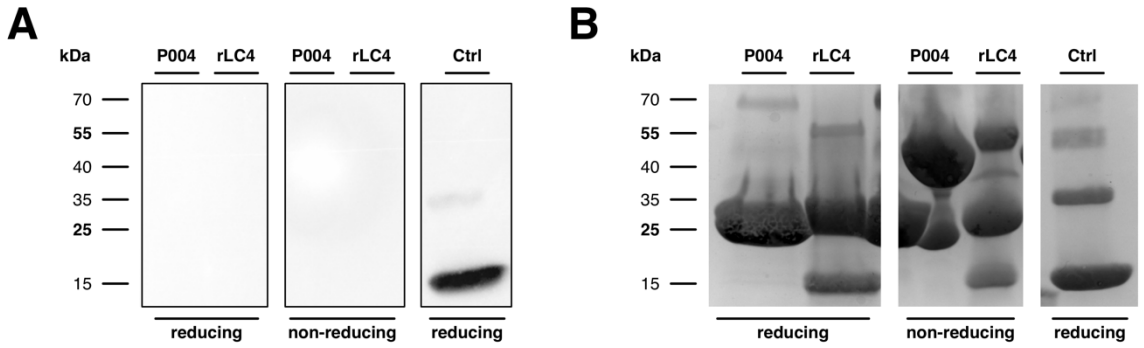

Figure 8.18: Analysis of phosphorylation state of rLC4 and P004 by Western blot analysis. To evaluate whether the *P. pastoris* expression system introduces post-translational phosphorylation, rLC4 and patient-derived sample P004 were analyzed via Western blot using a phospho-Serine/Threonine/Tyrosine-specific primary antibody (rabbit) and an HRP-conjugated goat anti-rabbit IgG (H+L) secondary antibody. (**A**) Western blot analysis of rLC4 and P004 under reducing and non-reducing conditions. A phosphoprotein standard with a well-defined phosphorylation pattern was included as positive control (ctrl). (**B**) Corresponding SDS-PAGE of the gel used for Western blotting. After electrotransfer, the gel was stained with a Coomassie-based staining solution to visualize total protein content. To enhance detection sensitivity, all samples were loaded at the highest possible concentrations.

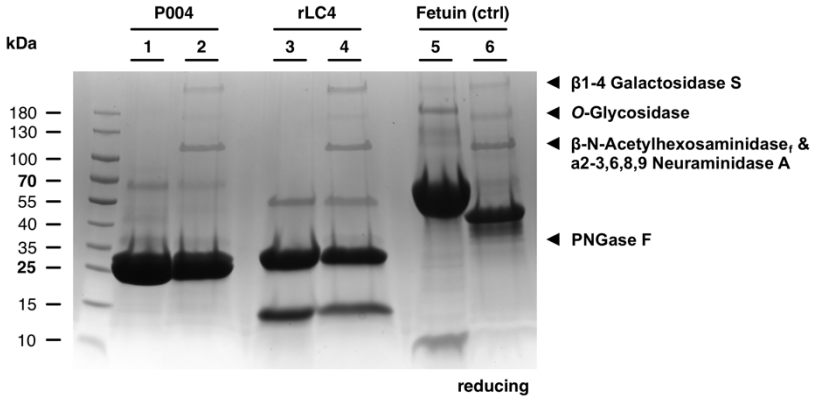

Figure 8.19: Analysis of glycosylation state of rLC4 and P004. To assess potential glycosylation introduced by the *P. pastoris* expression system, rLC4 and the corresponding patient-derived sample P004 were subjected to enzymatic deglycosylation using the Protein Deglycosylation Mix II Kit (New England Biolabs, #P6044S). The glycoprotein fetuin from bovine serum was included as a positive ctrl. **Lane 1:** untreated P004; **lane 2:** deglycosylated P004; **lane 3:** untreated rLC4; **lane 4:** deglycosylated rLC4; **lane 5:** untreated fetuin; **lane 6:** deglycosylated fetuin. The individual glycosidases used for the removal of N- and O-linked glycans are visible in the deglycosylated lanes and are annotated accordingly. Deglycosylation reactions were performed under reducing conditions.

References

Absmeier RM, Rottenaicher GJ, Svilenov HL, et al (2023) Antibodies gone bad – the molecular mechanism of light chain amyloidosis. The FEBS Journal 290:1398–1419. https://doi.org/10.1111/febs.16390

Achilli C, Ciana A, Minetti G (2018) Oxidation of cysteine-rich proteins during gel electrophoresis. JBM 5:1. https://doi.org/10.14440/jbm.2018.275

Adamcik J, Mezzenga R (2018) Amyloid Polymorphism in the Protein Folding and Aggregation Energy Landscape. Angew Chem Int Ed 57:8370–8382. https://doi.org/10.1002/anie.201713416

Ahmad M, Hirz M, Pichler H, Schwab H (2014) Protein expression in Pichia pastoris: recent achievements and perspectives for heterologous protein production. Appl Microbiol Biotechnol 98:5301–5317. https://doi.org/10.1007/s00253-014-5732-5

Akerström B, Björck L (1989) Protein L: an immunoglobulin light chain-binding bacterial protein. Characterization of binding and physicochemical properties. J Biol Chem 264:19740–19746

Amzel LM, Poljak RJ (1979) Three-Dimensional Structure of Immunoglobulins. Annu Rev Biochem 48:961–997. https://doi.org/10.1146/annurev.bi.48.070179.004525

Andrich K, Hegenbart U, Kimmich C, et al (2017) Aggregation of Full-length Immunoglobulin Light Chains from Systemic Light Chain Amyloidosis (AL) Patients Is Remodeled by Epigallocatechin-3-gallate. Journal of Biological Chemistry 292:2328–2344. https://doi.org/10.1074/jbc.M116.750323

Anfinsen CB (1973) Principles that Govern the Folding of Protein Chains. Science 181:223–230. https://doi.org/10.1126/science.181.4096.223

Atroshenko DL, Sergeev EP, Golovina DI, Pometun AA (2024) Additivities for Soluble Recombinant Protein Expression in Cytoplasm of Escherichia coli. Fermentation 10:120. https://doi.org/10.3390/fermentation10030120

Baden E, Sikkink L, Ramirez-Alvarado M (2009) Light Chain Amyloidosis – Current Findings and Future Prospects. CPPS 10:500–508. https://doi.org/10.2174/138920309789351949

Baneyx F, Mujacic M (2004) Recombinant protein folding and misfolding in Escherichia coli. Nat Biotechnol 22:1399–1408. https://doi.org/10.1038/nbt1029

Basnayake K, Stringer SJ, Hutchison CA, Cockwell P (2011) The biology of immunoglobulin free light chains and kidney injury. Kidney International 79:1289–1301. https://doi.org/10.1038/ki.2011.94

Basnayake K, Ying W-Z, Wang P-X, Sanders PW (2010) Immunoglobulin Light Chains Activate Tubular Epithelial Cells through Redox Signaling. Journal of the American Society of Nephrology 21:1165–1173. https://doi.org/10.1681/ASN.2009101089

Bechtel TJ, Weerapana E (2017) From structure to redox: The diverse functional roles of disulfides and implications in disease. Proteomics 17:1600391. https://doi.org/10.1002/pmic.201600391

Bergsagel PL, Kuehl WM, Zhan F, et al (2005) Cyclin D dysregulation: an early and unifying pathogenic event in multiple myeloma. Blood 106:296–303. https://doi.org/10.1182/blood-2005-01-0034

Berkmen M (2012) Production of disulfide-bonded proteins in Escherichia coli. Protein Expression and Purification 82:240–251. https://doi.org/10.1016/j.pep.2011.10.009

Bessette PH, Åslund F, Beckwith J, Georgiou G (1999) Efficient folding of proteins with multiple disulfide bonds in the *Escherichia coli* cytoplasm. Proc Natl Acad Sci USA 96:13703–13708. https://doi.org/10.1073/pnas.96.24.13703

Bhatwa A, Wang W, Hassan YI, et al (2021) Challenges Associated With the Formation of Recombinant Protein Inclusion Bodies in Escherichia coli and Strategies to Address Them for Industrial Applications. Front Bioeng Biotechnol 9:630551. https://doi.org/10.3389/fbioe.2021.630551

Bladé J, Fernández-Llama P, Bosch F, et al (1998) Renal Failure in Multiple Myeloma: Presenting Features and Predictors of Outcome in 94 Patients From a Single Institution. Arch Intern Med 158:1889. https://doi.org/10.1001/archinte.158.17.1889

Blancas-Mejia LM, Tellez LA, Del Pozo-Yauner L, et al (2009) Thermodynamic and Kinetic Characterization of a Germ Line Human λ6 Light-Chain Protein: The Relation between Unfolding and Fibrillogenesis. Journal of Molecular Biology 386:1153–1166. https://doi.org/10.1016/j.jmb.2008.12.069

Bliznyukov OP, Kozmin LD, Vysotskaya LL, et al (2005) Human Immunoglobulin Light Chains λ Form Amyloid Fibrils and Granular Aggregates in Solution. Biochemistry (Moscow) 70:458–466. https://doi.org/10.1007/s10541-005-0137-9

Bork P, Holm L, Sander C (1994) The Immunoglobulin Fold. Journal of Molecular Biology 242:309–320. https://doi.org/10.1006/jmbi.1994.1582

Bradwell AR (2005) Serum Free Light Chain Measurements Move to Center Stage. Clinical Chemistry 51:805–807. https://doi.org/10.1373/clinchem.2005.048017

Bradwell AR, Ph.D HDC-S, Ph.D GPM, Drayson MT (2002) Serum free light chain immunoassays and their clinical application. Clinical and Applied Immunology Reviews 3:17–33. https://doi.org/10.1016/S1529-1049(02)00064-8

Brahms S, Brahms J, Spach G, Brack A (1977) Identification of β,β-turns and unordered conformations in polypeptide chains by vacuum ultraviolet circular dichroism. Proc Natl Acad Sci USA 74:3208–3212. https://doi.org/10.1073/pnas.74.8.3208

Brautigam CA (2015) Calculations and Publication-Quality Illustrations for Analytical Ultracentrifugation Data. In: Methods in Enzymology. Elsevier, pp 109–133

Brenner DA, Jain M, Pimentel DR, et al (2004) Human Amyloidogenic Light Chains Directly Impair Cardiomyocyte Function Through an Increase in Cellular Oxidant Stress. Circulation Research 94:1008–1010. https://doi.org/10.1161/01.RES.0000126569.75419.74

Bridoux F, Leung N, Nasr SH, et al (2025) Kidney disease in multiple myeloma. La Presse Médicale 54:104264. https://doi.org/10.1016/j.lpm.2024.104264

Buchner J, Rudolph R (1991) Renaturation, Purification and Characterization of Recombinant Fab-Fragments Produced in Escherichia coli. Nat Biotechnol 9:157–162. https://doi.org/10.1038/nbt0291-157

Burns JA, Butler JC, Moran J, Whitesides GM (1991) Selective reduction of disulfides by tris(2-carboxyethyl)phosphine. J Org Chem 56:2648–2650. https://doi.org/10.1021/jo00008a014

Caponi L, Koni E, Romiti N, et al (2018) Different immunoreactivity of monomers and dimers makes automated free light chains assays not equivalent. Clinical Chemistry and Laboratory Medicine (CCLM) 57:221–229. https://doi.org/10.1515/cclm-2018-0412

Castillo-Corujo A, Uchida Y, Saaranen MJ, Ruddock LW (2024) *Escherichia coli* Cytoplasmic Expression of Disulfide-Bonded Proteins: Side-by-Side Comparison between Two Competing Strategies. J Microbiol Biotechnol 34:1126–1134. https://doi.org/10.4014/jmb.2311.11025

Čaval T, Hecht ES, Tang W, et al (2021) The lysosomal endopeptidases Cathepsin D and L are selective and effective proteases for the middle-down characterization of antibodies. The FEBS Journal 288:5389–5405. https://doi.org/10.1111/febs.15813

Cavallone E, Mousavi AH, Biolé C, et al (2024) Oxidative damage in immunoglobulin light chain and transthyretin cardiac amyloidosis – a closer look. Redox Experimental Medicine 2024:e240001. https://doi.org/10.1530/REM-24-0001

Chin CL, Goh JB, Srinivasan H, et al (2019) A human expression system based on HEK293 for the stable production of recombinant erythropoietin. Sci Rep 9:16768. https://doi.org/10.1038/s41598-019-53391-z

Choi JH, Lee SY (2004) Secretory and extracellular production of recombinant proteins using Escherichia coli. Applied Microbiology and Biotechnology 64:625–635. https://doi.org/10.1007/s00253-004-1559-9

Cohen SN, Chang ACY, Boyer HW, Helling RB (1973) Construction of Biologically Functional Bacterial Plasmids *In Vitro*. Proc Natl Acad Sci USA 70:3240–3244. https://doi.org/10.1073/pnas.70.11.3240

Cölfen H (2010) Analytical Ultracentrifugation. Macromolecular Bioscience 10:687–688. https://doi.org/10.1002/mabi.201000201

Connors LH, Jiang Y, Budnik M, et al (2007) Heterogeneity in Primary Structure, Post-Translational Modifications, and Germline Gene Usage of Nine Full-Length Amyloidogenic κ1 Immunoglobulin Light Chains. Biochemistry 46:14259–14271. https://doi.org/10.1021/bi7013773

Cowan AJ, Green DJ, Kwok M, et al (2022) Diagnosis and Management of Multiple Myeloma: A Review. JAMA 327:464. https://doi.org/10.1001/jama.2022.0003

Creighton TE, Goldenberg DP (1984) Kinetic role of a meta-stable native-like two-disulphide species in the folding transition of bovine pancreatic trypsin inhibitor. Journal of Molecular Biology 179:497–526. https://doi.org/10.1016/0022-2836(84)90077-9

Daly R, Hearn MTW (2005) Expression of heterologous proteins inPichia pastoris: a useful experimental tool in protein engineering and production. J Mol Recognit 18:119–138. https://doi.org/10.1002/jmr.687

Damodaran S, Kinsella JE (1981) The effects of neutral salts on the stability of macromolecules. A new approach using a protein-ligand binding system. Journal of Biological Chemistry 256:3394–3398. https://doi.org/10.1016/S0021-9258(19)69621-3

De Geyter J, Tsirigotaki A, Orfanoudaki G, et al (2016) Protein folding in the cell envelope of Escherichia coli. Nat Microbiol 1:16107. https://doi.org/10.1038/nmicrobiol.2016.107

De Marco A (2009) Strategies for successful recombinant expression of disulfide bond-dependent proteins in Escherichia coli. Microb Cell Fact 8:26. https://doi.org/10.1186/1475-2859-8-26

Del Pozo-Yauner L, Turbat-Herrera EA, Pérez-Carreón JI, Herrera GA (2022) From the Light Chain Sequence to the Tissue Microenvironment: Contribution of the Mesangial Cells to Glomerular Amyloidosis. Hemato 3:232–267. https://doi.org/10.3390/hemato3010019

Denoncin K, Collet J-F (2013) Disulfide Bond Formation in the Bacterial Periplasm: Major Achievements and Challenges Ahead. Antioxidants & Redox Signaling 19:63–71. https://doi.org/10.1089/ars.2012.4864

Deponte M, Hell K (2009) Disulphide Bond Formation in the Intermembrane Space of Mitochondria. Journal of Biochemistry 146:599–608. https://doi.org/10.1093/jb/mvp133

Dill KA (1990) Dominant forces in protein folding. Biochemistry 29:7133–7155. https://doi.org/10.1021/bi00483a001

Dispenzieri A, Kyle R, Merlini G, et al (2009) International Myeloma Working Group guidelines for serum-free light chain analysis in multiple myeloma and related disorders. Leukemia 23:215–224. https://doi.org/10.1038/leu.2008.307

Dunbar J, Deane CM (2016) ANARCI: antigen receptor numbering and receptor classification. Bioinformatics 32:298–300. https://doi.org/10.1093/bioinformatics/btv552

Dupré M, Duchateau M, Sternke-Hoffmann R, et al (2021) *De Novo* Sequencing of Antibody Light Chain Proteoforms from Patients with Multiple Myeloma. Anal Chem 93:10627–10634. https://doi.org/10.1021/acs.analchem.1c01955

Dutton RJ, Boyd D, Berkmen M, Beckwith J (2008) Bacterial species exhibit diversity in their mechanisms and capacity for protein disulfide bond formation. Proc Natl Acad Sci USA 105:11933–11938. https://doi.org/10.1073/pnas.0804621105

Džupponová V, Žoldák G (2023) Aggregation mechanism and branched 3D morphologies of pathological human light chain proteins under reducing conditions. Colloids and Surfaces B: Biointerfaces 221:112983. https://doi.org/10.1016/j.colsurfb.2022.112983

Edelhoch H (1967) Spectroscopic Determination of Tryptophan and Tyrosine in Proteins *. Biochemistry 6:1948–1954. https://doi.org/10.1021/bi00859a010

Edelman GM, Gall WEinar, Waxdal MJ, Konigsberg WH (1968) The covalent structure of a human γG-immunoglobulin. I. Isolation and characterization of the whole molecule, the polypeptide chains, and the tryptic fragments. Biochemistry 7:1950–1958. https://doi.org/10.1021/bi00845a045

Elkabetz Y, Ofir A, Argon Y, Bar-Nun S (2008) Alternative pathways of disulfide bond formation yield secretion-competent, stable and functional immunoglobulins. Molecular Immunology 46:97–105. https://doi.org/10.1016/j.molimm.2008.07.005

Ezawa T, Otomo R, Kariya Y, et al (2025) Multiple myeloma–associated non-crystalline proximal tubulopathy and crystalline cast nephropathy: Biochemical and structural features of disease-causing monoclonal kappa light chains. The FASEB Journal 39:e70296. https://doi.org/10.1096/fj.202402104R

Fabianek RA, Hennecke H, Thöny-Meyer L (2000) Periplasmic protein thiol:disulfide oxidoreductases of *Escherichia coli*. FEMS Microbiol Rev 24:303–316. https://doi.org/10.1111/j.1574-6976.2000.tb00544.x

Falk RH, Alexander KM, Liao R, Dorbala S (2016) AL (Light-Chain) Cardiac Amyloidosis. Journal of the American College of Cardiology 68:1323–1341. https://doi.org/10.1016/j.jacc.2016.06.053

Feige MJ, Hendershot LM (2011) Disulfide bonds in ER protein folding and homeostasis. Current Opinion in Cell Biology 23:167–175. https://doi.org/10.1016/j.ceb.2010.10.012

Feige MJ, Hendershot LM, Buchner J (2010) How antibodies fold. Trends in Biochemical Sciences 35:189–198. https://doi.org/10.1016/j.tibs.2009.11.005

Fink AL (1998) Protein aggregation: folding aggregates, inclusion bodies and amyloid. Folding and Design 3:R9–R23. https://doi.org/10.1016/S1359-0278(98)00002-9

Fleischman J, Porter R, Press E (1963) THE ARRANGEMENT OF THE PEPTIDE CHAINS IN γ-GLOBULIN. Biochemical Journal 88:220–228. https://doi.org/10.1042/bj0880220

Fox C, Cocchiaro P, Oakley F, et al (2016) Inhibition of lysosomal protease cathepsin D reduces renal fibrosis in murine chronic kidney disease. Sci Rep 6:20101. https://doi.org/10.1038/srep20101

Frand AR, Cuozzo JW, Kaiser CA (2000) Pathways for protein disulphide bond formation. Trends in Cell Biology 10:203–210. https://doi.org/10.1016/S0962-8924(00)01745-1

Frisch C, Kolmar H, Schmidt A, et al (1996) Contribution of the intramolecular disulfide bridge to the folding stability of REIv, the variable domain of a human immunoglobulin κ light chain. Folding and Design 1:431–440. https://doi.org/10.1016/S1359-0278(96)00059-4

Fujimoto T, Inaba K, Kadokura H (2019) Methods to identify the substrates of thiol-disulfide oxidoreductases. Protein Science 28:30–40. https://doi.org/10.1002/pro.3530

Furukawa Y, Kikuchi J (2015) Molecular pathogenesis of multiple myeloma. Int J Clin Oncol 20:413–422. https://doi.org/10.1007/s10147-015-0837-0

Gallardo PA, Vio CP (2022) Renal Physiology and Hydrosaline Metabolism. Springer International Publishing, Cham

Gámez B, Edwards CM (2018) Contributions of the Bone Microenvironment to Monoclonal Gammopathy of Undetermined Significance Pathogenesis. Curr Osteoporos Rep 16:635–641. https://doi.org/10.1007/s11914-018-0479-z

Gasteiger E, Hoogland C, Gattiker A, et al (2005) Protein Identification and Analysis Tools on the ExPASy Server. In: Walker JM (ed) The Proteomics Protocols Handbook. Humana Press, Totowa, NJ, pp 571–607

Glenner GG, Harbaugh J, Ohms JI, et al (1970) An amyloid protein: The amino-terminal variable fragment of an immunoglobulin light chain. Biochemical and Biophysical Research Communications 41:1287–1289. https://doi.org/10.1016/0006-291X(70)90227-5

Gomes CM, Faísca PFN (2019) Protein Folding: An Introduction. In: Protein Folding. Springer International Publishing, Cham, pp 1–63

Goto Y, Hamaguchi K (1979) The Role of the Intrachain Disulfide Bond in the Conformation and Stability of the Constant Fragment of the Immunoglobulin Light Chain1. The Journal of Biochemistry 86:1433–1441. https://doi.org/10.1093/oxfordjournals.jbchem.a132661

Graham RC, Karnovsky MJ (1966) GLOMERULAR PERMEABILITY. The Journal of Experimental Medicine 124:1123–1134. https://doi.org/10.1084/jem.124.6.1123

Greenfield NJ (2006) Using circular dichroism spectra to estimate protein secondary structure. Nat Protoc 1:2876–2890. https://doi.org/10.1038/nprot.2006.202

Grek CL, Zhang J, Manevich Y, et al (2013) Causes and Consequences of Cysteine S-Glutathionylation. Journal of Biological Chemistry 288:26497–26504. https://doi.org/10.1074/jbc.R113.461368

Grey HM, Kohler PF (1968) A case of tetramer Bence Jones proteinaemia. Clin Exp Immunol 3:277–285

Gudowska-Sawczuk M, Mroczko B (2023) Free Light Chains κ and λ as New Biomarkers of Selected Diseases. IJMS 24:9531. https://doi.org/10.3390/ijms24119531

Gudowska-Sawczuk M, Mroczko B (2019) Free Light Chains as a Novel Diagnostic Biomarker of Immune System Abnormalities in Multiple Sclerosis and HIV Infection. BioMed Research International 2019:1–7. https://doi.org/10.1155/2019/8382132

Gyurászová M, Gurecká R, Bábíčková J, Tóthová Ľ (2020) Oxidative Stress in the Pathophysiology of Kidney Disease: Implications for Noninvasive Monitoring and Identification of Biomarkers. Oxidative Medicine and Cellular Longevity 2020:1–11. https://doi.org/10.1155/2020/5478708

Haber E, Anfinsen CB (1961) Regeneration of enzyme activity by air oxidation of reduced subtilisin-modified ribonuclease. J Biol Chem 236:422–424

Hafner Česen M, Stoka V, Turk B (2016) Role of Lysosomes in Intracellular Degradation. In: Encyclopedia of Cell Biology. Elsevier, pp 789–797

Hand K, Wilkinson MC, Madine J (2018) Isolation and purification of recombinant immunoglobulin light chain variable domains from the periplasmic space of Escherichia coli. PLoS ONE 13:e0206167. https://doi.org/10.1371/journal.pone.0206167

Hartl FU, Bracher A, Hayer-Hartl M (2011) Molecular chaperones in protein folding and proteostasis. Nature 475:324–332. https://doi.org/10.1038/nature10317

Hatahet F, Ruddock LW (2009) Protein Disulfide Isomerase: A Critical Evaluation of Its Function in Disulfide Bond Formation. Antioxidants & Redox Signaling 11:2807–2850. https://doi.org/10.1089/ars.2009.2466

Heher EC, Rennke HG, Laubach JP, Richardson PG (2013) Kidney Disease and Multiple Myeloma. Clinical Journal of the American Society of Nephrology 8:2007–2017. https://doi.org/10.2215/CJN.12231212

Hochgräfe F, Mostertz J, Pöther D-C, et al (2007) S-Cysteinylation Is a General Mechanism for Thiol Protection of Bacillus subtilis Proteins after Oxidative Stress. Journal of Biological Chemistry 282:25981–25985. https://doi.org/10.1074/jbc.C700105200

Hsu C, Thomas OR, Overton TW (2016) Periplasmic expression in and release of Fab fragments from *Escherichia coli* using stress minimization. J of Chemical Tech & Biotech 91:815–822. https://doi.org/10.1002/jctb.4672

Huang ZQ, Sanders PW (1997) Localization of a single binding site for immunoglobulin light chains on human Tamm-Horsfall glycoprotein. J Clin Invest 99:732–736. https://doi.org/10.1172/JCI119218

Iram A, Naeem A (2014) Protein Folding, Misfolding, Aggregation and Their Implications in Human Diseases: Discovering Therapeutic Ways to Amyloid-Associated Diseases. Cell Biochem Biophys 70:51–61. https://doi.org/10.1007/s12013-014-9904-9

Jackson DA, Symons RH, Berg P (1972) Biochemical Method for Inserting New Genetic Information into DNA of Simian Virus 40: Circular SV40 DNA Molecules Containing Lambda Phage Genes

and the Galactose Operon of *Escherichia coli*. Proc Natl Acad Sci USA 69:2904–2909. https://doi.org/10.1073/pnas.69.10.2904

Jackson SE (1998) How do small single-domain proteins fold? Folding and Design 3:R81–R91. https://doi.org/10.1016/S1359-0278(98)00033-9

Janeway C (2001) Immunobiology: the immune system in health and disease. Garland Science

Jones DP, Carlson JL, Mody VC, et al (2000) Redox state of glutathione in human plasma. Free Radical Biology and Medicine 28:625–635. https://doi.org/10.1016/S0891-5849(99)00275-0

Jones HB (1848) III. On a new substance occurring in the urine of a patient with mollities ossium. Philosophical Transactions of the Royal Society of London 55–62

Jumper J, Evans R, Pritzel A, et al (2021) Highly accurate protein structure prediction with AlphaFold. Nature 596:583–589. https://doi.org/10.1038/s41586-021-03819-2

Kaplan B, Golderman S, Aizenbud B, et al (2014) Immunoglobulin-free light chain monomer-dimer patterns help to distinguish malignant from premalignant monoclonal gammopathies: A pilot study. American J Hematol 89:882–888. https://doi.org/10.1002/ajh.23773

Kaplan B, Livneh A, Sela B-A (2011) Immunoglobulin Free Light Chain Dimers in Human Diseases. The Scientific World JOURNAL 11:726–735. https://doi.org/10.1100/tsw.2011.65

Kaplan B, Ramirez-Alvarado M, Sikkink L, et al (2009) Free light chains in plasma of patients with light chain amyloidosis and non-amyloid light chain deposition disease. High proportion and heterogeneity of disulfide-linked monoclonal free light chains as pathogenic features of amyloid disease. Br J Haematol 144:705–715. https://doi.org/10.1111/j.1365-2141.2008.07522.x

Karyolaimos A, De Gier J-W (2021) Strategies to Enhance Periplasmic Recombinant Protein Production Yields in Escherichia coli. Front Bioeng Biotechnol 9:797334. https://doi.org/10.3389/fbioe.2021.797334

Katzmann JA, Clark RJ, Abraham RS, et al (2002) Serum reference intervals and diagnostic ranges for free kappa and free lambda immunoglobulin light chains: relative sensitivity for detection of monoclonal light chains. Clin Chem 48:1437–1444

Kazman P, Absmeier RM, Engelhardt H, Buchner J (2021) Dissection of the amyloid formation pathway in AL amyloidosis. Nat Commun 12:6516. https://doi.org/10.1038/s41467-021-26845-0

Kazman P, Vielberg M-T, Pulido Cendales MD, et al (2020) Fatal amyloid formation in a patient's antibody light chain is caused by a single point mutation. eLife 9:e52300. https://doi.org/10.7554/eLife.52300

Ke N, Berkmen M (2014) Production of Disulfide-Bonded Proteins in *Escherichia coli*. CP Molecular Biology 108:. https://doi.org/10.1002/0471142727.mb1601bs108

Khurana R, Gillespie JR, Talapatra A, et al (2001) Partially Folded Intermediates as Critical Precursors of Light Chain Amyloid Fibrils and Amorphous Aggregates. Biochemistry 40:3525–3535. https://doi.org/10.1021/bi001782b

Klein M, Kells DIC, Tinker DO, Dorrington KJ (1977) Thermodynamic and conformational studies on an immunoglobulin light chain which reversibly precipitates at low temperatures. Biochemistry 16:552–560. https://doi.org/10.1021/bi00622a032

Klimtchuk ES, Prokaeva T, Spencer BH, et al (2024) Conformational Differences in the Light Chain Constant Domain of Immunoglobulin G and Free Light Chain May Influence Proteolysis in AL Amyloidosis. Journal of Molecular Biology 436:168837. https://doi.org/10.1016/j.jmb.2024.168837

Knight MJ, Floret L, Patel N, et al (2022) The impact of forced degradation conditions on mAb dimer formation and subsequent influence on aggregation propensity. mAbs 14:2127172. https://doi.org/10.1080/19420862.2022.2127172

Kolaj O, Spada S, Robin S, Wall JG (2009) Use of folding modulators to improve heterologous protein production in Escherichia coli. Microb Cell Fact 8:9. https://doi.org/10.1186/1475-2859-8-9

Konen FF, Schwenkenbecher P, Jendretzky KF, et al (2021) The Increasing Role of Kappa Free Light Chains in the Diagnosis of Multiple Sclerosis. Cells 10:3056. https://doi.org/10.3390/cells10113056

Kourelis TV, Dasari S, Theis JD, et al (2017) Clarifying immunoglobulin gene usage in systemic and localized immunoglobulin light-chain amyloidosis by mass spectrometry. Blood 129:299–306. https://doi.org/10.1182/blood-2016-10-743997

Krata N, Zagożdżon R, Foroncewicz B, Mucha K (2018) Oxidative Stress in Kidney Diseases: The Cause or the Consequence? Arch Immunol Ther Exp 66:211–220. https://doi.org/10.1007/s00005-017-0496-0

Krayukhina E, Uchiyama S (2016) Analytical Ultracentrifugation. In: Senda T, Maenaka K (eds) Advanced Methods in Structural Biology. Springer Japan, Tokyo, pp 165–183

Kul A, Ozturk Kurt B (2024) Multiple Myeloma from the Perspective of Pro- and Anti-Oxidative Parameters: Potential for Diagnostic and/or Follow-Up Purposes? JPM 14:221. https://doi.org/10.3390/jpm14030221

Kumar SK, Rajkumar V, Kyle RA, et al (2017) Multiple myeloma. Nat Rev Dis Primers 3:17046. https://doi.org/10.1038/nrdp.2017.46

Kundu S, Jha SB, Rivera AP, et al (2022) Multiple Myeloma and Renal Failure: Mechanisms, Diagnosis, and Management. Cureus. https://doi.org/10.7759/cureus.22585

Kyle RA (2000) Multiple myeloma: an odyssey of discovery. Br J Haematol 111:1035–1044. https://doi.org/10.1046/j.1365-2141.2000.02318.x

Laemmli UK (1970) Cleavage of Structural Proteins during the Assembly of the Head of Bacteriophage T4. Nature 227:680–685. https://doi.org/10.1038/227680a0

Landgren O, Zeig-Owens R, Giricz O, et al (2018) Multiple Myeloma and Its Precursor Disease Among Firefighters Exposed to the World Trade Center Disaster. JAMA Oncol 4:821. https://doi.org/10.1001/jamaoncol.2018.0509

Laue TM (1992) Computer-aided interpretation of analytical sedimentation data for proteins. Analytical ultracentrifugation in biochemistry and polymer science 90–125

Lavatelli F, Natalello A, Marchese L, et al (2024) Truncation of the constant domain drives amyloid formation by immunoglobulin light chains. Journal of Biological Chemistry 300:107174. https://doi.org/10.1016/j.jbc.2024.107174

Leboulleux M, Lelongt B, Mougenot B, et al (1995) Protease resistance and binding of Ig light chains in myeloma-associated tubulopathies. Kidney International 48:72–79. https://doi.org/10.1038/ki.1995.269

LeMasters GK, Genaidy AM, Succop P, et al (2006) Cancer Risk Among Firefighters: A Review and Meta-analysis of 32 Studies: Journal of Occupational and Environmental Medicine 48:1189–1202. https://doi.org/10.1097/01.jom.0000246229.68697.90

Leung N, Rajkumar SV (2023) Multiple myeloma with acute light chain cast nephropathy. Blood Cancer J 13:46. https://doi.org/10.1038/s41408-023-00806-w

Levey AS, Eckardt K-U, Dorman NM, et al (2020) Nomenclature for kidney function and disease: report of a Kidney Disease: Improving Global Outcomes (KDIGO) Consensus Conference. Kidney International 97:1117–1129. https://doi.org/10.1016/j.kint.2020.02.010

Li C, Xu L, Zuo YY, Yang P (2018) Tuning protein assembly pathways through superfast amyloid-like aggregation. Biomater Sci 6:836–841. https://doi.org/10.1039/C8BM00066B

Lim A, Wally J, Walsh MT, et al (2001) Identification and Location of a Cysteinyl Posttranslational Modification in an Amyloidogenic κ1 Light Chain Protein by Electrospray Ionization and Matrix-Assisted Laser Desorption/Ionization Mass Spectrometry. Analytical Biochemistry 295:45–56. https://doi.org/10.1006/abio.2001.5187

Liu H, May K (2012) Disulfide bond structures of IgG molecules: Structural variations, chemical modifications and possible impacts to stability and biological function. mAbs 4:17–23. https://doi.org/10.4161/mabs.4.1.18347

Liu P, O'Mara BW, Warrack BM, et al (2010) A tris (2-carboxyethyl) phosphine (TCEP) related cleavage on cysteine-containing proteins. J Am Soc Mass Spectrom 21:837–844. https://doi.org/10.1016/j.jasms.2010.01.016

Liu P, Tarnowski MA, O'Mara BW, et al (2009) Characterization of S-thiolation on secreted proteins from *E. coli* by mass spectrometry. Rapid Comm Mass Spectrometry 23:3343–3349. https://doi.org/10.1002/rcm.4247

Liu S-Q, Ji X-L, Tao Y, et al (2012) Protein Folding, Binding and Energy Landscape: A Synthesis. In: Kaumaya P (ed) Protein Engineering. InTech

Liu Y, Huang H (2018) Expression of single-domain antibody in different systems. Appl Microbiol Biotechnol 102:539–551. https://doi.org/10.1007/s00253-017-8644-3

Lobstein J, Emrich CA, Jeans C, et al (2012) SHuffle, a novel Escherichia coli protein expression strain capable of correctly folding disulfide bonded proteins in its cytoplasm. Microb Cell Fact 11:753. https://doi.org/10.1186/1475-2859-11-56

Loi VV, Rossius M, Antelmann H (2015) Redox regulation by reversible protein S-thiolation in bacteria. Front Microbiol 6:. https://doi.org/10.3389/fmicb.2015.00187

Lu Y, Jiang Y, Prokaeva T, et al (2017) Oxidative post-translational modifications of an amyloidogenic immunoglobulin light chain protein. International Journal of Mass Spectrometry 416:71–79. https://doi.org/10.1016/j.ijms.2016.11.006

Malard F, Neri P, Bahlis NJ, et al (2024) Multiple myeloma. Nat Rev Dis Primers 10:45. https://doi.org/10.1038/s41572-024-00529-7

Mamipour M, Yousefi M, Hasanzadeh M (2017) An overview on molecular chaperones enhancing solubility of expressed recombinant proteins with correct folding. International Journal of Biological Macromolecules 102:367–375. https://doi.org/10.1016/j.ijbiomac.2017.04.025

Martin DJ, Ramirez-Alvarado M (2010) Comparison of amyloid fibril formation by two closely related immunoglobulin light chain variable domains. Amyloid 17:129–136. https://doi.org/10.3109/13506129.2010.530081

Matamouros S, Gensch T, Cerff M, et al (2023) Growth-rate dependency of ribosome abundance and translation elongation rate in Corynebacterium glutamicum differs from that in Escherichia coli. Nat Commun 14:5611. https://doi.org/10.1038/s41467-023-41176-y

Mazzini G, Ricagno S, Caminito S, et al (2022) Protease-sensitive regions in amyloid light chains: what a common pattern of fragmentation across organs suggests about aggregation. The FEBS Journal 289:494–506. https://doi.org/10.1111/febs.16182

McAuley A, Jacob J, Kolvenbach CG, et al (2008) Contributions of a disulfide bond to the structure, stability, and dimerization of human IgG1 antibody C_H 3 domain. Protein Science 17:95–106. https://doi.org/10.1110/ps.073134408

Mclaughlin RW, De Stigter JK, Sikkink LA, et al (2006) The effects of sodium sulfate, glycosaminoglycans, and Congo red on the structure, stability, and amyloid formation of an immunoglobulin light-chain protein. Protein Science 15:1710–1722. https://doi.org/10.1110/ps.051997606

Melnikova DL, Skirda VD, Nesmelova IV (2019) Effect of Reducing Agent TCEP on Translational Diffusion and Supramolecular Assembly in Aqueous Solutions of α-Casein. J Phys Chem B 123:2305–2315. https://doi.org/10.1021/acs.jpcb.8b12511

Mergulhão FJM, Summers DK, Monteiro GA (2005) Recombinant protein secretion in Escherichia coli. Biotechnology Advances 23:177–202. https://doi.org/10.1016/j.biotechadv.2004.11.003

Merlini G, Dispenzieri A, Sanchorawala V, et al (2018) Systemic immunoglobulin light chain amyloidosis. Nat Rev Dis Primers 4:38. https://doi.org/10.1038/s41572-018-0034-3

Merlini G, Wechalekar AD, Palladini G (2013) Systemic light chain amyloidosis: an update for treating physicians. Blood 121:5124–5130. https://doi.org/10.1182/blood-2013-01-453001

Messens J, Collet J-F (2006) Pathways of disulfide bond formation in Escherichia coli. The International Journal of Biochemistry & Cell Biology 38:1050–1062. https://doi.org/10.1016/j.biocel.2005.12.011

Micsonai A, Moussong É, Wien F, et al (2022) BeStSel: webserver for secondary structure and fold prediction for protein CD spectroscopy. Nucleic Acids Research 50:W90–W98. https://doi.org/10.1093/nar/gkac345

Miekka SI (1983) Heat-induced fragmentation of human plasma fibronectin. Biochimica et Biophysica Acta (BBA) - Protein Structure and Molecular Enzymology 748:374–380. https://doi.org/10.1016/0167-4838(83)90182-6

Migrino RQ, Hari P, Gutterman DD, et al (2010) Systemic and microvascular oxidative stress induced by light chain amyloidosis. International Journal of Cardiology 145:67–68. https://doi.org/10.1016/j.ijcard.2009.04.044

Miot M, Betton J-M (2004) Protein quality control in the bacterial periplasm. Microb Cell Fact 3:4. https://doi.org/10.1186/1475-2859-3-4

Mirsky A, Kazandjian L, Anisimova M (2015) Antibody-Specific Model of Amino Acid Substitution for Immunological Inferences from Alignments of Antibody Sequences. Molecular Biology and Evolution 32:806–819. https://doi.org/10.1093/molbev/msu340

Misra P, Blancas-Mejia LM, Ramirez-Alvarado M (2019) Mechanistic Insights into the Early Events in the Aggregation of Immunoglobulin Light Chains. Biochemistry 58:3155–3168. https://doi.org/10.1021/acs.biochem.9b00311

Misra P, Ramirez-Alvarado M (2021) Early events in light chain aggregation at physiological pH reveal new insights on assembly, stability, and aggregate dissociation. Amyloid 28:113–124. https://doi.org/10.1080/13506129.2021.1877129

Mitra A, Sarkar N (2022) The role of intra and inter-molecular disulfide bonds in modulating amyloidogenesis: A review. Archives of Biochemistry and Biophysics 716:109113. https://doi.org/10.1016/j.abb.2021.109113

Monera OD, Kay CM, Hodges RS (1994) Protein denaturation with guanidine hydrochloride or urea provides a different estimate of stability depending on the contributions of electrostatic interactions. Protein Science 3:1984–1991. https://doi.org/10.1002/pro.5560031110

Morgan G, Nau AN, Wong S, et al (2024) An updated AL-Base reveals ranked enrichment of immunoglobulin light chain variable genes in AL amyloidosis

Morgan GJ, Kelly JW (2016) The Kinetic Stability of a Full-Length Antibody Light Chain Dimer Determines whether Endoproteolysis Can Release Amyloidogenic Variable Domains. Journal of Molecular Biology 428:4280–4297. https://doi.org/10.1016/j.jmb.2016.08.021

Morgan GJ, Yan NL, Mortenson DE, et al (2019) Stabilization of amyloidogenic immunoglobulin light chains by small molecules. Proc Natl Acad Sci USA 116:8360–8369. https://doi.org/10.1073/pnas.1817567116

Musaogullari A, Chai Y-C (2020) Redox Regulation by Protein S-Glutathionylation: From Molecular Mechanisms to Implications in Health and Disease. IJMS 21:8113. https://doi.org/10.3390/ijms21218113

Muylaert C, Van Hemelrijck LA, Maes A, et al (2022) Aberrant DNA methylation in multiple myeloma: A major obstacle or an opportunity? Front Oncol 12:979569. https://doi.org/10.3389/fonc.2022.979569

Nakano T, Matsui M, Inoue I, et al (2011) Free immunoglobulin light chain: Its biology and implications in diseases. Clinica Chimica Acta 412:843–849. https://doi.org/10.1016/j.cca.2011.03.007

Nakashima F, Shibata T, Kamiya K, et al (2018) Structural and functional insights into S-thiolation of human serum albumins. Sci Rep 8:932. https://doi.org/10.1038/s41598-018-19610-9

Natesan R, Dykstra AB, Banerjee A, Agrawal NJ (2023) Heterogeneity in Disulfide Bond Reduction in IgG1 Antibodies Is Governed by Solvent Accessibility of the Cysteines. Antibodies 12:83. https://doi.org/10.3390/antib12040083

Neuberger MS, Caskey HM, Pettersson S, et al (1989) Isotype exclusion and transgene down-regulation in immunoglobulin-λ transgenic mice. Nature 338:350–352. https://doi.org/10.1038/338350a0

Neumeister P, Schulz E, Pansy K, et al (2022) Targeting the Microenvironment for Treating Multiple Myeloma. IJMS 23:7627. https://doi.org/10.3390/ijms23147627

Nick Pace C, Scholtz JM, Grimsley GR (2014) Forces stabilizing proteins. FEBS Letters 588:2177–2184. https://doi.org/10.1016/j.febslet.2014.05.006

Nikolaou PE, Georgoulis A, Liacos C, et al (2022) Understanding the molecular mosaic of cardiotoxicity of light chains in plasma cell dyscrasias and cardiac light chain amyloidosis with the use of patient derived full-length light chains. European Heart Journal 43:ehac544.2987. https://doi.org/10.1093/eurheartj/ehac544.2987

Nilson BH, Solomon A, Björck L, Akerström B (1992) Protein L from Peptostreptococcus magnus binds to the kappa light chain variable domain. Journal of Biological Chemistry 267:2234–2239. https://doi.org/10.1016/S0021-9258(18)45867-X

Nilson BHK, Lögdberg L, Kastern W, et al (1993) Purification of antibodies using protein L-binding framework structures in the light chain variable domain. Journal of Immunological Methods 164:33–40. https://doi.org/10.1016/0022-1759(93)90273-A

Ojima-Kato T (2024) Advances in recombinant protein production in microorganisms and functional peptide tags. Bioscience, Biotechnology, and Biochemistry 89:1–10. https://doi.org/10.1093/bbb/zbae147

Olsen KE, Sletten K, Westermark P (1998) Fragments of the Constant Region of Immunoglobulin Light Chains Are Constituents of AL-Amyloid Proteins. Biochemical and Biophysical Research Communications 251:642–647. https://doi.org/10.1006/bbrc.1998.9508

Pain R (2004) Determining the CD Spectrum of a Protein. CP Protein Science 38:. https://doi.org/10.1002/0471140864.ps0706s38

Palmer I, Wingfield PT (2012) Preparation and Extraction of Insoluble (Inclusion-Body) Proteins from *Escherichia coli*. CP Protein Science 70:. https://doi.org/10.1002/0471140864.ps0603s70

Petrilla C, Galloway J, Kudalkar R, et al (2023) Understanding DNA Damage Response and DNA Repair in Multiple Myeloma. Cancers 15:4155. https://doi.org/10.3390/cancers15164155

Pick M, Lebel E, Elgavish S, et al (2023) Amyloidogenic light chains impair plasma cell survival. haematol 108:3359–3371. https://doi.org/10.3324/haematol.2022.282484

Piehl DW, Blancas-Mejía LM, Wall JS, et al (2017) Immunoglobulin Light Chains Form an Extensive and Highly Ordered Fibril Involving the N- and C-Termini. ACS Omega 2:712–720. https://doi.org/10.1021/acsomega.6b00494

Pinto V, Bergantim R, Caires HR, et al (2020) Multiple Myeloma: Available Therapies and Causes of Drug Resistance. Cancers 12:407. https://doi.org/10.3390/cancers12020407

Plano F, Corsale AM, Gigliotta E, et al (2023) Monoclonal Gammopathies and the Bone Marrow Microenvironment: From Bench to Bedside and Then Back Again. Hematology Reports 15:23–49. https://doi.org/10.3390/hematolrep15010004

Ponniah K, Loo TS, Edwards PJB, et al (2010) The production of soluble and correctly folded recombinant bovine β-lactoglobulin variants A and B in Escherichia coli for NMR studies. Protein Expression and Purification 70:283–289. https://doi.org/10.1016/j.pep.2009.12.006

Poshusta T, Katoh N, Gertz M, et al (2013) Thermal Stability Threshold for Amyloid Formation in Light Chain Amyloidosis. IJMS 14:22604–22617. https://doi.org/10.3390/ijms141122604

Poshusta TL, Sikkink LA, Leung N, et al (2009) Mutations in Specific Structural Regions of Immunoglobulin Light Chains Are Associated with Free Light Chain Levels in Patients with AL Amyloidosis. PLoS ONE 4:e5169. https://doi.org/10.1371/journal.pone.0005169

Prade E, Zeck A, Stiefel F, et al (2021) Cysteine in cell culture media induces acidic IgG1 species by disrupting the disulfide bond network. Biotech & Bioengineering 118:1091–1104. https://doi.org/10.1002/bit.27628

Rajkumar SV (2024) Multiple myeloma: 2024 update on diagnosis, risk-stratification, and management. American J Hematol 99:1802–1824. https://doi.org/10.1002/ajh.27422

Rajkumar SV, Dimopoulos MA, Palumbo A, et al (2014) International Myeloma Working Group updated criteria for the diagnosis of multiple myeloma. The Lancet Oncology 15:e538–e548. https://doi.org/10.1016/S1470-2045(14)70442-5

Ralston GB (1993) Introduction to analytical ultracentrifugation. Beckman California:

Ramakrishnan V, Kumar S (2018) PI3K/AKT/mTOR pathway in multiple myeloma: from basic biology to clinical promise. Leukemia & Lymphoma 59:2524–2534. https://doi.org/10.1080/10428194.2017.1421760

Rennella E, Morgan GJ, Kelly JW, Kay LE (2019) Role of domain interactions in the aggregation of full-length immunoglobulin light chains. Proc Natl Acad Sci USA 116:854–863. https://doi.org/10.1073/pnas.1817538116

Rettenbacher LA, Von Der Haar T (2022) A quantitative interpretation of oxidative protein folding activity in Escherichia coli. Microb Cell Fact 21:268. https://doi.org/10.1186/s12934-022-01982-3

Ríos-Tamayo R, Krsnik I, Gómez-Bueno M, et al (2023) AL Amyloidosis and Multiple Myeloma: A Complex Scenario in Which Cardiac Involvement Remains the Key Prognostic Factor. Life 13:1518. https://doi.org/10.3390/life13071518

Rognoni P, Lavatelli F, Casarini S, et al (2013) A Strategy for Synthesis of Pathogenic Human Immunoglobulin Free Light Chains in E. coli. PLoS ONE 8:e76022. https://doi.org/10.1371/journal.pone.0076022

Roksnoer LCW, Heijnen BFJ, Nakano D, et al (2016) On the Origin of Urinary Renin: A Translational Approach. Hypertension 67:927–933. https://doi.org/10.1161/HYPERTENSIONAHA.115.07012

Rosano GL, Ceccarelli EA (2014) Recombinant protein expression in Escherichia coli: advances and challenges. Front Microbiol 5:. https://doi.org/10.3389/fmicb.2014.00172

Roth DB (2014) V(D)J Recombination: Mechanism, Errors, and Fidelity. Microbiol Spectr 2:2.6.18. https://doi.org/10.1128/microbiolspec.MDNA3-0041-2014

Rottenaicher GJ, Weber B, Rührnößl F, et al (2021) Molecular mechanism of amyloidogenic mutations in hypervariable regions of antibody light chains. Journal of Biological Chemistry 296:100334. https://doi.org/10.1016/j.jbc.2021.100334

Roussel A, Spinelli S, Déret S, et al (1999) The structure of an entire noncovalent immunoglobulin kappa light-chain dimer (Bence-Jones protein) reveals a weak and unusual constant domains association. European Journal of Biochemistry 260:192–199. https://doi.org/10.1046/j.1432-1327.1999.00136.x

Sabate R, De Groot NS, Ventura S (2010) Protein folding and aggregation in bacteria. Cell Mol Life Sci 67:2695–2715. https://doi.org/10.1007/s00018-010-0344-4

Saez NJ, Cristofori-Armstrong B, Anangi R, King GF (2017) A Strategy for Production of Correctly Folded Disulfide-Rich Peptides in the Periplasm of E. coli. In: Burgess-Brown NA (ed) Heterologous Gene Expression in E.coli. Springer New York, New York, NY, pp 155–180

Sakai T, Mashima T, Kobayashi N, et al (2023) Structural and thermodynamic insights into antibody light chain tetramer formation through 3D domain swapping. Nat Commun 14:7807. https://doi.org/10.1038/s41467-023-43443-4

Sandomenico A, Sivaccumar JP, Ruvo M (2020) Evolution of Escherichia coli Expression System in Producing Antibody Recombinant Fragments. IJMS 21:6324. https://doi.org/10.3390/ijms21176324

Sarto C, Intra J, Fania C, et al (2021) Monoclonal free light chain detection and quantification: Performances and limits of available laboratory assays. Clinical Biochemistry 95:28–33. https://doi.org/10.1016/j.clinbiochem.2021.05.006

Sathick IJ, Drosou ME, Leung N (2019) Myeloma light chain cast nephropathy, a review. J Nephrol 32:189–198. https://doi.org/10.1007/s40620-018-0492-4

Schäfer U, Beck K, Müller M (1999) Skp, a Molecular Chaperone of Gram-negative Bacteria, Is Required for the Formation of Soluble Periplasmic Intermediates of Outer Membrane Proteins. Journal of Biological Chemistry 274:24567–24574. https://doi.org/10.1074/jbc.274.35.24567

Schiffrin B, Brockwell DJ, Radford SE (2017) Outer membrane protein folding from an energy landscape perspective. BMC Biol 15:123. https://doi.org/10.1186/s12915-017-0464-5

Schrödinger, LLC (2015) The PyMOL Molecular Graphics System, Version 1.8

Schroeder HW, Cavacini L (2010) Structure and function of immunoglobulins. Journal of Allergy and Clinical Immunology 125:S41–S52. https://doi.org/10.1016/j.jaci.2009.09.046

Schuck P (2000) Size-distribution analysis of macromolecules by sedimentation velocity ultracentrifugation and lamm equation modeling. Biophys J 78:1606–1619. https://doi.org/10.1016/S0006-3495(00)76713-0

Schuck P (2016) Sedimentation Velocity Analytical Ultracentrifugation: Discrete Species and Size-Distributions of Macromolecules and Particles, 0 edn. CRC Press

Schuck P (2010) Sedimentation Patterns of Rapidly Reversible Protein Interactions. Biophysical Journal 98:2005–2013. https://doi.org/10.1016/j.bpj.2009.12.4336

Schuck P, Perugini MA, Gonzales NR, et al (2002) Size-Distribution Analysis of Proteins by Analytical Ultracentrifugation: Strategies and Application to Model Systems. Biophysical Journal 82:1096–1111. https://doi.org/10.1016/S0006-3495(02)75469-6

Schuck P, Zhao H (2017) Sedimentation velocity analytical ultracentrifugation: interacting systems. CRC Press

Schuck P, Zhao H, Brautigam CA, Ghirlando R (2016) Basic principles of analytical ultracentrifugation. CRC Press Boca Raton, FL

Schütz A, Bernhard F, Berrow N, et al (2023) A concise guide to choosing suitable gene expression systems for recombinant protein production. STAR Protocols 4:102572. https://doi.org/10.1016/j.xpro.2023.102572

Scott D, Harding SE, Rowe A (2007) Analytical ultracentrifugation: techniques and methods. Royal Society of Chemistry

Sequeira MA, Herrera MG, Dodero VI (2019) Modulating amyloid fibrillation in a minimalist model peptide by intermolecular disulfide chemical reduction. Phys Chem Chem Phys 21:11916–11923. https://doi.org/10.1039/C9CP01846H

Sevier CS, Kaiser CA (2002) Formation and transfer of disulphide bonds in living cells. Nat Rev Mol Cell Biol 3:836–847. https://doi.org/10.1038/nrm954

Shi J, Guan J, Jiang B, et al (2010) Amyloidogenic light chains induce cardiomyocyte contractile dysfunction and apoptosis via a non-canonical p38α MAPK pathway. Proc Natl Acad Sci USA 107:4188–4193. https://doi.org/10.1073/pnas.0912263107

Siegel D, Bilotti E, Van Hoeven KH (2009) Serum Free Light Chain Analysis for Diagnosis, Monitoring, and Prognosis of Monoclonal Gammopathies. Lab Med 40:363–366. https://doi.org/10.1309/LMPHODC7R1L0MEWW

Sikkink LA, Ramirez-Alvarado M (2008) Salts enhance both protein stability and amyloid formation of an immunoglobulin light chain. Biophysical Chemistry 135:25–31. https://doi.org/10.1016/j.bpc.2008.02.019

Singh A, Upadhyay V, Upadhyay AK, et al (2015) Protein recovery from inclusion bodies of Escherichia coli using mild solubilization process. Microb Cell Fact 14:41. https://doi.org/10.1186/s12934-015-0222-8

Sirac C, Batuman V, Sanders PW (2021) The Proximal Tubule Toxicity of Immunoglobulin Light Chains. Kidney International Reports 6:1225–1231. https://doi.org/10.1016/j.ekir.2021.02.026

Sölling K (1976) Polymeric Forms of Free Light Chains in Serum from Normal Individuals and from Patients with Renal Diseases. Scandinavian Journal of Clinical and Laboratory Investigation 36:447–452. https://doi.org/10.3109/00365517609054462

Solomon A, Waldmann TA, Fahey JL, McFarlane AS (1964) Metabolism of Bence Jones Proteins*. J Clin Invest 43:103–117. https://doi.org/10.1172/JCI104884

Solomon A, Weiss DT, Murphy CL, et al (1998) Light chain-associated amyloid deposits comprised of a novel κ constant domain. Proc Natl Acad Sci USA 95:9547–9551. https://doi.org/10.1073/pnas.95.16.9547

Sternke-Hoffmann R (2021) Looking for a white cat in a snowstorm-In depth thermodynamic and aggregation fingerprinting of patient-derived IgG light chains

Sternke-Hoffmann R, Boquoi A, Lopez Y. Niedenhoff D, et al (2020) Biochemical and biophysical characterisation of immunoglobulin free light chains derived from an initially unbiased population of patients with light chain disease. PeerJ 8:e8771. https://doi.org/10.7717/peerj.8771

Sternke-Hoffmann R, Pauly T, Norrild RK, et al (2023) Widespread amyloidogenicity potential of multiple myeloma patient-derived immunoglobulin light chains. BMC Biol 21:21. https://doi.org/10.1186/s12915-022-01506-w

Stevens PW, Raffen R, Hanson DK, et al (1995) Recombinant immunoglobulin variable domains generated from synthetic genes provide a system for in vitro characterization of light-chain amyloid proteins. Protein Science 4:421–432. https://doi.org/10.1002/pro.5560040309

Structural Genomics Consortium, Architecture et Fonction des Macromolécules Biologiques, Berkeley Structural Genomics Center, et al (2008) Protein production and purification. Nat Methods 5:135–146. https://doi.org/10.1038/nmeth.f.202

Sun H, Lou X, Shan Q, et al (2013) Proteolytic Characteristics of Cathepsin D Related to the Recognition and Cleavage of Its Target Proteins. PLoS ONE 8:e65733. https://doi.org/10.1371/journal.pone.0065733

Sun L-J, Dong H-R, Xu X-Y, et al (2021) Two kinds of rare light chain cast nephropathy caused by multiple myeloma: case reports and literature review. BMC Nephrol 22:42. https://doi.org/10.1186/s12882-021-02250-z

Svedberg T, Fåhraeus R (1926) A new method for the determination of the molecular weight of the proteins. Journal of the American Chemical Society 48:430–438

Svedberg T, Nichols JB (1923) Determination of size and distribution of size of particle by centrifugal methods. Journal of the American Chemical Society 45:2910–2917

Svedberg T, Rinde H (1924) The ultra-centrifuge, a new instrument for the determination of size and distribution of size of particle in amicroscopic colloids. Journal of the American Chemical Society 46:2677–2693

Tan E, Chin CSH, Lim ZFS, Ng SK (2021) HEK293 Cell Line as a Platform to Produce Recombinant Proteins and Viral Vectors. Front Bioeng Biotechnol 9:796991. https://doi.org/10.3389/fbioe.2021.796991

Tasbihi K, Bruns H (2025) Selinexor's Immunomodulatory Impact in Advancing Multiple Myeloma Treatment. Cells 14:430. https://doi.org/10.3390/cells14060430

Taylor EB, Ryan MJ (2019) Freedom isn't always free: immunoglobulin free light chains promote renal fibrosis. Journal of Clinical Investigation 129:2660–2662. https://doi.org/10.1172/JCI129704

Theillet F-X, Binolfi A, Frembgen-Kesner T, et al (2014) Physicochemical Properties of Cells and Their Effects on Intrinsically Disordered Proteins (IDPs). Chem Rev 114:6661–6714. https://doi.org/10.1021/cr400695p

Thio M, Blokhuis B, Nijkamp F, Redegeld F (2008) Free immunoglobulin light chains: a novel target in the therapy of inflammatory diseases. Trends in Pharmacological Sciences 29:170–174. https://doi.org/10.1016/j.tips.2008.01.004

Thomas JA, Chai Y-C, Jung C-H (1994) [42] Protein S-thiolation and dethiolation. In: Methods in Enzymology. Elsevier, pp 385–395

Tripathi NK, Shrivastava A (2019) Recent Developments in Bioprocessing of Recombinant Proteins: Expression Hosts and Process Development. Front Bioeng Biotechnol 7:420. https://doi.org/10.3389/fbioe.2019.00420

Tu BP, Weissman JS (2004) Oxidative protein folding in eukaryotes. The Journal of Cell Biology 164:341–346. https://doi.org/10.1083/jcb.200311055

Tucholski FT, Sternke-Hoffmann R, Pauly T, et al (2025) Tracking reduction-induced molecular changes in pathological free light chains by SV-AUC. Eur Biophys J. https://doi.org/10.1007/s00249-025-01788-2

Turk V (2001) NEW EMBO MEMBERS' REVIEW: Lysosomal cysteine proteases: facts and opportunities. The EMBO Journal 20:4629–4633. https://doi.org/10.1093/emboj/20.17.4629

Turk V, Stoka V, Vasiljeva O, et al (2012) Cysteine cathepsins: From structure, function and regulation to new frontiers. Biochimica et Biophysica Acta (BBA) - Proteins and Proteomics 1824:68–88. https://doi.org/10.1016/j.bbapap.2011.10.002

Uversky VN (2014) Introduction to Intrinsically Disordered Proteins (IDPs). Chem Rev 114:6557–6560. https://doi.org/10.1021/cr500288y

Van De Donk NWCJ, Pawlyn C, Yong KL (2021) Multiple myeloma. The Lancet 397:410–427. https://doi.org/10.1016/S0140-6736(21)00135-5

Van Holde KE, Johnson WC, Ho PS (2006) Principles of physical biochemistry

Veber A, Lenau D, Gkragkopoulou P, et al (2025) Impact of Light-Chain Variants on the Expression of Therapeutic Monoclonal Antibodies in HEK293 and CHO Cells. Antibodies 14:53. https://doi.org/10.3390/antib14030053

Von Hippel PH, Wong KY (1965) On the conformational stability of globular proteins. The effects of various electrolytes and nonelectrolytes on the thermal ribonuclease transition. J Biol Chem 240:3909–3923

Waldmann TA, Strober W, Mogielnicki RP (1972) The renal handling of low molecular weight proteins. J Clin Invest 51:2162–2174. https://doi.org/10.1172/JCI107023

Walker JM (ed) (2005) The Proteomics Protocols Handbook. Humana Press, Totowa, NJ

Walker KW, Gilbert HF (1994) Effect of redox environment on the in vitro and in vivo folding of RTEM-1 beta-lactamase and Escherichia coli alkaline phosphatase. Journal of Biological Chemistry 269:28487–28493. https://doi.org/10.1016/S0021-9258(18)46953-0

Wall J, Schell M, Murphy C, et al (1999) Thermodynamic Instability of Human λ6 Light Chains: Correlation with Fibrillogenicity. Biochemistry 38:14101–14108. https://doi.org/10.1021/bi991131j

Wang P-X, Sanders PW (2007) Immunoglobulin Light Chains Generate Hydrogen Peroxide. Journal of the American Society of Nephrology 18:1239–1245. https://doi.org/10.1681/ASN.2006111299

Wang SS-S, Chang C-K, Peng M-J, Liu H-S (2006) Effect of Glutathione Redox System on Lysozyme Refolding in Size Exclusion Chromatography. Food and Bioproducts Processing 84:18–27. https://doi.org/10.1205/fbp.05141

Welker E, Narayan M, Wedemeyer WJ, Scheraga HA (2001) Structural determinants of oxidative folding in proteins. Proc Natl Acad Sci USA 98:2312–2316. https://doi.org/10.1073/pnas.041615798

Willbold D, Strodel B, Schröder GF, et al (2021) Amyloid-type Protein Aggregation and Prion-like Properties of Amyloids. Chem Rev 121:8285–8307. https://doi.org/10.1021/acs.chemrev.1c00196

Wingfield PT (1995) Use of Protein Folding Reagents. CP Protein Science 00: https://doi.org/10.1002/0471140864.psa03as00

Yadati T, Houben T, Bitorina A, Shiri-Sverdlov R (2020) The Ins and Outs of Cathepsins: Physiological Function and Role in Disease Management. Cells 9:1679. https://doi.org/10.3390/cells9071679

Yadav P, Cockwell P, Cook M, et al (2018) Serum free light chain levels and renal function at diagnosis in patients with multiple myeloma. BMC Nephrol 19:178. https://doi.org/10.1186/s12882-018-0962-x

Yadav P, Cook M, Cockwell P (2015) Current Trends of Renal Impairment in Multiple Myeloma. Kidney Dis 1:241–257. https://doi.org/10.1159/000442511

Yadav P, Sathick IJ, Leung N, et al (2020) Serum free light chain level at diagnosis in myeloma cast nephropathy-a multicentre study. Blood Cancer J 10:28. https://doi.org/10.1038/s41408-020-0295-4

Yang P-C, Mahmood T (2012) Western blot: Technique, theory, and trouble shooting. North Am J Med Sci 4:429. https://doi.org/10.4103/1947-2714.100998

Ying W-Z, Li X, Rangarajan S, et al (2019) Immunoglobulin light chains generate proinflammatory and profibrotic kidney injury. Journal of Clinical Investigation 129:2792–2806. https://doi.org/10.1172/JCI125517

Ying W-Z, Wang P-X, Sanders PW (2012) Pivotal Role of Apoptosis Signal-Regulating Kinase 1 in Monoclonal Free Light Chain–Mediated Apoptosis. The American Journal of Pathology 180:41–47. https://doi.org/10.1016/j.ajpath.2011.09.017

Yuzhalin AE, Lim SY, Kutikhin AG, Gordon-Weeks AN (2018) Dynamic matrisome: ECM remodeling factors licensing cancer progression and metastasis. Biochimica et Biophysica Acta (BBA) - Reviews on Cancer 1870:207–228. https://doi.org/10.1016/j.bbcan.2018.09.002

Zanetti M, Capra JD (eds) (1999) The Antibodies, 1st edn. CRC Press

Zerfaß C, Buchko GW, Shaw WJ, et al (2017) Secondary structure and dynamics study of the intrinsically disordered silica-mineralizing peptide P_5 S_3 during silicic acid condensation and silica decondensation. Proteins 85:2111–2126. https://doi.org/10.1002/prot.25366

Zhang L, Chou CP, Moo-Young M (2011) Disulfide bond formation and its impact on the biological activity and stability of recombinant therapeutic proteins produced by Escherichia coli expression system. Biotechnology Advances 29:923–929. https://doi.org/10.1016/j.biotechadv.2011.07.013

Zhang Y, Wang Y, Li Y (2019) Major cause of antibody artifact bands on non-reducing SDS-PAGE and methods for minimizing artifacts. Protein Expression and Purification 164:105459. https://doi.org/10.1016/j.pep.2019.105459

Zhang Z, Li Z-H, Wang F, et al (2002) Overexpression of DsbC and DsbG markedly improves soluble and functional expression of single-chain Fv antibodies in Escherichia coli. Protein Expression and Purification 26:218–228. https://doi.org/10.1016/S1046-5928(02)00502-8

Zhao J, Zhang B, Zhu J, et al (2018) Structure and energetic basis of overrepresented λ light chain in systemic light chain amyloidosis patients. Biochimica et Biophysica Acta (BBA) - Molecular Basis of Disease 1864:2294–2303. https://doi.org/10.1016/j.bbadis.2017.12.009

Zheng Z, Chinnasamy N, Morgan RA (2012) Protein L: a novel reagent for the detection of Chimeric Antigen Receptor (CAR) expression by flow cytometry. J Transl Med 10:29. https://doi.org/10.1186/1479-5876-10-29

Zorlu T, Kayer MA, Okumus N, et al (2025) Challenges, Difficulties, and Delayed Diagnosis of Multiple Myeloma. Diagnostics 15:1708. https://doi.org/10.3390/diagnostics15131708

Zou C, Lu L, Wang S, et al (2022) The α-mating factor secretion signals and endogenous signal peptides for recombinant protein secretion in Komagataella phaffii. Biotechnol Biofuels 15:140. https://doi.org/10.1186/s13068-022-02243-6

List of figures

List of tables

Declaration of independence

I declare under oath that I have compiled this dissertation independently and without any undue assistance by third parties under consideration of the "Fundamental principles for safeguarding good scientific practice at Heinrich Heine University Düsseldorf". Furthermore, neither this dissertation, nor a similar work, has been submitted to another faculty. I have not made any unsuccessful attempt to obtain a doctorate.

Düsseldorf, April 11, 2026

_____

Florian T. Tucholski